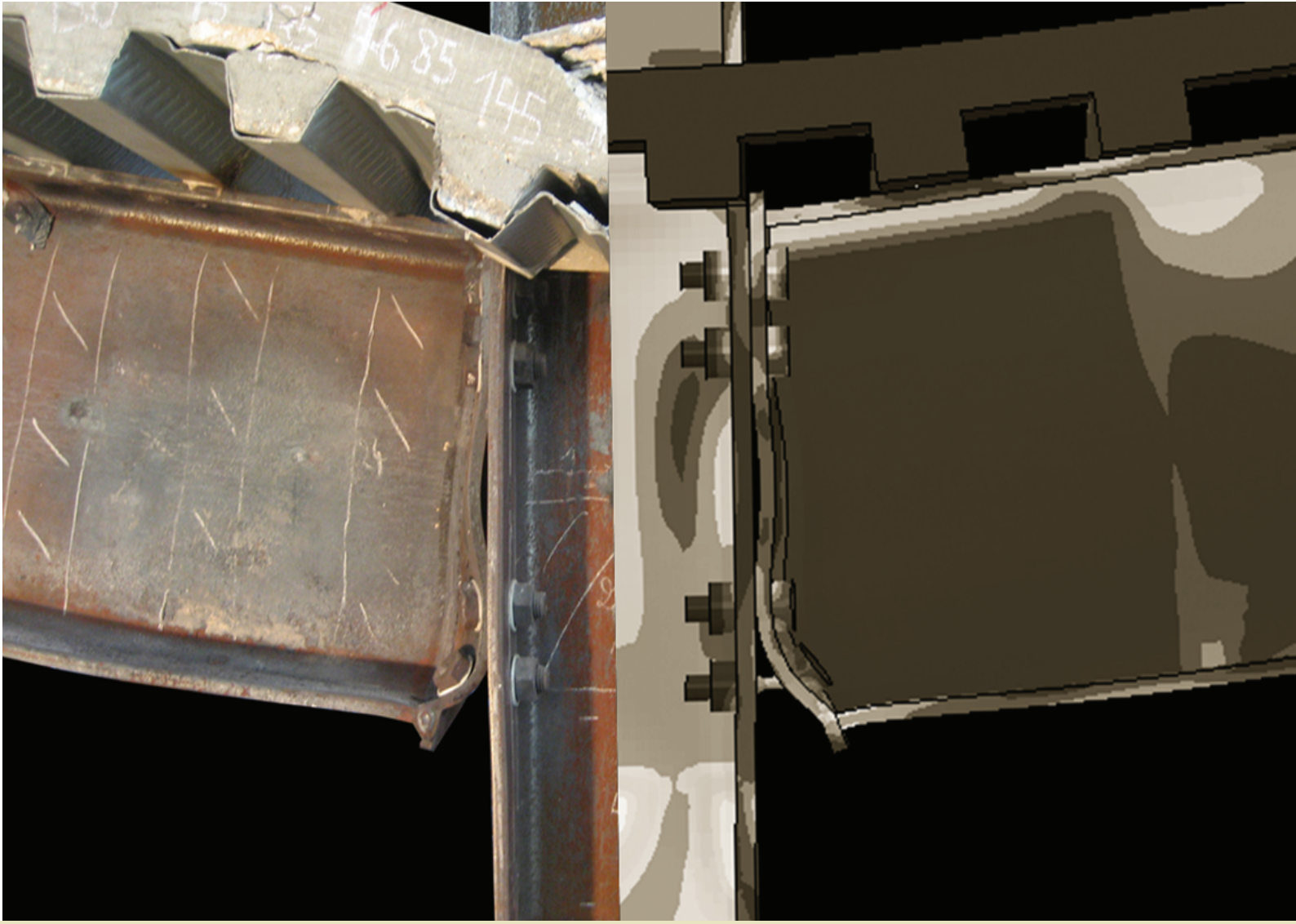

Cécile Haremza

ROBUSTNESS OF OPEN CAR PARKS UNDER LOCALISED FIRE

Tese de Doutoramento em Construção Metálica e Mista, orientada pela Professora Doutora Aldina Maria da Cruz Santiago, apresentada ao Departamento de Engenharia Civil da Faculdade de Ciências e Tecnologia da Universidade de Coimbra

Outubro, 2014

· U C ·

UNIVERSIDADE DE COIMBRA

Cécile Haremza

ROBUSTNESS OF OPEN CAR PARKS UNDER LOCALISED FIRE

Tese de Doutoramento em Construção Metálica e Mista, orientada pela Professora Doutora Aldina Maria da Cruz Santiago, apresentada ao Departamento de Engenharia Civil da Faculdade de Ciências e Tecnologia da Universidade de Coimbra

Outubro, 2014

UNIVERSIDADE DE COIMBRA

Doctoral Thesis in Civil Engineering defended January 6th, 2015, and approved *Summa Cum Laude*

President of the jury:

Luís Alberto P. Simões da Silva, Professor of the University of Coimbra, Portugal

Members of the jury:

Ali Nadjai, Professor of the School Built Environment, Belfast, United Kingdom

Paulo Jorge de M. M. Faria de Vila Real, Professor of the University of Aveiro, Portugal

João Pedro Ramôa Ribeiro Correia, Professor of the Instituto Superior Técnico, Lisbon, Portugal

João Paulo Correia Rodrigues, Professor of the University of Coimbra, Portugal

Rui António Duarte Simões, Professor of the University of Coimbra, Portugal

Aldina Maria da Cruz Santiago, Professor of the University of Coimbra, Portugal (supervisor)

Coimbra (Portugal), January 2015

FCTUC DEPARTAMENTO DE ENGENHARIA CIVIL
FACULDADE DE CIÊNCIAS E TECNOLOGIA
UNIVERSIDADE DE COIMBRA

Robustness of open car parks under localised fire

Tese apresentada para obtenção do grau de Doutor em Construção Metálica e Mista

Thesis presented in fulfillment of the requirements for the degree of Doctor of Philosophy in Steel and Mixed Construction

Autora

Cécile Haremza

Orientadora

Professora Doutora Aldina Maria da Cruz Santiago

ISISE, Departamento de Engenharia Civil – Universidade de Coimbra

Coimbra, 2014

In memory of my father,

Alain Haremza

RESUMO

O número crescente de carros a circularem na Europa nas últimas décadas, bem como o aumento de grandes centros comerciais, aeroportos e estações ferroviárias, aumentou consideravelmente o número de parques de estacionamento abertos. Uma maneira fácil e de baixo custo para a construção é a utilização de uma estrutura mista aço-betão. Em situação de incêndio, a combustão generalizada (flash-over) é improvável de ocorrer nesses espaços abertos, e devem ser considerados incêndios localizados. Um incêndio localizado, que se desenvolve num parque de estacionamento misto sem protecção contra incêndio, conduz ao aquecimento dos elementos estruturais mais próximos do incêndio: ligações, vigas e colunas. O colapso de uma coluna sujeita a incêndio localizado provoca grandes deslocamentos verticais nos andares superiores. Para atingir um equilíbrio nesta configuração deformada, e assim evitar o colapso progressivo do edifício, desenvolvem-se forças de membrana nas lajes e nas vigas. Portanto, durante este evento, as ligações viga-coluna estão sujeitas a sequências particulares de carregamento, envolvendo principalmente momentos flectores e esforços axiais. Essas ligações devem resistir à nova distribuição de esforços e ter ductilidade suficiente para poder sustentar grandes rotações, sem rupturas. Para tal, a estrutura deve ser dimensionada tendo em conta a robustez necessária para este evento acidental.

O trabalho de investigação apresentado nesta tese está inserido no projecto Europeu RFCS ROBUSTFIRE, e no projecto Nacional IMPACTFIRE. As diversas fases deste trabalho estão relacionadas com um caso de estudo que envolve uma configuração estrutural de um edifício típico de parque de estacionamento aberto. O cenário considerado é o colapso de uma coluna devido a um incêndio localizado (combustão de veículos), e são consideradas as restrições axiais devidas à estrutura não afectada pelo incêndio. Este trabalho tem como principal objectivo o estudo detalhado do comportamento de uma ligação mista aço-betão viga-coluna com placa de extremidade, aquecida pelo incêndio localizado, quando está sujeita a momentos flectores e esforços axiais variáveis. Numa fase inicial, realiza-se uma revisão das regras práticas actuais, e o estado da arte sobre a concepção e avaliação de parques de estacionamento abertos sujeitos a um incêndio localizado. Em seguida, a investigação centra-se em estudos experimentais, numéricos e analíticos:

i) Realizam-se sete ensaios experimentais em ligações mistas aço-betão viga-pilar sob diferentes combinações de momentos flectores e esforços axiais, considerando não só condições isotérmicas, mas também um cenário de temperatura transitória.

ii) Desenvolvem-se modelos numéricos 3D detalhados da ligação mista, de forma a reproduzir os ensaios experimentais.

iii) Finalmente, é estudada a influência de alguns parâmetros que afectam a robustez deste tipo de edifícios (tais como temperatura, vão da viga, tamanho da ligação, etc....), usando os modelos numéricos desenvolvidos e um procedimento analítico existente na bibliografia.

Em conclusão, devido à reduzida esbelteza da viga mista, são necessárias grandes deformações para que se observe o desenvolvimento de forças de membrana, e nestas condições, esta tipologia de ligação mista não possui capacidade de rotação suficiente para alcançar o equilíbrio na configuração deformada.

Palavras-Chave

Ligação mista aço-betão | Incêndio localizado | Interacção momento flector-esforço axial | Ensaios experimentais | Análises numéricas

ABSTRACT

The growing number of cars in Europe during the last decades, as well as the amount of large shopping centres, airports and railway stations, have considerably increased the number of open car park buildings. An easy and low cost way for the construction of these open car park buildings is to use a composite steel-concrete structure. Under fire situation, flash-over is unlikely to occur in these opened compartments and localised fires should be considered. When a localised fire develops in an unprotected steel composite car park, it leads to the heating of some of the nearby structural elements: connections, beams and columns. The loss of a column under localised fire induces large vertical displacements in the above floors. To reach equilibrium in the deformed configuration and avoid progressive collapse of the building, membrane forces in the slabs, and catenary forces in beam elements should develop. So, during the event, the beam-to-column connections are subject to particular load sequences mainly involving bending moments and axial forces. These connections are also required to have sufficient ductility in order to sustain large rotations without brittle damages. Therefore, sufficient robustness should be provided to the structure at the design stage.

The research work presented in this thesis is based on the European RFCS ROBUSTFIRE project, and the National IMPACTFIRE project. The various stages of this work are related to a case study involving a structural configuration that represents a typical open car park building. The considered scenario is the loss of a column due to a localised fire (burning cars), and the strong restraints to the beams provided by part of the building not directly affected by this accident are taken into account. The behaviour of steel-concrete composite beam-to-column joints in open car park buildings under column loss scenario, due to fire, is investigated in detail. The main objective is to provide a detailed analysis of the heated joint behaviour subject to variable bending moments and axial loads when the column fails. First, a review of current practice and state of the art in the design and assessment of open car parks subject to localised fire is performed. Then the investigation is based on experimental, numerical and analytical results:

i) Seven experimental tests are performed on composite steel-concrete beam-to-column joints under different combinations of bending moments and axial forces, considering isothermal conditions, and also one transient temperature scenario.

ii) Detailed 3D numerical models of the heated joint are developed to reproduce the experimental tests.

iii) Finally, the influence of some parameters that affect the robustness of this type of building (such as temperature, beam span, joint size, etc.…) are studied using the developed numerical models and an existing analytical procedure.

In conclusion, due to the low slenderness of the composite beam, high deformations are necessary to develop catenary action, and in these conditions, this topology of composite joint does not possess sufficient capacity of rotation to reach the equilibrium deformed configuration.

Keywords:

Steel-concrete joint | Localised fire | Bending moment-axial force interaction | Experimental tests | Numerical analysis

ACKNOWLEDGEMENTS

I would like to express my gratitude and appreciation to Professor Aldina Santiago for her excellent guidance, supervision, dedication and support throughout the years I have spent working with her; it was very enriching and also a real pleasure. Her experience in the field of structural fire engineering has also been a precious source of inspiration. The advices and comments of Professor Luís Simões da Silva have been a considerable help and of great value for the successful completion of this work.

Financial support from the European Union (Research Fund for Coal and Steel) under contract grant RFSR-CT-2008-00036 (ROBUSTFIRE project), and from Ministério da Educação e da Ciência (Fundação para a Ciência e a Tecnologia) for the research project IMPACTFIRE (PTDC/ECM/110807/2009), and material support provided by PECOL, FELIZ and MARTIFER are gratefully acknowledged. I would also like to express my gratitude to the partners of the ROBUSTFIRE project from the University of Liège, Imperial College London, Arcelor Profil Luxembourg, CSTB, Greisch Ingénierie, and CTICM for their interesting discussions and input in this work; a special thanks goes to Dr. Jean-François Demonceau (University of Liège) for sharing his experience and knowledge.

The assistance provided by Luís Gaspar, Rui Ferreira, Senhor David, Fernando Rodrigues, Nuno Torres, Francisco Sousa and Filipe Cruz, the former and current technical staff of the Laboratory of Structures of University of Coimbra was most appreciated for their advice, comments and commitment to experimental set-up and execution of the experimental tests.

A thank you to my former and current colleagues of the group of "Mecânica estrutural - ISISE" of the University of Coimbra for the interesting discussions, supports and great moments we have shared, at and outside work. Special thanks to Fernanda, for her support during the tough time we spent in the laboratory.

A special thanks goes to my family and friends for their continuous support, patience and for agreeing to let me live far from Belgium for many years; and also thanks to my Portuguese family for being present whenever needed. I apologize for my absences and the lack of time and attention that I should have given to all of you. Thank you Xano for your helpful technical advice, your support and encouragement during my bad moments, for your cheerfulness, patience and love; thank you for always being at my side. Et enfin, merci Théo de m'avoir donné toute l'énergie et la motivation pour terminer cette thèse grâce à tes magnifiques sourires !

TABLE OF CONTENTS

NOTATIONS

Lowercases

b_c	Width of the column cross-section
b_{eff}	Effective width of the concrete/composite slab in the vicinity of the joint
$b_{eff,conn}$	Width of the concrete/composite slab contributing to the joint behaviour
$b_{eff,c,wc}$	Effective width of column web in compression
$b_{eff,t,wb}$	Effective length of the equivalent T-stub representing the end-plate in bending
d	Distance from the extreme fibre of the design compression zone to the extreme fibre of the design tensile zone of the structural section
f_{cd}	Design value of the cylinder compressive strength of concrete
f_{ck}	Characteristic value of the cylinder compressive strength of concrete at 28 days
$f_{ck,cube}$	Concrete cube compressive strength
f_{cm}	Mean value of concrete cylinder compressive strength
f_{ct}	Axial tensile strength of concrete
f_u	Ultimate resistance of the connection component
$f_{u,\theta,steel}$	Steel ultimate strength at temperature θ
f_y	Yield strength
$f_{y,\theta,steel}$	Steel yield strength at temperature θ
$f_{y,wb}$	Yield strength of the beam web
h	Initial height of the column
$\dot{h}$	Heat flux received by the unit of surface area exposed to fire at the ceiling level
h_c	Height of the column cross-section
h_i	Distance between row i and the reference axis

$\dot{h}_{net}$	Net heat flux received by the fire exposed unit surface area at the level of the ceiling
h_{Rf}	Horizontal distance between the beam support and half of the column flange thickness
k_1	Adjustment factor: non-uniformity of temperature in the section
k_2	Adjustment factor: non-uniformity of temperature along the beam
k_{wc}	Reduction factor due to the longitudinal compressive stress in the column
q_k	Uniformly distributed load
r	Horizontal distance between the vertical axis of the fire and the point along the ceiling where the thermal flux is calculated
t_{wb}	Beam web thickness
y	Parameter from Hasemi's method
z	Height along the flame axis (Heskestad method) / Distance between the centre of compression and the centre of tension
z_0	Virtual origin of z axis (Heskestad method)
z'	Vertical position of the virtual heat source (Hasemi's method)
z_{conc}	thickness of the concrete/composite slab contributing to the joint behaviour

Uppercases

A_d	Design value of indirect actions from fire
D	Diameter of the fire
E_{cm}	Secant modulus of elasticity of concrete
F	Vertical load applied to the specimen
F_{Ed}	Compression load
$F_{Rd,i}$	Force sustained by row i
F_{Rd}^{-}	Ultimate resistance of the row, when the joint is subject to hogging bending moment
F_{Rd}^{+}	Ultimate resistance of the row, when the joint is subject to sagging bending moment
$G_{k,j}$	Characteristic values of permanent actions j

H	Vertical distance between the fire source and the surface area exposed to fire at the ceiling level
H_s	Vertical distance between the floor and the fire source
K_a	Beam axial restraint stiffness
L	Span of the beam
L_h	Horizontal length of the flame
L_f	Vertical length of the flame
M	Bending moment
M_{b1}	Applied bending moment at the beam
M_{Ed}	Design bending moment
$M_{fi,Ed}$	Design bending moment for fire situation
$M_{fi,\theta,Rd}$	Design moment resistant at temperature θ
M_{joint}	Bending moment at the joint
N	Axial load
N_b	Axial load at the beam
N_{Ed}	Design axial load
$N_{p\ell,Rd}$	design resistance
P	Design value of a prestressing load
Q	Rate of heat release of the fire
Q_c	Convective part of the rate of heat release
Q_H^*	Non-dimensional rate of heat release
Q_k	Single axis load
$Q_{k,i}$	Characteristic values of the variable actions i
R_F	Reaction load at the beam support
V_{Ed}	Mean shear

Lowercase Greek letters

α_c	Coefficient of heat transfer by convection
$\alpha_{concrete}$	Coefficient of expansion of concrete material
α_{steel}	Coefficient of expansion of steel material

β	Transformation parameter that reflects the importance of the shear in the column web panel at the point where the column web is under compression
γ_b	Partial factor for bolt
γ_c	Partial factor for concrete
γ_{M0}	Partial factor for resistance of cross-sections
γ_s	Partial factor for steel
$\gamma_{s,reinforcement}$	Partial factor for steel reinforcement
δ_{max}	Maximum vertical displacement
δ_v	Vertical displacement of the joint
$\delta_{vert,max}$	Maximum axial contraction of axially loaded elements (e.g. column)
ε_b	Strain of the bolt material
ε_c	Strain of the concrete material
$\varepsilon_{c,tension}$	Tensile strain of the concrete material
ε_f	Emissivity of the fire
ε_m	Surface emissivity of the member
ε_{nom}	Nominal strain measure
ε_s	Strain of the steel material
ε_{tru}	Logarithmic strain value
θ_{crit}	Critical temperature
θ_m	Surface temperature of the member
θ_{max}	Maximum temperature
θ_{90min}	Temperature of the member after 90 minutes of ISO fire
ϱ	Reduction factor for plate buckling
σ	Stephan Boltzmann constant
$\sigma_{com,Ed}$	Normal stresses coming from axial loading of the column
σ_{nom}	Nominal stress measures
σ_{tru}	True stress value
ϕ_{fail}	Rotation of the joint at failure

ϕ_{tens}	Required rotation of the joint from which tensile forces appear in the axial restraint to beam
$\psi_1 Q_k$	Frequent value of a variable action
$\psi_2 Q_k$	Quasi-permanent value of a variable action
ω	Reduction factor to allow for the possible effects of interaction with shear in the column web panel

Uppercase Greek letters

Φ	Configuration factor / Rotation of the connection
$\Phi_{j,u}$	Ultimate joint rotation

Abbreviations

BFC	Beam web and flange in compression
BT	Bolt in tension
BWT	Beam web in tension
C	Compression
CFB	Column flange in bending
CFJ	Composite flush end-plate joint
CSC	Concrete slab in compression
CTICM	Centre Technique Industriel de la Construction Mécanique
CWC	Column web in compression
CWS	Column web in shear
CWT	Column web in tension
EPB	End-plate in bending
ECCS	European Convention for Constructional Steelwork
FE	Finite element
FEM	Finite element method
FJ01	Flush end-plate joint n°1
FJ02	Flush end-plate joint n°2
FJ03	Flush end-plate joint n°3

FM	T-stub Failure Mode (1, 2 or 3)
INERIS	Institut National de l'Environnement Industriel et des Risques
PEEQ	Equivalent plastic strain (Abaqus results)
R	Fire resistance demands
RFCS	Research Fund for Coal and Steel
RT	Longitudinal steel reinforcement in tension
SFJ	Steel flush end-plate joint
T	Tension
TSWA	Top and seat with web angle
UFM	Ultimate failure mode

Chapter 1

1 Introduction

1.1 Overview

The growing number of cars in Europe during the last decades, as well as the number of large shopping centres, airports and railway stations, considerably increased the number of car park buildings (Le Pense, 2002). Nowadays, part of these car parks are built above the ground ("open" car parks) because of a lower price per parking place, lower energy consumption, use of natural light and natural ventilation (ArcelorMittal, 2007). Consequently, an easy and low cost way for the construction of open car park buildings is to use a composite steel-concrete structure. Steel and composite construction has also the advantages to optimise the occupation of the car park and to improve the return on investment by gaining floor area (ArcelorMittal, 1996). However, the increase of the market share for steel and composite car parks in Europe is somewhat limited by the lack of information on how these structures behave under fire. The combination between fire loading due to burning cars allow a very fast fire growth rate, but the large natural ventilation in this kind of buildings keeps the fire localised to the ignition zone. A localised fire which develops in an unprotected steel composite car park leads to the heating of some of the nearby structural elements (connections, beams and columns). This may result locally in a significant reduction of the carrying capacity of one column and subsequently to the loss of global stability of the car park. One way to prevent this type of failure consists, at the design stage, to check successively – according to the location of the fire in the structure – the stability of the structure in which one column would have been removed. Such a procedure is certainly safe but may be considered as time consuming and uneconomical. The use of active measures, as sprinklers may obviously be considered; but such a solution increases the construction costs and requires a constant maintenance. Moreover a severe fire may affect the proper functioning of these active measures. An economical alternative consists in providing the structure with sufficient robustness. In this approach, the structure is designed in such a way that an unforeseen event does not lead to a disproportionate structural collapse. In other words, the structure is designed in a usual

way, under classical loading situations, but should be able to undergo the complete or partial loss of a structural element (here a column) without losing its global stability (Figure 1.1). The development, locally in the structure, of large deformations or displacements is accepted, as long as progressive collapse is prevented (Jaspart *et al.*, 2008).

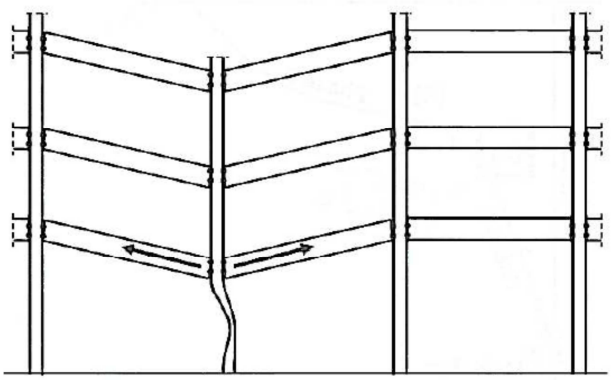

Figure 1.1: Loss of a column and development of catenary action in the beams (Jaspart *et al.*, 2011)

The loss of a column under localised fire induces large vertical displacements in the above floors, as well as high membrane forces in slabs, and catenary forces in beam elements. In addition, during this event, the beam-to-column joints are subject to particular load sequences involving bending moments, shear forces and axial forces (M-V-N interactions). In order to behave properly in such conditions, structural redundancy and local ductility at elevated temperatures are required from the various structural elements. Ductility of joints is mainly required in order to avoid brittle damages and to dissipate energy by undergoing large deformations after initial yielding without any significant reduction in strength. Ductility in a system can be achieved by enabling the joints to provide large rotations, so that membrane forces in the members can be activated, allowing a redistribution of internal forces. These joints, heated by localised fire, are subject to varying bending moments (decrease or even inversion of bending moment), combined to axial tensile loads.

The work presented in the thesis herein is developed within the ROBUSTFIRE project, a European Research Fund for Coal and Steel (RFCS) project. The various stages of this work are related in a case study involving a structural configuration that represents a typical open car park building, and the considered scenario is the loss of a column due to a localised fire (burning cars). This structural configuration heated by the localised fire and subject to the column loss scenario is the focus of experimental work and validation of numerical models. Some parameters that influence the robustness of such a building are also studied using the developed models. The experimental tests are performed on composite steel-concrete beam-to-column joints under different combinations of bending moments and axial forces, considering mainly isothermal conditions, but also one case of transient temperature scenario.

The next section (1.2) introduces the behaviour of beam-to-column joints: the component method defined in Eurocodes is reminded, and the behaviour of joints in accidental situation (fire and/or column loss scenario) is described.

1.2 Behaviour of beam-to-column joints

1.2.1 The component method

The component method is an analytical approach to design and characterize steel and composite joints. This method was first developed for steel bolted beam-to-column connections by Zoetemeijer (1974). Later, the efficiency and accuracy of the approach was highly recognized and implemented in the European codes (EN 1993-1-8, 2005; and EN 1994-1-1, 2004). The full behaviour of partial semi-rigid joint behaviour is described in Jaspart (1999).

The basic principle of the method consists in determining the complex non-linear response of the joint through the subdivision into basic components. These components represent specific parts of a joint; they contribute to one or more structural properties of the joint, and they are activated either in tension, in compression or in shear. Each basic component is characterized by a nonlinear force-displacement response, which can be obtained by means of experimental tests or analytical expressions, and each one is modelled by means of translational springs. The moment-rotation response of a whole joint can be evaluated by assembling, into a mechanical model, all the individual components. The spring model for a composite steel-concrete joint subject to hogging bending moment developed by Fang *et al.* (2011) is shown in Figure 1.2; each spring represents a basic component identified in Table 1.1.

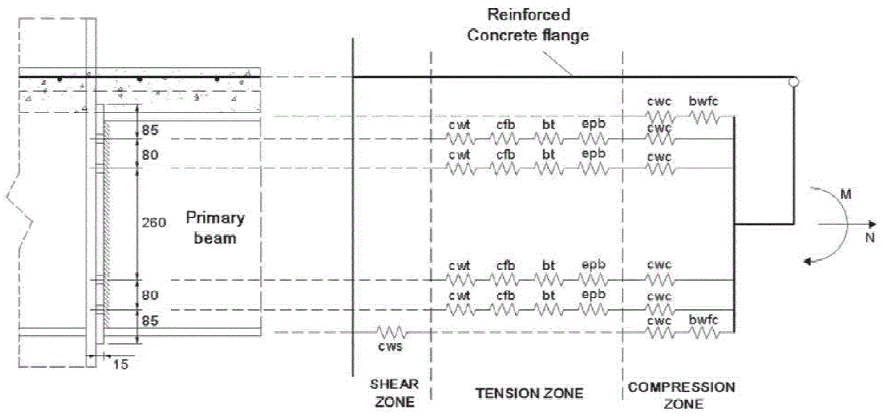

Figure 1.2: Spring model for a composite steel-concrete joint subject to hogging bending moment and axial tension load (Fang *et al.*, 2011)

The application of a global plastic analysis requires the evaluation of the rotation capacity for both members and joints, and the available rotation capacity of a joint depends on the available deformation capacity of its components. The load-deformation behaviour

of the basic components can be distinguished in three classes due to their mode of failure (Simões da Silva *et al.*, 2001), with high ductility (e.g. CFB/EPB), limited ductility (e.g. CWC), or brittle ductility (e.g. BT).

Table 1.1: List of the basic components that are part of composite steel-concrete flush end-plate joint

Joint component		Zone
Steel reinforcement in tension	RT	Tension zone
End-plate in bending	EPB	
Column flange in bending	CFB	
Column web in transverse tension	CWT	
Beam web in tension	BWT	
Bolts in tension	BT	
Concrete slab in compression	CSC	Compression zone
Beam flange and web in compression	BFC	
Column web in transverse compression	CWC	
Column web panel in shear	CWS	Shear zone

The two components specific to composite steel-concrete joints (Table 1.1) are: *longitudinal steel reinforcement in tension* (under hogging bending moment) and *concrete slab in compression* (under sagging bending moment). The behaviour of longitudinal steel reinforcement in tension may be assumed as elasto-perfectly-plastic and may be stressed up to its design yield strength (EN 1994-1-1, 2004). It is assumed that all the reinforcement within the effective width of the concrete flange is used to transfer forces, and the layers of longitudinal reinforcement bars in the composite slab are assumed as bolt-rows in tension. Regarding the deformation of the component, the code provides stiffness coefficients for two composite joint configurations, single and double-sided joints. This stiffness coefficient depends essentially on the elongation length of the longitudinal reinforcement contributing to its deformation. In terms of deformation capacity, depending on the steel ductility class, higher or lower deformation capacity may be obtained. To ensure ductility for a plastic distribution of forces, reinforcement bars ductility class B or C should be used (Demonceau, 2008). When the composite joint is subject to sagging bending moment (bottom row in tension), the concrete slab component is activated under compression; but no formula is provided in EN 1994-1-1 (2004) to define resistance and stiffness. Recently, analytical formula to consider concrete slab component resistance was provided by Demonceau (2008) (see chapter 5).

1.2.2 Behaviour of joints under fire

Traditionally, beam-to-column joints were assumed to have sufficient fire resistance due to cooler temperatures and slower rate of heating, caused by the concentration of mass on

the joint area; two reviews of past research works are described in Simões da Silva *et al.* (2005) and Al-Jabri *et al.* (2008). The behaviour of steel and composite joints under nominal temperature-time curves or Natural fire conditions (including heating and cooling phases) has been largely studied based on experimental, numerical and analytical research works. Real fires and experimental observations showed that, on several occasions, steel joints also fail because of high strains induced by the distortional deformation of the connected members (Santiago, 2008). Beam-to-column connections in a fire are exposed to a combination of forces and moments, significantly different to the single bending moment and shear force assumed at ambient design. The additional moments and axial forces in the beam originate from restraint thermal expansion, large vertical deflections and rotations, and effects of cooling on a plastically deformed structure (Block, 2006).

Most of the previous research works were focused on the connection behaviour during the heating phase of the fire, while Santiago (2008), Zhao *et al.* (2011), Hanus (2010) and Lopes *et al.* (2013) also put emphasis on the behaviour of steel and composite steel-concrete connections during the cooling phase.

During the heating phase, members in frames that are restrained axially by other cooler members, experience significant temperature-induced compression forces that are coupled with bending actions, which produce local buckling of the steel section. The combined compression, bending, geometric nonlinearity and thermally degraded material properties may lead to inelastic local buckling (Figure 1.3a) or to the development of plastic hinges as temperatures increase. At high temperatures, these flange local buckling and yielding reduce the stiffness at a localised region (typically near a connection), so that the member rapidly develops tensile actions that can result in catenary actions (Figure 1.3b) (Heidarpour, 2007).

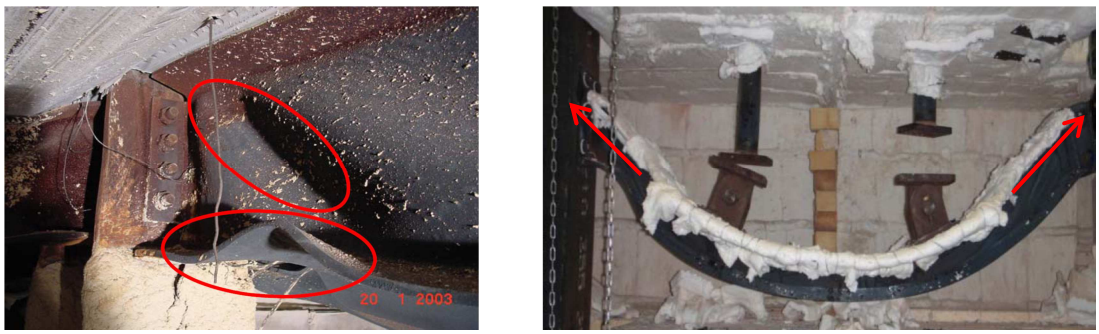

a) b)

Figure 1.3: a) Local buckling of beam web in shear and beam flange in compression (Santiago, 2008); b) Catenary actions (Simões da Silva *et al.*, 2013)

Under combinations of shear force, tying force and elevated temperatures, failure modes of flush end-plate connections can change of component failure: from more ductile components (as the end-plate) to more brittle components (bolts), as the bolt strength reduces faster than structural steel with increase of temperatures. At elevated temperatures, the use of thick end-plates can enhance the peak resistance, but reduces the rotational capacity of the connection (Yu *et al.*, 2008a). According to Hu *et al.* (2008b), the review of

experimental results of flexible end-plate connections indicated that the minimum tying resistance of 75 kN defined by the tying method (EN 1991-1-7, 2006) might not be assured in a fire situation. As the rotation capacity of end-plate connections is reduced at increasing temperatures, the connections may not possess the extensive ductility required for catenary action and may fracture before catenary action is fully developed (Hu *et al.*, 2008b).

During the cooling phase, due to thermal contraction, tensile forces increase in the beam; this contraction of the beam depends on the temperature development and mainly on the tensile restraint. Connections and bolts are particularly vulnerable to these tensile forces. In this stage, the lower bolt row shows the highest principal strains, which results from the reversal of bending moment. Indeed, the large sagging moments develop since the Young modulus and resistance recover their values, and the temperature decreases faster on the bottom flange than on the top (Santiago, 2008). The risk of bolt broken during cooling phase of real fire (Figure 1.4a, b) is really possible if two conditions are met: high heating level and restrained effect (under high temperatures and high stiffness of axial restraints, tensile forces increase). During the cooling down, tensile forces that occur in the connection gradually increase in the hours after the fire, until the time that the construction has completely cooled down. Therefore, connection failure during the cooling phase may occur unexpectedly, even hours after the fire and at surprisingly low steel temperatures (Santiago, 2008). Moreover, after a heating - cooling fire, there is a part of joint strength that is not back when the joint is cooled, referred to as "non reversible" strength, and indications for design of steel joints are not yet provided by Eurocodes (Zhao *et al.*, 2011).

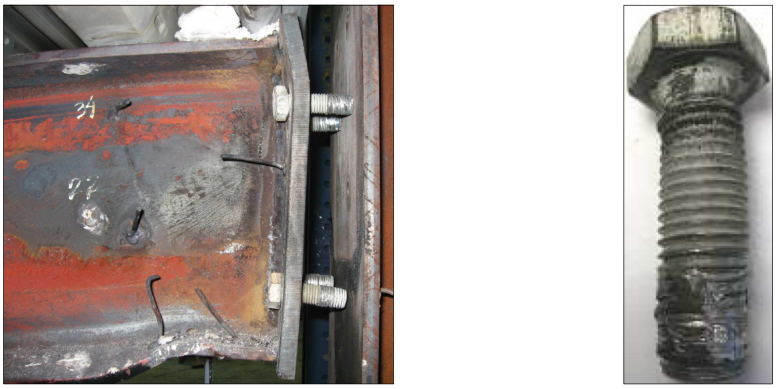

a) b)

Figure 1.4: a) Joint failure and b) bolt stripping (Santiago, 2008)

Block (2006), Sulong (2007), Sarraj *et al.* (2007), Santiago (2008), Fang (2012) and Demonceau *et al.* (2013) developed new models based on the component-based approach, to study numerically connections under elevated temperatures subject to the combination of forces and moments. They notably concluded that, by incorporating the actual stiffness and strength characteristics of the connection, the fire resistance of a beam could be enhanced compared to the case of an idealized pin-representation. In addition, the joint behaviour under heating and cooling phases (compressive and tensile loads), can be assessed.

1.2.3 Joint ductility under column loss robustness scenario

In this section, the recent and relevant developments on the behaviour of bolted joints under the column loss scenario are presented at ambient and elevated temperatures. A more detailed literature review about the progressive collapse design and assessment may be found in the Ph.D. thesis of Fang (2012).

The importance of structural resistance on the progressive collapse of buildings, subject to accidental loads (such as blast or impact), was first highlighted by the partial collapse of the Ronan Point apartment in London in 1968, in which a full cascading failure was initiated by a local damage due to gas explosion. After this event, UK building regulations were the first, in 1985, to address requirements for the avoidance of disproportionate collapse, followed by the other design codes such as Eurocodes or US codes. EN 1991-1-7 (2006) describes the principles and application rules for the assessment of accidental actions on buildings and bridges (impact forces, actions due to internal explosions, actions due to local failure from an unspecified cause). In this code, robustness is defined as *the ability of a structure to withstand events like fire, explosions, impact or the consequences of human error, without being damaged to an extent disproportionate to the original cause*. This means that the structure should have sufficient resistance and ductility in order to avoid that an initial local damage leads to a progressive collapse of the structure. Annex A of EN 1997-1-7 (2006) provides rules and methods for designing buildings with an acceptable level of robustness to sustain localised failure without a disproportionate level of collapse. Two different strategies are possible: i) strategies based on identification of the accidental actions (fire, explosion, flood, impact or earthquake) and ii) strategies based on limiting the extension of localised failure (Figure 1.5). The recommended strategies range from measures to prevent or reduce the accidental action, to the design of the structure to sustain the action. When the accidental actions are not identified, the strategies are based on limiting the extent of localised failure: the aim is to provide sufficient robustness to the structure in order to survive during a period sufficient to facilitate the safe evacuation and rescue of personnel from the building and its surroundings. To prevent progressive collapse, different design methods are available, classified as direct or indirect design methods. The direct design approach relies extensively on structural analysis and is concerned with quantifying the structural resistance under local damage scenarios or levels of extreme loading (Fang *et al.*, 2011). Two methods are typically used in the direct design approach: i) designing the structure with enhanced redundancy, so that in the event of a localised failure (e.g. failure of a single member), the stability of the whole structure or of a significant part of it, would not be endangered (alternative load path method); ii) designing key elements, on which the stability of the structure depends (key element method). The indirect design approach focuses on enhancing structural robustness through continuity, redundancy and ductility between the structural members (tying method). This approach is more prescriptive than the direct design method, though both approaches are typically found in the design codes. These strategies allow local failure to occur when subject to an extreme load, but seek to

provide alternate load paths so that the initial damage can be contained and major collapse can be prevented.

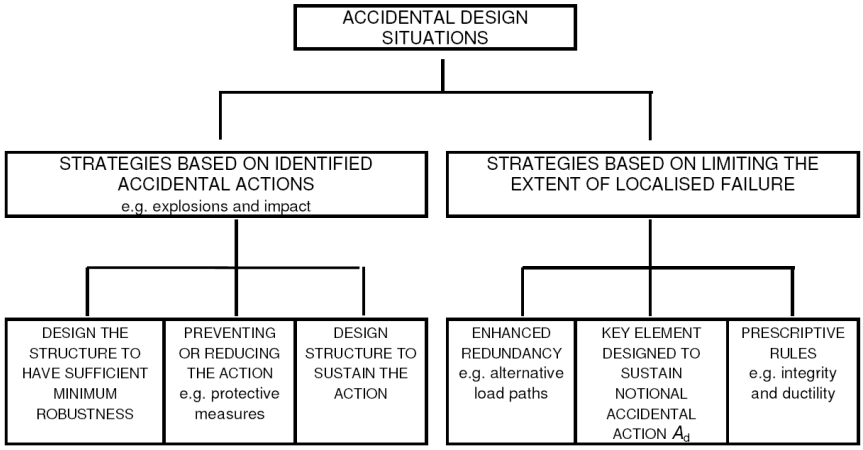

Figure 1.5: Strategies for accidental design situations (EN 1991-1-7, 2006)

One of the key mechanisms to mitigate the spread of "domino" effect is to redistribute the applied load on damaged members through catenary action (Yang and Tan, 2011a). However, only a very few practical guidelines on how to achieve this goal are provided, and even basic requirements to fulfil are not clearly expressed (Jaspart and Demonceau, 2007). Following the World Trade Centre disaster, some researchers have identified joint integrity as a key parameter to maintaining structural integrity under catenary action, and have conducted extensive research works on it. It was shown that the development of the catenary action is beneficial for structures against progressive collapse, but for fully developing catenary action, no weak sections should exist and the requirement of continuity for the beam-to-column connection should be fulfilled (Liu, 2010). Low ductility joints can induce a premature failure prior to the development of catenary action (Foley *et al.*, 2008; Simões da Silva *et al.*, 2003), because tying capacity does not develop before the connections become sufficiently distressed and start to shed load; and an appropriate balance between strength, stiffness and ductility in the connections is really important (Nethercot, 2011). According to the recent European COST action (TU0601 - Robustness of structures), robustness is related to internal structural characteristics such as redundancy, ductility and joint behaviour characteristics, and the consequences of structural collapse strongly depend on the specific scenario of events (Faber, 2011). However, there are relatively very few research studies of the joint behaviour when subject to abnormal loads, especially for bolted steel connections (Yang and Tan, 2011b).

Previously, the European RFCS Robustness project (Kuhlmann *et al.*, 2009) derived robustness requirements in order to develop good practice recommendations for the design of robust steel and composite structures. Extensive experimental and theoretical investigations on the behaviour of steel and composite joints in framed structures were performed, and special focus was given to the exceptional events: loss of a column, loss of a bracing, fire and earthquake. The method used in the Robustness project was the

redundancy approach, or alternate load path method, to ensure that the structure subject to the loss of a column and the unaffected part of the structure have sufficient robustness and do not collapse. In this approach, the structural steel building should have inherent sufficient ductile material behaviour allowing deformations when local failure occurs (Kuhlmann *et al.*, 2007). Experimental tests performed within Robustness project are described in chapter 3. At the University of Liège, the exceptional scenario "loss of a column" in a building structure has been under investigation for a few years with the final objective to propose design requirements to ensure an appropriate robustness of structures under the considered scenario (Demonceau *et al.*, 2011). In particular, simplified analytical methods have been developed to predict the static and dynamic response of 2D steel and composite frames further to a column loss (Demonceau, 2008; Luu, 2009; Comeliau, 2009); investigations are presently in progress to extend these methods to 3D structures. A simplified analytical method was also developed to draw the entire M-N curve of steel and composite steel-concrete joints at ambient and elevated temperatures (Cerfontaine, 2004; Demonceau, 2008; Demonceau *et al.*, 2013). This method is described in detail in chapter 5.

Kozłowski *et al.* (2011) and Yang and Tan (2011a, b) have recently performed experimental tests of steel and composite steel-concrete sub-frames subject to the middle column removal scenario, considering the effect of axial restraints to beams. These tests are described in chapter 3. It was notably evidenced that there is a need to investigate the influence of height of composite beam as well as other details of the joint on the robustness behaviour of frame systems.

Based on a detailed numerical model, Alashker *et al.* (2010) investigated key parameters (deck thickness, steel reinforcement, and the numbers of bolts in the shear tab connection) influencing the robustness of generic composite floors subject to the removal of a centre column. It was shown that increasing the thickness of the steel deck and reinforcement mesh could mitigate the potential for progressive collapse, but only when there is sufficient capacity and ductility of the connections; and, adding more bolts in fin-plate connections might not be that beneficial in increasing overall collapse strength.

A design-oriented methodology for progressive collapse assessment of multi-storey buildings was developed at Imperial College (Izzuddin *et* al., 2007 and 2008; Vlassis *et al.*, 2008; Pereira, 2012), and it allows to determine ductility demand and supply. Pereira (2012) studied a rate-sensitivity of robustness of multi-storey steel-composite buildings under column loss. The research focused on the development of an enhanced deterministic robustness assessment framework which considers material rate-sensitivity and accurate component ductility. It was included a detailed nonlinear component response up to its failure, which inherently defines the ductility limit of a steel-composite frame with partial-strength connections. He showed that explicit modelling of the joint components and the consideration of successive component failures provides higher individual beam ductility and strength.

Thermal effects such as thermal expansion, thermal bowing, and material deterioration can considerably complicate the prediction of structural behaviour, and these are not yet considered in current guidelines dealing with progressive collapse (Fang, 2012).

Sun *et al.* (2012) developed a robust combined static-dynamic procedure in Vulcan, allowing tracing the progressive collapse of structures under fire conditions (with flash-over). Sun wrote that results from previous research works suggest that it is now possible to eliminate fire protection to some steel beams without compromising its overall structural fire resistance safety, but the steel columns are critical members and their behaviour affects the overall stability of the frame. The influences of load ratio, beam section and bracing systems, based on a simplified 2D modelling of a frame with rigid connections, were studied under fire. Sun *et al.* (2012) concluded that i) the bracing system is helpful to prevent the frame from progressive collapse; ii) the axial force in the connections jointed to the failure column should be paid special attention in design, and iii) the stiffer lateral system can generate larger axial force in the connections, and smaller vertical deformation of failed column at re-stable position (but the global failure temperature of the frame is not sensitive to the lateral stiffness of the frame).

Using the advanced non-linear finite element program ADAPTIC (Izzuddin, 1991), Fang *et al.* (2012 and 2013) investigated the progressive collapse resistance of the fire damaged eight-storey reference steel-composite car park studied in the present thesis (see description in section 1.3). Dynamic effects associated with idealised sudden column loss scenarios were considered in the model, in order to predict a reliable ductility demand of the car park subsequent to column loss due to vehicle fire (Fang, 2012). Figure 1.6 shows the modelling strategy of the car park, that takes account of bending and axial resistances of the joint, as well as the degraded joint performance under elevated temperatures. According to the ductility of the joint components, maximum axial and yielding deformations were suggested in Kuhlmann *et al.* (1998) and Simões da Silva *et al.* (2002). The load-deformation behaviour of the basic components was distinguished in three classes due to their mode of failure (high, limited or brittle ductility - see section 1.2.1), and all the components classified with high ductility were considered to have an infinite deformation capacity in tension. Fang *et al.* (2013) suggested new values for high ductility components: maximum deformations of 25 mm and 35 mm should be employed as an additional failure criterion for all bolt-rows in endplate connections and cleat/angle/fin plate connections at ambient temperature, respectively.

Fang *et al.* (2012) concluded that the collapse mode of the typical car park under vehicle fire near an internal column can be mainly governed by the failure of the surrounding unaffected members, e.g. peripheral ambient joints in the cooler part of the slab, while the behaviour of the localised fire-affected part might be less important. In this study, Fang *et al.* (2012) considered web stiffeners in the reference car park for all major axis joints, and failure of the peripheral ambient joint under hogging bending moment is due to the rupture of the reinforcement in tension. The localised fire-affected joint fails because of shear failure of the joint leading to punching shear of the fire affected floor, which increases the

potential for progressive collapse (Fang *et al.*, 2013). It is found that only protect steel beams and steel decks with fire coating can be unexpectedly ineffective for localised fire conditions and in some cases may even cause adverse effects on structural robustness under localised fire due to the elimination of thermal expansion. Some solutions to improve structural robustness under localised fire were suggested, such as applying column and joint fire protections without applying beam and slab fire protections, or improving the joint ductility and slab resistance.

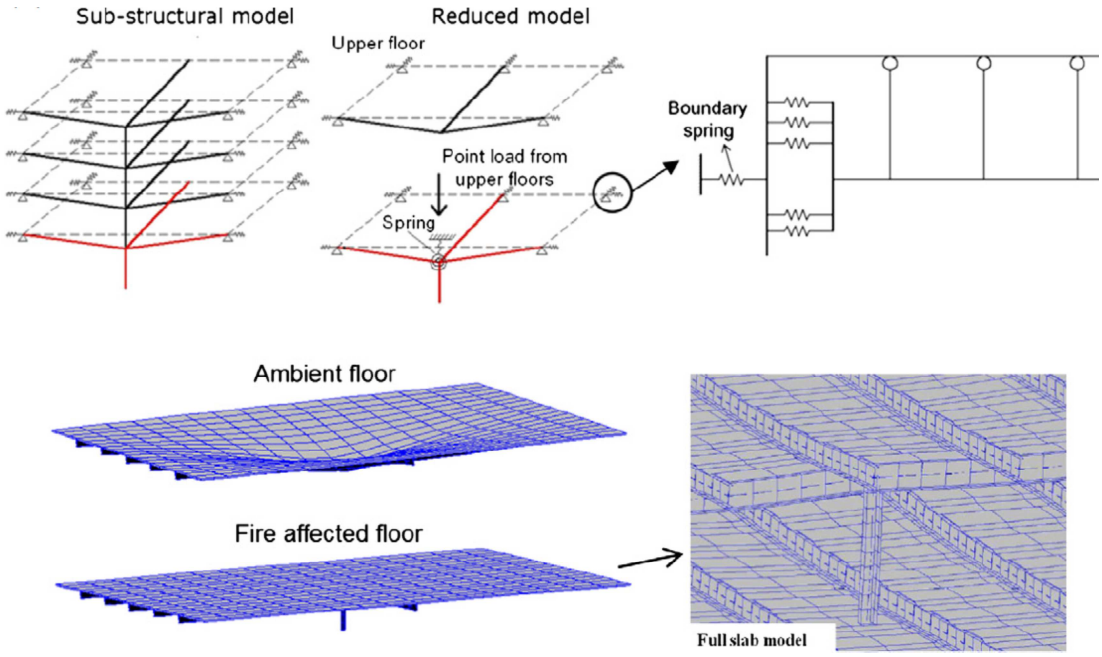

Figure 1.6: Modelling strategy of the reference car park (Fang *et al.*, 2013)

1.3 Purpose and scope of this research

1.3.1 The European RFCS ROBUSTFIRE project

The European RFCS ROBUSTFIRE project (Demonceau *et al.*, 2013) focused on the study of the behaviour of steel and composite open car park structures subject to the loss of a column due to fire. A design philosophy aiming at the economical design of car parks exhibiting a sufficient robustness under localised fire was developed in the present project, and practical design guidelines for the application of this design philosophy throughout Europe were derived (Demonceau *et al.*, 2013). In order to reach this goal, the project was divided into five basic tasks:

i) *Definition of the problem and selection of the appropriate investigation ways:* derivation of all structural requirements for car park structures (dimensions, layout, loads, fabrication/construction/erection constraints, realistic fire scenarios, etc.…), and design of a reference structure under normal loading and in accordance with Eurocodes;

ii) *Study of the structural individual response of the affected structural elements* (columns, beams, connections, floor) through experimental and/or numerical investigations, and derivation of analytical approaches for the prediction of the individual response of the abovementioned structural elements;

iii) *Study of the structural response under selected fire scenario(s):* evaluation of the distribution of temperatures in the structure and in the constitutive structural elements during the exceptional event, development of various numerical procedures for the evaluation of the stability and the resistance of the structure further to the event (sophisticated models with different levels of sophistication), derivation of a simplified event-independent and Eurocode compatible approach for the evaluation of the robustness of the structure (simplified model);

iv) *Derivation of design recommendations*;

v) *Application of the "event-independent" robustness requirements on a case study*.

A typical open car park structure with eight floors was specially designed for the project (task i)). This building was defined as the most common as possible so that the design rules derived from the studies of this building can be used for general design rules for open car park buildings, ensuring sufficient robustness under fire conditions. The selected structure was a braced open car park building with eight floors of 3 m height, composite slabs, composite beams and steel columns (Figure 1.7). The main and secondary beams were defined by IPE 550 and IPE 450, respectively (steel grade equal to S355). The cross-section of steel columns varied according to the floor (HEB 550 at the bottom two floors, HEB 400 and HEB 300 at the middle floors, and HEB 220 at the top two floors), and the steel grade of the columns was S460. The lateral bracing of the structure was ensured by concrete ramps (at both sides) required for the car circulation.

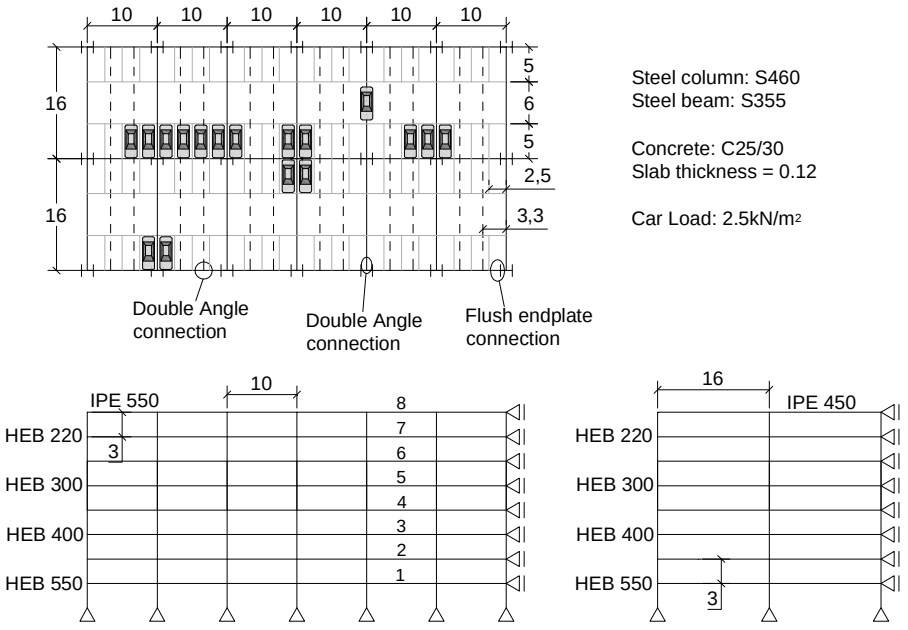

Figure 1.7: Steel composite open car park building designed for the ROBUSTFIRE project

At the end, the project provided a simplified model which allows checking the robustness of the car park through a "scenario-independent" approach. This model limits the investment of a design office in terms of calculation costs, but in return, it provides a non-excessive but actual level of conservatism. More sophisticated models were also available to practitioners who would prefer to follow a numerical approach (choice of the model, distribution of temperatures, substructure to be studied, loads and boundary conditions to apply). Through the present project, the practitioners have nowadays at their disposal design approaches, at different levels of sophistication, allowing checking the robustness of composite car parks under localised fire.

1.3.2 Objectives of the thesis

The thesis reflects the author participation in the research ROBUSTFIRE project, as a member of the research group ISISE-SMCT at the Civil Engineering Department of the University of Coimbra. The work of the thesis is mainly focused on the study of the behaviour of composite steel-concrete beam-to-column joints in open car park buildings; the investigation is based on experimental, numerical and analytical work. The main objective of this research is to provide a detailed analysis of the heated joint behaviour when it is subject to variable bending moments and axial loads. In order to reach this goal, the work is divided in four main tasks:

i) *A review of current practice and state of the art in the design and assessment of open car parks subject to localised fire is performed*;

ii) *The required knowledge on the behavioural response of the joint directly affected by the localised fire is investigated by complex experimental tests.* These experimental tests are developed at the Steel Construction Laboratory of the Department of Civil Engineering at the University of Coimbra. Seven composite steel-concrete joints are tested under variable mechanical (bending and axial forces) and thermal loadings. The composite joint at the fifth floor of the open car park building designed for the ROBUSTFIRE project (Figure 1.7) is considered. It is composed of two unprotected composite steel-concrete beams IPE 550 steel cross-sections (grade S355), concrete C25/30, and one unprotected HEB 300 cross-section steel column, grade S460. Ten steel reinforcement bars of diameter 12 mm are placed in the composite slab at each side of the column to take part in the composite joint resistance.

iii) *Detailed numerical models of the joint subject to combined bending moment, axial loads and temperatures are developed and calibrated against the tests*. The numerical part of the work corresponds to a detailed three-dimensional finite element (FE) model reproducing the experimental tests. The objective of this work is to observe, in detail, the combined bending moment and axial loads in the heated joint. The structural frame is modelled combining 3D beam and solid elements with contact interactions, thereby taking into account the effect of the local failure modes. Due to the complex behaviour of a restrained beam under fire, the FE

model allows for the inclusion of initial geometrical imperfections, non-linear temperature gradient, geometrical and material nonlinearity and temperature dependent material properties. These models are calibrated against the experimental tests results, and provide a complex model for further studies of the composite joint behaviour when the column fails.

iv) *Additional extensive study of the joint behaviour under combined bending moment and axial load is performed based on numerical and analytical results (at ambient and elevated temperatures).* Based on FE and analytical results, the influence of some parameters such as temperature, beam span, joint size, etc.… on the robustness of tall open car park buildings is observed.

1.4 Organisation of the thesis

The thesis is divided into six chapters. In the first chapter, a global overview of the behaviour of beam-to-column joints at ambient temperature, under fire and subject to high ductility demand (robustness study) is described, and the objectives and organization of the research are drawn.

The second chapter provides a general idea about the open car park buildings in fire situation: from the structural behaviour under a localised fire observed in real fire tests to the verification and design rules published in different countries, including an example of application of fire design.

Chapter three describes and discuss the experimental program performed to investigate the behaviour of the composite joint directly affected by the localised fire, and subject to combined bending moment, axial loads and elevated temperatures. The column loss robustness scenario due to the localised fire is considered.

Chapter four describes the numerical models of the composite steel-concrete joint subject to the loss of a column at ambient and elevated temperatures. The detailed three-dimensional model is calibrated with the experimental tests results, and the combined bending moment and axial loads in the heated joint is observed and discussed against the experimental evidences.

In chapter five, the behaviour of the joint is analysed based on: i) numerical results (obtained from FE models developed in chapter four) and ii) analytical results (using the analytical method developed at the University of Liège). This analytical procedure is presented in detail and its applicability to steel and composite joints under elevated temperatures is demonstrated. At the end, based on the results, knowledge about the effect of some parameters that influence the robustness of tall open car park buildings, such as temperatures, beam span length, joint size, etc…, is enlarged.

Finally, chapter 6 points the main conclusions of this research, the design considerations for open car parks with sufficient robustness, and important subjects to be further developed.

Chapter 2

2 Design of steel and composite open car parks under fire

2.1 Introduction

Steel and concrete are the most commonly used materials for car parking, and open car park buildings with unprotected steel or composite steel-concrete structures is a solution frequently used in many countries of the centre and north of Europe, or even in United-States, Canada or Japan. There are many advantages of a composite steel-concrete structure for open car park buildings: i) shorter on-site construction schedule due to the prefabricated elements, and consequently lower construction cost, as well as lower environmental impacts during construction; ii) flexible column spacing up to around 16 m, allowing to locate the columns at the back of the parking bay which facilitates vehicles maneuvers (Cajot *et al.*, 2003); iii) reduced column section size in comparison to a concrete structure, which increases the parking spaces; and iv) reduced weight, and smaller foundations, in comparison to concrete structures (ArcelorMittal, 2007). Moreover, steel structures are robust, sustainable, of easy maintenance and can easily accommodate vertical enlargement (Corus, 2004).

This solution has become quite competitive since the National regulations have been adapted taking into account the document: *Fire safety in open car parks*, the oldest reference in this subject, published in 1993, ECCS - *European Convention for Constructional Steelwork* (ECCS, 1993). This document was a first attempt to clear up the differences between fire safety requirements of open car parks for all European countries, according to information and test results available throughout the world. However, the fire safety requirements, including structural fire ratings and provision of active fire protection system such as sprinklers, still vary between different building codes. In some countries, steel or composite steel-concrete structures are not recommended because they are required to be fire rated by the building code, and is conditioned by the fire resistance demands (R) from the National

regulations. In that case, concrete structure will be more cost effective, despite the numerous advantages of a composite steel-concrete structure.

A car park as part of a building can be classified as open or closed depending on the ventilation condition. The main advantages of open car parks are: i) lower energy consumption, ii) natural light, that contributes to the human comfort and safety of users, iii) natural ventilation, and iv) attractive architectural design. In addition, open car parks present specific characteristics that must be considered in the fire design.

Every fire in a building starts as a small localised fire, and the fire ceases to be localised when flash-over occurs (Franssen and Vila Real, 2010). Where flash-over is unlikely to occur or has not yet occurred, thermal actions of a localised fire should be considered (EN 1991-1-2, 2002). In large compartments like car parks, airport terminals, big industrial halls, or even at open spaces, uniformly distributed temperatures characteristics of post-flashover stages are totally unlikely to occur (Kamikawa *et al.*, 2003).

The structural behaviour of the car park under fire can be analysed by specific combinations of mechanical and thermal loads defined in EN 1990 (2002), EN 1991-1-1 (2002) and EN 1991-1-2 (2002). The methodology proposed in Annex C of EN 1991-1-2 (2002) for localised fires can be adapted to calculate the thermal loads of open car parks. In this case, fire scenarios are used to define the curve of the real rate of heat release of the burning vehicles, and thus to obtain an adequate fire characterization, against the traditional nominal fire curves defined by EN 1991-1-2 (2002). The vertical position of the virtual heat source, the height, the diameter of the fire, the rate of heat release and the distance between the fire source and the ceiling define the heat flux to the structural elements. Finally, simplified and advanced calculation methods are presented in EN 1993-1-2 (2005) and EN 1994-1-2 (2005) for calculating the resistance of structural elements in fire, depending on the fire safety requirements of each country. In France, CTICM - *Centre Technique Industriel de la Construction Métallique* - validated this computing method to justify the use of unprotected steel frame resistance for the fire design, and the French legislation allowed this design methodology since 2004 ("*Arrêté ministériel du 2 mars 2004*").

The objectives of this chapter are: i) to present a fire engineering methodology, for assessing the structural behaviour of steel and composite open car parks under fire, based on a Natural Fire Concept; ii) to compare the legislation of several European countries regarding the fire safety in this kind of building; and iii) to illustrate this design methodology through its application to an open composite car park with eight floors (Demonceau *et al.*, 2013) and to compare the results with those obtained through advanced calculation methods.

The work described in this chapter has been published in Haremza *et al.* (2013b).

2.2 Literature review

2.2.1 Steel columns subject to localised fire

Annex C of EN 1991-1-2 (2002) proposes a simplified analytical methodology to assess the thermal action of a localised fire. The heat flux received by the members located at the ceiling level is calculated by one of the simplified methods: i) Heskestad's method, when the flames are not impacting the ceiling (Heskestad, 1995), and ii) Hasemi's method, when the flames are impacting the ceiling (Hasemi and Tokunaga, 1984). In open car park buildings, the height of each storey is usually short to optimize the building size (the minimum free height under beam for cars and vans is at least equal to 2.1m (ArcelorMittal, 2007)), and flames of burning cars impact the ceiling; so, in this work, more emphasis is given to the Hasemi's method (details are provided in section 2.5.3). Hasemi's method provides the heat flux received by the surface area at the ceiling level. The background of the method is experimental: a gas burner was placed under an unconfined flat ceiling, the height of the ceiling was adjusted in each test, and the heat flux to the ceiling surface was recorded (Schleich *et al.*, 1999b). Thus, the method cannot be used for vertical members such as columns, and no other simplified method is provided by the codes. In Tondini *et al.* (2014), the fire performance of a composite steel-concrete open car park was recently analysed according to: i) the simplified method presented in EN 1991-1-2 (2002), and ii) an advanced analysis that relies on numerical FDS (*Fire dynamic simulator*)-SAFIR coupling. In the simplified model, the column temperature was assumed to be uniform and equal to the calculated Hasemi's temperature at the top of the column. Much more conservative results were obtained with the simplified method: the results showed the collapse of the structure after 27 minutes, whereas the structure survived the whole duration of the most critical fire scenario (86 min.) when the advanced analysis was used.

Recently, many researchers have investigated the thermal behaviour of steel columns subject to localised fire (Kamikawa *et al.*, 2003; Wald *et al.*, 2009; Byström *et al.*, 2014; Ferraz, 2014; and Zhang *et al.*, 2014). The experimental and numerical results showed that temperatures in steel column are influenced by: i) the position of the localised fire (distance to the fire source, column adjacent to the fire, or column surrounded by the fire), ii) the plume height (impacting or not impacting the ceiling), and iii) the ventilation conditions. The temperature evolution along the height of the column was proved to be dependent on the fire model (impacting or not impacting the ceiling). For columns exposed to fires impacting the ceiling, average temperature rises very slowly along the height of the column, but near the ceiling, an exponential increase is reached. For columns exposed to fires not impacting the ceiling, the maximum temperatures are reached in the lower part of the column (Ferraz, 2014). For columns surrounded by the fire, the failure situation is assumed to be equal to columns subject to post-flashover fires (Zhang *et al.,* 2014). For columns adjacent to a localised fire, the buckling temperature of the column may be much lower than those for columns subject to uniform heating conditions (Zhang *et al.*, 2014). The

European RFCS project LOCAFI - *Temperature assessment of a vertical steel member subjected to localised fire* - is actually in development and should soon bring additional results.

In the numerical models, for columns adjacent to the localised fire (Figure 2.1a), the flame can be modelled by a solid from which a flux is emitted (Sokol, 2009; Vassart *et al.*, 2011; Zhang *et al.*, 2014). This model relies on a representation of the flames by solid surfaces that change properties depending on the intensity of the fire sources (Vassart *et al.*, 2011). When the flames do not impact the ceiling, a solid cylinder can be used (Figure 2.1b); when the flames impact the ceiling, geometries may involve a cylinder for the main part of the flame and a disk on the top to reflect the flames impacting and spreading on the ceiling (Figure 2.1c).

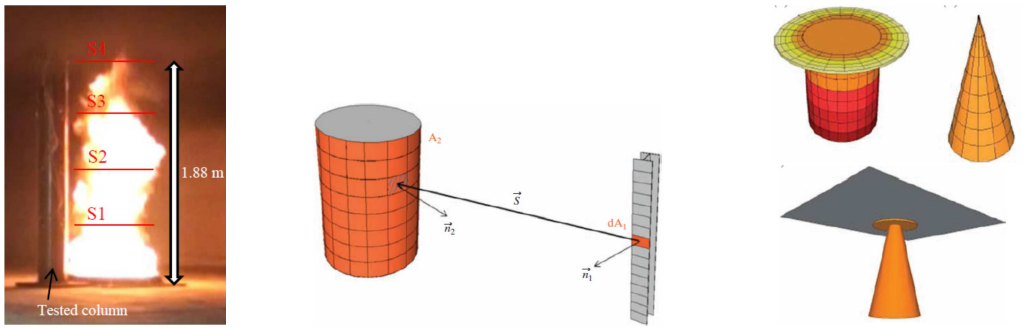

Figure 2.1: a) Fire plume when the column is adjacent to the localised fire (Ferraz, 2014); b) Radiative flux from source to element and c) different shapes of the flame (Tonicello *et al.*, 2012)

2.2.2 Open car park buildings subject to localised fire

From experimental tests performed in real steel-concrete car parks, Butcher *et al.* (1968) was the first to conclude that a burning car is unlikely to cause uncontrollable fire spread within a car park and the damage to the car park building is not critical. These results were confirmed by Gewain (1973), which added that steel provides adequate safety against structural collapse under a car fire. Bennetts *et al.* (1987) concluded that the probability to involve more than two cars in a fire is very low because the fire brigades arrive before, and the safety could be assured with unprotected steel. More recently, in 2000, three car fire tests were carried out in a two-level braced car park with unprotected steel and concrete slabs, by CTICM, within the European Project – *Demonstration of real fire tests in car parks and high buildings* (Joyeux *et al.*, 2002; Zhao and Kruppa, 2004). The aim of these tests was to prove to the French authorities that fire severity achieved by this realistic scenario is lower than the fire severity obtained by the fire curve ISO 834; consequently, reduction or even no fire protection could be accepted. From the two first tests with three cars, the central one being the first to be ignited up (Figure 2.2), the authors concluded that the fire engineering methodology based on the scenarios is adequate: the fire spread from one car to another, but structural deformations were far from leading to the collapse of the structure, although some bolt failures were observed.

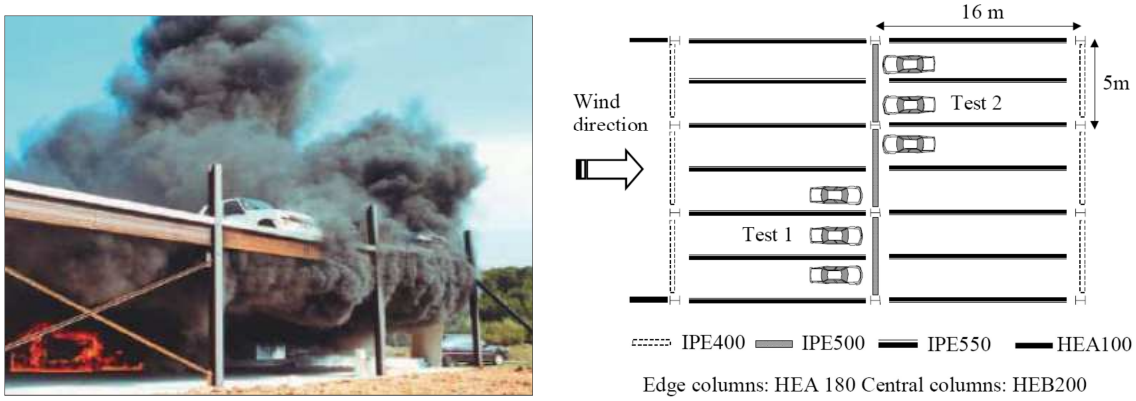

Figure 2.2: Fire scenarios for the tests 1 and 2 (Joyeux *et al.*, 2002)

Table 2.1 presents the peak values of temperatures in steel members according to the previous experimental studies; the older fire tests showed lower temperatures than the recent French test. The evolution of the composition of cars (more plastic, therefore a faster combustion) and the high fuel capacity may explain these higher temperatures.

Table 2.1: Maximum steel temperatures reached in fire tests in various countries

Full scale fire tests	Maximum measured steel temperatures,.	
	Beam	Column
UK, 1968 (Zhao and Kruppa, 2004)	275 ºC	360ºC
Japan, 1970 (ECCS, 1993)	245ºC	242ºC
USA, 1973 (Butcher *et al.*, 1968)	226ºC	-
Australia, 1985 (Bennetts *et al.*, 1987)	340ºC	320ºC
France, 2000 (Joyeux *et al.*, 2002)	700ºC	640ºC

Additionally to the previous tests, some statistics of real fires in car parks were analysed in Paris, New Zealand, Brussels, etc… based on the reports from fire brigades. In Paris, three is the maximum number of cars involved in fires and it corresponds to only 10% of the fires in open car park buildings. All fires in car parks (with cars or other fire load) were stopped before 1 hour, with 5.5% of car fires extinguished before the arrival of firemen (Joyeux *et al.*, 2002). In New Zealand, only 3% of fires involved multiple vehicles (Li and Spearpoint, 2007). Statistics collected in Marseille, Toulouse and Brussels in open car parks (Li, 2004), noticed that a maximum of two cars were involved in a fire, and in Toulouse, only 6.1% of the fires happened in open car parks.

These previous statistics and experimental tests show that fires in open car park buildings: i) have never led to any local collapse of the structure, and most of unprotected steel open sided steel-framed car parks has sufficient inherent resistance to withstand the fire effects; ii) are not frequent; iii) rarely involve more than three adjacent vehicles; iv) have never killed someone (only a few persons were recorded to be injured, and they were the

owners of the cars). The main reasons that justify previous evidences are: in contrast to closed car parks, open car parks are characterized by high ventilation that keeps the fire limited on the ignition zone. Indeed, in an open car park building, the fire propagates from a burning car to another by radiation, convection and/or scattering of the fuel: by radiation, fire propagates sequentially from a car to another, but when the fifth or sixth car is burning, the combustion of the first one has already ended; the propagation of the fire by convection in an open car park building well ventilated is unlikely to occur because hot gases have little impact on the cars; and the scattering of the fuel only happens in inclined floors (Cwiklinski, 2001).

A detailed literature review can be found in the Ph.D. Thesis of Li (2004); the review covers the study of severity of the vehicle fires in a parking building situation, detailed statistics of vehicle fires in parking buildings, and experiments on the severity of vehicles fires. Li (2004) also evaluated the probabilities of such fires, and presented a cost-benefit analysis model for the provision of sprinklers in parking buildings.

Recently, the behaviour of the composite slab of an open car park building subject to a localised fire was studied numerically by Zhao *et al.* (2011). Steel and concrete composite floor system was used, all steel beams were kept unprotected, and the membrane action was considered in fire design. It was shown that: i) the total deflection of the steel and concrete composite floor under localised car fires can become very important, but does not exceed that of a fully vertically restrained composite floor under generalised compartment fire; ii) tensile strain develops during the heating phase in the concrete slab at the edge part of buildings, which requires to link the reinforcing steel mesh of concrete slab with edge steel members in order to avoid possible cracks of concrete; iii) during the cooling phase, the tensile strain in the concrete slab could increase at the edge part of the floor, and therefore leading to more risk of the failure of connection between concrete slab and edge steel beams (Zhao *et al.*, 2011).

2.3 Fire scenarios

The fire scenario (position of the vehicles) should represent the most unfavourable situation for the elements (or substructure). The vehicles' type mostly used in fire scenarios are cars, classified according their calorific potential or combustion energy (E) (Joyeux *et al.*, 2002); five classes of cars are defined: class 1 - E = 6000 MJ (ex. Peugeot 106); class 2 - E = 7500 MJ (ex. Peugeot 306); class 3 - E = 9500 MJ (ex. Peugeot 406), and classes 4 and 5 - E = 12 000 MJ (ex. Peugeot 605 or 806). According to French statistical studies of actual fires in car parks, 90% of the vehicles involved in a fire are classified as class 1, 2 or 3 (Joyeux *et al.*, 2002). The INERIS - *Institut National de l'Environnement Industriel et des Risques* (Cwiklinski, 2001), considers that fire scenarios with cars of class 3 should be used to evaluate the structural stability of the car park under fire, and the fire resistance of the structure should be ensured during the entire fire scenario, or at least, if allowed by

National requirements, up to a certain resistance time *R* of the elements defined as for the ISO curve. In addition, a scenario including a commercial vehicle (van containing 250 kg of highly flammable material: E = 19 500 MJ) corresponds to an extreme situation and should only be used to check the global behaviour of the structure, assuming local collapse, without progressive collapse (Fraud *et al.*, 2004).

In this section, five fire scenarios recommended or already used for the study of fires in car parks are presented and described. ECCS (1993) indicates that one or two vehicles in fire correspond to the most critical scenario in an open car park. One car burning at mid-span under the beam (corresponding to the maximum bending moment position) is defined as scenario 1 (Figure 2.3). The scenario 2 involves two burning cars, one on each side of the column; this fire event was considered being the most dangerous for the columns (ECCS, 1993). INERIS defines three additional fire scenarios (Fraud *et al.*, 2004): i) scenario 1 of ECCS, but with a commercial vehicle under the beam, ii) scenario 3 - involving seven class 3-cars, with possibility of a commercial vehicle in places 0 or 1a (Figure 2.3), iii) scenario 4 - involving four class 3-cars parked face to face, with possibly a commercial vehicle in places 0, 1a, 1b or 2. According to INERIS, and for all scenarios, the fire spread time from a vehicle to another is 12 minutes (Fraud *et al.*, 2004); the initial document prepared by ECCS recommended a time delay equal to 15 minutes (ECCS, 1993). The evolution of the composition of vehicles may also explain the decrease in the time delay (see Section 2.2.2). Another scenario already considered by CTICM (Joyeux *et al.*, 2002) is scenario 5 (Figure 2.3): three class 3-cars, parked side by side. According to the same statistical source, a scenario of 3 class 3-cars (scenario 5) involved in a fire is an envelope scenario of around 98.7% of all possible scenarios.

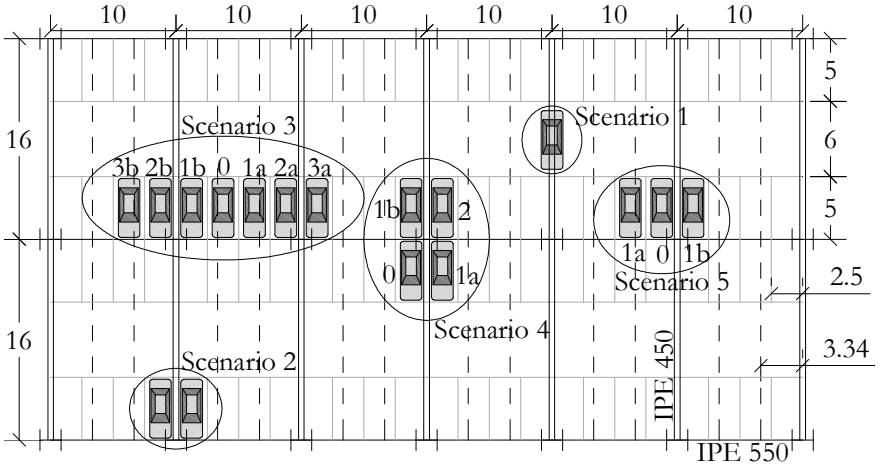

Figure 2.3: Fire scenarios (represented in the car park studied in the thesis; dimensions in m).

2.4 Rate of heat release from vehicles

The model of a car under fire presented in the ECCS report (1993) is based on experimental fire tests: it was observed that the flames extend out of the car, mainly through the windscreen and the rear window. The hot gases in the flames and above them move upward due to buoyancy; this flow of gases corresponds to the fire plume. The burning car is divided into two plumes, which are called as the front and the rear fire plumes (Figure 2.4), and the sum of the heat releases included in the two fire plumes is equal to the heat release of the vehicle.

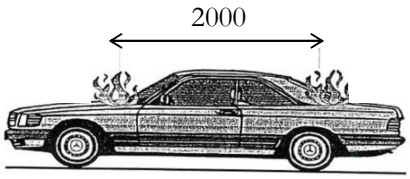

Figure 2.4: Front (F) and rear (R) fire plumes (ECCS, 1993)

In order to calculate the heat release, cars under fire have been experimentally studied in several countries (Li, 2004). Most of the tests were performed in closed conditions. In the 90's (1994), Mangs and Keski-Rahkonen carried out the first tests in opened conditions. It was obtained that the total heat release of a European car from the 70's, burning in an open car park building, is equal to 4000 MJ. Between 1993 and 1996, the European project – *Development of design rules for steel structures subjected to natural fires in closed car parks* (Schleich *et al.*, 1999a) – developed a design guide for closed car park structures subject to localised natural fires and established more realistic standards in Europe. Within this project, ten full-scale calorimetric fire experiments on old and recent European cars were performed by CTICM. In the first six tests, class 3-cars from the 70's and 80's were tested, while in the last four tests, newer cars (reference time: 1995) were used to simulate an open car park (Cwiklinski, 2001). Based on these tests, reference curves of rate of heat release for two class 3-cars (one car as fire source and another one subject to the spread of fire with 12 minutes of delay) were defined (Schleich *et al.*, 1999a). These curves allow simulating multiple burning cars: Figure 2.5 presents the references curves for three consecutive burning class 3-cars, with maximum 8.3 MW. For commercial vehicles, CTICM suggests a maximum value of rate of heat release equal to 18 MW; this value is considered as a "safe value" for design, but this is not a measured value (Fraud *et al.*, 2004).

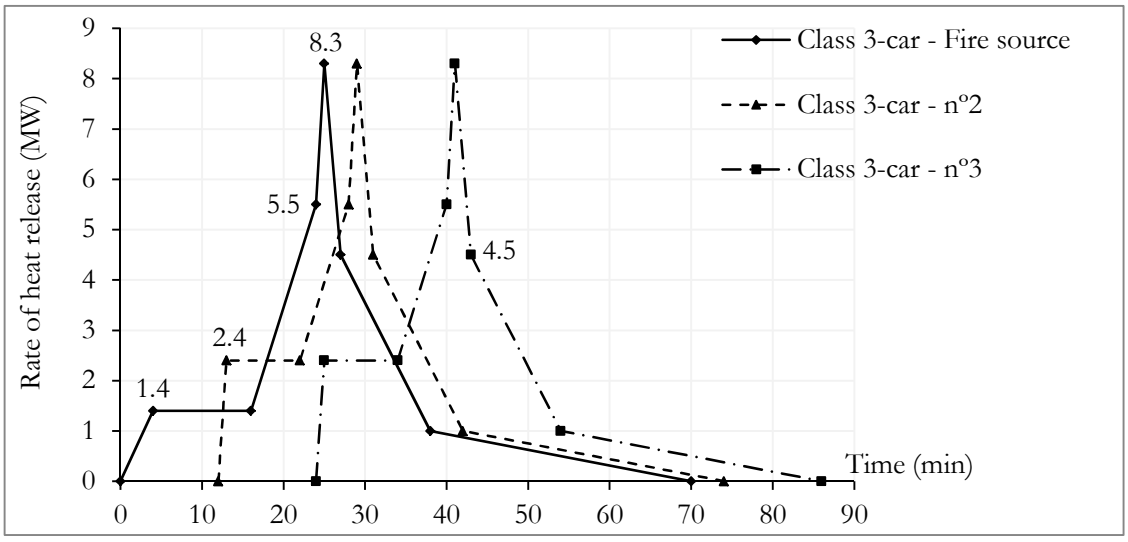

Figure 2.5: Curves of rates of heat release from burning of 3 vehicles, class 3.

2.5 Structural behaviour

2.5.1 Combination of actions

The combination of actions for car parks under fire corresponds to the accidental design situations presented in EN 1990 (2002):

$$\sum_{j\geq 1} G_{k,j} + P + A_d + \psi_{1,1} Q_{k,1} + \sum_{i\geq 2} \psi_{2,i} Q_{k,i} \quad \text{(Eq. 2.1)}$$

$$\sum_{j\geq 1} G_{k,j} + P + A_d + \sum_{i\geq 1} \psi_{2,i} Q_{k,i} \quad \text{(Eq. 2.2)}$$

Where: $G_{k,j}$ are the characteristic values of permanent actions *j*; P is the design value of a prestressing load (if available); A_d is the design value of indirect actions from fire; and $Q_{k,i}$ are the characteristic values of the variable actions *i*. The difference between (Eq. 2.1) and (Eq. 2.2) is the coefficient ψ applied to the leading variable action $Q_{k,1}$: the coefficients for the frequent value ψ_1 and for the quasi-permanent value ψ_2 are considered in (Eq. 2.1) and (Eq. 2.2), respectively. In case of a car park (traffic with vehicles smaller than 30 kN), the coefficient for the frequent value ψ_1 and for the quasi-permanent value ψ_2 are respectively equal to 0.7 and 0.6; guidance may be given in the National Annex. The simplified combination of actions can be written as:

$$1.0\ G_k + 0.7 \text{ (or } 0.6) \ Q_k \quad \text{(Eq. 2.3)}$$

Note that (Eq. 2.2) will lead to the situation where no horizontal action is considered in the fire situation, because the quasi-permanent value of the wind ψ_2 is equal 0.0 (Franssen

and Vila Real, 2010). For this reason, the Portuguese National Code NP EN 1991-1-2 (2010) recommends to use the coefficient for the frequent value ψ_1, equal to 0.7.

2.5.2 Mechanical loads

The load model which should be used, given by EN 1991-1-1 (2002), is a load q_k uniformly distributed on the floors, for global design resistance, and a concentrated load Q_k, for local design resistance. A single axis with the load Q_k applied on two square surfaces (Figure 2.6) should be located in the position which will produce the most adverse effect of the action. Concerning characteristic values of the live loads, the EN 1991-1-1 (2002) recommends that q_k be selected within the range 1.5 to 2.5 kN/m^2 and Q_k be selected within the range 10 to 20 kN; the recommended values are underlined, but they may be set by the National Annex.

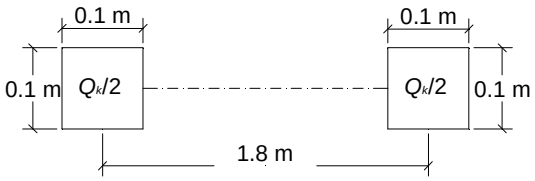

Figure 2.6: Dimensions of axis load

2.5.3 Thermal loads

The steel temperature of structural elements can be calculated in two ways: i) a simplified method that assumes a uniform temperature throughout the steel cross-section, and ii) an advanced method that considers the evaluation of the temperature field in the cross-section using finite element models. In this section, the simplified method given in EN 1991-1-2 (2002) is considered. The heat flux received by the members located at the ceiling level due to a localised fire is calculated by one of the simplified methods presented in Annex C of this code: i) Heskestad's method, when the flames are not impacting the ceiling, and ii) Hasemi's method, when the flames are impacting the ceiling. The length of the flame L_f is obtained by:

$$L_f = -1{,}02D + 0{,}0148Q^{2/5} \quad \text{[m]} \qquad \text{(Eq. 2.4)}$$

where D [m] is the diameter of the fire (for a vehicle with an area equal to 12 m^2, D = 3.9 m (Schleich *et al.*, 1999a) and Q [W] is the rate of heat release of the fire, established in accordance with Annex E.4 of EN 1991-1-2 (2002). In this Annex, the heat release for car park occupancy is not specified; however, the experimental values presented in section 2.4 are considered in this study.

2.5.3.1 Heskestad's method

When the flames are not impacting the ceiling ($L_f < H$), EN 1991-1-2 (2002) suggests that the temperature in the plume along the symmetrical vertical flame axis is given by (Eq. 2.5) (Heskestad's method):

$$\theta_{(z)}=20 + 0{,}25\mathcal{Q}_c^{2/3}\left(z - z_0\right)^{-5/3} \leq 900 \quad [^oC] \qquad \text{(Eq. 2.5)}$$

Where the heat flux $\mathcal{Q}_c$ [W] is the convective part of the rate of heat release ($\mathcal{Q}_c = 0.8\,\mathcal{Q}$), z [m] is the height along the flame axis and z_0 [m] is the virtual origin of z axis. More details can be found in Annex C of EN 1991-1-2 (2002).

2.5.3.2 Hasemi's method

When the flame is impacting the ceiling ($L_f \geq H$), the net heat flux $\dot{h}_{net}$ [W/m^2] received by the fire exposed unit surface area at the level of the ceiling is given by:

$$\dot{h}_{net}=\dot{h} - \alpha_c\left(\theta_m-20\right)+\Phi\,\varepsilon_m\,\varepsilon_f\,\sigma\left[(\theta_m + 273)^4- (20 + 273)^4\right] \quad [W/m^2] \qquad \text{(Eq. 2.6)}$$

where $\dot{h}$ is the heat flux received by the unit of surface area exposed to fire at the ceiling level, α_c is the coefficient of heat transfer by convection [W/m^{2}K], θ_m is the surface temperature of the member [ºC], Φ is the configuration factor, ε_m is the surface emissivity of the member, ε_f is the emissivity of the fire and σ is the Stephan Boltzmann constant (5.67 x 10-8 W/m^{2}K^4).

The heat flux was measured by radiometers located at the ceiling level during the experimental tests (Arbed, 2001). These radiometers measure the temperatures of hot gases (θ_g) mixed with the influence of the cold ambience (θ_{amb}) around the localised fire, and the heat flux $\dot{h}$ received by the unit of surface area exposed to fire is given by:

$$\dot{h}= \alpha_c\left(\theta_g-\theta_{amb}\right)+\Phi\,\varepsilon_m\,\varepsilon_f\,\sigma\left[\left(\theta_g + 273\right)^4- (\theta_{amb} + 273)^4\right] \quad [W/m^2] \qquad \text{(Eq. 2.7)}$$

On the fire exposed surfaces, the net heat flux $\dot{h}_{net}$ should be determined considering heat transfer by convection and radiation (EN 1991-1-2, 2002) as:

$$\begin{aligned}\dot{h}_{net} &= \dot{h}_{net,c} + \dot{h}_{net,r} = \alpha_c\left(\theta_g-\theta_m\right) + \Phi\,\varepsilon_m\,\varepsilon_f\,\sigma\left[\left(\theta_g + 273\right)^4- (\theta_m + 273)^4\right] \\ &= \\ &\alpha_c\left(\theta_g-\theta_{amb}\right) + \alpha_c\left(\theta_{amb}-\theta_m\right) + \Phi\,\varepsilon_m\,\varepsilon_f\,\sigma\left[\left(\theta_g + 273\right)^4- (\theta_{amb} + 273)^4\right] + \\ &\Phi\,\varepsilon_m\,\varepsilon_f\,\sigma\left[(\theta_{amb} + 273)^4- (\theta_m + 273)^4\right]\end{aligned} \qquad \text{(Eq. 2.8)}$$

Finally, (Eq. 2.6) is found, with θ_{amb} = 20ºC.

Hasemi´s method is a simple tool for the evaluation of the localised effect of a fire on horizontal elements located above the fire, and it cannot be used for vertical elements such as columns.

The net heat flux $\dot{h}$ from the fire of each vehicle to the horizontal structural members depends of the following parameters (Figure 2.7): H_s [m] is the vertical distance between

the fire source and the floor (equal to 0.3 m according ECCS (1993)); H [m] is the vertical distance between the fire source and the surface area exposed to fire at the ceiling level; r [m] is the horizontal distance between the vertical axis of the fire and the point along the ceiling where the thermal flux is calculated; y is a parameter that depends on the diameter D, the rate of heat release Q and on the distances H and r. The net heat flux $\dot{h}$ is calculated according (Eq. 2.9) (EN 1991-1-2, 2002):

$$\begin{aligned} \dot{h} &= 100\,000 && \text{if } y \leq 0.3 \\ \dot{h} &= 136\,300 - 121\,000\, y && \text{if } 0.3 < y \leq 1 \\ \dot{h} &= 15\,000\, y^{-3,7} && \text{if } 1 < y \end{aligned} \qquad [\mathrm{W/m^2}] \qquad \text{(Eq. 2.9)}$$

Where y is calculated by:

$$y = \frac{r + H + z'}{L_h + H + z'} \qquad \text{(Eq. 2.10)}$$

Where z' is the vertical position of the virtual heat source as given by (Eq. 2.11) [m], and L_h is specified according to (Eq. 2.12):

$$\begin{aligned} z' &= 2.4D\left(\left(Q^*_D\right)^{2/5} - \left(Q^*_D\right)^{2/3} \right) \text{ when } Q^* < 1.00 \\ z' &= 2.4D\left(1.0 - \left(Q^*_D\right)^{2/5} \right) \text{ when } Q^* \geq 1.00 \end{aligned} \qquad \text{(Eq. 2.11)}$$

$$\frac{L_h + H}{H} = 2.90\left(Q^*_H\right)^{0.33} \qquad \text{(Eq. 2.12)}$$

With:

$$Q^*_H = \frac{Q}{1.11 \times 10^6 H^{2.5}} \text{ and } Q^*_D = \frac{Q}{1.11 \times 10^6 D^{2.5}}. \qquad \text{(Eq. 2.13)}$$

The heat flux from several localised fires is the sum of the heat fluxes obtained for each fire, with a maximum value of 100 $\mathrm{kW/m^2}$ (Eq. 2.9); this limit was deduced from experimental tests made by Hasemi (Arbed, 2001).

The temperature of a beam at the ceiling level can be defined using the Hasemi's method, where the distance H needs to consider the beam profile section height. No recommendation is provided in the code to define this distance; Franssen and Vila Real (2010) consider two situations:

i) For a section located just above the fire source: the distance between the fire source and the beam bottom flange can be considered and lead to safe results (it is assumed that all surfaces have the same level as the bottom flange),

ii) For a section located far away from the fire source: the Hasemi's method is theoretically only applicable for surfaces located at the ceiling level and the beam

top flange can be considered as a safe approximation (the flame is normally constrained under the ceiling).

According to Schleich *et al.* (1999b), the net heat flux ($\dot{h}$) may be multiplied by a correction factor equal to 0.85 to account that the flame is deviated under the beam; however, this proposal is not considered in EN 1991-1-2 (2002).

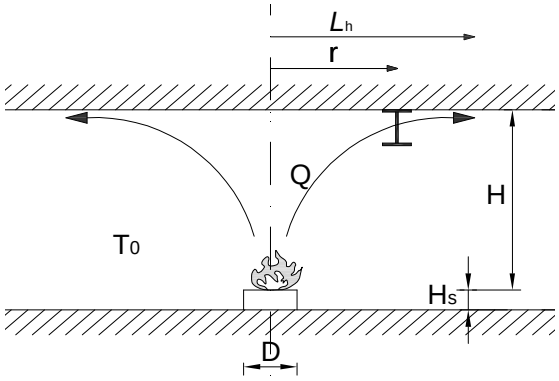

Figure 2.7: Parameters used in the Hasemi's method to calculate the heat flux from the vehicle to the surface area exposed to fire at the ceiling level

2.5.4 Fire design of steel members

According to EN 1993-1-2 (2005) and EN 1994-1-2 (2005), there are three approaches to design structures exposed to fire: i) fire testing (very expensive and time consuming), ii) simplified methods, and iii) advanced methods. The simplified methods are based on conservative assumptions and allow the design of individual members. The advanced calculation methods apply engineering principles in realistic and specific situations; they can be applied to the fire analysis of any structural member. In the application example presented in section 2.7, these two last approaches are compared.

2.5.5 Structural fire behaviour of steel members

The best characterization of the structural fire response of open car parks is the real evidence or experimental tests that reproduce closely the reality, such as the study performed in 2000 by CTICM (Joyeux *et al.*, 2002). The three fire tests were performed in a real unprotected composite steel-concrete car park; the first one included three class 3-cars (scenario 5 in Figure 2.3). The tested structure was defined by beams IPE 550 and columns HEB 200 and a steel-concrete composite slab connected to the beams by shear connectors; no fire protection was considered in the steel profiles. The fire test took 1 hour and 20 min. and the maximum gas temperature near the ceiling reached 1040°C above the vehicle 0; however, the average gas temperature during the 15 minutes of higher temperatures was 510°C, which means that a peak temperature was reached only during a very short time. The maximum temperature in the beam lower flange at a distance of 2.5 m from the column (half length of the vehicle) was 700°C with a gradient of 250°C in the cross-section of the beam. The column flange exposed to fire reached 640°C and 480ºC respectively at

2 m and 1 m above the ground, with a gradient in the cross-section of 140°C and 150ºC respectively. The maximum vertical displacement of the beam was -70 mm (or 0.4% of the length); after cooling phase, a residual deformation of +25 mm was observed. Just above the cars, lateral buckling and local buckling of the lower flange of the beam were observed. In the beam-column joint, 6 bolts (in a total of 8) broke, but no collapse of the structure was observed.

2.6 Fire requirements in different European countries

The definition of open car park can differ from country to country. ECCS (1993) considers that a car park may be considered as "open" if for every parking level, the ventilation areas in the walls are situated in at least two opposite facades, equal to at least 1/3 of the total surface area of all the walls, and correspond to at least 5% of the floor area of one parking level. Table 2 presents the limitations, the general requirements for fire ISO 834 and the indication of acceptance or not of alternative design conditions in different European countries. It is showed that in some countries, this type of building does not require (or very few) any time of resistance under fire (ex.: R0 in Italy or R15 in U.K.). Portugal is one of the countries with the highest requirements for fire resistance of structural elements (from R60 to R180); however, the use of Natural Fire as an alternative to ISO fire is accepted and it is also allowed limiting or avoiding any fire protection on steel elements. This table also shows that, actually, still some of European countries prescribe long fire time of resistance under the ISO fire, and do not indicate anything about the use of Natural Fire (Hungary, Spain and Poland). In France and Finland, the use of bare steel is allowed if the fire safety is proved by tests or scientific studies.

According to the ECCS report (1993), steel structures in open car parks do not require fire protection, and therefore have economic advantages. The fire safety of these structures is ensured by the following conditions: i) the design at room temperature (or "cold design"), according to the current rules, is the basic condition for the stability of the structure in the fire situation; no additional measures for fire neither a special "hot" design are required; ii) beams with composite steel concrete section including shear studs should be used; for economic reasons, it is recommended to use light weight sections (IPE, HEAA and UB); iii) large flange sections (HEA, HEB, UC) should be considered for the columns; and iv) horizontal forces must be supported by frames or bracings (protected against fire). Additionally, CTICM (Fraud *et al.*, 2004) indicates: i) use the same cross-sections for all columns in the same floor; these columns must be filled with concrete between the flanges, ii) use of concrete stairs to increase the horizontal stability and to be used as emergency stairs; iii) use a minimum steel grade of S355, and minimum concrete class of C30/37; iv) steel beams connected to the concrete slab by shear studs with a minimum degree of connection of 80%; v) concrete slabs built in situ or precast concrete; the essential point is the static and structural integration of the slab in the load-bearing system (ECCS, 1993).

Table 2.2: Resistance requirements of open car parks in Europe, according to the ECCS (1993), and updated in accordance with the INERIS (Cwiklinski, 2001) and other documents

COUNTRY	Limitations						General requirements for fire ISO 834	Alternative design conditions	
	Minimum percentage of openings (%)		Maximum						
	Openings /floor	Openings /walls and façades (*1)	Dist. between opposite façades (m)	nº of stories	Building height (m)	Floor area per story (m^2)		No fire protection	Natural fire (*3)
Germany	-	33	70	-	22	-	R0 (*5)	/	/
Austria	-	33	70	-	22	-	Up to R90	Yes	Yes
Belgium (Moniteur Belge, 2007)	-	17	60	-	-	-	R0 (*5)	/	Yes
Denmark	5	-	24	-	-	-	R0 (*5) to R60	Yes	Yes
Spain	-	-	-	-	-	-	R60 to R120 (*2)	-	-
Finland	10	30	-	8	-	9000	R60	No (*4)	Yes
France (ArcelorMittal, 2007)	5	-	75	-	-	-	Up to R60	No (*4)	Yes
Netherlands	-	30	54	-	20	-	R0 (*5) to R30	/	/
Hungary	-	-	-	-	-	-	R30 to R90 (*2)	No	No
Italy	15	60	-	-	-	-	R0	-	-
Luxemburg (ArcelorMittal, 1996)	-	50	-	-	-	-	R0 (*5) to R30	/	/
Norway	-	33	-	-	16	5400	R10 to R60	Yes	-
Poland	-	-	-	-	25	4000	R60	No	-
Portugal (Diário da República, 2008a); (Diário da República, 2008b)	*(The code does not distinct open and closed car park buildings)*						R60 to R180	-	Yes
U.K.	5	-	90	-	15.2	-	R15	Yes	Yes
Sweden	-	-	-	-	-	-	Up to R90 (*2)	Yes	Yes
Switzerland	-	25	70	-	-	-	R0 (*5)	/	/

(*1): Total area of openings / total area of walls and façades surrounding one parking level.

(*2): General requirements of National Building Code.

(*3): Use of Natural Fire as an alternative to ISO fire to prove the fire resistance.

(*4): Bare steel is allowed if this can be proved by tests or scientific studies.

(*5): If specific structural conditions defined in National code are met.

As open car park buildings have general/typical dimensions with few variables, Corus in UK (Corus, 2004), ArcelorMittal in the center of Europe (ArcelorMittal, 1996, and 2007) and OneSteel (2004) in Australia have already developed some typical sizing data sheets or examples in order to avoid the advanced sophisticated calculations.

2.7 Example of application

The design methodology based on fire scenarios is exemplified by the application to the open composite steel-concrete car park with 8 floors described in chapter 1 (Figure 1.7). The main and secondary beams are defined by IPE 550 and IPE 450, respectively (steel grade equal to S355). In this example, four localised fires scenarios are studied in order to check the design of the secondary beam with two spans of 16 m each (IPE 450), the main beam with spans of 10 m (IPE 550) and the column of the fourth floor (HEB 300).

The fire scenario chosen for the secondary beams is scenario 1, with a vehicle under the mid-span of the beam (critical situation for the cross-section with sagging bending moment), whereas scenarios 4 and 5 correspond to the worst scenarios for the column study (Figure 2.3). Only class 3-cars are considered. For the main beam (IPE 550), scenario 3 is the worst fire scenario.

The design fire load is calculated considering (Eq. 2.1) with $\psi_1 = 0.7$ and $q_k = 2.5$ kN/m^2; (Eq. 2.14) and (Eq. 2.15) provide the design loads for the secondary beam and the primary beam, respectively.

$$1.0\ G_k + 0.7\ Q_k = 1.0 \text{ x } 7.77 \text{ kN/m} + 0.7 \text{ x } 8.18 \text{ kN/m} = 13.50 \text{ kN/m} \qquad \text{(Eq. 2.14)}$$

$$1.0\ G_k + 0.7\ Q_k = 1.0 \text{ x } 25.91 \text{ kN/m} + 0.7 \text{ x } 26.16 \text{ kN/m} = 44.22 \text{ kN/m} \qquad \text{(Eq. 2.15)}$$

2.7.1 Design according to the simplified method in the temperature domain

The fire design of a structural element can be performed in the temperature domain, time domain or resistance domain. Two domains are checked for the study of the secondary beam:

i. *Temperature domain*: it is considered that the element has a uniform temperature distribution and the failure is expected to occur when this temperature exceeds the critical temperature (θ_{crit}). In case of a localised fire, temperature is not uniform along the beam and using a critical temperature of the element is very conservative.
ii. *Resistance domain*: the resistant bending moment of the structural element $M_{fi,0,Rd}$ should be compared to the applied bending moment $M_{fi,Ed}$ (assuming no lateral buckling because of the concrete slab).

Steel temperatures can be easily determined with program Elefir-EN (Vila Real and Franssen, 2010), considering the following data: i) definition of the localised fire according to the number of vehicles included in the scenario, ii) curve of the rate of heat release of each car (Figure 2.5); iii) diameter of the fire, D (for each car: D = 3.9 m); iv) distance H between the heat source and the surface area exposed to fire (see section 2.5.3.2), with H_s = 0.3 m; and v) horizontal distance between the vertical axis of the fire and the point along the ceiling where the thermal flux is calculated, r (m) (Figure 2.7). For each scenario, the flame length L_f (Eq. 2.4) is greater than the height of the floor: the flame impacts the ceiling, so the Hasemi's method is considered.

The critical temperature (θ_{crit}) is also calculated with the program Elefir-EN (Vila Real and Franssen, 2010), according to EN 1993-1-2 (2005). The beam is exposed on 3 sides (the top flange supports the concrete slab), the adjustment factor k_1 (non-uniformity of temperature in the section) is equal to 0.7 and the adjustment factor k_2 (non-uniformity of temperature along the beam) is considered equal to 1. Figure 2.8a shows the results of the critical fire scenario 1; the critical temperature is equal to 653°C and a maximum temperature (θ_{max}) of 706°C is reached in the beam after 28 min. In this case, it is necessary to protect the beam using 4 mm of cement with vermiculite, for example. If resistance domain is considered, the composite behaviour of the beam can be considered. The maximum sagging bending moment $M_{fi,Ed}$ is equal to 244.5 kNm (mid-span), and at 28 min. of fire (706ºC), the bending moment resistance of the composite beam is $M_{fi,0,Rd}$ = 255 kNm, assuming a uniform distribution of temperatures in the steel beam, and the concrete slab remaining at ambient temperature. So no fire protection is needed.

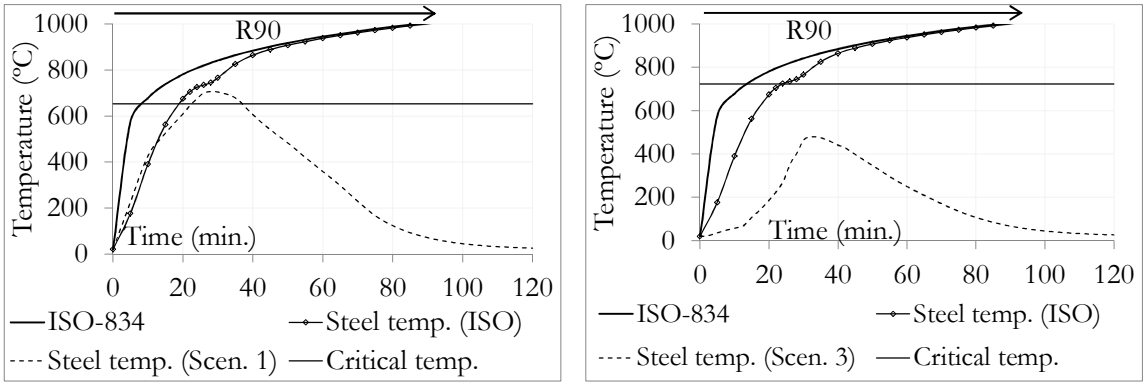

a) Beam IPE 450 (scenario 1) b) Beam IPE 550 (scenario 3)

Figure 2.8: Comparison between the steel temperature in beams IPE 450 and IPE 550 subject to ISO 834 fire and to the most unfavorable fire scenarios for each beam

Scenario 3 with seven cars (Figure 2.3) is the critical fire scenario for the main beam (IPE 550). Figure 2.8b shows the temperature curves: the critical temperature is equal to 724ºC and a maximum temperature of 543°C is reached in the beam after 32 min.; no fire protection is needed, even in the more conservative temperature domain. However, if Portugal regulation is considered, the structure resistance should be R90 (this building has more than 9 m in height, and it is 2nd category of risk (Diário da República, 2008a,b));

moreover, if curve ISO 834 is used to check this structure for the resistance R90, 11 mm and 16 mm of cement with vermiculite are needed to protect main and secondary beams, respectively. Table 2.3 in section 2.7.3 summarizes and compares these results.

2.7.2 Design according to the advanced calculation methods

The design of the same structure through an advanced calculation method is now presented and the results are compared with those obtained in section 2.7.1. Since with the method based on fire scenarios, no fire protection is needed to the main beam, advanced calculation method will only be applied to composite secondary beam (scenario 1). Additionally, the advanced calculation methods are also used to evaluate the fire resistance of the column (scenarios 4 and 5). The finite element program Abaqus (2012) is used to perform the thermal and structural analyses.

2.7.2.1 Thermal analysis

The thermal loads for the beams are defined taking into account the following procedure: i) the gas temperatures that surround the beam are calculated using the program Elefir-EN: as the flame impact the ceiling, the Hasemi's method is considered and the gas temperature corresponds to the flame temperature (H = 2.25m); ii) a heat transfer analysis is performed in Abaqus for each composite section located along the beam (emissivity factor equal 0.7 and convection coefficient equal to 35 W/m^{2}K); the model of the composite beam is developed using 2D deformable element DC2D4. Figure 2.9 depicts the temperatures evolution in the steel beam section for each scenario; the presented curves correspond to the cross-sections with maximum temperatures: mid-span of the beam for scenario 1, and at 2.5 m from the column for scenarios 4 and 5.

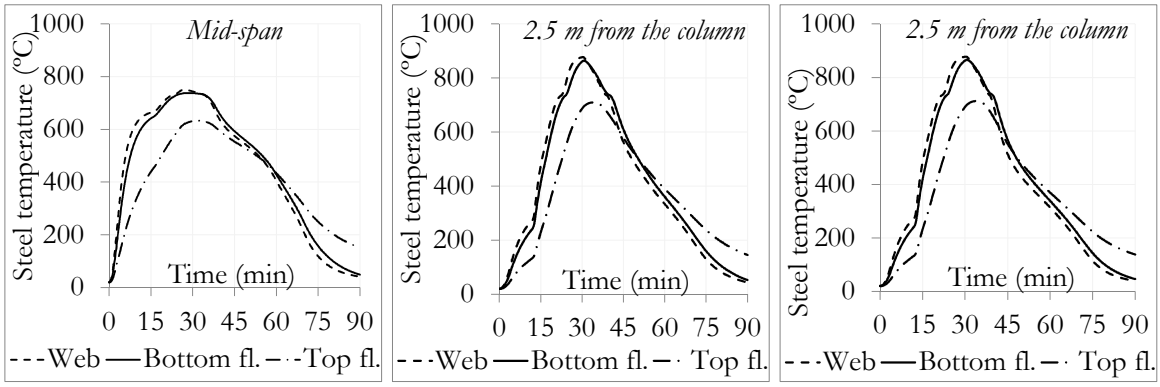

a) Scenario 1 b) Scenario 4 c) Scenario 5

Figure 2.9: Temperature evolution in the secondary beam IPE 450

Figure 2.10a-c presents the variation of the average temperature in each section of the secondary beam during the fire for each scenario, while Figure 2.10d presents the variation of the average temperatures in each section of the secondary beam versus the position, at 30 min. of fire. In these charts are represented the weighted average temperatures of the steel beam section.

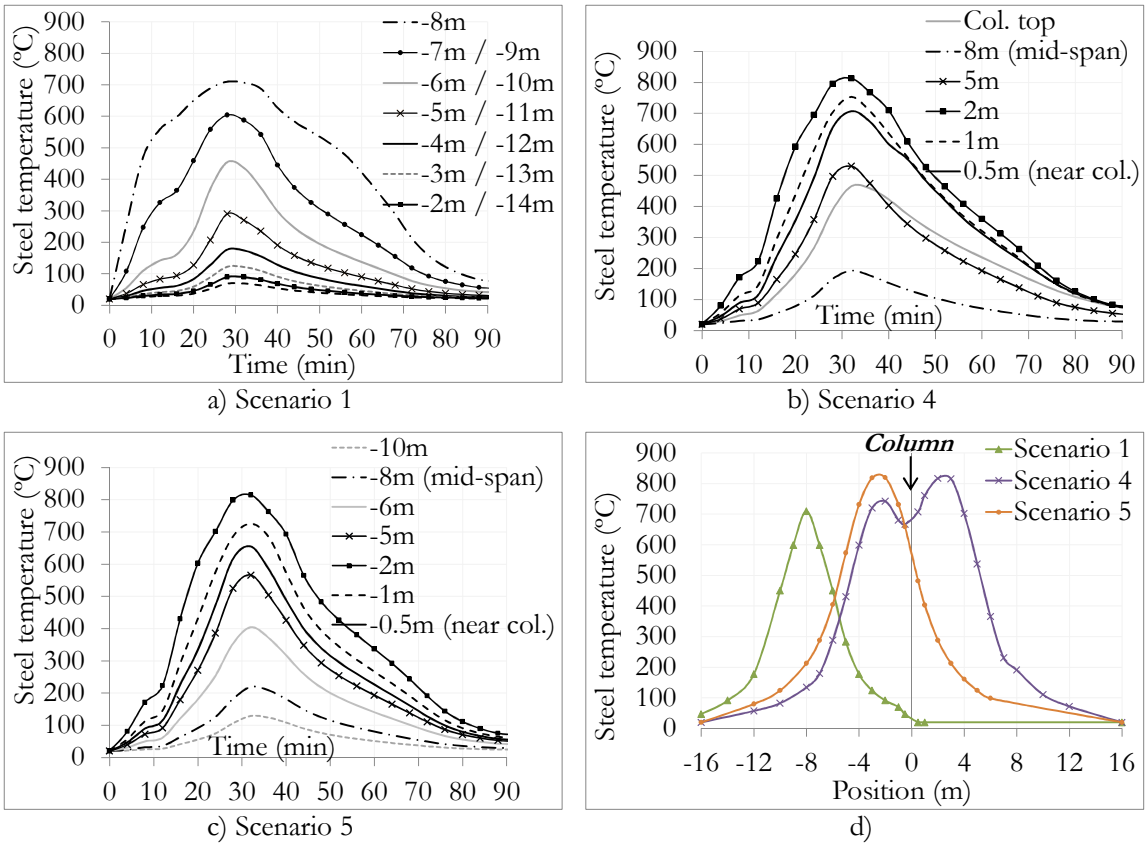

Figure 2.10: Variation of the weighted average temperatures in section of the secondary beams IPE 450: a),b),c) *versus* time; and d) after 30 min. of fire *versus* position along the beams

2.7.2.2 Mechanical analysis

In this example, the two dimensional frame includes the secondary beams of 16 m length each (Figure 2.11) and the columns (weak axis). The composite beams are modelled with an equivalent rectangular section (identical section and inertia than the real composite beam; additionally inertia considering cracked concrete is considered near the supports). The beams affected by the fire scenarios, developed at the fourth floor, are modelled by beam elements for the steel profile, and shell elements for the slab (the composite slab is simplified to a reinforced concrete slab of thickness equal to 120 mm). The width of the slab is 3.4 m, which corresponds to the effective width at mid-span. The initial deformation of h/1000 (3 mm) is applied to the columns. Beam elements are used for the beams and the columns not directly affected by the fire. Mechanical loads correspond to the values presented at the beginning of section 2.7. Only third, fourth and fifth floors are modelled, taking into account loads from the upper floors.

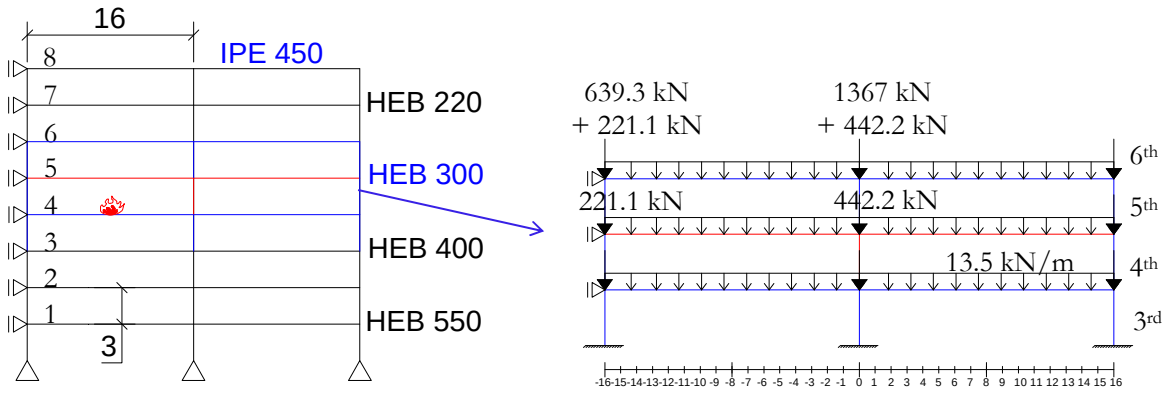

Figure 2.11: Studied car park versus numerical 2D frame (loaded)

The calculated temperature gradients are directly applied to the steel beam sections in the static analysis, using the option "predefined fields". The concrete slab is assumed to be at ambient temperature throughout the analysis. This assumption was based on the results from the CTICM tests (Joyeux *et al.*, 2002): maximum temperature equal to 250°C was measured at the bottom of the slab and in an area restricted to the area of fire.

The scenario 4 corresponds to the worst fire scenario for the column, with four class 3-cars burning around it. Because no accurate (and simple) method is defined to calculate the column temperature in case of a localised fire, the temperature at the column top is assumed to be the same than an HEB 300 beam (calculated by Hasemi´s method). This temperature is applied uniformly along the column height (except below the heat source, at 0.3 m above the floor, where 20ºC are considered as temperatures should remain low enough to consider that no material degradation is induced). The concrete properties are set in accordance with EN 1992-1-2 (2004), and steel properties vary with temperature, as defined in EN 1993-1-2 (2005).

Figure 2.12 shows the development of the vertical displacement at the beam mid-span for each fire scenario. For the scenario 1, a maximum displacement equal to 122 mm downwards (which includes the initial displacement of 21 mm due to the mechanical loading) is reached after 15 min. of fire. After the fire, the beam shows a residual camber, with a displacement at mid-span equal to 102 mm upwards. Because i) of the high thermal gradients in the cross-section of the composite beam (unheated concrete slab), and ii) the axial restraint to thermal expansion due to the lateral bracing and the unaffected part of the building, high compression loads develop at the beam bottom flange, which invert the bending moment from sagging to hogging moment. This thermal bowing develops at the beam mid-span after 17 min. of fire.

Under scenario 4, the column is not able to resist to the entire fire and fails by yielding of the cross-section after 28 min. of fire (three plastic hinges are developed at the top, bottom and at mid-height of the column - Figure 2.13). However, according to the statistics, this scenario never happened in reality in an open car park building, and the

application of uniform temperatures along the column height is a very conservative hypothesis (Schleich *et al.*, 1999a). An additional verification of the column, based on the realistic fire scenario 5 including three burning cars, is performed. For this scenario, the column temperatures measured during the first French test (Joyeux *et al.*, 2002) are assumed: average values of 405ºC and 570ºC were measured at 1 m height and at 2 m height, respectively. The column and the beams resist to this fire scenario, with maximum 196 mm of beam vertical displacement at 32 min (Figure 2.12).

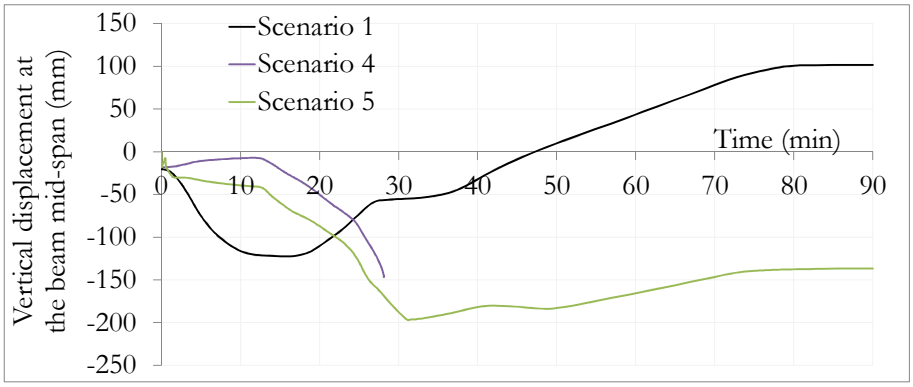

Figure 2.12: Evolution of the beam IPE 450 mid-span vertical displacement during fire

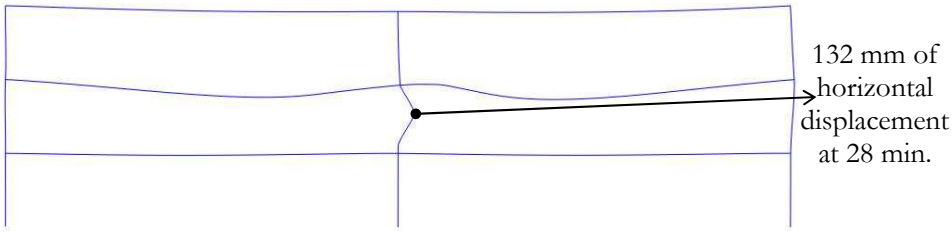

Figure 2.13: Frame deformation at 28 min of fire (scenario 4): column failure (scale 5)

Standard ISO 834-1 (1999), relating to fire resistance tests, indicates that failure of an element subject to bending under fire should be considered when the maximum vertical displacement δ_{max} exceeds the values indicated by (Eq. 2.16):

$$\delta_{max} \leq \frac{L^2}{400d} = 1123 \text{ mm} \qquad \text{(Eq. 2.16)}$$

Where L [mm] is the span of the beam and d [mm] is the distance from the extreme fibre of the design compression zone to the extreme fibre of the design tensile zone of the structural section. The maximum displacements of the studied beam are lower than these values, and it can be considered that the beam does not fail under any of these fire scenarios. For the column, the same standard limits the maximum axial contraction $\delta_{vert,max}$ of axially loaded elements to (Eq. 2.17):

$$\delta_{vert,max} \leq \frac{h}{100} = 30 \text{ mm} \qquad \text{(Eq. 2.17)}$$

Where h [mm] is the initial height. The studied column reached this limit after 28 min. of fire in scenario 4, but reached smaller contraction (max. 24 mm) in scenario 5. French prescriptions (Fraud *et al.*, 2004) usually prescribe to add concrete between the column flanges in order to protect the column (see section 5), which is a solution that could be done if scenario 4 needs to be checked.

2.7.3 Summary of the results

Table 2.3 summarizes the results obtained for the beams and the column, according to the simplified and advanced methods.

Table 2.3: Summary of the design results for beams IPE 450 and IPE 550

	Simplified method			Advanced method		
	Temperature / resistance domain					
	Scenario 1	Scenario 3	ISO 834	Scenario 1	Scenario 4	Scenario 5
IPE 550 (θ_{crit}= 724ºC)	---	θ_{max}= 543ºC (32 min.)	$\theta_{t=90min}$= 1001ºC	---	---	---
Prot.: ex.: cement with vermiculite*	---	No need	11 mm thick	---	---	---
IPE 450 (θ_{crit}= 653ºC / $M_{fi,Ed}$ = 244.5)	θ_{max}= 706ºC (28 min.) / $M_{fi,\theta,Rd}$ = 255 kNm	---	$\theta_{t=90min}$= 1001ºC	δ_{max} = 122 mm (15 min.)	---	δ_{max} = 196 mm (32 min.)
Prot.: ex.: cement with vermiculite*	4 mm thick / No need**	---	16 mm thick	No need	---	No need
Column HEB 300	---	---	---	---	δ_{vert} > 30 mm	$\delta_{vert,max}$ = 24 mm
Prot.: ex.: concrete between flanges*	---	---	---	---	Need!	No need

*Prot. = fire protection ** If resistance of the composite beam is considered

2.8 Concluding remarks

The fire design of steel and composite structures from open car park can be made in accordance with Eurocodes: EN 1991-1-1 (2002) defines the mechanical loads, while Annex C of EN 1991-1-2 (2002) presents a simplified method for determining the flame temperature around the beams. The calculation of these temperatures depends on the total rate of heat release, which is determined based on the fire scenarios. The reference curve for the rate of heat release was defined based on experimental tests results performed on

actual vehicles. Finally, EN 1993-1-2 (2005) and EN 1994-1-2 (2005) present the calculation models for these structures.

From previous experimental tests in real open car park buildings, it was concluded that most of unprotected steel open sided steel-framed car parks has sufficient inherent resistance to withstand the effects of any fires that are likely to occur. These results have encouraged to change the legislations in several European countries, allowing to build steel or composite steel-concrete open car parks without fire protection, taking into account a design based on the actual performance of the structure and not on prescribed nominal design curves (that in most of the cases, require fire protection with considerable thickness).

EN 1991-1-2 (2002) proposes the Hasemi´s method which is a simple analytical tool for the evaluation of the localised effect of a fire on horizontal elements located above the fire. For horizontal elements, the simplified method based on fire scenarios is fast to use, and it was shown in the example that unprotected composite steel-concrete beams (secondary or primary) resist to the localised fire. Design of columns under localised fires can only be done, for now, using advanced models; no accurate and simple method is available to calculate the column temperature due to a localised fire. When the assessment of the real strength of the structures is required, allowing optimizing the design, the choice must involve the use of advanced calculation methods rather than simplified methods (Joyeux *et al.*, 2001). The example presented in this chapter clearly showed the advantage of using the design methodology based on fire scenarios against the use of ISO curve; it was verified that the unprotected composite steel-concrete structure resists to the studied fire scenarios.

In conclusion, the design methodology based on fire scenarios allow optimizing the structure to benefit from an appropriate level of fire safety, reducing the fire protection and therefore the final cost of this type of building. However, nowadays, the use of advanced calculation methods instead of simplified ones is still required for optimized designs of open car park buildings. In the codes, simplified analytical methods to design steel members under localised fire do not provide: i) any method to define temperatures in vertical elements such as columns, and ii) any way to consider the failure of the element based on its temperature. Indeed, the critical temperature provided in EN 1993-1-2 (2005) is only valid for steel elements subject to uniform temperature distribution; as observed in recent research works, the behaviour of a column subject to localised fire may be totally different than from that in a standard fire (Zhang *et al.*, 2014).

In the simplified models developed to apply the design methodology, rigid beam-to-column joints were considered. The behaviour of the heated composite beam-to-column joint is studied in detail in the following chapters, under a scenario that would lead to the total collapse of the column.

Chapter 3

3 Experimental tests on beam-to-column joints subject to localised fire, bending moments and axial loads

3.1 Introduction

The work presented in this chapter is focused on seven experimental tests performed at the University of Coimbra. In these tests, the effect of the localised fire (that leads to the column loss) is simulated by the application of elevated temperatures in the composite joint zone. The considered temperatures are based on previous observations: in the past, real tests performed in composite steel-concrete open car park buildings subject to burning cars showed that the temperatures in the beam bottom flanges are lower than 500ºC (see chapter 2); however temperatures of 700ºC are measured in recent tests performed in France (Joyeux *et al.*, 2002), probably due to the manufacturing evolution of cars, with more combustible plastic materials as well as higher petrol tank capacity. Seven beam-to-column sub-frames are tested: one reference test at ambient temperature; five tests at 500ºC or 700ºC; and a demonstration test, for which the sub-frame is subject to an increase of temperature up to the failure of the column. The effect of the beam axial restraint coming from the unaffected part of the building is also studied: three tests without axial beam restraint; two tests with total axial beam restraint; and two tests with realistic axial beam restraint. Table 3.1 presents the objectives of each test.

Before the description of the seven experimental tests, relevant experimental works performed recently are described in the next section.

The work described in this chapter has been published in Haremza *et al.* (2013a).

Table 3.1: Objectives of the seven experimental tests of sub-frames subject to the loss of a column

Test	Objectives
1	Derivation of the joint properties at 20ºC – No axial restraint
2	Derivation of the joint properties at 500ºC – No axial restraint
3	Derivation of the joint properties at 700ºC – No axial restraint
4	Derivation of the joint M-N curve at 500ºC – Total axial restraint
5	Derivation of the joint M-N curve at 700ºC – Total axial restraint
6	Derivation of the joint M-N curve at 700ºC – Realistic axial restraint
7	Demonstration of the real joint behaviour of a sub-frame subject to the loss of a column due to a localised fire – Realistic axial restraint

3.2 Recent and relevant research works

In European RFCS Robustness project (Kuhlmann *et al.*, 2009), a sub-structure subject to the loss of a column was tested at Liège University (Demonceau, 2008). The aim of this test was to study the behaviour of a composite sub-structure subject to the loss of a column at ambient temperature, monitoring the development of catenary action and the effect on the behaviour of semi-rigid and partial-strength composite beam-to-column joints. The bottom storey of a composite building composed of three main frames and three storeys was isolated, and the sub-structure width was reduced according to the laboratory facilities (Figure 3.1). The IPE140 steel beam cross-section (S355) was fully connected to a concrete slab 120 mm thick (C25/30). Composite beam-to-column flush end-plate connections with two bolt rows (M20, grade 8.8 and steel end-plate 8 mm thick) were considered, and beams were connected to steel columns HEA 160 (S355). Axial restraints coming from the undamaged structure were simulated by two horizontal jacks.

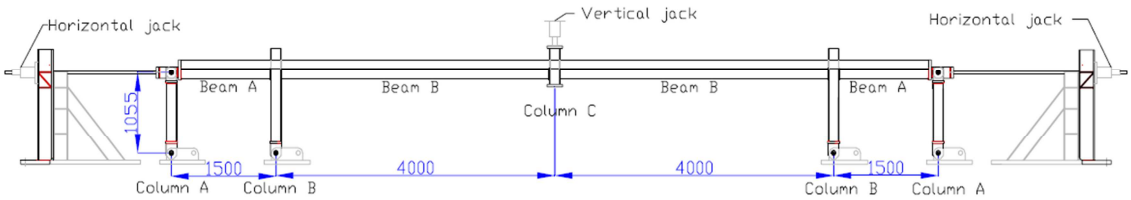

Figure 3.1: Sub-structure configuration tested at the University of Liège (Demonceau, 2008)

The support of the middle column was removed and a vertical load increased at the top of the column. Four distinct stages were observed (Figure 3.2a): i) elastic stage (O-A), ii) yielding stage (A-B), iii) plateau stage (B-C), and iv) catenary stage (C-E). At the first stage, small deflections were developed, and slight concrete cracking was observed in the vicinity of the hogging joints, but the whole subsystem remained largely within the elastic range. Subsequently, yielding of steel components (e.g. column web in compression) was initiated. This was followed by a plateau range, where concrete cracking was further developed. Finally, the subsystem stepped into the catenary stage until the reinforcement rebars were completely ruptured at hogging joints; Figure 3.2b shows the sagging joint at the end of the test. A certain level of resistance was retained when the steel connections worked alone, and the ultimate rotation of the beam was approximately 190 mrad. The test allowed to

measure the membrane forces developed in the beams, and to confirm the composite joints ductile behaviour under tensile forces and bending moments (Demonceau and Jaspart, 2010).

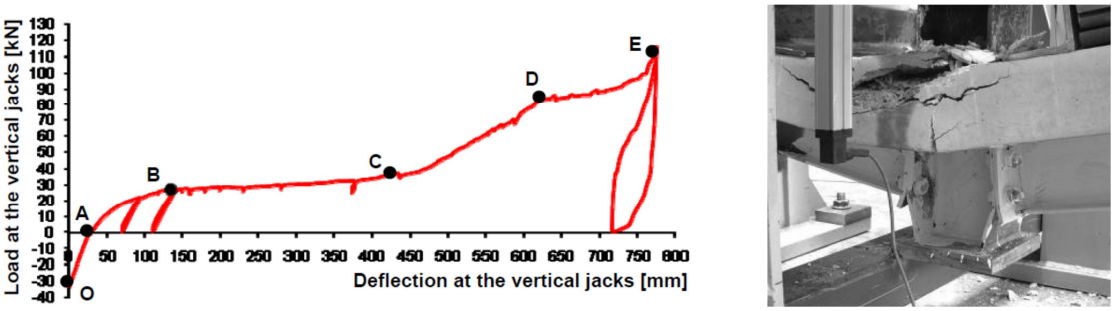

a) b)

Figure 3.2: a) Vertical load *versus* vertical displacement of the joint; b) sagging joint at the end of the test (Demonceau and Jaspart, 2010)

Within the Robustness project, at Stuttgart University, experimental tests were also performed on beam-to-column composite steel-concrete joints subject to bending moment and axial forces. It was shown that for well-designed ductile joints, only ductile components (rebars in tension, beam flange in compression, end-plate and column flange in bending) are activated to move from the pure bending moment to the maximum tension load, which ensure ductility supply (Demonceau, 2008).

Giżejowski *et al.* (2013) performed experimental tests of steel and composite steel-concrete sub-frames subject to the middle column removal scenario, testing flush end-plate and extended end-plate joints. Axial restraints to beams were considered (Figure 3.3). They concluded that composite joints in the investigated frame had much lower ductility if compared to that obtained in the test conducted by Demonceau and Jaspart (2010) (Kozłowski *et al.*, 2011). It shows that there is a need to investigate the influence of height of composite beam as well as other details of the joint on the robustness behaviour of frame systems. The robustness of frameworks by joint ductility may further be enhanced by i) application of steel joints with thin end-plates (10 mm), which is profitable for ductile behaviour; ii) choosing optimal sizes of fillet welds, distances between the bolt rows, as well as between the welds and neighbouring bolt rows. The other factors having an impact on the joint robustness are the reinforcement ratio and the arrangement of shear studs in composite slab near the joint (Giżejowski *et al.*, 2013).

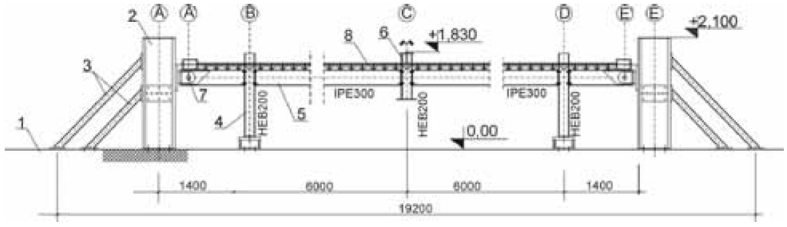

Figure 3.3: Tested composite steel-concrete substructure (Kozłowski *et al.*, 2011)

Yang and Tan (2011a, b) conducted experimental tests of steel and composite bolted joints (simple and semi-rigid connections) subject to catenary action, under the column removal scenario (Figure 3.4). The studied joint types included web cleat, top and seat angle (TSA), top and seat with web angle (TSWA) (8 mm and 12 mm angles), fin plate, flush end plate, and extended end plate. The behaviour and failure modes of these different connections, including their abilities to deform in catenary mode, was provided, and a better understanding of the performance of angle connections subject to catenary action under a column removal scenario was achieved. The test results indicate that angle connections, such as web cleat and TSWA, performed better in the development of catenary action than other types of connections (Yang and Tan, 2011b). Yang and Tan (2012) also performed some numerical models validated with the experimental results using Abaqus program. Parametric studies have been conducted and the simulation results demonstrated that under a middle column removal scenario: i) increasing the number of bolt rows increases the load-carrying capacity and rotation stiffness; however, the connection ductility is adversely affected by the increase of bolt rows, which means this effect is not always beneficial; ii) connection configurations play an important role to form catenary action. Then by improving the arrangement of bolts in configurations of flush end-plate connections, significant increase of load carrying and rotation capacities was achieved. Current acceptance criteria of rotation capacities for steel joints such as web cleat, fin plate, flush end plate and TSWA connections, are probably too conservative as they only consider pure flexural resistance; the proposed connection acceptance criteria of rotation capacities should consider the contribution of catenary action.

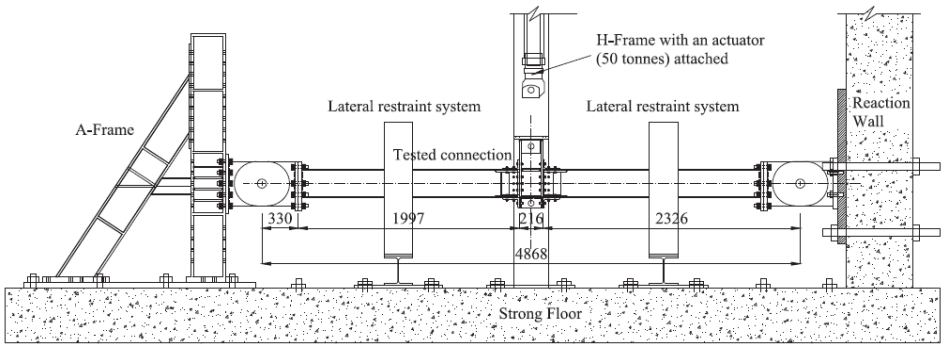

Figure 3.4: Prototype beam-column joint and elevation view of the test set-up (Yang and Tan, 2012)

Finally, it can be pointed out that all the experimental tests available in the literature, and that simulate a column loss scenario, do not consider the effect of fire. The experimental work presented in this chapter considers a fire scenario that leads to the column failure; so the composite joint is subject to a combination of bending moments, axial loads and elevated temperatures.

3.3 Experimental tests

3.3.1 Sub-frame and testing arrangement

The tested sub-frame is selected from the fifth floor of the typical open car park structure specially designed for the European ROBUSTFIRE project (see chapter 1, section 1.3.1). Because of the laboratory dimensions, the beam span length is reduced from 10 m in the real building to 3 m in the tested sub-frame. The seven beam-to-column frames tests, including the corresponding beam axial restraint, are presented in Figure 3.5. The sub-frame is defined by two unprotected composite beams IPE 550 steel cross-sections, grade S355, and one unprotected HEB 300 cross-section steel column, grade S460 (Figure 3.7). A reaction frame, perpendicular to the plane of the tested sub-frame, is used to fix the hydraulic jack that applied the mechanical loading, which is linked by a pin to the top of the column. The column base of the sub-frame is hinged and fixed to a reinforced concrete footing. A smaller steel profile HEB 140 cross-section is used at the bottom column in order to allow: i) the concreting of the specimens at the floor level (Figure 3.6), ii) the simulation of the column loss under fire in test 7. Two small hydraulic cylinders are located on the beam top flanges in order to introduce the hogging bending moment at the joint, and another hydraulic cylinder is located at the column base (except for the test 7) in order to simulate the column loss (see section 3.3.3). The flexural column buckling is restrained: i) at the top of the joint (lateral restraint in Figure 3.8), and ii) at the bottom column (identified as *column restraint* in Figure 3.7). This restraints system allows vertical displacements of the column, and prevents any horizontal displacement or rotation in the plane or out of the plane of the sub-frame.

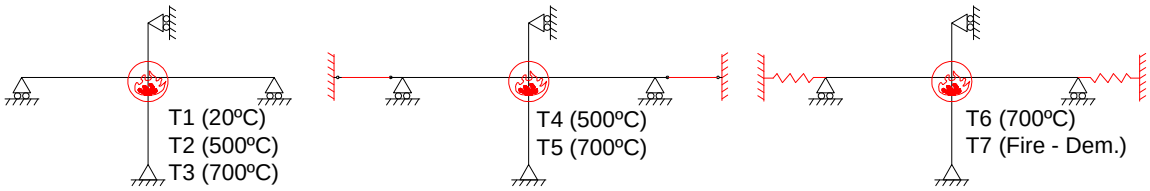

Figure 3.5: Seven experimental tests

Figure 3.6: Specimens after the concreting of the composite slabs, at the floor level

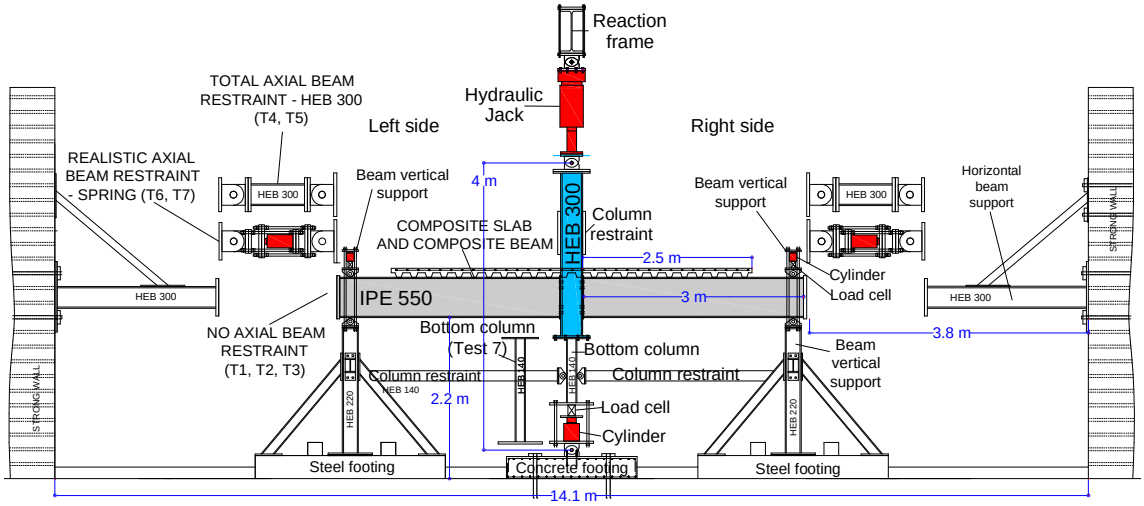

Figure 3.7: General layout, longitudinal view

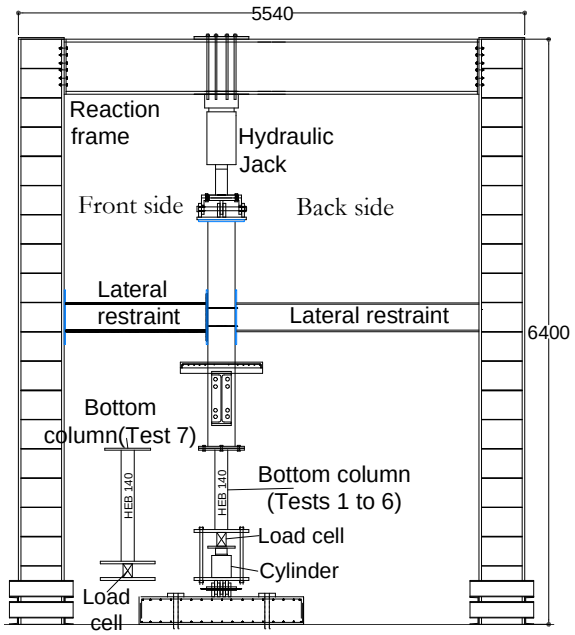

Figure 3.8: General layout, lateral view

The joint configuration is representative of usual joint typologies used in open composite steel–concrete car park structures (Figure 3.9); bolts M30, grade 10.9, and a steel end-plate 15 mm thick, S355, are used. Material properties are discussed in detail in section 3.4. In order to ensure the composite behaviour of the beam-to-column joint, ten longitudinal steel bars of diameter 12 mm are placed in the composite slab (five at each side of the column). The composite joint is designed for the ROBUSTFIRE project (Demonceau *et al.*, 2013), and the bolts are slightly oversized in order to avoid any shear failure during the experimental tests. The composite slab comprises a steel deck and light-weight in situ concrete composite floor, with 900 mm width, 1 mm thick steel sheeting and reinforced concrete C25/30. In order to simplify the concreting, the ribs are placed perpendicularly to the beam. Nevertheless, difficulties were experienced during concreting

and the average total slab thickness is 130 mm instead of the 120 mm defined by Demonceau *et al.* (2013); due to an error during concreting of test 5, on one side, the thickness of the concrete slab above the two ribs in contact with the steel column is 103 mm instead of 71 mm shown in Figure 3.9. In accordance with the maximum spacing defined by Eurocode 4 part 1.1 (EN 1994-1-1, 2004), constructional longitudinal (8 mm diameter) and transversal reinforcements (6 mm diameter) are added.

The steel beam is partially connected to the composite slab by 22 shear studs (diameter = 22 mm; height = 100 mm); this number of shear studs was designed for the composite beam to resist to the design hogging and sagging bending moments M_{Ed} (-535 kNm and 765 kNm respectively). The beam is not composite all along its length (Figure 3.7); a section of steel beam is needed to easily fix the vertical displacements at the supports, needed to apply the initial hogging bending moment at the end of the beams (see section 3.3.3). This structural consideration is accepted because the reduced slab length is enough for the anchorage of the longitudinal steel reinforcement included in the behaviour of the composite joint.

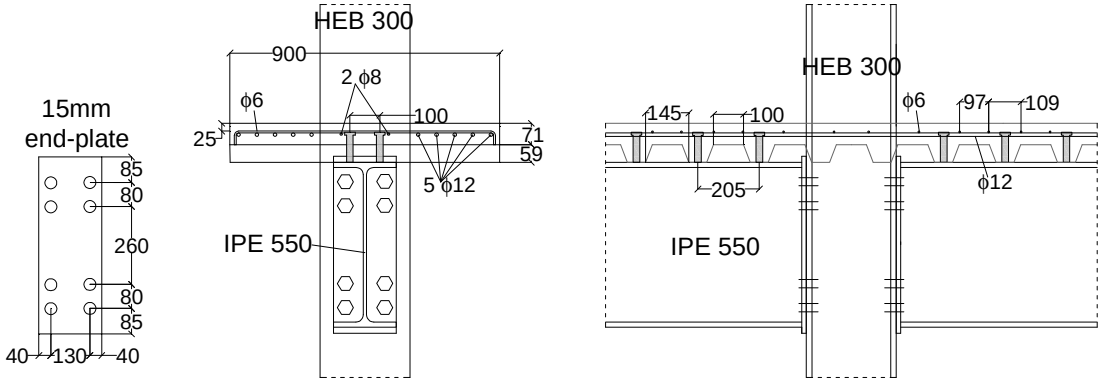

Figure 3.9: Tested joint

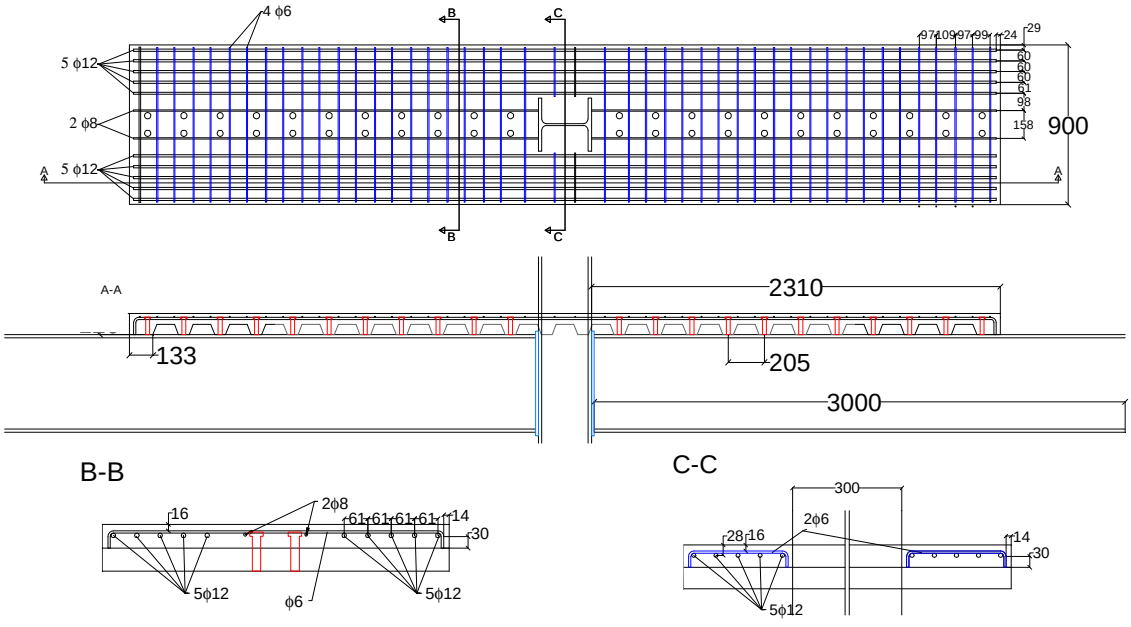

Figure 3.10: Details of the composite slab and longitudinal steel reinforcement

3.3.2 Description of the loading sequence

3.3.2.1 Tests 1 to 6

Each test, from test 1 to test 6, is divided into 3 main steps (see Figure 3.11): step 1 - application of an initial hogging bending moment in the joint, step 2 - heating of the joint zone up to 500°C or 700°C (except for test 1 at 20°C), and step 3 - simulation of the loss of the column and increase of the sagging bending moment up to the failure of the joint. A small pre-loading of bolts is applied for all the experimental tests (about 120 kN), and the axial restraints are connected to the beams since the beginning of the tests.

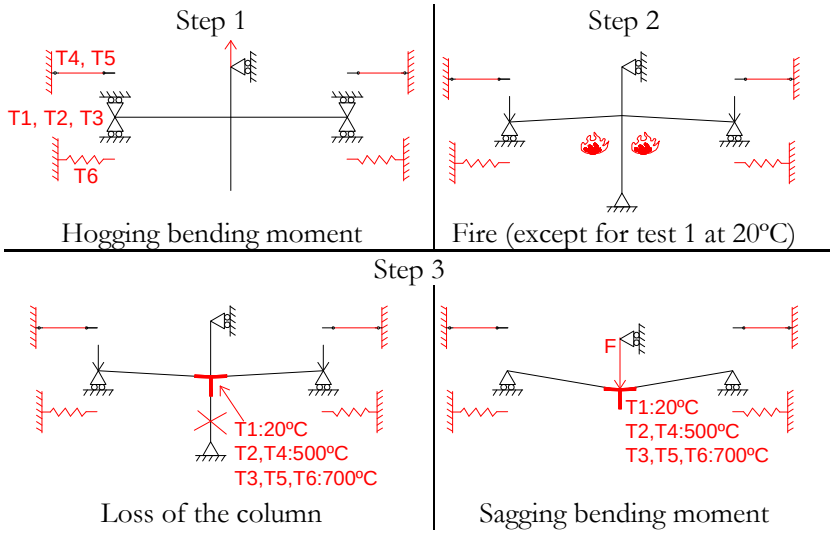

Figure 3.11: Outline of the tests 1 to 6

In step 1, the internal loads in the joint are simulated as in the real car park. The hogging bending moment is calculated in a simple 2D model in Abaqus (2012) (see Appendix D.1), applying the loads at the service limit state (SLS) defined during the design of the car park structure (Demonceau *et al.*, 2013). For the beam-to-column connections between the composite beams and the HEB 300 column, a hogging bending moment equal to -450 kNm is calculated (fifth floor of the building); this moment is applied to test 1 at ambient temperature. According to EN 1991-1-2 (2002), effects of actions under fire may be deduced from those determined in normal temperature design (M_{Ed} = -550 kNm) by calculating a reduction factor η_{fi} (Eq. 3.1); characteristic values of permanent action and leading variable actions are considered, i.e. G_k=26.4 kN/m and $Q_{k.1}$=26.7 kN/m, respectively, and the combination factor ψ_{fi} corresponds to $\psi_{1,1}$ = 0.7 (EN 1990, 2002). The resulting hogging bending moment considered in tests under elevated temperatures is -330 kNm.

$$\eta_{fi}=\frac{G_k+\psi Q_{k.1}}{\gamma_G G_k+\gamma_{Q1} Q_{k.1}}=\frac{G_k+0.5Q_{k.1}}{1.35G_k+1.5Q_{k.1}}=60\% \qquad \text{(Eq. 3.1)}$$

These hogging moments are applied to the joint by increasing the vertical load at the column top in the upward direction, whereas the vertical displacements of the beams ends are locked (Figure 3.11). During step 2, temperatures increase with a linear rate of 300ºC/hour, up to the target temperature in the beam bottom flanges: 500ºC for tests 2 and 4, and 700ºC for tests 3, 5 and 6. Temperatures are kept constant throughout step 3, for which the progressive loss of the column is simulated. Then, the vertical load at the column top is increased in the downward direction with a linear rate of 0.01 mm/sec. (deflection control), in order to increase the sagging bending moment in the joint and to reach the joint failure. During the increase of the sagging bending moment, the column is assumed to be completely failed (no residual bearing capacity). To obtain a better characterization of the elastic stiffness of the joint, an "unloading-reloading" is performed at the beginning of the step 3 for tests 3, 4 and 5.

3.3.2.2 Test 7

This test is divided into 4 steps (Figure 3.12): step 1 - application of an initial hogging bending moment in the joint (-330 kNm); step 2 - application of a constant compressive load at the column top (+250 kN); step 3 - heating of the joint zone and the bottom column, respectively up to 400ºC and 800ºC; step 4 - heating of the joint zone up to the failure of the sub-frame.

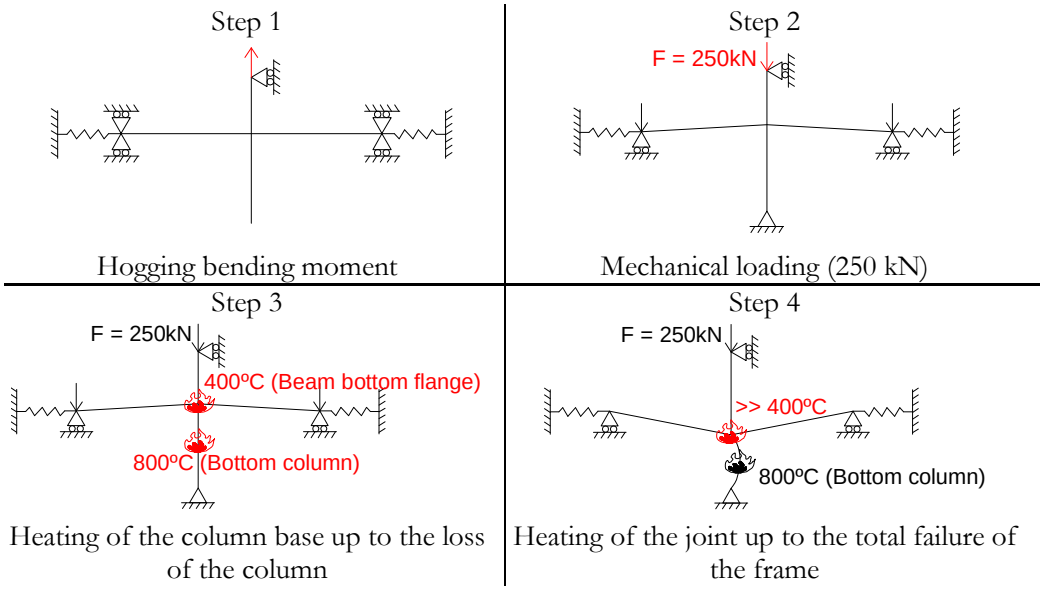

Figure 3.12: Outline of the test 7

The mechanical loading applied at the column top is kept constant during steps 3 and 4. Due to the maximum ranges of the loading and measuring equipment, the steel section of the bottom column is reduced from HEB 300 to HEB 140 in order to reach the column buckling failure under 800ºC or less (in step 3) when it is subject to 250 kN of compression load (709ºC is the critical temperature of the steel profile HEB 140 under this compression load (column length of 1.3 m)). The temperature is increased up to: i) 800ºC in the bottom column; ii) 400ºC in the joint (measured in the beam bottom flanges), under faster heating

rate in the bottom column. The joint temperature is limited to 400ºC in order to avoid joint failure before the collapse of the column; this value is defined by taking into account the constant temperature tests: at 500ºC, 400 kN is reached at the column top, and under 700ºC, only 200 kN is reached; moreover, additional compression load due to thermal expansion effects should be considered. Finally, in step 4, after the column loss, the joint temperature is increased up to the failure of the sub-frame, and the load at the column top (+250 kN) is kept constant. The concrete slab is only heated by heat transfer from the steel beam and column. In the constant temperature tests (see further section 3.5.1), it is shown that this heat transfer is sufficient for the concrete to reach temperatures close to the measured temperatures during real tests with burning cars, performed in car park buildings. In the French tests (Joyeux *et al.*, 2002), the maximum concrete temperature was 260ºC at 25 mm from the slab bottom part, whereas 700ºC was measured in the steel beam bottom flange .

3.3.3 Mechanical and thermal loadings

Steel temperatures are increased using Flexible Ceramic Pad (FCP) heating elements (concrete is not directly heated). In tests 2 to 6, the heated zone is defined by the joint, a length of 0.6 m of the beam to each side of the joint and 0.8 m of column (Figure 3.13). In test 7 (demonstration test), the entire lower part of the column is heated; because the number of electrical elements could not be increased, the heated length of the beam is reduced to 0.4 m (Figure 3.14). A Servosis hydraulic jack ($F_{max.}$ = 1000 kN; $\Delta_{max.}$ = 280 mm) is used to apply the mechanical loading at the column top (Figure 3.7).

Figure 3.13: Heated connection zone using Ceramic Pad Heating elements, thermally insulated by rock-wool of density 128 kg/m^3 (tests 2 to 6)

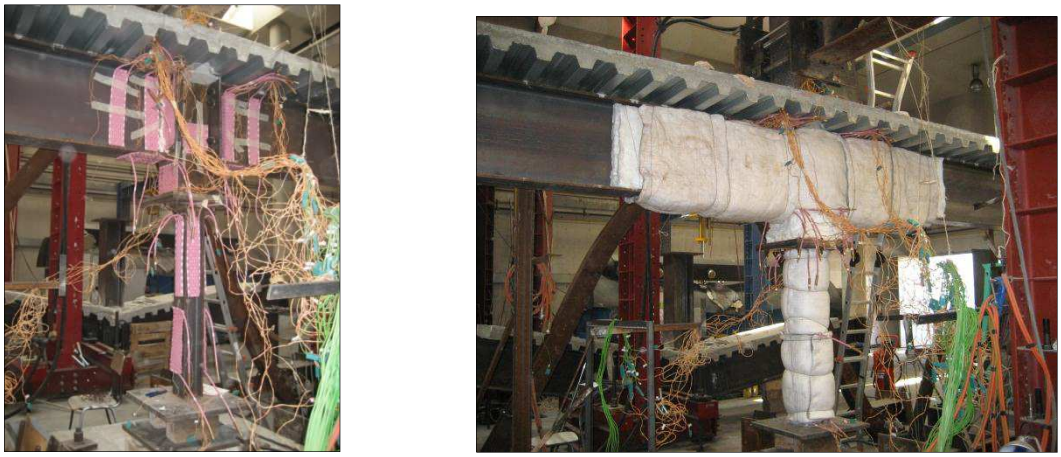

Figure 3.14: Heated zone using Ceramic Pad Heating elements, thermally insulated by rock-wool of density 128 kg/m³ (test 7 - Demonstration test)

The beam vertical supports, shown in Figure 3.7, restrained the vertical displacements needed to introduce the hogging bending moment at the joint. A load cell and a hydraulic cylinder are located on the beam top flanges (see Figure 3.20) to measure the vertical reaction and to apply the initial pre-loading, as illustrated in Figure 3.15: i) any vertical displacement of the beams ends is restrained at the supports, then, a pre-load is applied, using the cylinders, in order to keep constant the beam position (the column is free at the base); ii) the hydraulic jack increased the vertical load at the column top and pulled the column upwards; iii) the support at the column base is put in contact; iv) the load at the column top is decreased and transferred to the column base support.

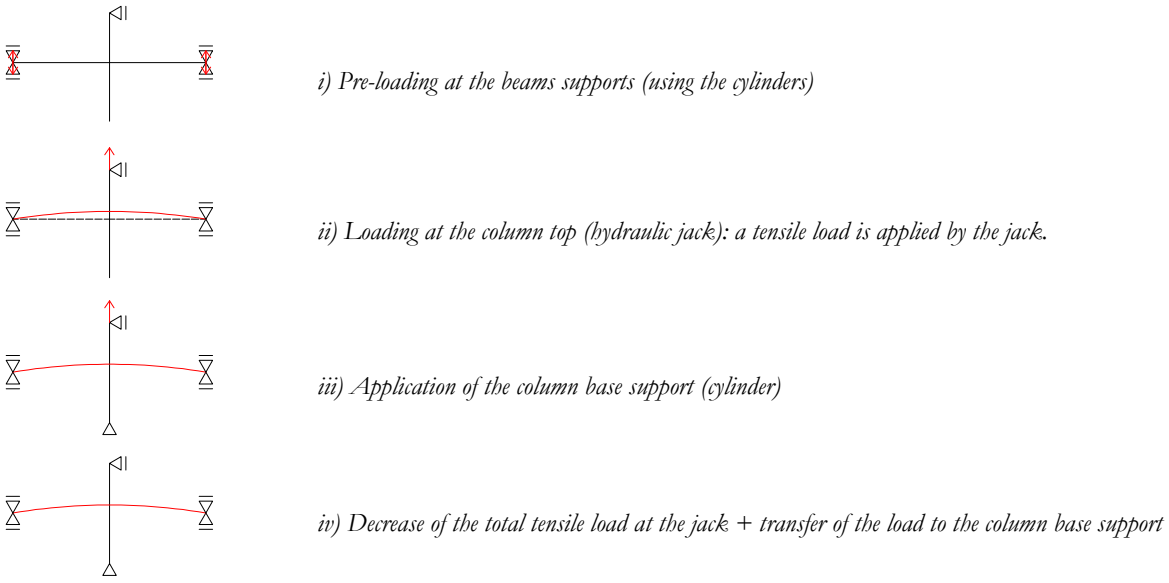

Figure 3.15: Steps to introduce the initial hogging moment in the joint

Figure 3.20 also shows the hydraulic cylinder located at the column base, except for test 7. This cylinder kept a constant vertical displacement of the column during the application of the initial loads and the increase of temperatures, and is finally taken out by

decreasing the oil pressure in order to simulate the column loss. During the heating phase (step 2) of tests 2 to 6, the axial load in the column is variable because of the thermal expansion of the column, and the oil pressure in the cylinder is adapted to keep the constant vertical position.

In order to define the required capacities of the measuring/loading equipment (load cells, displacement transducers, and hydraulic jack or cylinders), preliminary numerical simulations of the sub-frames are carried out in Abaqus (2012), and the global behaviour is predicted (see Appendix D.2).

3.3.4 Beam axial restraints

The effect of the beam axial restraint coming from the unaffected part of the building is studied, and three different restraints stiffness's are considered: tests 1, 2 and 3 - no beam axial restraint; tests 4 and 5 - total beam axial restraint; and tests 6 and 7 - realistic beam axial restraint. When no restraint is applied, the beams are free to deform axially. For the total beam axial restraint, a steel beam with profile HEB 300, linked from the end of the tested beams to strong walls is used (Figure 3.16). The axial load is calculated from the strains measured in HEB 300 by five strain gauges: two on the top flange, two on the bottom flange and one on the web, from which the stresses are derived, and finally the axial load restraint (see Figure 3.20 in section 3.3.5).

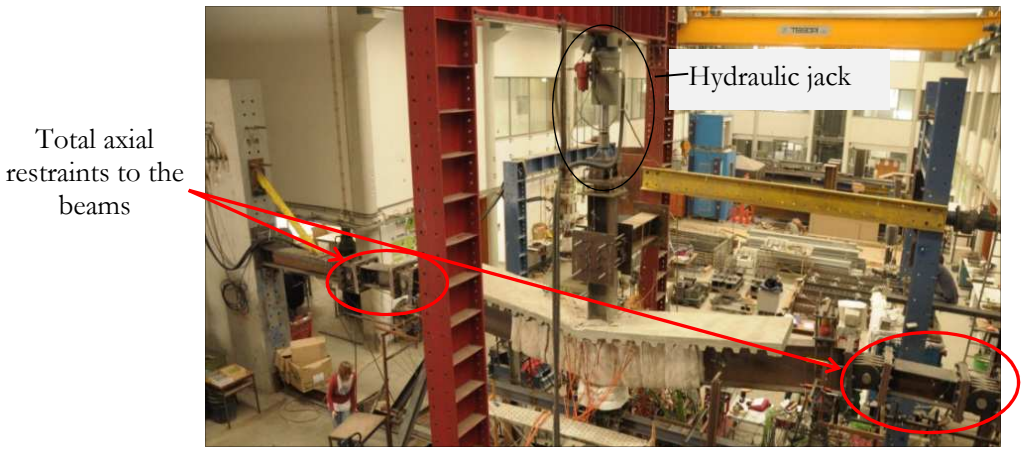

Figure 3.16: Total axial restraints to the beam (at the end of test 5)

In the real car park, stiffness of the beam axial restraint provided by the part of the building not directly subject to the fire can be estimated (see Appendix B.1). In the laboratory, reduced value (50 kN/mm) is used (because of the limitation of the material capacity); the realistic beam axial restraints (*spring restraints*) are simulated using hydraulic double stroke cylinders (Figure 3.17). Each one is independently and manually controlled: in order to adjust the spring stiffness, the oil pressure (measured by pressure transducers) is adapted at the hydraulic pump according to the measured axial displacements. The applied load by the cylinder is limited to 654 kN in compression and 304 kN in tension. The spring axial load is derived from the measured oil pressure using the following expression:

$$F\,[\mathrm{N}] = A\,[\mathrm{cm}^2] \times p\,[\mathrm{bars}] \times 9.81[\mathrm{N}/(\mathrm{bars}\times\mathrm{cm}^2)]$$

Where A is the cylinder effective area (133 cm^2 in compression and 62 cm^2 in tension) and p is the measured pressure in the cylinder. The total restraints, as well as the realistic restraints, are pinned and allow the rotation.

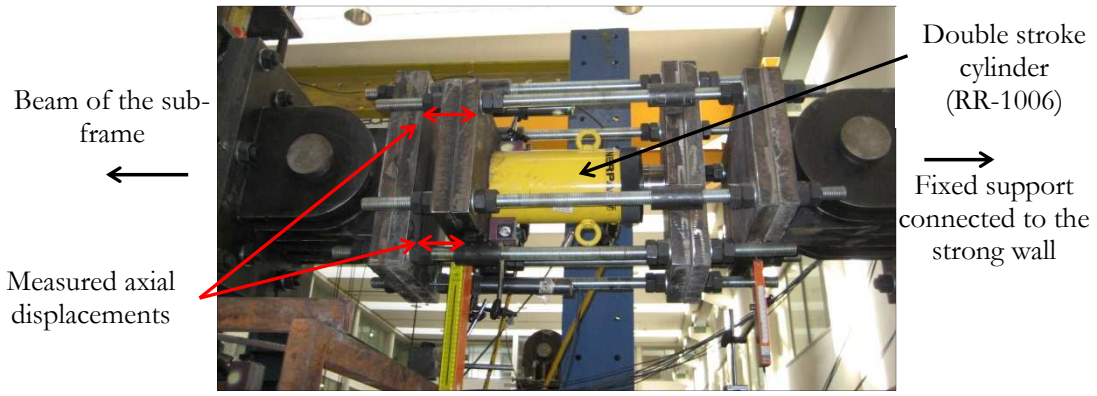

Figure 3.17: Spring restraint (left)

3.3.5 Instrumentation of test specimens

The main requirements of the instrumentation are to measure the temperatures, the distribution of internal/reaction forces and the deformed shape of the structural elements. 70 to 96 thermocouples of K type with two 0.7 mm wires are used to measure the temperatures in the heated steel elements (end-plates, bolts, beams, and column) and in the composite slab (Figure 3.18). Around 30 displacement transducers, outside the heated zone (Figure 3.19), are used in order to measure the displacements and deformations of the specimen, and to check the parasitic displacements of the reaction structures (such as footings and frames). Load cells measure the reaction loads at each beam support, at the column top, and at the column base (Figure 3.20). The reaction loads from the beams axial restraints are calculated from: i) the pressure measured in cylinders in case of the spring restraints (Figure 3.17); ii) strain gauges in case of the total restraints (Figure 3.20).

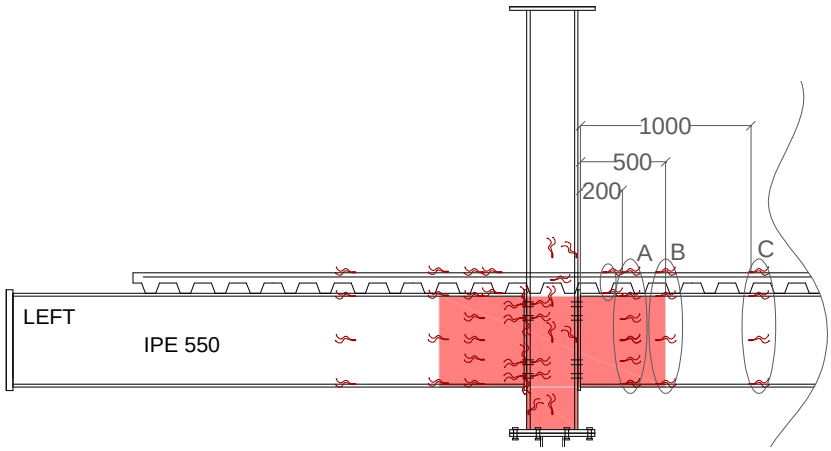

Figure 3.18: Position of the thermocouples in the heated zone

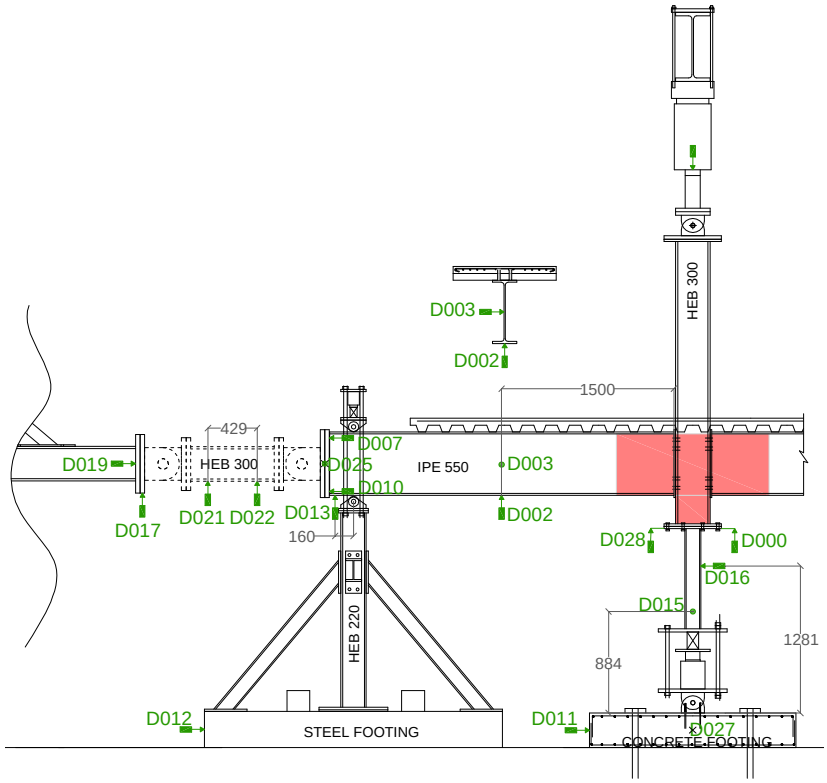

Figure 3.19: Position of the displacement transducers on the left side (same layout on the right side)

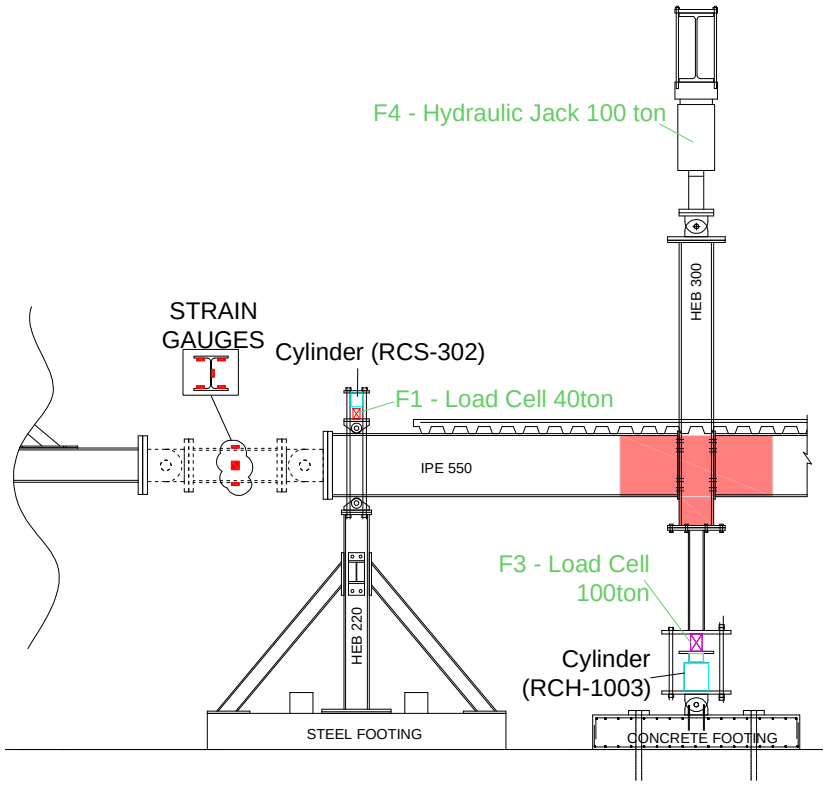

Figure 3.20: Load cells, hydraulic cylinders, and strain gauges for the test with total beam axial restraint (on the left side)

3.4 Control tests

For future calibration of numerical and analytical models against the test results, control tests are performed to determine material properties of the steel joint components and concrete slab. Mechanical properties of the beam and column are defined by a total of 36 tensile coupon tests. The coupons are extracted from the webs and flanges, and three tensile tests are performed for each one, at 20ºC, 500ºC and 700ºC. Steady-state tests are considered, for which the coupon is heated up to a specific temperature and then tested in tension (constant displacement speed). Figure 3.21 shows the testing furnace and some steel coupons before and after the tests at 20ºC and 700ºC. An overview of the results is presented in this section; and a detailed analysis of the tests results is provided in Appendix A. Unfortunately, no coupon tests are carried out for the end-plate material.

a) b)

Figure 3.21: a) Testing furnace and b) steel coupons before or after the tests

Figure 3.22 presents the stress-strain curves from the tensile tests performed at 20ºC, 500ºC and 700ºC of the flanges: a) of the IPE 550 steel beam (S355J0 + M), and b) of the HEB 300 steel column (S460M). One test is presented at each temperature, and the measured stress-strain curve is compared to theoretical stress-strain curves from EN 1993-1-2 (2005), considering strain hardening at ambient temperature. For these theoretical results, the ambient temperature nominal mechanical properties of steel profiles are defined according to EN 10025-4 (2004). It can be observed, from the test results, that the ductility is reduced at 500ºC, then slightly increased at 700ºC, because of steel chemical transformations (Imedio *et al.,* 2004). The Elastic modulus decreases with temperature (see detailed values in Appendix A.3), and EN 1993-1-2 (2005) provides safe results except for high strength steel S460 under 500ºC. Indeed, in this Eurocode, the degradation definition of various structural steel grades material properties under fire conditions are based on tests results predominantly obtained on steel grade S235, and it is assumed that the recommended specifications are available for all the structural steel grades. However, Schneider and Lange (2009) pointed out that EN 1993-1-2 (2005) overestimates the elevated-temperature yield strengths if used for S460; and according to Qiuang *et al.* (2012), the degradation of mechanical properties of steels under fire conditions is dependent on steel grades. Average values of the tests results are provided in Table 3.2.

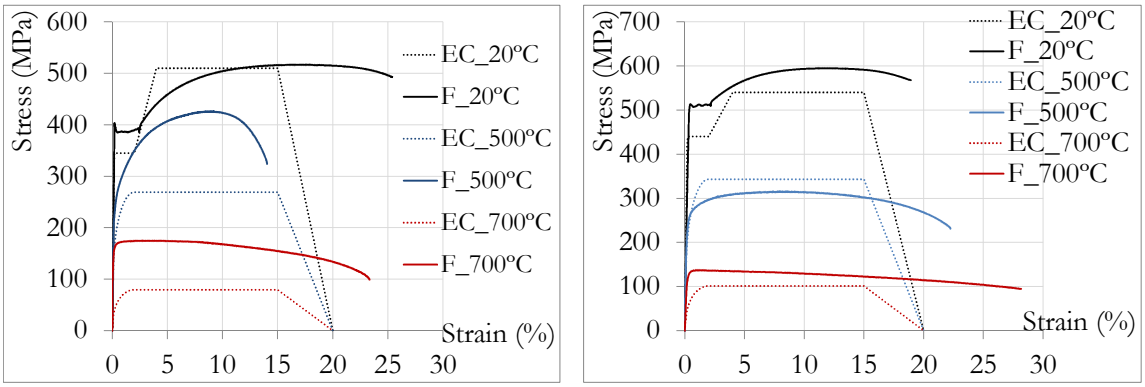

Figure 3.22: Comparisons of stress-strain curves obtained from EN 1993-1-2 (2005) (EC), and tests performed at 20°C, 500°C and 700°C for steel: a) S355J0 + M (flange-F); b) S460M (flange-F)

Table 3.2: Mechanical properties of steels S355 and S460

		EN 10025-4 (2004) EN 1993-1-2 (2005)	Tests results		
Steel	Temp (°C)	Yield strength f_y (MPa)	Yield strength R_e (MPa)	Tensile strength R_m (MPa)	Elongation after fracture A (%)
S355J0 + M IPE 550 (flange)	20	345	396	517	32.47
	500	269.1	326	431	29.65
	700	79.35	169	171	48.83
S460M HEB 300 (flange)	20	440	516	599	27.2
	500	343.2	292	325	23.2
	700	101.2	137	137	41.95

Mechanical properties of the bolts M30, grade 10.9 are defined by 15 tensile coupon tests (see detailed results in Appendix A 3.2). Three tensile tests are performed at ambient temperature, and two tests are performed at each temperature equal to 200°C, 400°C, 500°C, 600°C, 700°C and 800°C (steady-state tests). Figure 3.23 depicts the stress/strain curves, and Table 3.3 presents the mechanical properties for each temperature: i) nominal values defined by EN 1993-1-8 (2005) and EN 1993-1-2 (2005) and ii) measured values from the tests (average values). Tests show that yield and ultimate stresses increase at 200°C before decreasing at higher temperature. Such behaviours could be attributed to the dynamic strain aging (DSA), austenite to martensite transformation, and high temperature softening in addition to tempering of bainite (Akbarpour and Ekrami, 2008). The ductility is significantly increased from 600°C, and the Young's modulus decreases with temperatures.

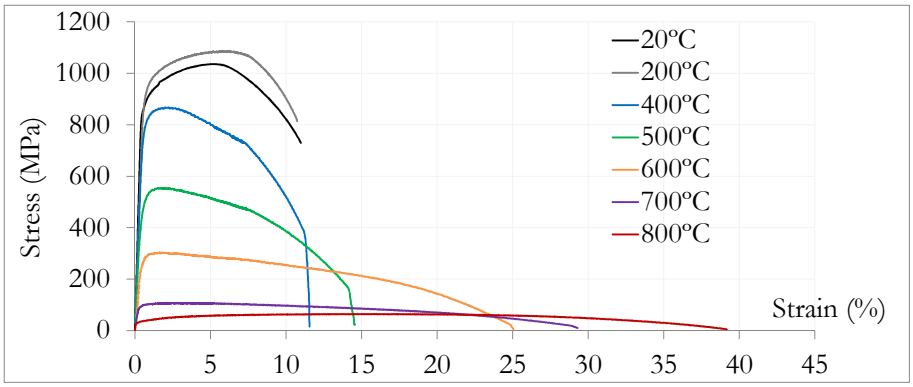

Figure 3.23: Stress-strain curves of bolts M30 10.9 at 20ºC, 200ºC, 400ºC, 500ºC, 600ºC, 700ºC and 800ºC

Table 3.3: Mechanical properties of bolts M30, grade 10.9

	EN 1993-1-8 (2005) EN 1993-1-2 (2005)		Tests results		
Temp. (ºC)	Yield strength f_y (MPa)	Tensile strength f_u (MPa)	Yield strength $R_{p0.2\%}$ (MPa)	Tensile strength R_m (MPa)	Elongation after fracture A (%)
20	900	1000	932	1044	15.3
200	841.5	935	935	1086	14.2
400	697.5	775	783	841	17.3
500	495	550	509	558	22.95
600	198	220	298	333	41.85
700	90	100	99	112	61
800	60.3	67	60	91	76.9

Compression tests on 24 concrete blocks are performed. Three tests are performed after 7 days, 14 days, 28 days and then at the day of each test (detailed results are available in Appendix A.4). The concrete properties C25/30 at 28 days are confirmed according to NP EN 206-1 (2007): i) the average of each three tests cube strength ($f_{ck,cube}$ = 35 MPa) is higher than the C25/30 characteristic cube strength plus 1 (31 MPa), and is smaller than the C30/37 characteristic cube strength plus one (38 MPa); ii) each individual value is higher than the C25/30 characteristic cube strength minus 4 (26 MPa).

3.5 Experimental results

In order to simplify the presentation of tests results as well as the comparisons between them, the results of only one connection from each internal joint are presented: either the connection where bolts failed, or, in case of no bolt failure, the most deformed connection (left connection for tests 1, 2, 3, 5 and 7, and right connection for tests 4 and 6).

3.5.1 Tests 1 to 6

3.5.1.1 Temperatures results

Tests 2 to 6 are performed under constant temperatures, controlled at the beams bottom flanges (at 250 mm from each end-plate): bottom flanges reached 500ºC in tests 2 and 4, and 700ºC in tests 3, 5 and 6. Figure 3.24 depicts the temperature evolution during tests 2 and 3 in the left side of the frame - at 200 mm from the connection (in the bottom flange, web and top flange), at the column centre (left flange and web), in bolt row 4, and in the concrete rib in contact with the steel beam near the joint. Similar temperatures are measured on the other side of each joint, as well as for tests 4, 5 and 6 (with slightly higher temperatures in test 6 in comparison to test 3 - all the temperature results are provided in Appendix B.3). Concrete temperatures did not rise above 300ºC.

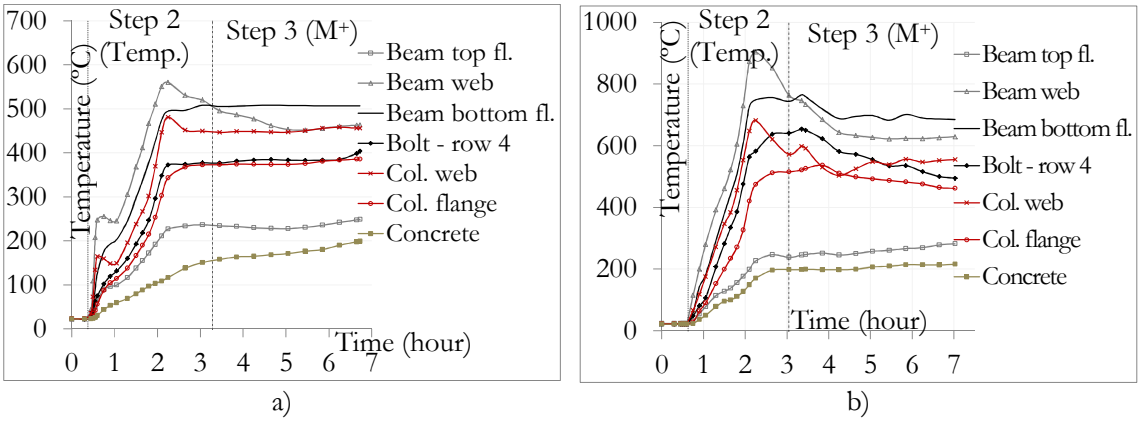

Figure 3.24: Evolution of the temperatures during a) test 2 at 500ºC, b) test 3 at 700ºC

3.5.1.2 Simplified analytical prediction of the joint sagging bending moment resistance

A simplified analytical prediction of pure sagging bending moment resistance is performed for the composite joint, in accordance with the component method recommended in EN 1994-1-1 (2004). The three tests without axial restraints are considered: test 1 (20ºC), test 2 (500ºC), and test 3 (700ºC). Measured material properties (f_y) without partial safety factors are used. At elevated temperatures, the strength reduction of each component is based on the measured temperatures in the tests, and the reduction factors defined in EN 1994-1-2 (2005) are used. In this chapter, a simplified analytical calculation is performed, assuming that the neutral axis is at the level of the ribs of the composite slab; so the centre of compression is considered at mid-thickness of the concrete slab above the ribs (the beam top flange is not in compression). Note that a more detailed and accurate analytical prediction of the ultimate joint resistance is provided in chapter 5. Table 3.7 presents the distribution of internal forces within the connection calculated for each of the three tests. The resistance of the basic components is considered and, based on the assumption that no compressive load is developed in the beam top flange, the sagging bending moment resistance is limited by the concrete slab in

compression. For the bolt rows in tension, the behaviour is controlled by the end-plate in bending (ductile component); the plastic resistance is reached for bolt rows 3 and 4 (bottom bolt rows), and the residual tensile forces are linearly distributed in bolt rows 1 and 2 (top bolt rows). Bending moment resistances of both tests 1 and 2 are similar, because temperatures in test 2 only slightly decrease the strengths of beam bottom flange and column web components; strengths of other components remain equal to the ambient temperature values (temperatures lower than 400°C).

Table 3.4: Analytical sagging bending moment resistance of the connection derived from the distribution of internal forces for tests 1, 2 and 3 (no beam axial restraint)

	Test 1 (20°C)	Test 2 (500°C)	Test 3 (700°C)	Lever arm (m)
Compression force in concrete slab – F_c *(kN)*	1041.76	1020.20	979.26	0
Tension force in bolt row 1 – F_1 *(kN)*	148.02	139.40	208.59	0.16
Tension force in bolt row 2 – F_2 *(kN)*	222.26	209.32	309.72	0.24
Tension force in bolt row 3 (End-plate in bending) F_3 *(kN)*	138.83	138.83	95.30	0.50
Tension force in bolt row 4 (End-plate in bending) F_4 *(kN)*	532.65	532.65	365.64	0.58
Analytical plastic bending moment (kNm)	454.86	450.38	366.94	

3.5.1.3 Mechanical results and failure modes

The joint rotation is estimated using the vertical displacements measured at: i) 1500 mm from the end-plate (D002 and D008 in Figure 3.25), and ii) at the column top (hydraulic jack or D000 and D028). The reaction loads at the beams supports are used to calculate the bending moment, considering the lever arm measured from the beam support to the mid-thickness of the column flange.

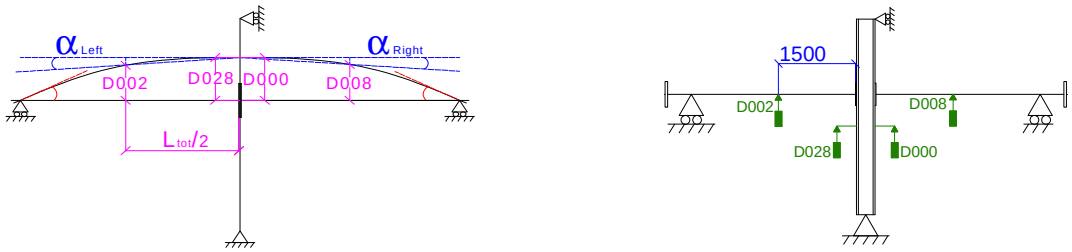

Figure 3.25: Estimated rotation of the joint using the measured displacements

For each test, Figure 3.26 and Figure 3.27 depict the evolution of: the total vertical reaction load (total load applied at the column) *versus* the vertical displacement measured at the column top, and the bending moment *versus* the rotation of each connection, respectively. In step 1, the initial hogging bending moment is applied: -501 kNm for reference test 1, and -330 kNm for tests 2 to 6. At the beginning of the heating phase (step 2), the column reaction increases under thermal expansion effects and reaches a maximum value: the minimum hogging bending moment reaches around -500 kNm in tests 3, 5 and 6 (under 700°C), and around -357 kNm in tests 2 and 4 (under 500°C). Finally, this reaction load decreases because of the degradation of steel properties at elevated temperatures.

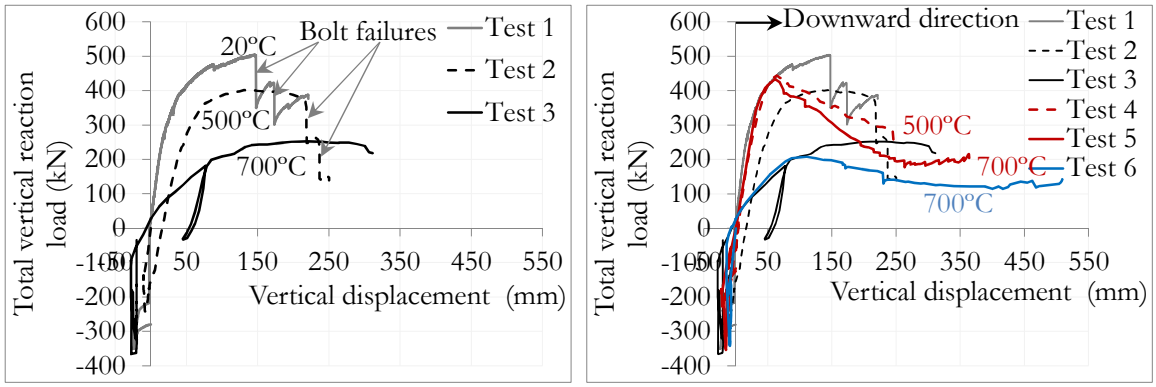

a) Tests 1, 2 and 3 (no axial restraints) b) Tests 1 to 6

Figure 3.26: Total reaction load *versus* vertical displacement measured at the column top

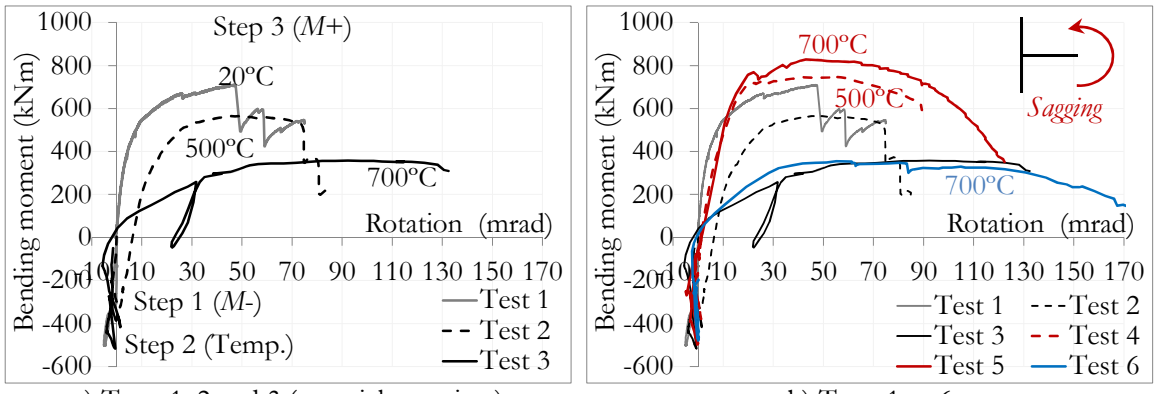

a) Tests 1, 2 and 3 (no axial restraints) b) Tests 1 to 6

Figure 3.27: Joint bending moment *versus* rotation at the connection

Under sagging bending moment (step 3), concrete crushing in compression is the first failure mode observed, due to the joint rotation and the resulting high compressive strain at the upper concrete surface. Failure is really progressive: first the concrete crushed against the column flanges (Figure 3.28a), then the entire slab width failed at the upper concrete surface (Figure 3.28b), and finally over the entire thickness (Figure 3.28c).

Bolts failures happened in tests 1, 2 and 6 (respectively under 47.5 mrad, 73.6 mrad and 83.3 mrad of joint rotation); the other tests are stopped because the maximum vertical displacement of the hydraulic jack at the column top is reached. The failed bolts occurred in the bottom bolt rows, because of higher tensile forces under sagging bending moment; they are illustrated in Figure 3.29. After the test, during the cooling phase, the deformation of the sub-frame is maintained constant and one bolt, from bottom bolt row, failed in tests 3 and 4, due to the high tensile stresses induced by the heated part of the joint recovering strength and stiffness, with a reduction of thermal strains. During test 1 at ambient temperature, strain gauges measured the extensions of: i) steel beam web and flanges near the connection, ii) bolts, iii) steel reinforcements, and iv) column web; these results are shown in Appendix B.2.

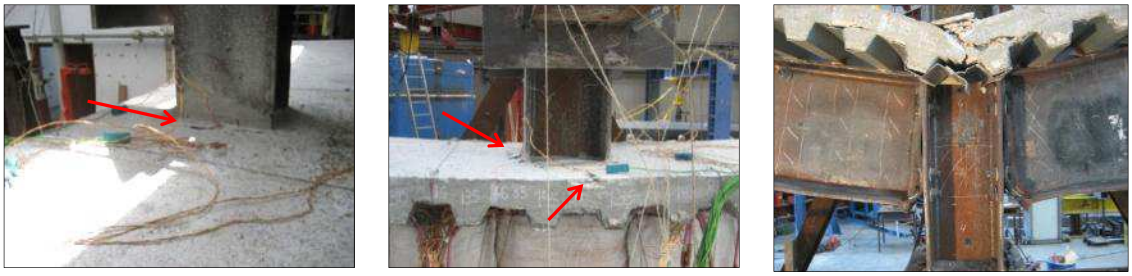

a) b) c)

Figure 3.28: Concrete crushed: a) against the column flanges; b) along the entire slab width; c) at the end of the test (front view of test 6)

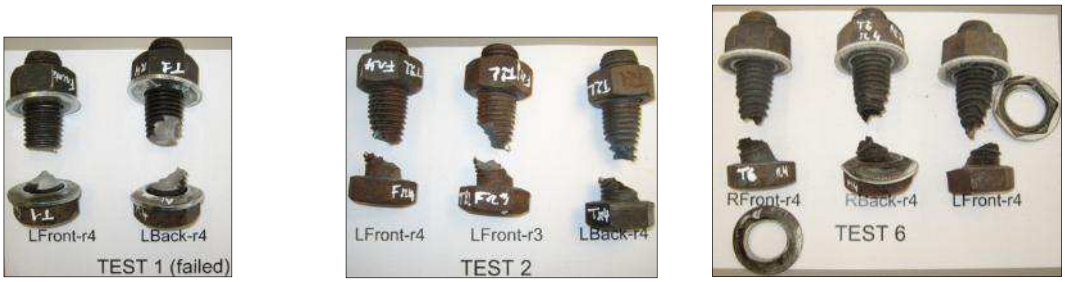

a) b) c)

Figure 3.29: Bolts failed a) in test 1 at 20ºC; b) in test 2 at 400ºC; and c) in test 6 at 550/600ºC

The evolution of the bending moment at the joint *versus* the beam axial load is presented in Figure 3.30a for tests 4, 5 and 6. During step 1, the reaction loads and displacements due to the mechanical loadings are not sufficient to develop axial forces in the beams axial restraints. During the heating phase (step 2), due to the thermal expansions of beams, the beams ends move in the outward direction, and compression loads are applied by the restraints. After the column loss (step 3), the axial restraints increase the compression loads because beams ends continue to move outwards; two reasons are highlighted:

i. *The main reason is the low slenderness (high cross-section height and short beam span) of the composite beam*. When the column begins to go downward (Figure 3.31), the joint is subject to sagging bending moment: the concrete slab is in compression against the column flange whereas the joint bottom part is in tension. While the concrete is resisting, it prevents any inward horizontal displacement of the composite section. It is only after the concrete crushing in compression (or after large vertical column displacement), that the composite beam begins to displace inward.

ii. *The horizontal displacement of the beam end is measured at the centroid of the steel beam and not at the centroid of the composite section*. When the centroid of the composite beam begins to displace inward, the measured horizontal displacement at the centroid of the steel beam end continues the outward movement (Figure 3.31).

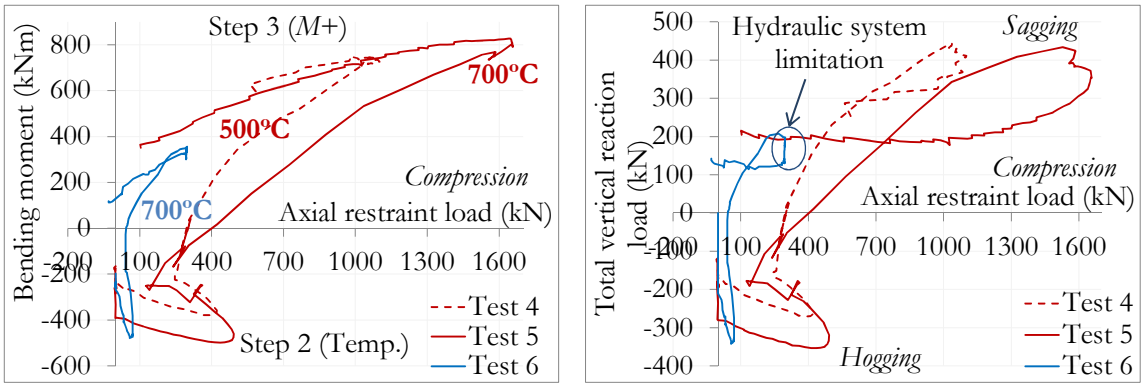

Figure 3.30: a) Joint bending moment *versus* axial loads at the joint; b) Total reaction load *versus* axial loads at the joint

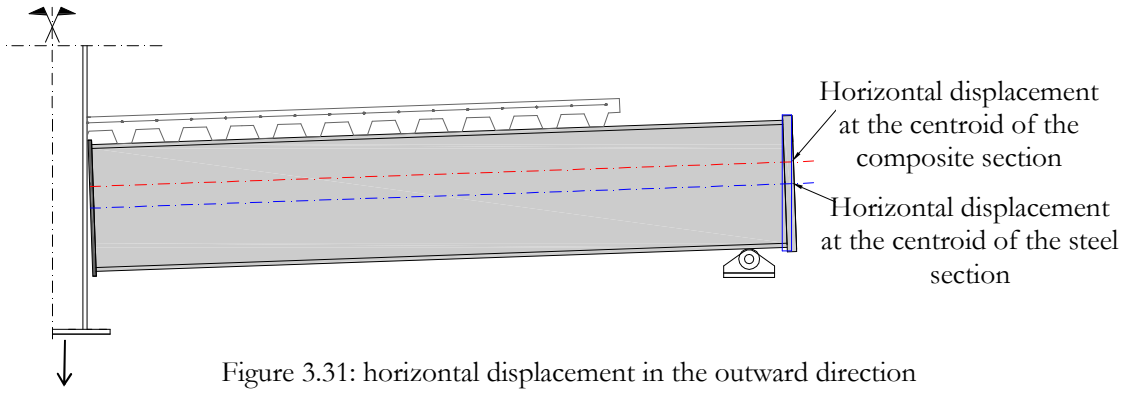

Figure 3.31: horizontal displacement in the outward direction

In tests 4 and 5 (total beam axial restraints), axial compression loads increase more than in test 6 (spring restraint), because the horizontal displacement at the beam end is much restrained. So the concrete crushes under smaller deformations due to these elevated compression loads: when the beams ends try to displace outwards, the axial restraint loads increase and the concrete crushes for joint rotations of about 25 mrad in tests 4 and 5, and 35 mrad in test 6. Finally, tensile axial loads are reached only at the end of test 6. Figure 3.32 and Figure 3.33 show the final deformations of the tests at 20ºC, 500ºC and 700ºC: the steel end-plates are deformed in the bottom and centre parts and show a high ductility. The deformation at the centre of the end-plate happen because of the joint configuration: i) high distance between bolt rows 2 and 3 (260 mm), ii) the end-plate (15 mm) is thinner than the column flange (19 mm), and iii) an initial gap is noticed just after the bolts pre-loading, before the test (0.6 mm is measured for the reference test). Moreover, it seems that the beam web is pulling the end-plate due to the sagging bending moment (tensile loads at the bottom part). Due to high stresses/deformations, a crack at the base steel end-plate, just above the weld, is observed at the end of the ambient temperature test (Figure 3.32a). Figure 3.34 shows local deformations of the beams observed in tests 4 and 5 (local deformation of the beam web in test 4, local deformation of the beam flange in test 5 as well as shrinkage of the bottom flange).

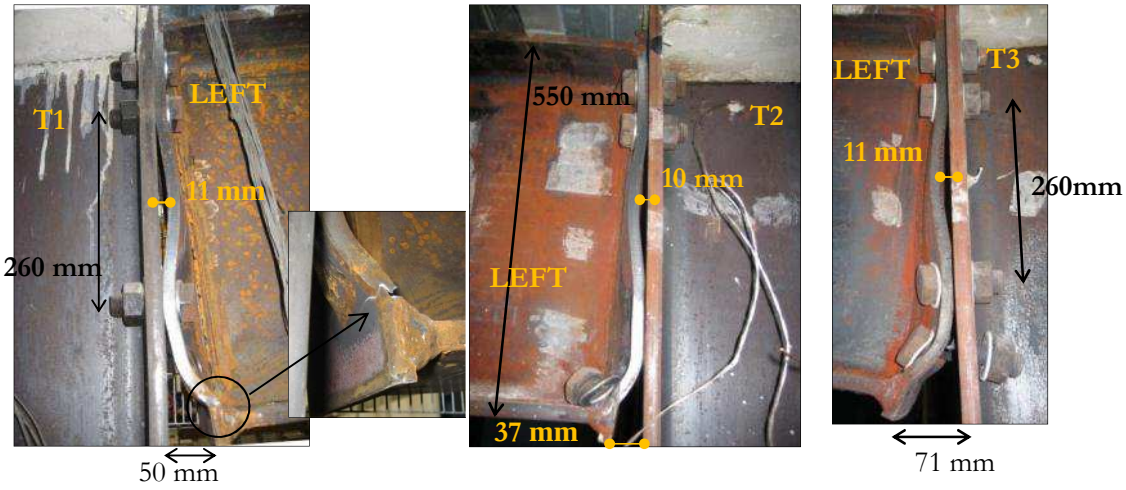

a) b) c)

Figure 3.32: Deformations of the connections in a) test 1 (20ºC), b) test 2 (500ºC) and c) test 3 (700ºC)

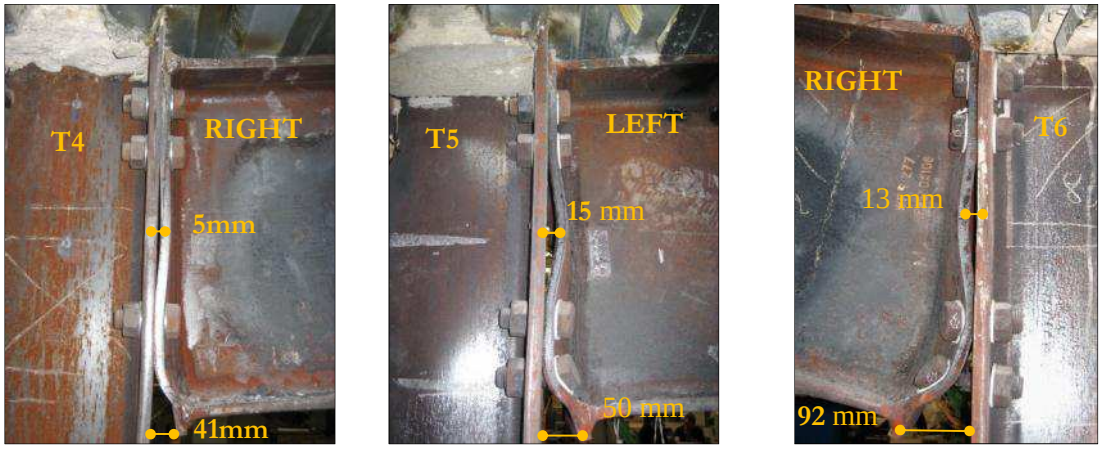

a) b) c)

Figure 3.33: Deformations of the connections in a) test 4 (500ºC – total axial restraint), b) test 5 (700ºC – total axial restraint) and c) test 6 (700ºC – spring axial restraint)

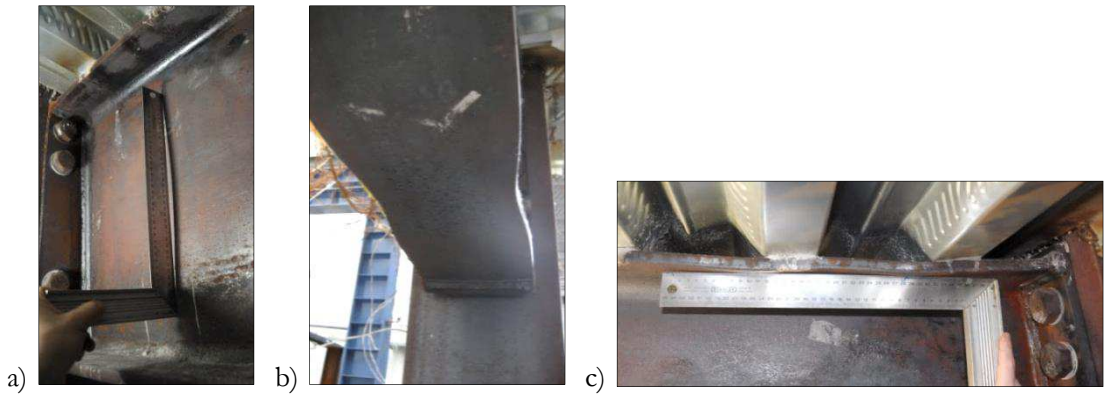

a) b) c)

Figure 3.34: Local deformations of: a) beam web in test 4 (500ºC – total axial restraint); b) beam bottom flange (shrinkage) in test 5 (700ºC – total axial restraint); and c) beam top flange in test 5.

Finally, Table 3.5 summarizes the main results of each test: the failure modes, the local deformations, the connection rotation at the end of the test and the symmetrical or unsymmetrical behaviour of the joint defined by the column rotation (in tests 3 and 7, the column rotated and the joint deformation is not symmetrical). The final deformation of sub-frame for test 6 is shown in Figure 3.35. Additional pictures of the experimental tests are shown in Appendix B.4.

Table 3.5: Failure modes and local deformation of each test

Test	Temp. (ºC)	Restraint (kN/mm)	Connection rotation* (mrad)	Col. rotation* (mrad)	Failure modes	Local deformations at:
T1	20	0	74.9	-6	Concrete crushing in compression; failure of 2 bolts in tension (left side); crack at the end-plate (bottom – left).	the end-plates (bottom and centre).
T2	500	0	84.8	Not measured	Concrete crushing in compression; failure of 3 bolts in tension (left side).	the end-plates (bottom and centre).
T3	700	0	132.4	-33	Concrete crushing in compression; failure of 2 bolts in tension (left side) during the cooling phase.	the end-plates (bottom and centre); column web (bottom part); beam bottom flange (left).
T4	500	Total	89.4	2	Concrete crushing in compression; failure of 2 bolts in tension (right side) during the cooling phase.	the end-plates (bottom and centre); column web (top part); beams webs; column flange (left).
T5	700	Total	122.3	6	Concrete crushing in compression.	the end-plate bottom and centre; column web (bottom part); beam bottom and top flanges (right).
T6	700	50	183.5	10	Concrete crushing in compression; failure of 3 bolts in tension (2 on the right - 1 on the left).	the end-plates (bottom and centre); beams bottom flanges.
T7**	400; 800	50	149.8	-63	Bottom column failure; concrete crushing in compression; failure of 3 bolts in tension (left side); crack at the end-plate bottom (left).	the end-plates (bottom and centre).

* Rotations measured at the end of each test;

** Test 7 (demonstration test) is presented in section 3.5.2.

Figure 3.35: Final deformation of the tested structure (test 6)

3.5.1.4 Comparisons of the results

The behaviour of the joint subject to sagging bending moment and variable axial loads is studied under constant temperatures (20ºC, 500ºC and 700ºC). From the results, the effects, on the joint behaviour, of the temperatures and of the beam axial restraint can be reached. Table 3.6 presents the values of the plastic and maximum sagging bending moments obtained from each test, as well as the corresponding axial load and connection rotation. The corresponding plastic bending moment reached in the experimental tests $M^+_{plastic}$ is calculated by a bilinear approximation of the moment-rotation curve based on the slope of initial and post-limit stiffness's (Jaspart, 1991).

Table 3.6: Plastic and maximum sagging bending moments ($M^+_{plastic}$ and M^+_{max}) in tests 1 to 6, and results corresponding to maximum sagging bending moment M^+_{max}

	T1	T2	T3	T4	T5	T6
Temperature	20ºC	500ºC	700ºC	500ºC	700ºC	700ºC
Beam axial restraint	0	0	0	total	total	50 kN/mm
$M^+_{plastic}$ (kNm)	507.1	490.23	329.5	703.9	713.5	312.4
M^+_{max} (kNm)	710.1	565.0	357.1	746.4	828.0	355.5
Rotation θ_{M+max} (mrad)	46.9	49.5	92.3	54.9	43.0	55.1
Axial load N (kN)	0	0	0	-990.7	-1646.7	-297.3

Effect of the temperatures

The three first tests, performed without beam axial restraint, show that the increase of temperature:

i. *Decreases the maximum sagging bending moment of the joint:* 20% from test 1 (20ºC) to test 2 (500ºC), 50% from test 1 to test 3 (700ºC);
ii. *Increases the rotation capacity and the ductility of the joint*, by: i) increasing the connection rotation corresponding to the maximum sagging moment (6% from test 1 to test 2, 97% from test 1 to test 3, and 87% from test 2 to test 3); ii) increasing the maximum joint rotation at the first bolt failure (in tests 1 and 2, the first bolt fails for respectively 49 mrad and 74 mrad of rotation (increase of 55%), and no bolts fail at 132 mrad of rotation in test 3);

iii. *Decreases the initial stiffness*: 36% and 49% from test 1 (20ºC) to test 2 (500ºC) and test 3 (700ºC), respectively.

Table 3.7 presents the comparison between experimental and analytical sagging bending moment resistances. At ambient temperature (test 1), the analytical sagging bending moment is lower than the experimental value (difference of 10%). At elevated temperatures (tests 2 and 3), theoretical and experimental resistances also show differences, of 8% for test 2 (500ºC), and -11% for test 3 (700ºC). However, more accurate comparisons between analytical and experimental results are provided in chapter 5.

Table 3.7: Comparisons between the analytical prediction of the joint sagging bending moment resistance (see section 3.5.1.2) and the experimental results

	Test 1 (20ºC)	Test 2 (500ºC)	Test 3 (700ºC)
Analytical plastic bending moment (kNm)	454.86	450.38	366.94
Experimental plastic bending moment (kNm)	507.1	490.23	329.5
Differences (%)	10.30	8.13	-11.36

Test 4 (500ºC) and test 5 (700ºC) are performed with total beams axial restraints, and it is expected to reach higher sagging bending moments in test 4 than in test 5 because of the lower temperatures and consequently higher steel resistance in test 4. However, the maximum sagging bending moment reached in test 5 (700ºC) is 11% higher than in test 4 (500ºC), even with the reduced steel properties. The compression load is 66% higher of test 5 probably because of higher compression resistance of the concrete slab due to the non-uniform concrete slab thickness in test 5 (see section 3.3.1). As the concrete is only slightly heated, the concrete properties are only slightly decreased by temperatures, and the compression resistance of the joint is increased by the slab thickness, even under higher steel temperatures.

Effect of the beam axial restraints

Some findings are obtained from the tests concerning the beam axial restraint, and consequently, the compression axial load in the joint:

i. *Increase of the maximum sagging bending moment*: the joint rotation corresponding to the first bolt failure in test 2 is 74 mrad; under the same rotation in test 4, the sagging bending moment is increased by 32%, due to the axial compression load equal to 773 kN. This increase only happens for small values of compressive axial loads; higher compressive axial loads would decrease the bending moment resistance of the joint (see the entire M-N behaviour of the joint in chapter 5). Note that, from test 3 to test 6, the effect of axial restraint on the joint resistance cannot be observed (difference of 0.5% between maximum bending moments), due to higher temperatures measured in test 6 (see section 3.5.1.1), and very low values of axial compressive loads in test 6.
ii. *Increase of the joint rotation capacity and, consequently, the joint ductility*: the compression load from the axial restraint combined with sagging bending moment moved the

neutral axis of the connection downward, allowing the development of additional compression loads in the concrete slab, and the reduction of the tensile loads in the bottom bolt rows. Once the concrete crushes against the column slab and along the entire slab width, tests 4 and 5 are still able to continue to deform without failure: from the maximum sagging bending moment and the end of the test, the rotation increases by 113% in test 4 and by 184% in test 5;

iii. *Increase of the initial stiffness of the bending moment/rotation curves*: 83% from test 2 to test 4 (500°C), and 54% from test 3 to test 5 (700°C).

3.5.2 The demonstration test (test 7)

3.5.2.1 Temperatures results

Figure 3.36 presents the temperatures evolution during the entire test 7 in the left beam - at 200 mm from the connection (in the bottom flange, web and top flange), in the column HEB 300 (left flange and web), in the bottom column HEB 140 (left flange and web), in bolt from row 4, and in the concrete rib in contact with the steel beam near the joint. In step 3 (1st increase of temperature), the beams bottom flanges are heated up to 400°C, whereas webs, joint components and column HEB 300 reach slightly lower temperatures (from 300°C to 400°C). The bottom column (HEB 140) reaches its maximum resistance capacity and fails under the average temperature of 658°C (maximum temperature of 718°C measured in the web). At the end of the step 3, the average temperature at the bottom column is 733°C. In step 4 (2nd increase of the temperature), the temperatures in the beam-to-column joint are increased up to 800°C in the beams bottom flanges, and the entire sub-frame collapses. At the end of the test, maximum temperatures measured at the joint are: 585°C in bolts, 671°C in beam end-plate, 729°C in column web and 596°C in column flange. The maximum temperature measured in the shear studs in the composite slab is 179°C, and temperatures reached 280°C and 200°C respectively at the steel sheet and in the concrete in contact with the column - at 40 mm from the surface of the slab.

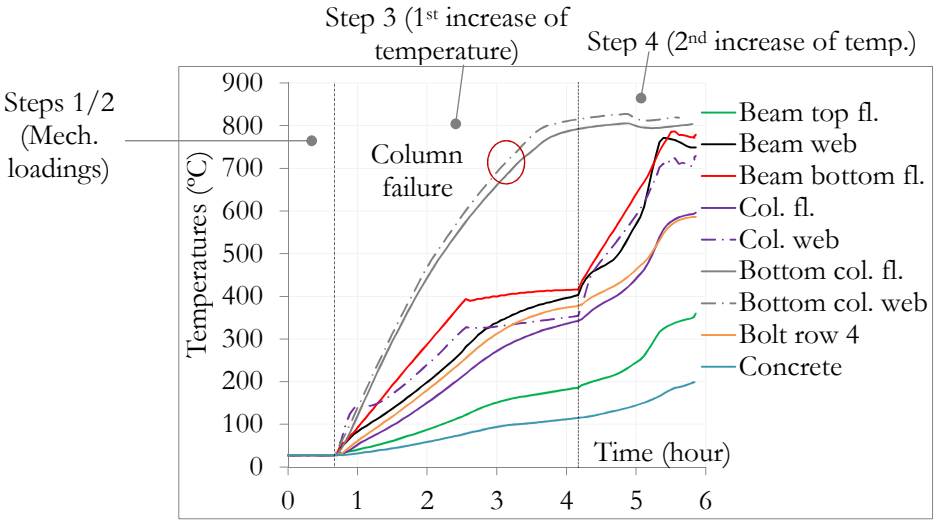

Figure 3.36: Temperatures evolution during the demonstration test

3.5.2.2 Mechanical results and failure modes

The bending moment/rotation and bending moment/axial load curves are depicted in Figure 3.37. A hogging bending moment equal to -281 kNm is initially reached during step 1. During step 2, the hydraulic jack increases the load at the column top up to reach +250 kN (see Figure 3.12); the axial force in the bottom column is equal to 341 kN (load at the top of the column + self-weight of the sub-frame + reaction loads at the beams ends due to the application of the hogging bending moment in step 1).

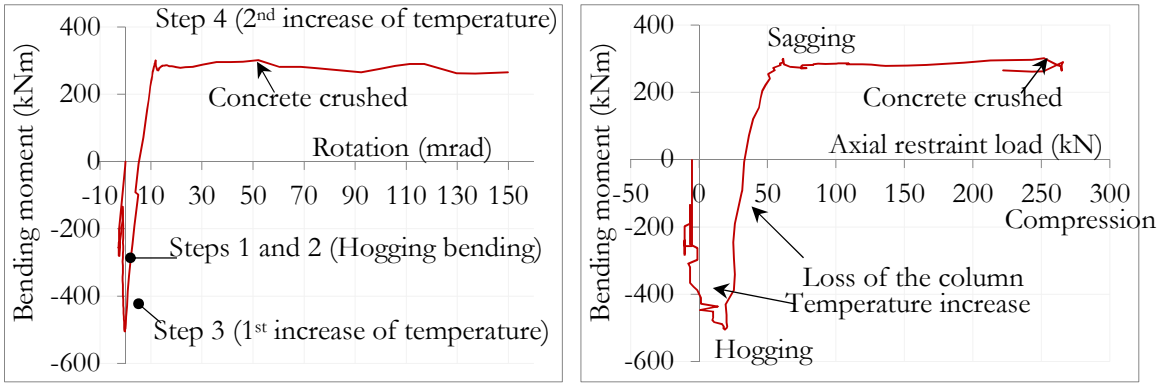

Figure 3.37: a) Joint bending moment *versus* rotation at the connection; b) Joint bending moment *versus* axial load restraint

In step 3, the beams are heated up to 400ºC in the bottom flanges (Figure 3.36); the bottom column is heated up to 800ºC. First, the reaction loads increased under thermal expansion effects, and the axial force in the bottom column reached 604 kN (hogging bending moment equal to -505 kNm); then the bottom column reached its maximum resistance capacity under 658ºC and failed. The failure of the column is progressive, and is defined as the moment at which the vertical reaction load came back to its initial value at the beginning of the step 3 (341 kN – see Figure 3.38). Figure 3.39 presents the evolution of the vertical displacements *versus* time. At the end of the step 3, the column displacement is equal to -25 mm in the downward direction and the sagging bending moment is increased up to +300 kNm.

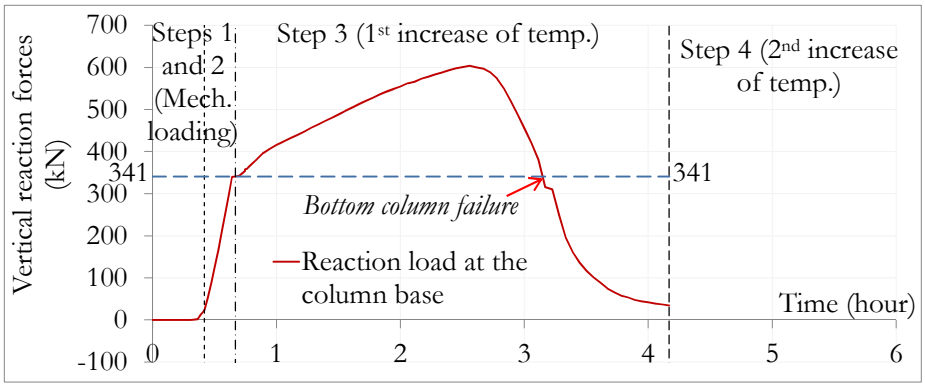

Figure 3.38: Vertical reaction load at the column base *versus* time

Concerning the effect of the axial restraints, during steps 1 and 2, the reaction loads and displacements due to the mechanical loadings are not sufficient to develop beam axial loads. Due to the thermal expansion in step 3, the beams ends are moving outwards and the compression axial load reaches 61 kN (see Figure 3.37b). Later, in step 4, after the column loss, beams ends continue to move in the outward direction and the spring restraints increase the compression loads (see the explanation presented in section 3.5.1.3).

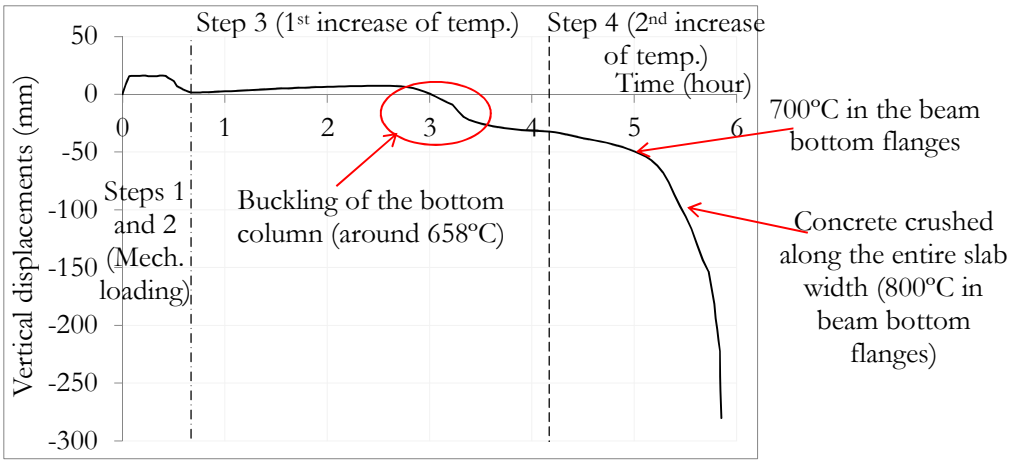

Figure 3.39: Vertical displacement of the column *versus* time

During step 4, the temperature in the joint increases under the constant load (+250 kN), applied at the top of the column, and reaches 770ºC in the beam bottom flanges. At this moment, the concrete slab crushes in compression against the column flanges, and the vertical displacement increases faster (Figure 3.39). Once the concrete slab crushes along the entire slab width, the sub-frame rapidly collapses (beam bottom flanges temperature reach 800ºC). After that, the sagging bending moment is slightly decreased from 290 kNm to 265 kNm at the end of the test, and the axial compression load at the spring restraint (left side) decreases from 266 kN to 222 kN. For safety reasons, the test is stopped at a vertical displacement equal to 280 mm and connections rotations equal to 150 mrad (left) and 37 mrad (right). The day after the test, failure of three bolts is observed (Figure 3.40): i) in the bottom bolt rows (two bolts from row 4, and one bolt from row 3) - because of higher tensile forces under sagging bending moment, and ii) in the left connection due to an asymmetric joint deformation. However, bolts failures are not noticed on bending moment/rotation curve because failures are very smooth at elevated temperatures, as described in the bolt tensile tests presented in section 3.4. Figure 41 shows the three failed bolts.

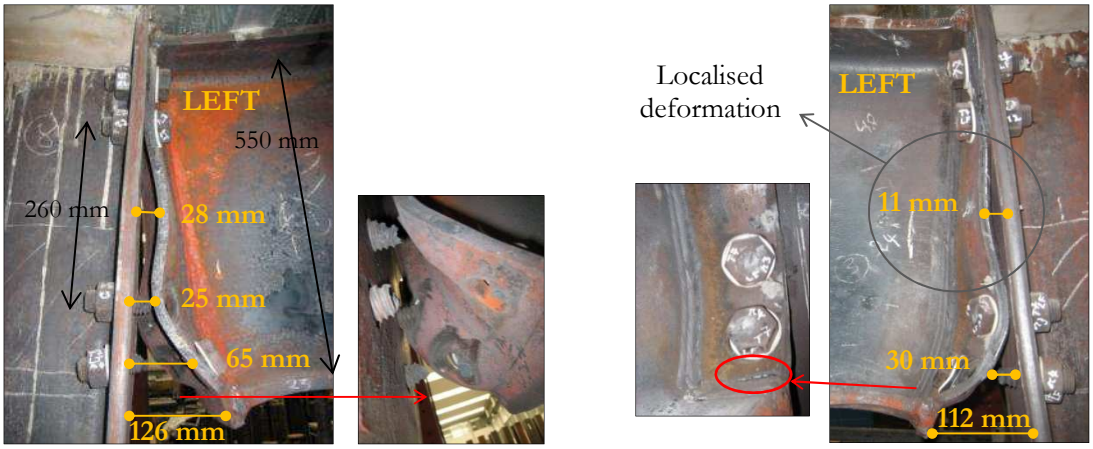

a) b)

Figure 3.40: Final deformations of the left connection: a) view from the back side; b) view from the front side

Figure 41: Bolts failed in test 7 (Left (L) connection, rows (r) 3 and 4)

The steel end-plates are deformed in the bottom and centre part because of the tensile loads at the bottom part of the composite connection under sagging bending moment (similar to deformations observed in the previous tests (see section 3.5.1.3)). A crack at the base steel end-plate, just above the weld, is also observed due to high stresses/deformations (Figure 3.40b). Figure 3.42 shows the final deformations of the sub-frame and a detailed view of the deformed bottom column.

a) b)

Figure 3.42: Final deformations of the sub-frame: a) view from the front side; b) detailed view of the deformed bottom column (view from the back side)

3.6 Concluding remarks

The main objective of the experimental tests is to observe the effect of the combined bending moment and axial loads in the heated beam-to-column composite steel-concrete joints following the loss of the column. The effect of the localised fire (that led to the column failure) is simulated by the application of elevated temperatures in the composite joint. Seven beam-to-column sub-frames are tested at the University of Coimbra: one reference test at ambient temperature; five tests at 500ºC or 700ºC; and a demonstration test, for which the sub-frame is subject to an increase of the temperature up to the failure of the column. The six first tests represent "theoretical" reference situations that allow understanding the influence of various factors affecting the joint response and their resistance and rotation capacity; the seventh one is a tentative to reproduce the real loading and behaviour of the joint. The effect of the beam axial restraint coming from the unaffected part of the building is also studied: three tests without beam axial restraint; two tests with total beam axial restraint; and two tests with realistic beam axial restraint.

From the tests performed without axial beam restraint (tests 1, 2 and 3), the effect of temperatures can be observed: the joint rotation capacity and the ductility increase with temperatures, by 6% at 500ºC and 97% at 700ºC, whereas the maximum sagging bending moment is reduced by 20% at 500ºC and 50% at 700ºC.

From the tests performed with total beam axial restraint (tests 4 and 5), it is observed higher sagging bending moment resistances without bolt failure. The observed increase in moment capacity is in line with previous experimental and analytical results (Lima *et al.*, 2004; Simões da Silva *et al.*, 2004), resulting from the beneficial effect of low compressive axial forces, that also lead to increase the joint rotation capacity and ductility. However, these beneficial effects only happen for small values of compressive axial loads; higher compressive axial loads would decrease the bending moment resistance of the joint (the entire M-N behaviour of the joint is studied in chapter 5).

The objective of the demonstration test is to show the real behaviour of the sub-frame joint when subject to a localised fire which leads to the loss of a column. When the bottom column reaches 658ºC, the column fails; beyond that, once the beam reaches 700ºC, the vertical displacement of the joint begins to increase faster, then the composite slab crushes, and finally the sub-frame collapses.

Finally, catenary action is not attained in any tests; failure of the bolts in the bottom bolt row is observed for small vertical displacements during the development of the compression loads. These tests highlight the importance of the influence of slenderness of composite beams on the robustness behaviour of the frame. Additional investigation is performed in chapter 5.

Chapter 4

4 Numerical models of heated composite steel-concrete beam-to-column joints subject to bending moments and axial loads

4.1 Introduction

This chapter presents a numerical study of the detailed behaviour of the composite joints tested in chapter 3. These numerical studies are performed using the commercial general finite element packages Abaqus, v6.12 (2012). The various capabilities of Abaqus allow simulating complex engineering problems, including structural behaviour under fire conditions (Wang, 2002). In Abaqus, complex geometries, interactions between materials and elements, relevant non-linear material properties at elevated temperatures, and large deformations can be modelled. All modes of structural behaviour involved in fire can be simulated using a large library of finite elements, which enable the creation of an efficient and detailed model. So Abaqus is capable to simulate composite structures subject to fire, as well as modelling detailed behaviour of connections in fire. This program has been chosen to perform the numerical studies of this thesis.

This chapter is divided in two parts: 1st- two benchmark examples are presented to validate the utilization of the Abaqus program for steel and composite structures subject to fire, using beam and shell elements; 2nd- a detailed three-dimensional finite element (FE) model simulates the effect of the column failure on the composite joint behaviour, so the joint is simultaneous subject to mechanical (bending and axial forces) and thermal loadings.

4.2 Benchmark studies

In order to gain confidence in the FE results, two benchmark studies validate the utilization of the Abaqus program for steel and composite steel-concrete structures subject to fire, using beam and shell elements. The two following structures are analysed: A) a two-dimensional steel sub-structure subject to a natural fire; B) two composite steel-concrete beams simply supported, one tested at ambient temperature and another subject to the standard fire ISO 834. The model A is calibrated from the available experimental test results as well as the numerical results obtained by the program CEFICOSS published by Franssen *et al.* (1995). The model B is based on experimental results as well as numerical results obtained by the program VULCAN, published by Huang *et al.* (1999).

In Abaqus program, the available coupled thermal-stress analysis requires the use of elements with both temperature and displacement degrees of freedom. If beam or shell elements are used, which only have displacement degrees of freedom but no temperature degree of freedom, temperature distributions under fire can be obtained by performing a heat transfer analysis. The heat flow from the environment to the section is assumed to be convective and radiative. These first thermal results are then used in a static or dynamic analysis, where temperature gradients in the elements cross-sections are applied as predefined temperatures.

The detailed presentation of the benchmark studies can be found in Appendix C.

4.3 Validation of the detailed 3D numerical model of heated composite steel-concrete joint

4.3.1 Introduction

The detailed three-dimensional FE model is developed in Abaqus (2012) and simulates the effect of the column failure on the composite joint behaviour. The joint is subject to mechanical (bending and axial forces) and thermal loadings (constant temperatures). The joint is modelled combining 3D solid and contact elements, thereby taking into account the effect of the local failure modes. Due to the complex behaviour of a restrained beam under fire, this model allows for the inclusion of initial geometrical imperfections, non-linear temperature gradient, geometrical and material nonlinearity and temperature dependent material properties. The model is calibrated against results reached from three experimental tests described in chapter 3 (test 1 at ambient temperature, test 3 under 700ºC, and test 6 under 700ºC with spring beam axial restraint K_a). The behaviour of the joint is investigated and discussed in detail.

4.3.2 Description of the numerical model

4.3.2.1 Boundary conditions

In order to save computational time, the symmetry of the joint is taken into account in the model; only one fourth of the column, half of the end-plate, four bolts and one fourth of the composite slab are modelled (Figure 4.1).

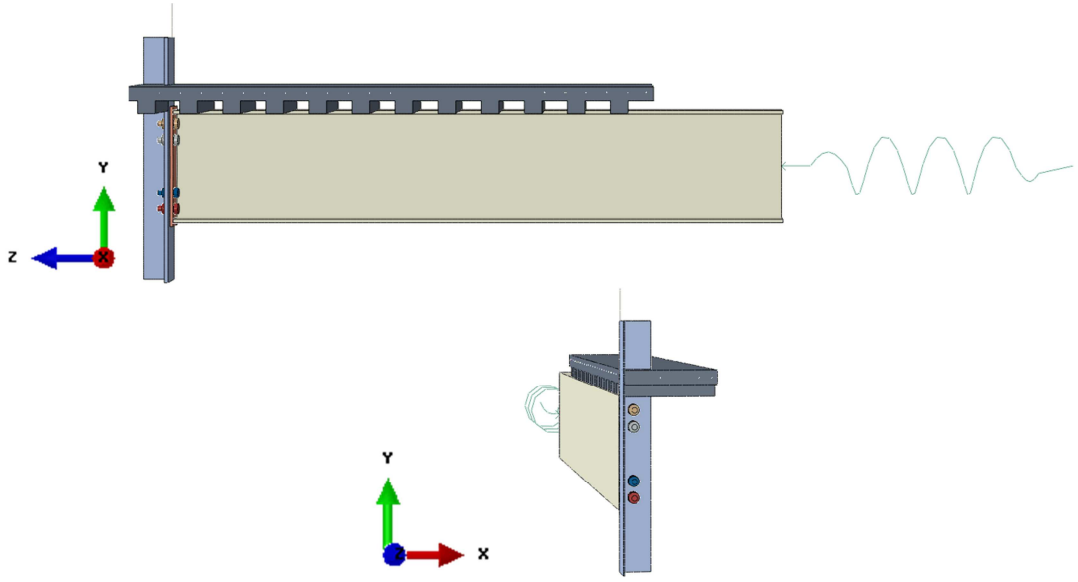

Figure 4.1: 3D FE model of the composite steel-concrete frame in Abaqus

The displacements out of the plane (x-direction in Figure 4.1) of: i) the column flange, ii) the column web in contact with concrete, and iii) the beam flanges are restrained, but the local buckling of the webs is accepted. The beam support is located at a distance of 2.79 m, measured from the end-plate. The y-direction at the beam support is restrained, leaving free the z-direction; the top of the column is free in the y-direction, and the z-direction is restrained all along the column web and the slab width. The application of the hogging and sagging bending moments in the joint is simulated by displacement control at the top of the column. For FE model where beam axial restraint (K_a) is considered, a spring element is used at the beam end (Figure 4.1), with a linear elastic behaviour (K_a = 50 kN/mm, as in test 6).

Because the purpose of this study is the joint behaviour, only the geometrical imperfections in the end plate are reproduced in Abaqus: the measured initial deformation of the end-plate (gap of 0.6 mm between the end-plate centre and the column flange) is reproduced using a sinusoidal shape between bolt rows 2 and 3.

4.3.2.2 Element types and mesh

The main steel joint members are modelled with three-dimensional 8-node linear brick reduced integration solid elements (C3D8R). Bolts M30 are modelled with a reduced diameter size d_s equal to 26.73 mm, equivalent to the resistant section A_s (561 mm^2); the

hole around the bolt shank is 3 mm higher than the bolt diameter, as in the real connection. Bolt head and nut are modelled circular and include the two washers that were used during the tests; the bolt threads are not modelled (Figure 4.2a). In order to simplify the model and save computational time, the upper part of the steel column, away from the joint zone, is modelled using general B31 beam elements. The Abaqus "Coupling" function joins these two finite elements. The steel sheeting of the composite slab is not considered, and the shape of the ribs is simplified by an equivalent rectangular section of width 84 mm (the simplification of the ribs shape is validated in Appendix D.3.3). The longitudinal and transversal steel reinforcements are modelled with two-node three-dimensional truss elements (T3D2) (Figure 4.2b). These steel bars are linked to the concrete slab by means of an embedded constraint which neglects any relative slip and debonding of the mesh with respect to the concrete (Qureshi *et al.*, 2011). In order to have full integration and avoid any problem of hourglass modes in the slab, incompatible mode elements (C3D8I) are used. Partial shear connection between the concrete slab ribs and the steel beam is taking into account by modelling the shear studs with solid C3D8R elements (see section).

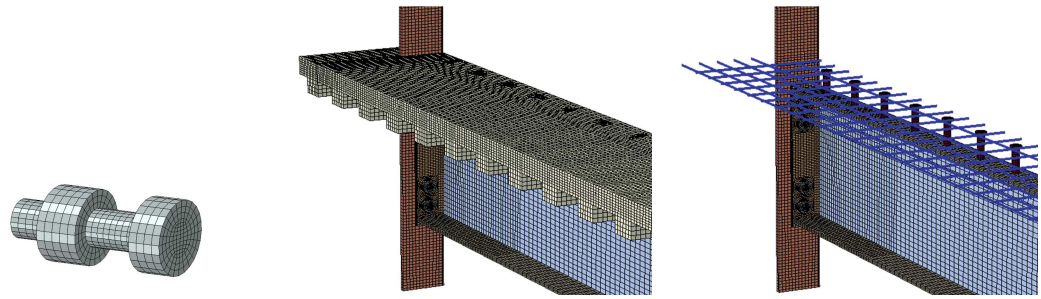

a) b)

Figure 4.2: 3D meshed FE model in Abaqus: a) bolt, and b) rebars and shear studs detail

The bolts and the end-plate are meshed similarly (element size 3-5 mm), whereas the column has a coarser mesh (element size 6-10 mm). Three elements are defined on the thicknesses of the end-plate and the web and flange of the beam in order to correctly model the local deformations out of their plane (Yu *et al.*, 2008).

4.3.2.3 Shear connection between composite slab and steel beam

To calibrate the 3D numerical model of the composite joint, three different solutions to model the shear connection between steel and concrete are tested, from the simplest one to the most advanced:

1- TIE: full shear and normal connection modelled by a tie connection in Abaqus;
2- Spring elements: horizontal and vertical springs connected between steel flange and concrete slab; their behaviour is defined as in the benchmark example B (see Appendix C.3);
3- Solid elements to represent each shear stud (see Figure 4.3a): these studs are fully connected to the beam flange (tie connection) and contact interactions are defined between each shear stud and concrete (see next section).

Results are shown in Figure 4.3b. The third solution provides: i) the best results in comparison to the experimental test results, under hogging and sagging bending moments, ii) easiest numerical calculation: the FE model is able to reach large deformations.

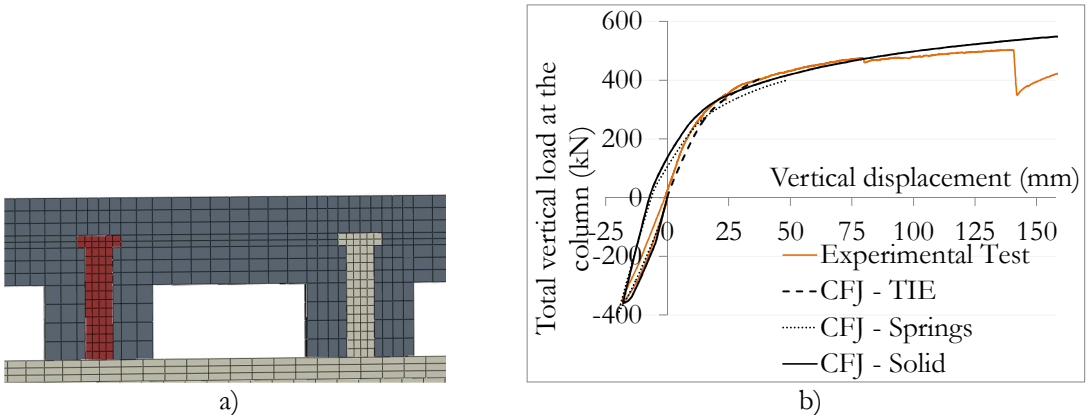

Figure 4.3: a) Detail of the shear stud in the slab; b) Bending moment *versus* rotation at the joint left side – Comparisons between experimental and FEM results

4.3.2.4 Contact interactions

In order to gain confidence in modelling contact interactions, simple tests with contacts between bolt and plate from bolted connections (Yu *et al.*, 2008) are modelled using a static analysis at ambient temperature (see Appendix D3.1). In the current model, contact interactions are defined between: i) each shear stud and the surrounding concrete, ii) the end-plate and the column flange, iii) the concrete slab and the steel column, iv) the concrete ribs and the steel beam, and iv) each bolt and the column flange and the end-plate (nut - column flange; bolt head - end-plate; bolt shank - column flange hole; bolt shank - end-plate hole). Contacts are defined as surface-to-surface contact with a small sliding option. Normal contact is defined as "hard contact" with default constraint enforcement method, and separation is allowed after contact. A friction coefficient of 0.25 is used in the tangential behaviour of steel to steel contact (Bursi and Jaspart, 1997), with penalty friction formulation, and no friction is assumed between concrete and steel surfaces. Welds are not modelled; steel beam is fully connected to the end-plate using the Tie option; shear studs are also tied to the steel beam.

4.3.2.5 Mechanical and thermal loadings

The general static analysis is used. Several numerical steps are defined: step 1 - pre-loading of bolts; step 2 - hogging bending moment; step 3 - heating; step 4 - loss of the column (the column bottom support is inactivated); step 5 - sagging bending moment. Pre-loading of bolts is simulated using the "Bolt load" option. The adjust length method is used for each bolt (adjust of 0.07 mm), which reproduces the small pre-loading applied in the experimental tests (about 120 kN). During the application of the pre-load, displacements of the bolt heads and of the steel end-plate are restrained. Then the application of the hogging and sagging bending moments in the joint are simulated by displacement control at the top of the column. In step 3 (heating), temperatures are specified into specific points as

predefined fields, and one amplitude curve defining the evolution of the temperature measured during the test is introduced for each section type (Figure 4.4); detailed values of temperatures are provided in Appendix D.3.4. In order to improve the convergence of the model, an artificial viscous damping is also defined for each step.

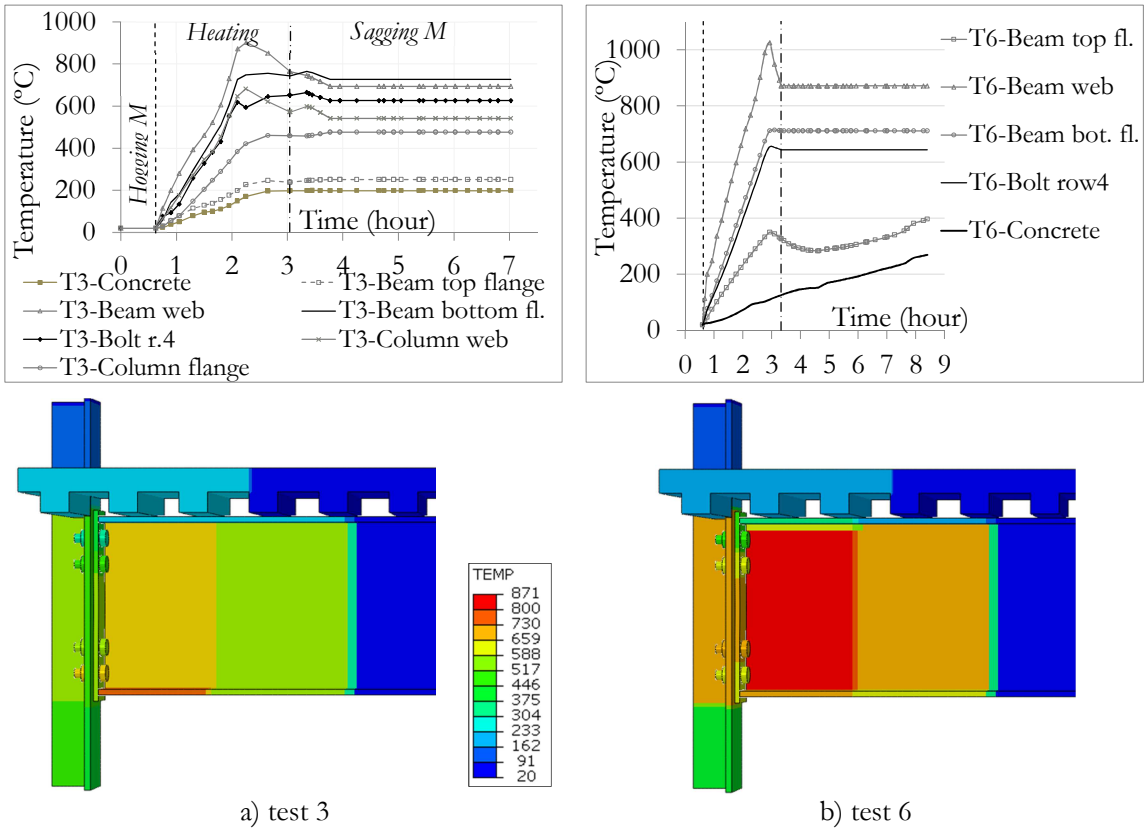

a) test 3 b) test 6

Figure 4.4: Temperatures distribution in the joint

4.3.3 Mechanical properties at ambient and elevated temperatures

4.3.3.1 Steel properties

For good correlation with experimental results, the full actual stress-strain relationship of the materials must be adopted in the numerical simulation. The constitutive laws (at ambient and elevated temperatures) are determined based on coupon tests (see section 3.4). From the tensile test results, standardized stress-strain curves of structural steels S355J0+M and S460M (Figure 4.5) are defined using: i) at ambient temperature, the Menegotto-Pinto model (for materials of sharp-knee type) (Kato *et al.*, 1990), and ii) at elevated temperatures, the stress-strain relationship for carbon steel defined in EN 1994-1-2 (2005) (strain hardening is not considered). The high-temperature creep effect on the deformation of structural steel is considered by using the temperature–stress–strain relations defined from EN 1994-1-2 (2005). The reduction factors for the effective yield strength, the proportional limit and the elastic modulus at elevated temperatures are calculated based on the measured value at 20°C (see detailed values in Appendix A.3). As the real properties of the end-plate material are not known (see chapter 3), the beam web material properties (at ambient

temperature) are used in Abaqus. At elevated temperatures, reduction factors defined in EN 1994-1-2 (2005) are considered.

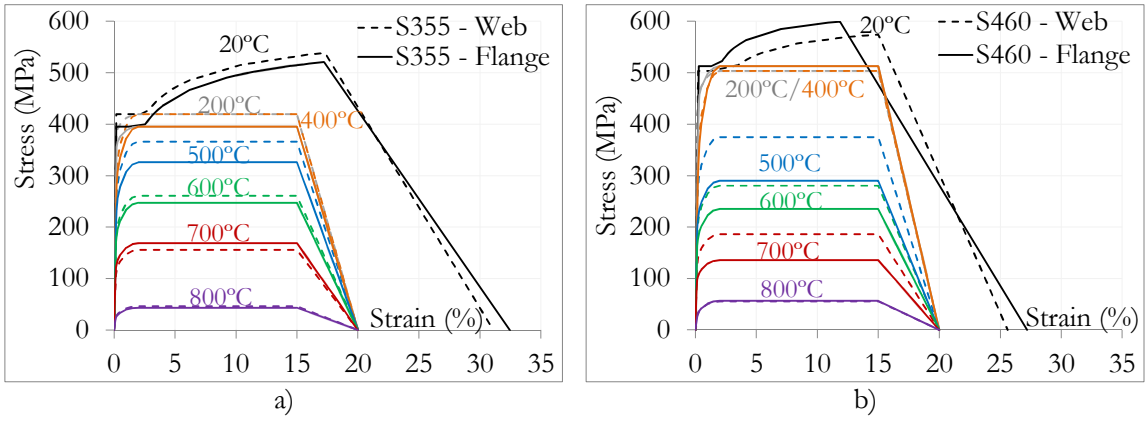

Figure 4.5: Stress-strain curves of steel from the webs and flanges of columns HEB 300 (S460) and beams IPE 550 (S355), and from the end-plate (S355 - 15 mm thickness)

For Abaqus simulation, the nominal stress-strain measures (σ_{nom},ε_{nom}), obtained from the standardized curves, are converted to the true stress-logarithmic strain values (σ_{tru},ε_{tru}) for the definition of the uniaxial material response (see Figure 4.6). These quantities are defined with respect to the current length and cross-sectional area of the coupon, and are related to the engineering values by means of the following relationships:

$$\sigma_{tru}=\sigma_{nom}(1+\varepsilon_{nom}) \quad \text{and} \quad \varepsilon_{tru}=\ln(1+\varepsilon_{nom}) \qquad \text{(Eq. 4.1)}$$

The descending branch is not taken into account in Abaqus simulations and a horizontal plateau is considered after reaching the maximum steel strength, in order to facilitate the convergence of the model and to reach high deformations. The coefficient of expansion is assumed constant and equal to α_{steel} = 1.4 10^{-5}/°C.

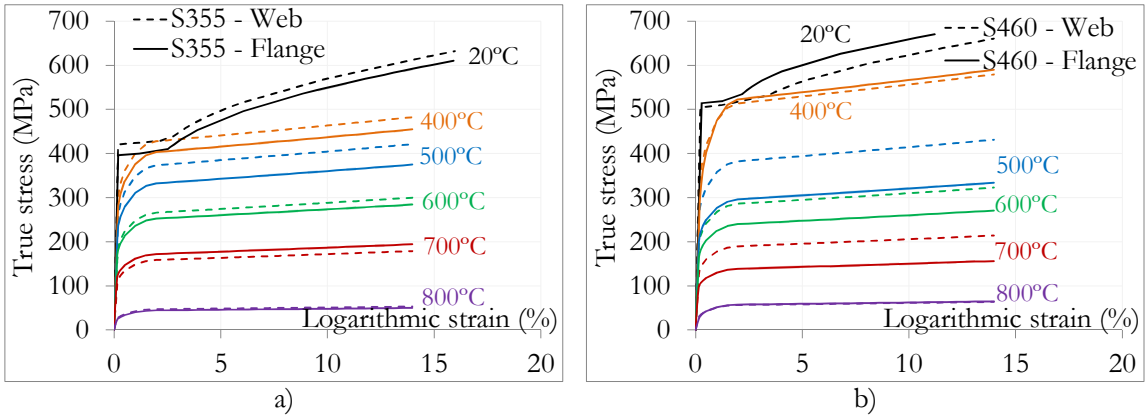

Figure 4.6: True stress-logarithmic strain steel curves at elevated temperatures for: a) the flange and web of columns HEB 300 (S460) and b) the flange and web of beams IPE 550 (S355)

Steel rebars are assumed as elastic-perfectly plastic material, with the elastic modulus equal to 200 GPa, and the yield strength equal to 500 MPa. For the shear studs of 22 mm diameter, material properties are adopted from (Nguyen and Kim, 2009) and the material is

modelled by a tri-linear stress strain curve: elastic modulus equal to 208 GPa; yield stress (416 MPa) determined at 0.2%; and ultimate stress (480 MPa) achieved at 0.6%.

4.3.3.2 Properties of M30 grade 10.9 bolts

At ambient temperature, the nominal stress-strain curves obtained from the tensile tests of the black bolts M30, grade 10.9 are idealized by a bi-linear curve with a yield strength equal to 932 MPa (ε_{nom} = 0.45 %) and the ultimate tensile strength equal to 1044 MPa (ε_{nom} = 5 %). At elevated temperature, the reduction factors of the tensile strength and the elastic modulus are calculated based on the tests average results (see Appendix A.3), and the Hanus' model for the stress–strain diagram of bolts at elevated temperatures is used (Hanus *et al.*, 2011) (see Figure 4.7a). The true stress-strain values defined by (Eq. 4.1) are used in Abaqus; a plateau is defined from ultimate stresses, as shown in Figure 4.7b. Table 4.1 presents the average values of strain to fracture at each temperature obtained from the tensile tests; these values are considered to determine the bolt failure in the FE model.

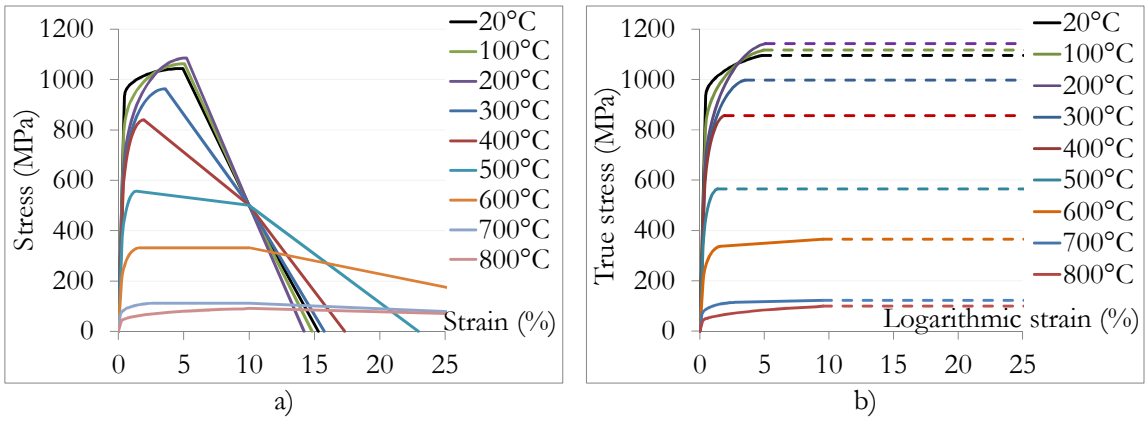

Figure 4.7: Stress-strain curves of steel from black bolts M30, grade 10.9 under ambient and elevated temperatures: a) nominal values; b) true stress-logarithmic strain steel curves in Abaqus

Table 4.1: Average values of strain to fracture from tensile tests results on bolts M30, grade 10.9

Temperature (ºC)	Average strain to fracture (%)
20	11.27
200	9.91
400	11.40
500	13.68
600	24.83
700	38.05
800	43.39

4.3.3.3 Concrete properties

Concrete properties are defined according to EN 1992-1-1 (2004), and the stress-strain behaviour of the concrete C25/30 in compression is shown in Figure 4.8a. The concrete resistance in compression is defined by compression tests on concrete cubes (see chapter 3). In Abaqus, the concrete damaged plasticity model is used and the properties measured

at 28 days are considered (at ambient temperature: f_{ck} = 28.8 MPa and E_{cm} = 32 514 MPa); the true stress-strain values are defined by (Eq. 4.1) and from ultimate stresses, a plateau is considered (see Figure 4.8b). The behaviour of the reinforced concrete in tension is defined by the maximum tensile stress defined in EN 1992-1-1 (2004) (2.8 MPa); in Abaqus, a plateau is defined from strain $\varepsilon_{c,tension}$ = 0.1 ‰. The reduction of the concrete properties at elevated temperatures is defined according to EN 1992-1-2 (2004). The coefficient of expansion is assumed constant and equal to $\alpha_{concrete}$ = 1.8 10^{-5}/°C.

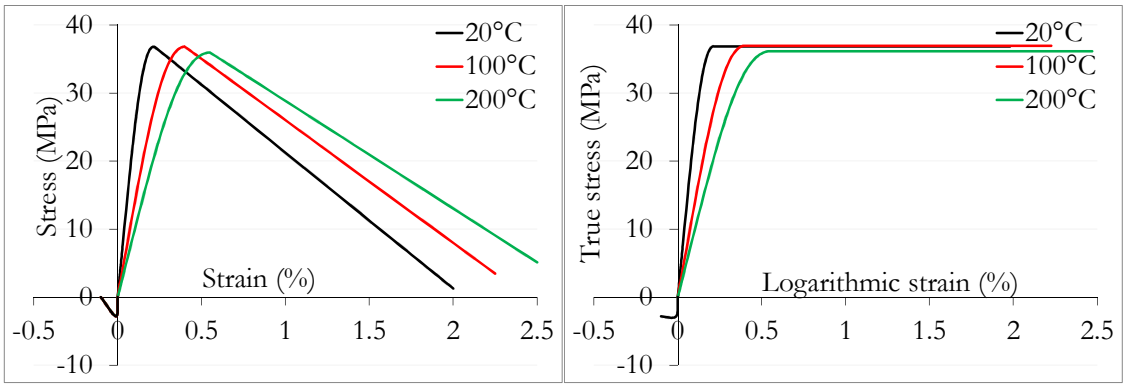

Figure 4.8: Stress-strain behaviour of the concrete in compression: a) nominal values; b) true stress-logarithmic strain curves used in Abaqus

4.3.4 Experimental and numerical response of the beam-to-column joint at ambient and elevated temperatures

The comparison between experimental tests and FE results is based on: i) the force-displacement and moment-rotation curves for the three tests 1, 3 and 6, and ii) the moment-axial load curve for test 6. The reaction load at the column top and the vertical displacement of the joint define the force-displacement curve. In the FE models, the joint rotation is taken from the vertical and horizontal displacements measured at 30 cm from the end-plate (Figure 4.9), so that local deformations of the end-plate do not influence the real rotation of the entire joint. The bending moment is calculated using the reaction load at the beam support R_F ($M = R_F$ x h_{Rf}), where h_{Rf} is the horizontal distance between the beam support and half of the column flange thickness. The axial load in test 6 is measured in the axial restraint at the beam end.

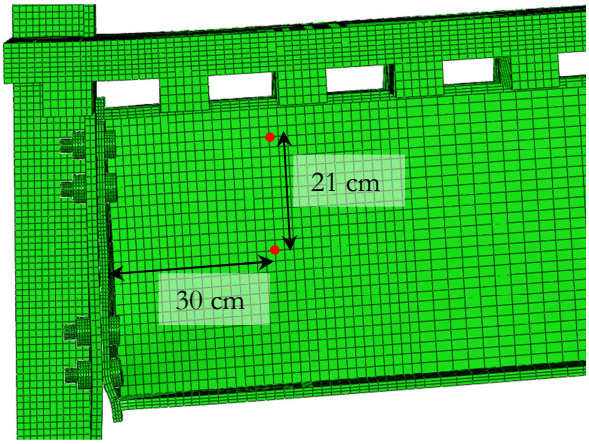

Figure 4.9: Selected nodes in the FE model to obtain the connection rotation

4.3.4.1 Beam-to-column joint at ambient temperature (test 1 – 20ºC)

The evolution of the total load applied at the column *versus* the vertical displacement of the joint, and the bending moment *versus* the rotation of the connection are depicted in Figure 4.10. The response of both experimental test and FE model are very close, with similar initial stiffness's under hogging or sagging bending moments.

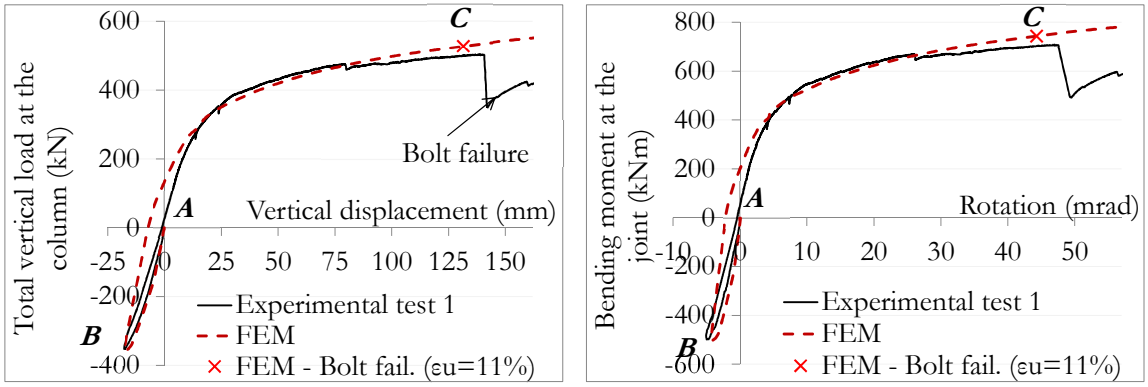

Figure 4.10: a) Applied load - vertical displacement; b) Bending moment - joint rotation

Under hogging bending moment, the behaviour of the joint is well predicted by the FE model and a maximum value around M = -500 kNm is reached (Table 4.2). The concrete slab reaches ultimate stresses under tension and cracks appear at the surface; yielding under tension is shown in Figure 4.11; other components in tension such as rebars or bolts do not even yield. The column web yields under compression loads; however, no instability is observed and the ultimate stresses are not reached (Figure 4.12a).

Table 4.2: Comparison of the FE results with the experimental results (test 1)

		Force at the column F (kN)	Vertical displ. at the column top δ_v (mm)	Joint bending mom. M (kNm)	Joint rotation Φ (mrad)
Hogging bending moment	Test	-351	-18	-500	-5
	FEM	-360	-18	-508	-4
	Diff. (%)	*2.6*	*-3.3*	*1.4*	*15.6*
At bolt failure	Test	502	147	707	48
	FEM	523	126	738	44
	Diff. (%)	*4.2*	*-14.6*	*4.3*	*-6.8*

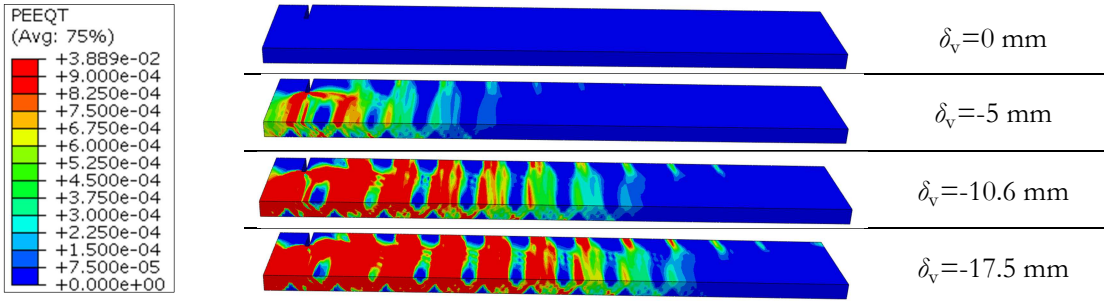

Figure 4.11: Evolution of the equivalent plastic strains in uniaxial tension (PEEQT) in the concrete slab during the application of the hogging bending moment ($f_{ct} \geq 2.9$ MPa and $\varepsilon_c \geq 0.01\%$)

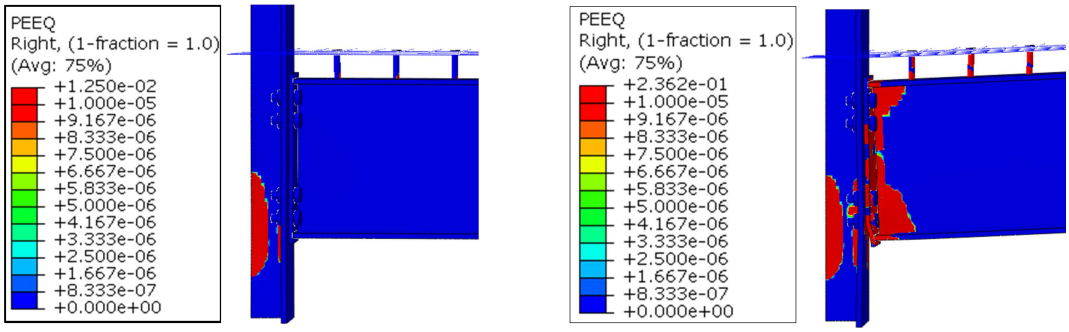

Figure 4.12: Distribution of the equivalent plastic strains (PEEQ) in the joint (yielded components): a) under hogging bending moment; b) at bolt failure

Figure 4.10 shows differences between the residual deformation of the joint after the hogging bending moment and the loss of the column: once the load is reversed (F = -360 kN to zero), the vertical displacement measured during the experimental test reached zero, whereas the FE model shows a residual vertical displacement δ_v = -7.2 mm. However, this residual displacement is small and the error may be attributed to measurement inaccuracies during the experimental test (notably due to the large size of the specimen). Under sagging bending moment, a good agreement between the experimental and numerical results is shown: the material degradation is well reproduced by the FE model until the maximum load, corresponding to the bottom bolt row failure. In the FE model, the bolt failure is assumed when the average equivalent bolt strain on the section reaches the fracture strain measured during the tensile tests (11.3% - red cross in Figure 4.10); Table 4.2 shows the corresponding values of force, displacement, bending moment

and rotation. At bolt failure, the higher resistance obtained by the FE model can be explained by the non-consideration of the descending branches of $\sigma - \varepsilon$ curves in all the material properties.

Figure 4.13a presents the final deformations of the joint, after the failure of two bolts identified in the bottom bolt rows of the *left* connection, due to a slight asymmetric joint deformation (see chapter 3). Under sagging bending moment, the deformations of the joint in the FE model when the bolt fails (Figure 4.13b) are similar to the experimental deformations. After the test, a deformation of the end-plate was observed at its mid-height. This local deformation is also observed in the FE model (gap of 2.2 mm). In the test, due to high stresses/deformations, a crack appeared at the steel end-plate above the welds, after the bolt failure. In the FE model, Figure 4.14a shows that almost the entire end-plate is yielded, and ultimate strains (17.3%) are reached at the same location than the crack observed in the tests (Figure 4.14b).

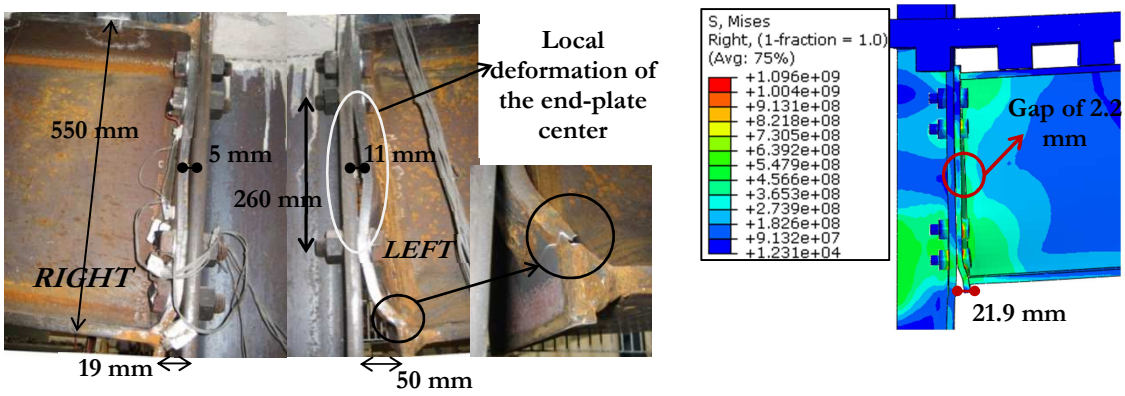

a) b)

Figure 4.13: Deformation of the joint: a) at the end of the experimental test 1 (δ_v = 209 mm); b) when the bolt fails in the FE model (δ_v = 126 mm)

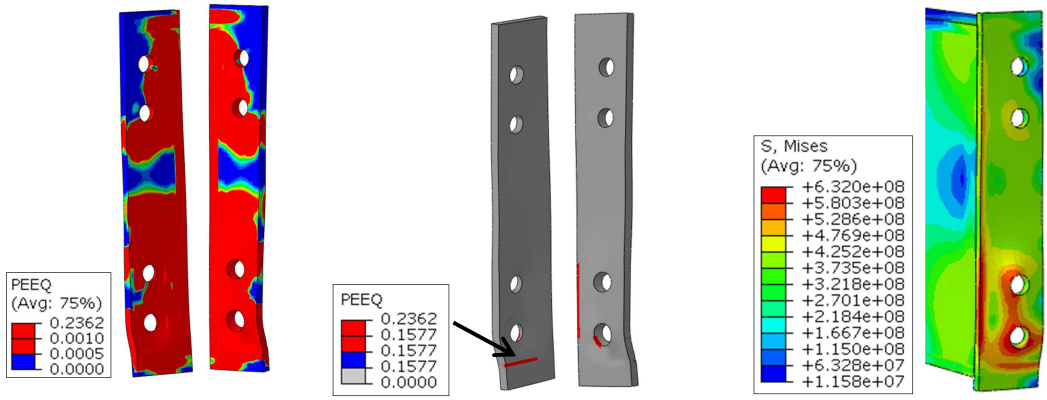

a) b) c)

Figure 4.14: At the bolt failure: Equivalent plastic strain (PEEQ) in the end-plate corresponding to: a) the yielding (f_y = 419 MPa; ε_y = 0.19%) and b) the ultimate stresses (f_u = 539 MPa; ε_u = 17.3%); c) von Mises stresses

Figure 4.12b shows the yielded parts of the composite joint at bolt failure. It is observed that shear studs are strongly solicited due to the slip between the concrete slab and the steel beam (partial shear connection); more details of the effect of the shear connection on the joint behaviour are provided in chapter 5.

The deformations of the joint under hogging and sagging bending moments (points *B* and *C* of the moment-rotation curve in Figure 4.10) are depicted in Figure 4.15; the joint vertical displacement is also shown. This figure illustrates the load distribution in the following activated joint components (represented by arrows): concrete in compression (CSC), reinforcement in tension (RT), bolts in tension (BT) and beam flanges in compression (BFC). The load in a component is obtained by integration of the *NFORC* values over its cross-section (*NFORC* are the forces at the nodes of an element provided by Abaqus). So, loads distribution in end-plate in bending (EPB), column flange in bending (CFB) or column web in compression (CWC) is not represented due to the difficulty to delimit the corresponding effective lengths. Under hogging bending moment, the neutral axis is located between bolts rows 2 and 3, while, under sagging bending moment (at bolt failure), it is located between the top bolt row and the beam top flange. Figure 4.14c presents the von Mises stresses at the end-plate (at bolt failure); the bolt group mechanism (bolt rows 3 and 4) is highlighted.

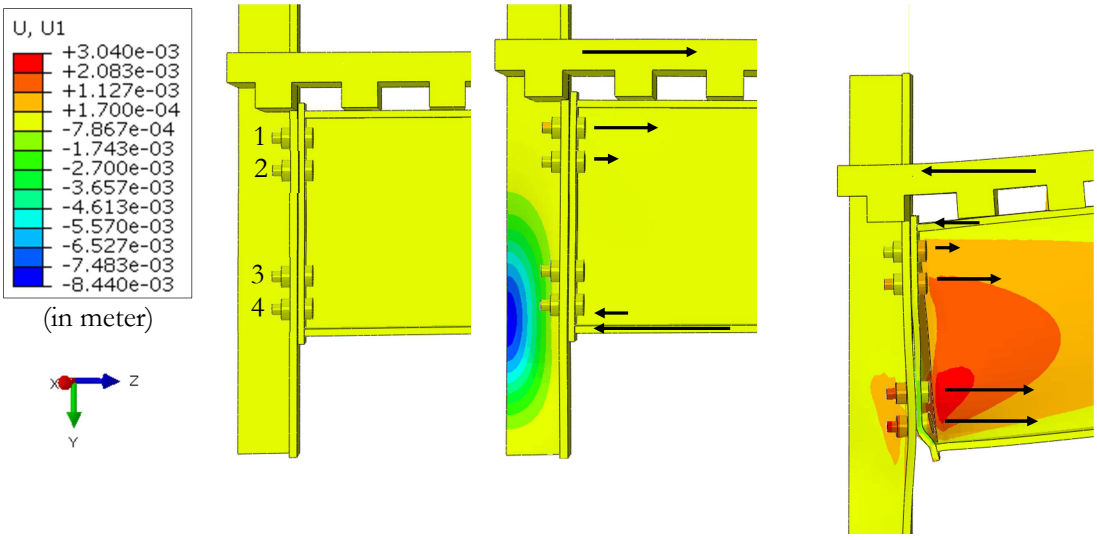

A- δ_v= 0 mm B- δ_v= -18 mm C- δ_v= 131 mm (bolt failure)

Figure 4.15: Deformation of the joint (scale x 2), vertical displacements and load distribution in the activated joint components (test 1)

Figure 4.16 depicts the evolution of the deformation of the bottom bolt row, the von Mises stresses, the yielding and the fracture strains (11.3%): these stresses and strains are induced by the deformation of the bottom part of the end-plate and are limited in the shank zone in contact with the end-plate, as observed is the experimental test (failure near the bolt head, see Figure 4.17).

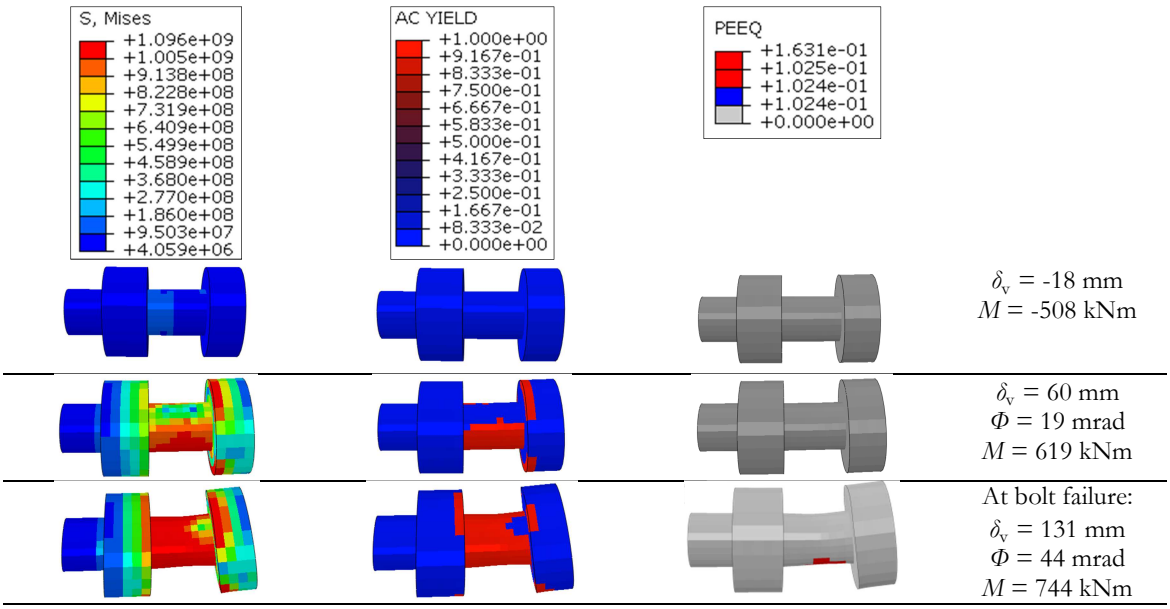

Figure 4.16: Evolution of the bottom bolt row deformation under sagging bending moment (scale x 1): a) von Mises stresses, b) Yielding, and c) Equivalent ultimate plastic strain PEEQ (ε_b > 11.3%)

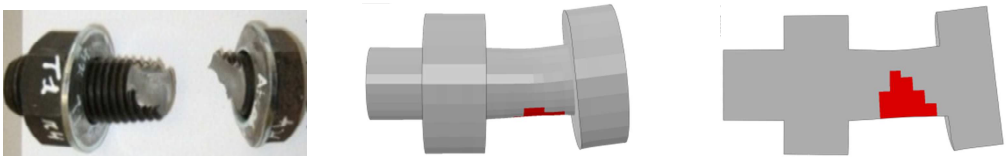

Figure 4.17: Failure of the bolt: a) at the experimental test; b) in the FE model (Equivalent strains at fracture)

The evolution of the minimum principal stresses and the equivalent ultimate plastic strains in the concrete slab in compression is depicted in Figure 4.18. It is clearly showed that only the top part of the concrete slab thickness is under compression loading, while the bottom part is under tension.

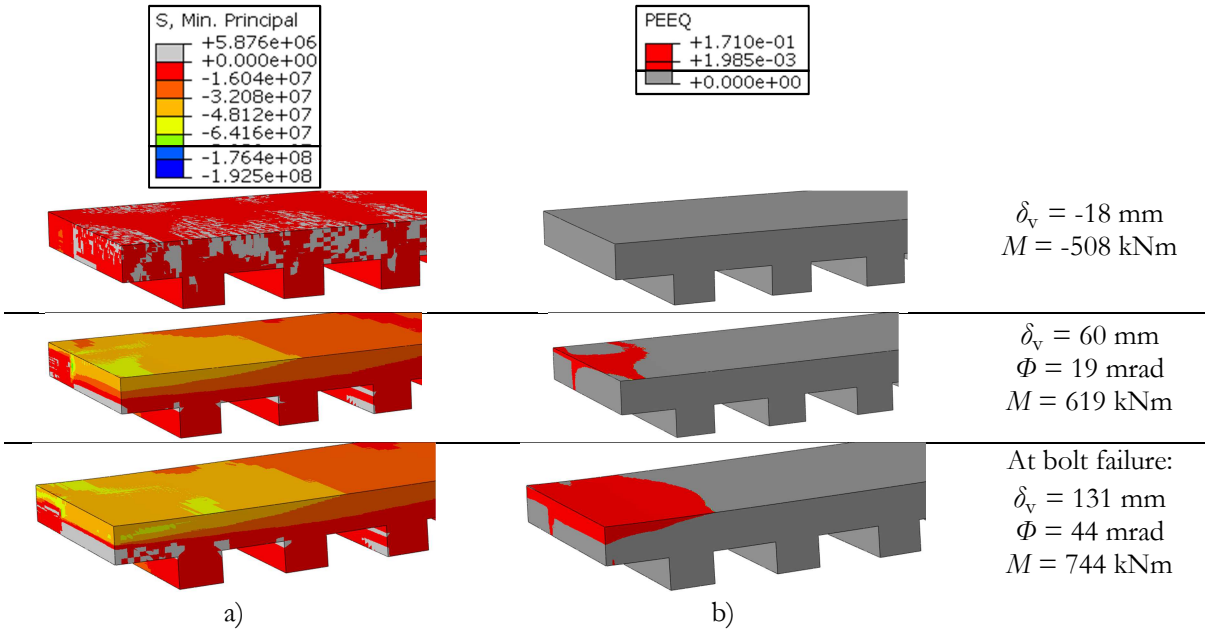

Figure 4.18: Concrete slab under sagging bending moment (scale x 1): a) the minimum principal stresses, and b) equivalent ultimate plastic strain PEEQ (ε_c > 0.2%)

4.3.4.2 Beam-to-column joint at elevated temperatures (test 3 – 700ºC)

The evolution of the total load applied at the column *versus* the vertical displacement of the joint, and the bending moment *versus* the joint rotation under 700ºC are depicted in Figure 4.19. The numerical results are compliant with the experimental response. The deformation of the joint under hogging bending moment (points *A* and *B* of the force-displacement curve (initial hogging moment and heating)) and sagging bending moment (point *C*) are depicted in Figure 4.20; the vertical displacement and the load distribution in activated joint components are also shown.

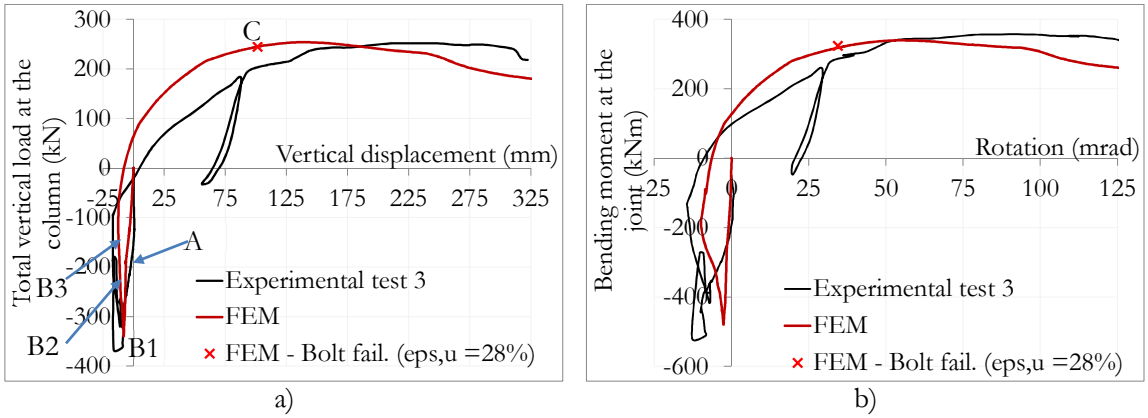

Figure 4.19: a) Applied load - vertical displacement; b) Bending moment - joint rotation

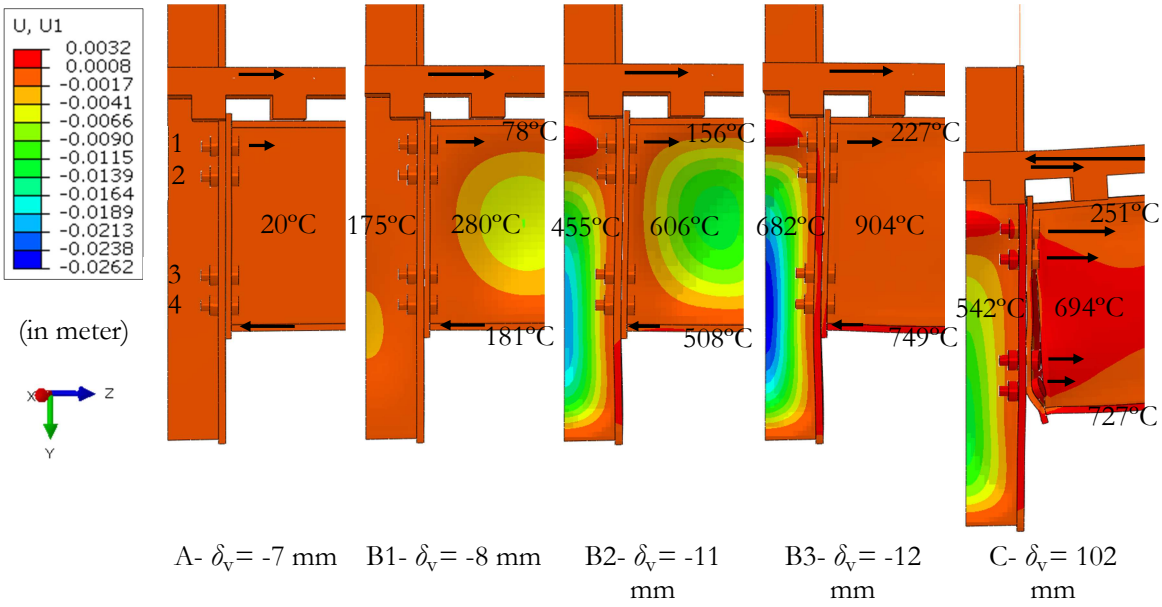

Figure 4.20: Deformation of the joint (scale x2) and vertical displacements: A) under hogging bending moment, B1) under heating (minimum hogging moment at 32 min.), B2) under heating (1h13min.), B3) under heating (1h30min.), C) under sagging bending moment (at bolt failure)

Under hogging bending moment and heating, the neutral axis remains between the bolt rows 1 and 2, even if the local deformations of the column and beam webs change with the increase of temperatures: B1- at the beginning, the beam web has higher out of plane deformation than the column web, then B2/3- out of plane deformation of the column web increases and reaches a maximum of 26 mm after 1h30min. (B3), when it reaches its maximum temperature (682°C). Results corresponding to point B1 are detailed in Table 4.3 and compared with the experimental results. Discrepancies can be observed mainly for the vertical displacement and rotation of the joint; again, they could be attributed to measurement inaccuracies during the experimental test (due to the large size of the specimen but also because the heated joint zone was not accessible to the measuring devices).

Table 4.3: Comparison of the FEM results with the experimental results (test 3)

		Force at the column F (kN)	Vertical displ. at the column top δ_v (mm)	Connection bending mom. M (kNm)	Connection rotation Φ (mrad)
Min. load during the temp. increase (B1- hogging bending mom.)	Test	-366	-16	-517	-10
	FEM	-340	-8	-480	-3
	Diff. (%)	-7.0	-49.3	-7.3	-71.5
Max. load (sagging bending mom.)	Test	252	231	357	90
	FEM	254	133	338	50
	Diff. (%)	0.6	-42.7	-5.3	-44.2

Under sagging bending moment, a proper agreement between the experimental and numerical results is shown: the material degradation is reproduced by the FE model up to a

maximum load equal to the measured maximum load in the test (Figure 4.19). However, the corresponding vertical displacement δ_v/rotation Φ is lower than measured in the test (Table 4.3). The FE model presents similar stiffness than the "unloading-reloading", which explains the smaller deformations obtained under the maximum load. In the FE model, the bottom bolt row fails under $\Phi_{j,u}$ = 37 mrad (M = 323 kNm); the failure is assumed once the equivalent bolt strain average on the section reaches the fracture strain obtained from the tensile tests (28% at 626°C). Under sagging bending moment (at bolt failure), the neutral axis is located between the rebars and the concrete in compression (Figure 4.20C). The failure of the bottom bolt row was not noticeable during the test; it was probably reached during the cooling phase (see chapter 3).

Figure 4.21 compares the final experimental deformation of the connection to the FEM deformation when the bolt fails. Similar deformations are obtained. Figure 4.21c shows the yielded parts of the composite joint at bolt failure. Webs of beam and column have already reached their yield strains during the heating phase, due to the thermal dilatation prevented by the beam flanges (lower temperature) and the parts of the beam and column that remain at ambient temperature. At bolt failure, the column flange (476°C) is the less yielded component, because the main deformation of the connection happens in EPB and bolts.

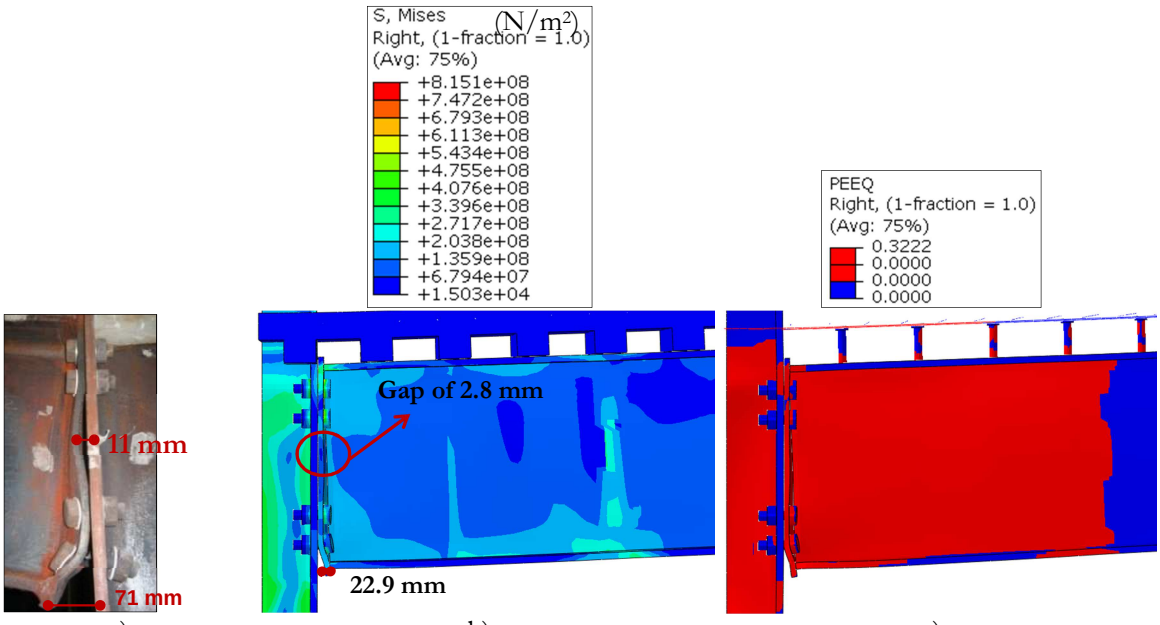

Figure 4.21: a) Deformation of the joint at the end of the experimental test (322 mm of vertical displ.); b) FEM deformation of the joint when the bolt fails and von Mises stresses (102 mm of vertical displ.); c) Equivalent plastic strains (yielded components) at bolt failure

Figure 4.22 depicts the evolution of the deformation of the bottom bolt row, but also the von Mises stresses, the yielding and fracture strains (28%). As for test 1, these stresses and strains are limited in the shank zone in contact with the end-plate, as observed in the experimental test (failure near the zone between the column flange and the end-plate, see Figure 4.23).

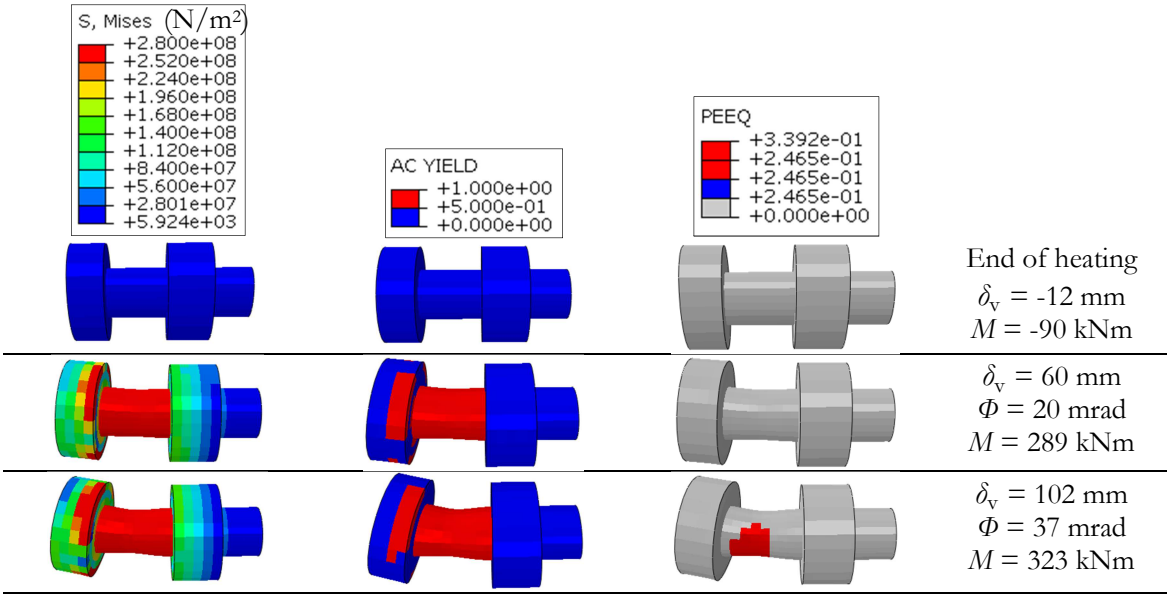

Figure 4.22: Evolution of the bottom bolt row deformation under sagging bending moment and 626ºC (scale x 1): a) von Mises stresses, b) Yielding, and c) Equivalent plastic strain PEEQ at failure ($\varepsilon_{nom} \geq 28\%$)

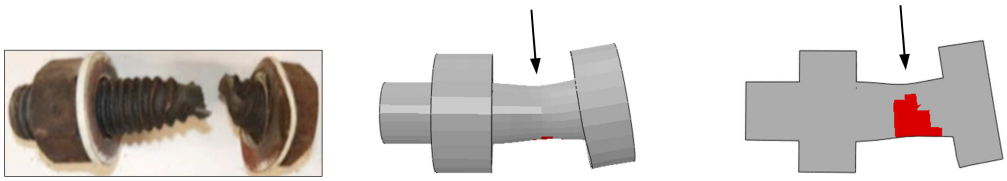

Figure 4.23: Failure of the bolt (626ºC): a) observed at the end of the experimental test; b) in the FE model (Equivalent plastic strains corresponding to failure)

The evolution of the minimum principal stresses and the equivalent plastic strains (ultimate, indicating concrete crushing) in the concrete slab in compression is depicted in Figure 4.24. As observed in test 1, only the top part of the composite slab is under compression loading and the bottom part is under tension. The concrete is only heated to 200ºC and concrete properties are not reduced. However, a smaller area of concrete crushes under compression (Figure 4.24b) in comparison to the ambient temperature test (Figure 4.18b), due to the smaller developed bending moment.

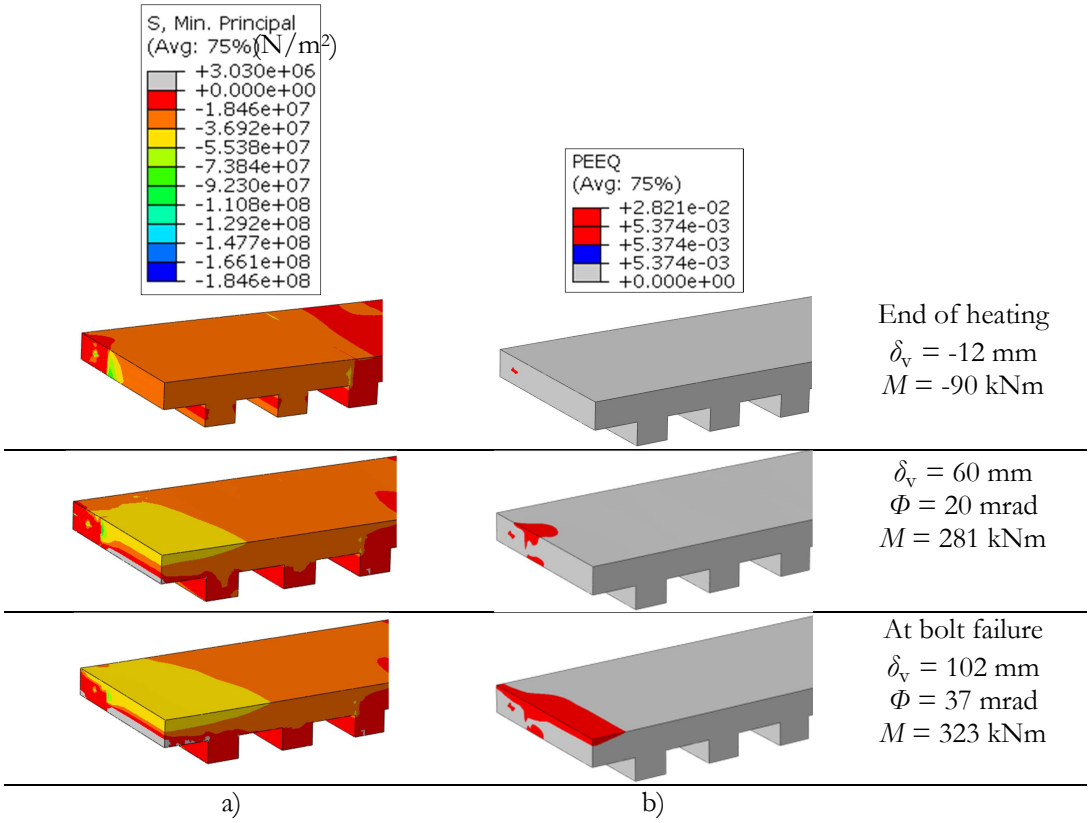

Figure 4.24: Concrete slab under sagging bending moment (scale x 1): a) the minimum principal stresses, and b) equivalent ultimate plastic strain PEEQ (ε_{nom} > 0.55%)

4.3.4.3 Beam-to-column joint at elevated temperatures and subject to axial loads (test 6 – 700ºC)

For the test 6 under 700ºC (K_a = 50 kN/mm), the evolution of the total load applied at the column *versus* the vertical displacement of the joint is depicted in Figure 4.25a, and Figure 4.25b shows the deformed joint when the bolt failed.

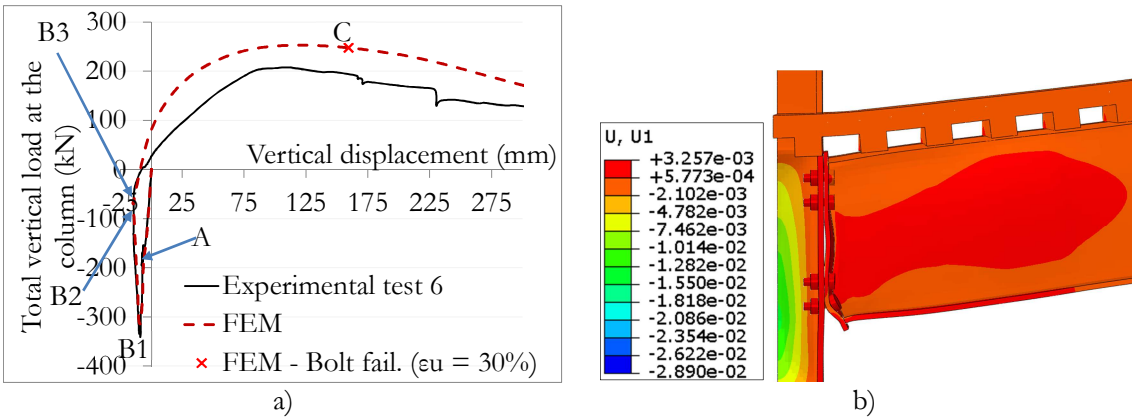

Figure 4.25: test 6 - a) Applied load - vertical displacement; b) Deformation of the joint when the bolt fails (scale x 2)

A proper agreement between the experimental and numerical results is shown. Under hogging bending moment, good results are obtained by the FE model for the load applied at the column and the joint bending moment, as shown in Table 4.4. During the heating phase, as observed in the experimental tests, the beams ends move in the outward direction due to thermal expansions of beams, and compression loads are applied by the axial restraints. After the column loss, under sagging bending moment, the axial restraints increase the compression loads because beams ends continue to move outwards (see chapter 3); the bending moment *versus* the joint rotation and the bending moment *versus* the beam axial load are depicted in Figure 4.26.

Table 4.4: Comparison of the FEM results with the experimental results (test 6)

		Load at the column (kN)	Vertical displ. at the column top (mm)	Connection bending mom. (kNm)	Connection rotation (mrad)	Beam axial load (kN)
Min. load during the temp. increase (hogging mom.)	Test	-342	-9	-483	-2	58
	FEM	-314	-9	-416	-3	115
	Diff. (%)	-8.18	0.87	-14.01	19.91	97.44
Max. load (sagging mom.)	Test	208	111	331	39	268
	FEM	253	127	454	38	670
	Diff. (%)	21.86	14.92	36.94	-0.22	150.04

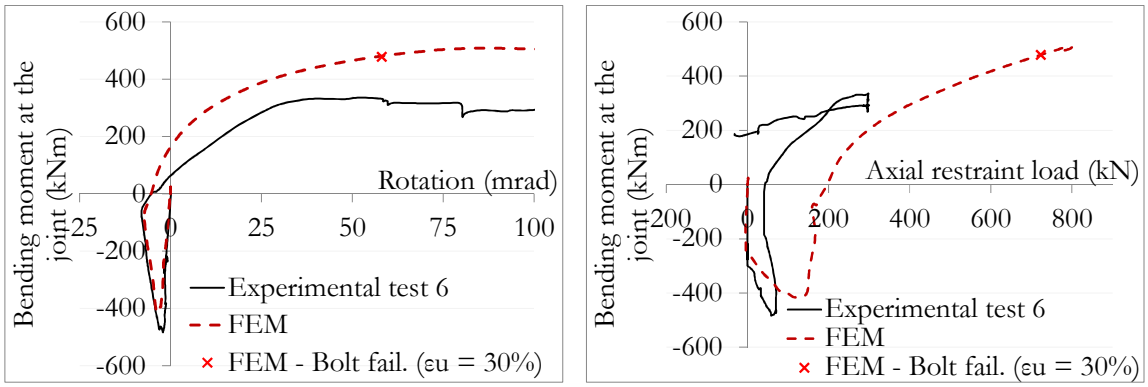

a) b)

Figure 4.26: a) Bending moment - joint rotation and b) Bending moment – axial load (test 6)

The initial stiffness of the FE model (Figure 4.25a) is slightly higher than observed in the test. The material degradation is well reproduced by the FE model, but some discrepancies appear for the loads measured at the column top and at the beam axial restraint (Figure 4.26 and Table 4.4). In the FE model, a higher axial compression load is observed in the beam restraint, which increases the sagging bending moment within the joint. During the experimental test, the measured beam axial load and initial stiffness under sagging bending moment may be reduced by the effects of the creep. Creep is defined as a time-dependant plastic strain under constant stress and temperature. It is a phenomenon that mostly influences the fire resistance of restrained steel members subject to elevated temperatures, and its influence is higher as the axial restraint stiffness is increased (Kodur

and Dwaikat, 2010). Huang *et al.* (2006) also showed that modelling creep in axially and rotationally restrained steel columns influences their failure behaviour in a significant way. Moreover, where heating rate is slow (for example for insulated members), the effect of high temperature creep becomes dominant and should be accounted for in the analysis (Kodur and Dwaikat, 2010). Both experimental tests 3 and 6 ran during about 8 hours, with slow heating followed by constant temperature state (700ºC) and increase of stresses; so creep effects could affect the deformation of the frame and the reaction loads, mainly in test 6 subject to the influence of the beams axial restraints. The temperature–stress–strain relations defined from EN 1993-1-2 (2005) compensate the transient effect of creep by underestimating the stress causing plastic strain (Anderberg, 1988). However, according to (Kodur and Dwaikat, 2010), these relations do not properly account for high-temperature creep; indeed, creep characteristics change with time, as stress and temperature, and it is impossible to fully include the effect of creep in static stress–strain curves that do not incorporate the time factor (whether rates or absolute times). In Abaqus, the subroutine CREEP can be defined using the magnitude of the creep strain rate; two creep laws are also available and can be used in the material properties definition (the power law and the hyperbolic sine law). However, modelling creep effects in the 3D FE model is a very complex problem: 1st data necessary to define the creep laws are not available in the literature and 2nd, even simplified definition of creep material properties in the 3D FE model makes it very difficult to converge. In the current FE model, creep is not defined as a time-dependent material property and the effect of creep is underestimated, which can stiffen the structural response by decreasing the deflections and increasing the restraint forces. Note that concrete creep due to elevated temperatures is not contemplated due to the low measured temperatures in the slab (lower than 300ºC).

In both experimental test and FE model, concrete crushing in compression is the first failure mode observed, due to the joint rotation and the resulting high compressive strain at the upper concrete surface (see chapter 3). In the FE model, the ultimate strain under 200°C is set equal to 5.5‰, as defined in EN 1992-1-2 (2004), and the 1st elements that reach the failure are located in the concrete in contact with the column flange. The evolution of the minimum principal stresses and the equivalent plastic strains (ultimate) in the concrete slab under compression (during sagging bending moment) are depicted in Figure 4.27. As observed in previous models, only the top part of the composite slab in under compression loading, while the bottom part is under tension.

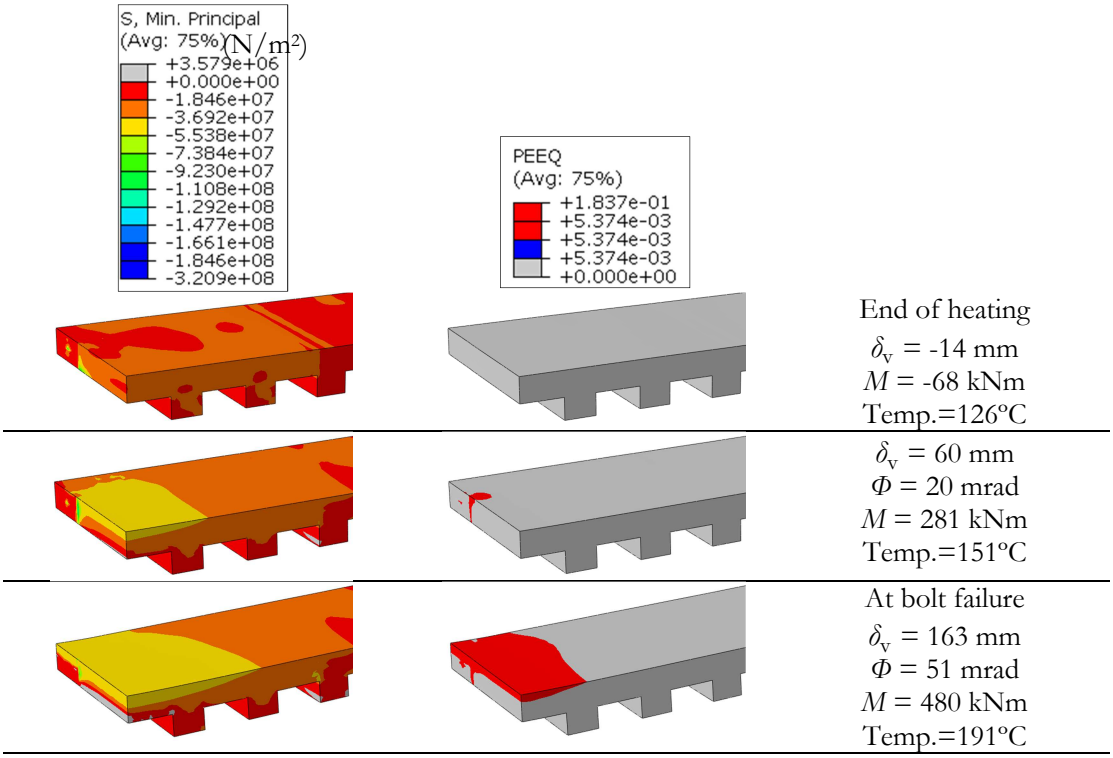

Figure 4.27: Concrete slab under sagging bending moment (scale x 1): a) Minimum principal stresses, and b) Equivalent ultimate plastic strain PEEQ (ε_{nom}> 0.55%)

In the FE model, the bottom bolt row fails at $\Phi_{j,u}$ = 51 mrad of rotation (M = 460 kNm); the failure is assumed once the equivalent bolt strain average on the section reaches the strain to fracture (30%) at 643ºC. Figure 4.28 compares the final experimental deformation of the connection to the FEM deformation when the bolt fails. The failure of the bottom bolt row was not noticeable during the test; however, the moment-rotation curve (Figure 4.26a) shows that a bolt failure was probably reached under Φ = 83.3 mrad of joint rotation (M = 300 kNm).

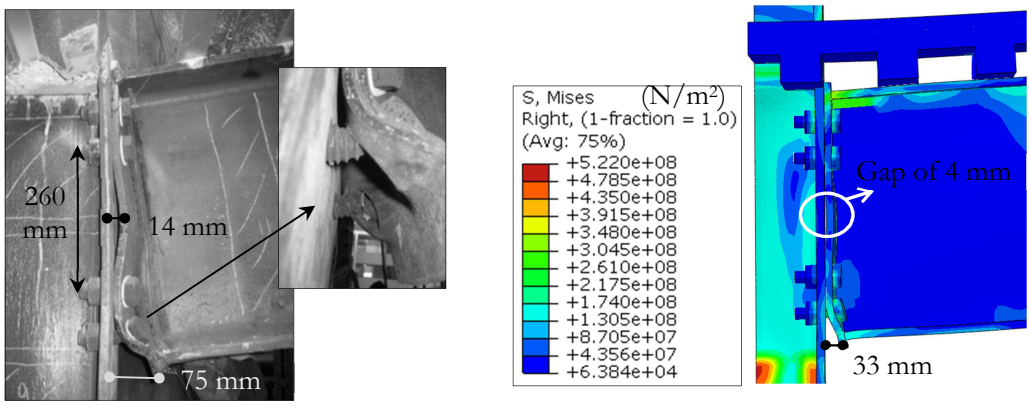

Figure 4.28: a) Deformation of the joint at the end of the experimental test (δ_v = 513 mm); b) FEM deformation of the joint when the bolt fails (δ_v = 163 mm)

The deformation of the joint under hogging bending moment (points *A* and *B* of the force-displacement curve) and sagging bending moment (point *C*) are depicted in Figure 4.29. Under hogging bending moment (point *A*) and during heating (point *B*1), the neutral axis is located between bolts rows 2 and 3. At the end of heating (point *B*3), the top part of the slab is under compression loads. Under sagging bending moment (at bolt failure), the neutral axis is located between the longitudinal reinforcement and the top part of the concrete slab in compression.

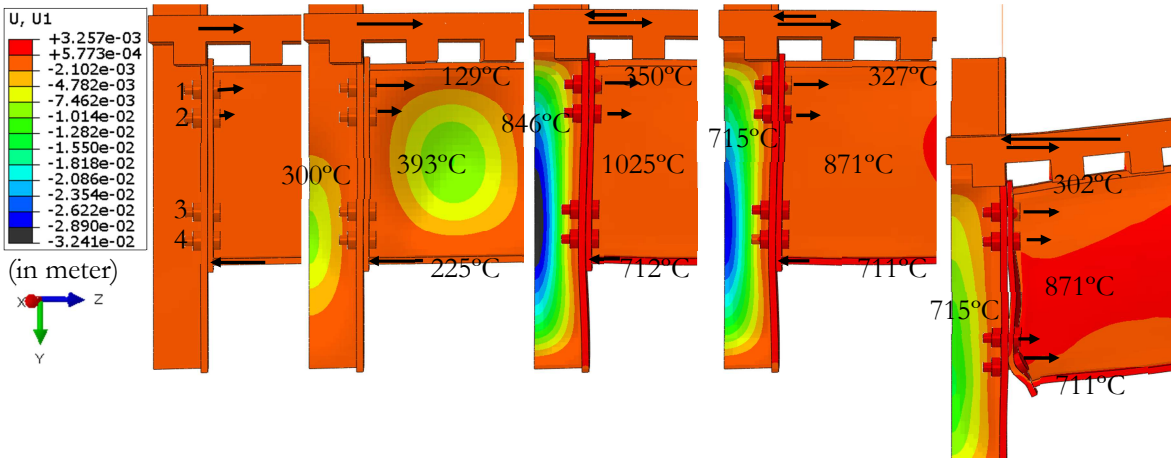

A- δ_v = -6 mm | B1- δ_v = -9 mm | B2- δ_v = -15 mm | B3- δ_v = -14 mm | C- δ_v = 163 mm

Figure 4.29: Deformation of the joint (scale x 2) A) under hogging bending moment, B1) under heating (41 min.), B2) under heating (minimum hogging moment at 2h20min.), B3) under heating (at the end, at 2h43min.), C) under sagging bending moment (at bolt failure)

Figure 4.30 shows the yielded parts of the composite joint at bolt failure. Because of the slight thermal dilatation of the concrete linked to the reinforcement, additional stresses are observed in the reinforcement (in comparison to the ambient temperature test). Webs of beam and column also yield during the heating phase, due to the thermal dilatation prevented by the beam flanges (lower temperature) and the cooler parts of the beam and column. At bolt failure, all the components yield in the heated zone.

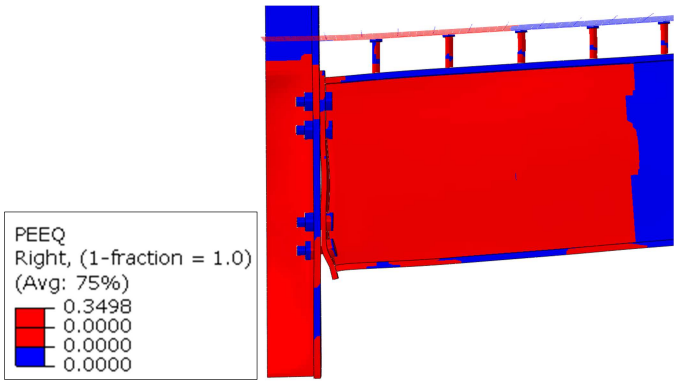

Figure 4.30: Equivalent plastic strains (yielded components) in the joint at bolt failure

Figure 4.31 depicts the evolution of the deformation of the bottom bolt row, the von Mises stresses, the yielding and the strains to fracture (30%): these stresses and strains are also localised in the shank zone, as for previous models.

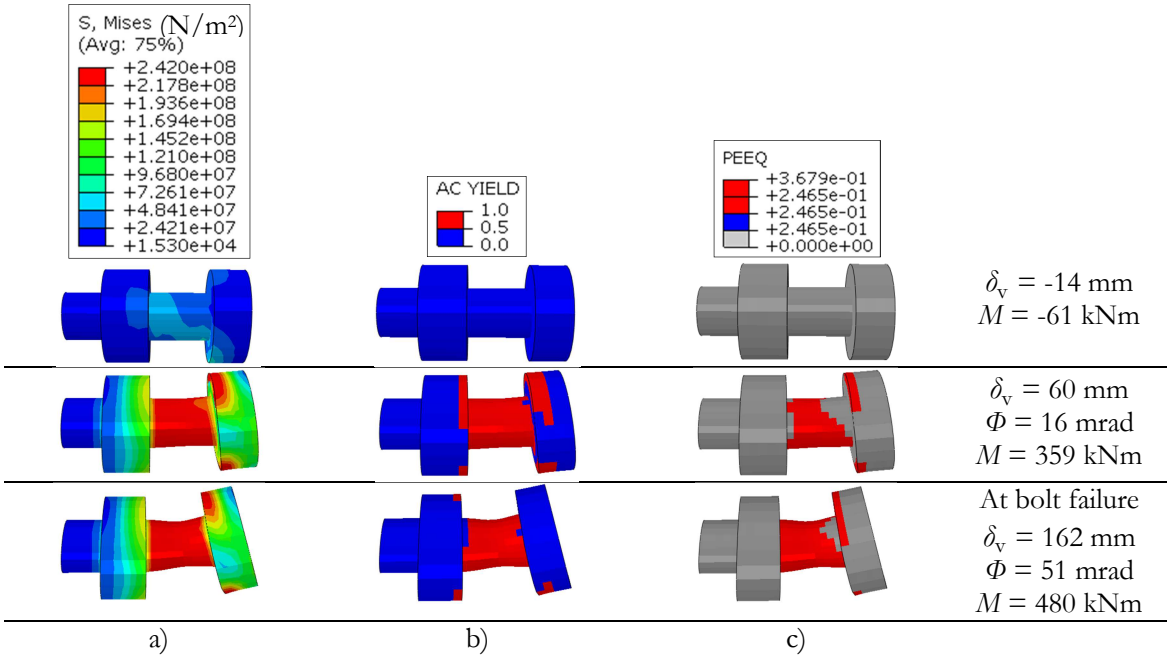

Figure 4.31: Evolution of the bottom bolt row deformation under sagging bending moment and 643°C (scale 1): a) von Mises stresses, b) Yielding, and c) Equivalent plastic strain PEEQ at failure ($\varepsilon_{nom} \geq 30\%$)

4.3.4.4 Discussion of the behaviour of the joint based on the numerical results

Figure 4.32 depicts the evolution of the bending moment at the joint *versus* the joint rotation for the three FE models (tests 1, 3 and 6); Table 4.5 provides detailed values at bolt failure. In test 1, the joint reaches a vertical displacement, rotation and bending moment higher than for test 3. The lower resistance in test 3 is due to the elevated temperatures that reduce the material properties. The lower rotation capacity is due to different distribution of forces in the activated components. In test 3, the shear connection between composite slab and steel beam is less "requested", due to the more deformable joint, and lower sliding is observed (the behaviour is similar to a full shear connection). So, all the bolt rows are in tension, and the top part of the concrete slab is the unique component in compression (see Figure 4.20). In test 1, two main components are in compression: the top part of the concrete slab and the top flange of the beam (Figure 4.15). The effect of the partial shear connection in the composite beam is studied in chapter 5, section 5.4.5. Test 6 is subject to higher temperatures than test 3, which corresponds to weaker material properties. However, the resistance and capacity of rotation of the joint are higher due to the beneficial effect of the axial compression loads at beam end. Additional investigation is provided in chapter 5.

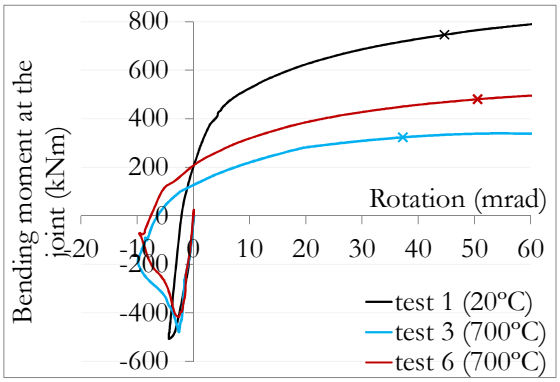

Figure 4.32: Bending moment - joint rotation of the three tests models

Table 4.5: Comparison of the FEM results (tests 1, 3 and 6) at bolt failure

	Vertical displacement δ_v (mm)	Rotation of the connection Φ (mrad)	Bending moment M (kNm)
Test 1	131	44	744
Test 3	102	37	323
Test 6	162	51	480

Figure 4.33 presents the three joints at bolt failure; it shows that end-plates of tests 3 and 6 are more deformable than end-plate of test 1, due to elevated temperatures that increase the material ductility. At ambient temperature, a slight deformation of the column flange is observed, which helps to increase the joint rotation before reaching bolt failure.

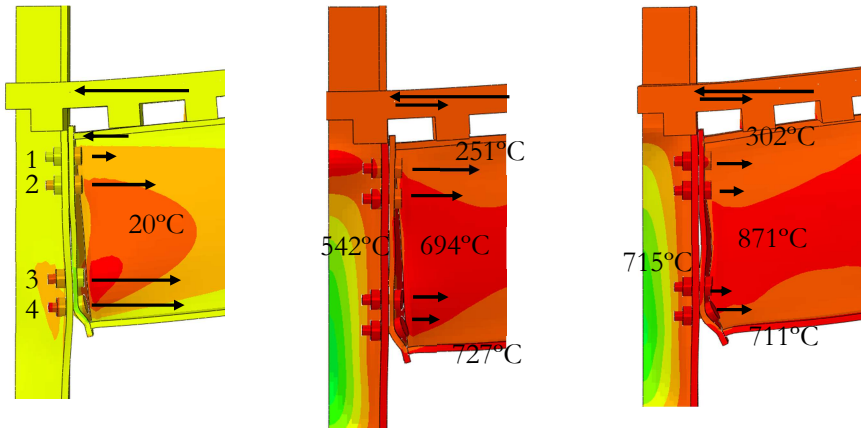

Test 1 - δ_v= 131 mm, Φ = 44 mrad

Test 3 - δ_v= 102 mm, Φ = 37 mrad

Test 6 - δ_v= 162 mm, Φ = 51 mrad

Figure 4.33: Deformation of the joints (scale x 2) and load distribution in the activated joint components

4.4 Concluding remarks

This chapter presents FEM analyses of steel and composite steel-concrete elements using the non-linear finite element package Abaqus, v6.12.

A preliminary validation of the FEM program is performed for analysis of steel and composite steel-concrete structures subject to fire; beam and shell elements are used. These benchmarks examples help to gain confidence in the FEM results.

Afterwards, 3D FE models of the beam-to-column joint subject to the loss of the column due to a localised fire are developed in Abaqus and calibrated against three experimental tests. The global behaviour of the composite steel-concrete joint in Abaqus is accurately modelled, the joint failure is easily approximated and accurate deformation predictions up to failure is provided at ambient and elevated temperatures (700ºC in the beam bottom flange). These FE models allow assessing the detailed behaviour throughout the entire robustness scenario, including stresses, extensions, deformations, etc….

In the model of test 6 (700ºC and K_a = 50 kN/mm), some discrepancies appear for the loads measured at the column top and at the beam axial restraint, and higher resistance is provided by the FE model. This is justified by the creep effects that may affect the deformation of the frame and the reaction loads during the experimental test, mainly for test 6 subject to the influence of the beams axial restraints. The creep effects are not modelled in the FE model and should be considered in further developments.

In the next chapter, the FE models are used to investigate the influence of various parameters (temperature, beam axial restraint K_a, beam span length, etc…) on the fire response of the joint, and the combined bending moment and axial loads in the joint is studied in details.

Chapter 5

5 M-N behaviour of joints

5.1 Introduction

Under extreme loading, joints play an important role in providing ductility and resistance for steel-composite structures. Once the column fails, the joint suffers a vertical displacement downwards, and its bending moment changes from hogging (M^-) to sagging (M^+) bending moment. The joint is also subject to axial loads created by the beam axial restraints coming from the unaffected part of the building. Under fire scenario, additional loss of joint resistance due to elevated temperatures needs to be considered, and the joint is subject to combined bending moment, axial loads and temperatures. Once the sub-frame reaches large deformations without failure, catenary action is developed in the frame and the joint is subject to tensile loads. Therefore, joints need i) ductility (rotation capacity) to accommodate large deformations without failure and ii) resistance to be able to sustain the new loading.

The objective of the study presented in this chapter is to provide additional information on the joint behaviour at failure when it is subject to sagging bending moments, axial loads and elevated temperatures after the loss of a column due to a localised fire. The behaviour of the joint is analysed based on numerical and analytical results. The FE models presented in chapter 4 are used for the study. Due to the complexity of the 3D numerical model and its time-consuming, the analytical procedure developed at the University of Liège (Demonceau *et al.*, 2013) is also employed to predict the M-N curves of joints. This analytical procedure is presented in detail at the beginning of this chapter, and its applicability to steel and composite joints at elevated temperatures is demonstrated. Finally, based on the results, it is expected to enlarge knowledge of the effect of some parameters that influence the robustness of tall open car park buildings.

5.2 Analytical procedure to predict the M-N behaviour of joints

5.2.1 Introduction

The component model, presented in EN 1993-1-8 (2005) and EN 1994-1-1 (2004), provides an analytical method to design steel and composite joints subject to pure bending moment solicitations. This method is based on the assumption that the axial force N_{Ed} in the connected member does not exceed 5% of the design resistance $N_{pl,Rd}$ of its cross-section. The University of Liège developed an analytical procedure, based on the component model, which is able to evaluate the nonlinear response of steel and composite steel-concrete joints subject to bending moments, axial loads and elevated temperatures. The analytical procedure only considers the joint at failure, and the entire M-N curve of any bolted beam-to-column joint can be drawn. This procedure was first developed for steel joints (Cerfontaine, 2004), then it was adapted for composite steel-concrete joints (Demonceau, 2008) and finally enlarged for steel and composite joints subject to elevated temperatures (Demonceau *et al.*, 2013).

The methodology for steel joints, composite steel-concrete joints and joints subject to elevated temperatures is described in this section. In the next section (5.3), its applicability to steel and composite joints subject to elevated temperatures is demonstrated by two examples.

5.2.2 M-N behaviour of steel joints

5.2.2.1 Introduction

The analytical procedure to define the M-N curve of steel joints is presented in the following section. The theoretical considerations are illustrated throughout the text by an example of application to a steel connection tested by Santiago (2008). In Santiago (2008), experimental and numerical results are provided for six beam-to-column sub-frames subject to a natural fire. The sub-frame was composed by two thermally insulated steel columns (HEA 300 cross-section of steel grade S355) and an unprotected beam (IPE 300 cross-section of steel grade S355) with 5.70 m free span, supporting a concrete slab. The objective was to evaluate the behaviour of various typologies of steel joints under a natural fire and their influence on the structural global behaviour. In the present work, the flush end-plate joint typology FJ03 is considered, with end-plate 16 mm thick of steel grade S275 and two bolt rows M20, grade 8.8 (Figure 5.1a).

5.2.2.2 M-N curve

The analytical procedure is in full agreement with the Eurocode component model (EN 1993-1-8, 2005), and it is based on the assumption that all the components activated at failure are fully ductile: a plastic redistribution of the forces is considered within the joint without any displacement limitations.

In the method, the connection is divided into different rows: some of them can be activated in tension (at the level of each bolt row), others in compression (at the level of the beam flanges axes). Each row is numbered from the top to the bottom; Figure 5.1b depicts the 4 rows defined for the FJ03 connection: 1) beam top flange (BTF), 2) 1st bolt row, 3) 2nd bolt row, and 4) beam bottom flange (BBF). The position of each row is defined in relation to a reference axis, by the distance h_i (from the reference axis to row i). This reference axis corresponds to the point where axial load and bending moments are assumed to be applied (here at mid-height of the steel beam profile), and the distance h_i is considered positive for rows above this axis, and negative for rows below.

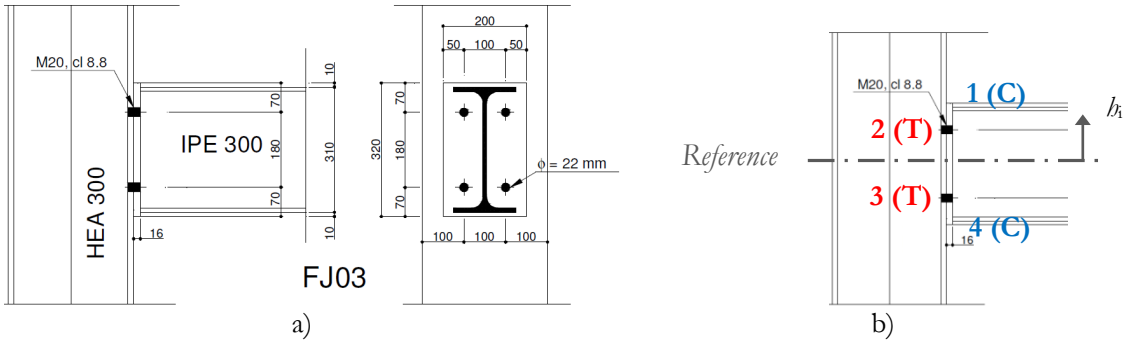

Figure 5.1: a) Geometry of the flush end-plate joint FJ03 (Santiago, 2008); b) Identification of the rows and position of the reference axis

The resistance of a row is defined by the weakest basic component resistance involved in the row, and the resistance of each basic component is calculated according to the formulas provided by EN 1993-1-8 (2005). Table 5.1 presents the resistance of each component involved in the rows of the example; these values are calculated with all safety factors equal 1.0 and using the ultimate strengths obtained from tensile tests (Santiago, 2008). The resistances are limited by: i) column web in compression (CWC) for rows in compression (1 and 4), and ii) end-plate in bending (EPB), mode 2, for rows in tension (2 and 3).

The resistance of the group defined by rows 2 and 3 is lower than the sum of each separated resistance, which means that the failure in tension is governed by the group resistance. Under pure hogging bending moment (M^-), row 2, in tension, should be the most loaded in order to provide the highest value of hogging bending moment resistance: $F^-_{Rd,2}$ = 297 kN, and the resistance of row 3 is defined by the group resistance: $F^-_{Rd,3}$ = 575 - 297 = 279 kN, where $F^-_{Rd,i}$ is the ultimate resistance of row i, defined under M^-. Under pure sagging bending moment (M^+), row 3 is the most loaded; Table 5.2 presents the resistance of each row, F^-_{Rd} and F^+_{Rd}, considering group effects, under hogging and sagging bending moments, respectively.

Table 5.1: Resistances of all the components in the steel joint (kN)

Row		h_i (mm)	***CWC***	BFC	CWS	CFB	***EPB***	CWT	BWT	BT
1 (top)	C	145	***605***	1073	956					
2	T	90				368	***297***	593	850	368
3	T	-90				368	***297***	593	850	368
Group 2-3	*T*					*736*	***575***	*1166*	*1540*	*736*
4 (Bottom)	C	-145	***605***	1073	956					

C = compression / T = tension

Table 5.2: Resistance of each row considering the group effects

Row	h_i (mm)	Under M^- F_{Rd}^- (kN)	Under M^+ F_{Rd}^+ (kN)	Weakest components
1	145	605	605	CWC
2	90	297	576-297 = **279**	EPB
3	-90	576-297 = **279**	297	EPB
4	-145	605	605	CWC

When the connection is subject to a combination of bending moment and axial force, a row is activated or not, depending on the position of the neutral axis, and whether the upper rows are in tension or in compression. The activated rows can easily be determined, depending of the position of the neutral axis. In the method, these activated rows are supposed to sustain a force equal to their resistance (plastic redistribution), while the other rows sustain a force equal zero. The neutral axis position is chosen between the top and the bottom of the joint (e.g. upper row 1, then between rows 1 and 2, then between rows 2 and 3, etc…). For each position of the neutral axis, the corresponding loading (M, N) can be calculated using the equilibrium equations (Eq. 5.1) (Demonceau *et al.*, 2013).

$$N = \sum_{\text{activated rows i}} F_{Rd,i} \qquad \text{and} \qquad M = \sum_{\text{activated rows i}} F_{Rd,i} \times h_i \qquad \text{(Eq. 5.1)}$$

where $F_{Rd,i}$ is the force sustained by row *i*, and h_i is the distance between row *i* and the reference axis. Table 5.3 presents the calculation of bending moment and axial force resistances for various chosen position of the neutral axis. Each position provides a point (M,N) of the curve (*a, b, c, d, e* under M^+, and *a, b', c', d', e'* under M^-). As in previous chapters, the resistance of each row is defined positive in compression, and negative in tension.

Figure 5.2 presents the two M-N interaction curves, under sagging and hogging bending moments; the load distribution in the connection is also represented at each point. The ductile resistance interaction diagram derived from this procedure corresponds to a plastic resistance surface, and the joint can resist to any couples (M_{Ed}, N_{Ed}) remaining inside this surface. For any point of the curve, the failure of the connection is assumed when the forces in the rows cannot increase anymore, except in one row *k*; it is assumed that this failure is reached when the last row (other than row *k*) reaches its ultimate resistance F_{Rd}

(Cerfontaine, 2004). This last row defines the ultimate failure mode (UFM) of the connection. Cerfontaine (2004) observed that the slope of any segment of the M-N curve corresponds to the lever arm h_k, and for each one, the load in row k varies from 0 to its maximum resistance $F_{Rd,k}$.

Table 5.3: Calculation of bending moment and axial force resistances for various positions of the neutral axis

		Under M^-					Under M^+				
Row	h_i (mm)	*a*	*b'*	*c'*	*d'*	*e'*	*a*	*b*	*c*	*d*	*e*
1	145	605	0	0	0	0	605	605	605	605	0
2	90	0	0	-297	-297	-297	0	0	0	-279	-279
3	-90	0	0	0	-279	-279	0	0	-297	-297	-297
4	-145	605	605	605	605	0	605	0	0	0	0
	M (kNm)	0	-88	-114	-89	-2	0	88	114	89	2
	N (kN)	1210	605	308	30	-575	1210	605	308	30	-575

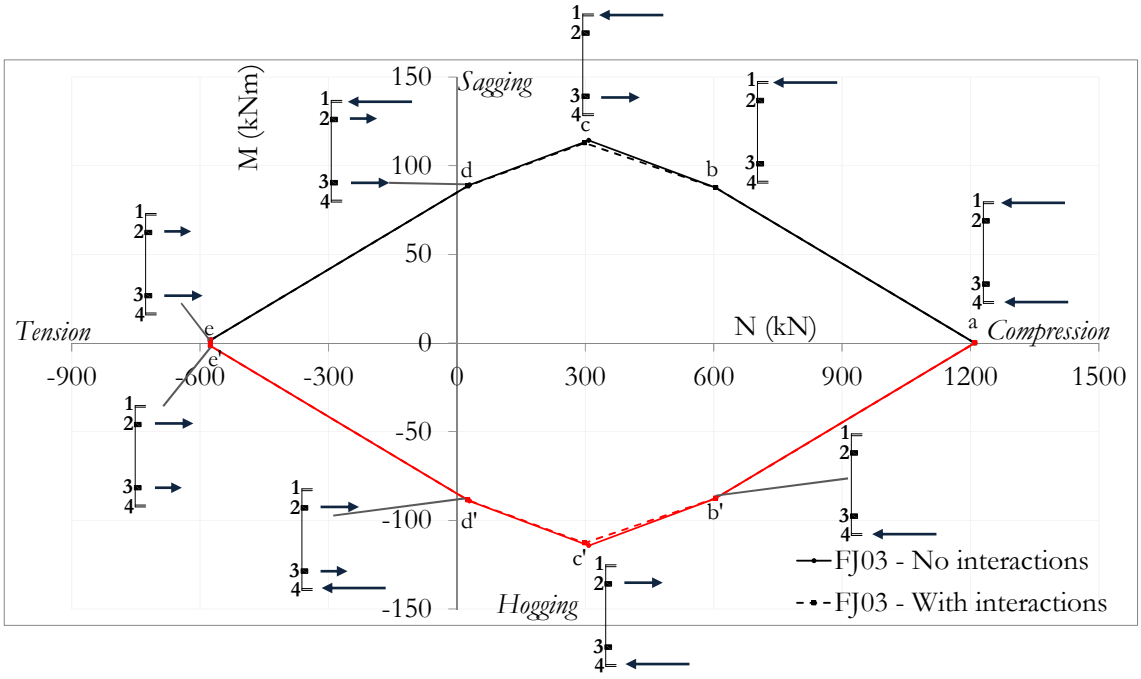

Figure 5.2: M-N curve of the steel connection FJ03 under M^- and M^+

Note that under pure tension (N = -575 kN), the ends of both curves are not coincident (points *e* and *e'*) because the bending moments are different (2 kNm and -2 kNm, respectively). This difference provides from the changing load distribution in bolt rows 2 and 3 under M^- and M^+, because of the group effects (see Table 5.3). As the lever arms (h_2 = 90 mm and h_3 = -90 mm) are kept constant, two different values of bending moments are obtained.

The (*M,N*) point of the curve corresponding to pure M^+ is on the segment *e-d* (Figure 5.2). On this segment, the ultimate resistances of rows 2 and 3 are reached, and the load in

row 1 varies from 0 (point *e*) to $F_{Rd,1}^{+}$ (point *d*). So, under pure M^{+}, the ultimate resistance of row 1, $F_{Rd,1}^{+}$, is not reached, and row 1 corresponds to row *k* defined by Cerfontaine (2004): row 1 is the only row where forces could increase more, but its value is limited to verify the equilibrium of (Eq. 5.2). Table 5.4 depicts the load distribution under pure M^{-} and M^{+} deduced from the M-N curve (segments *d-e* and *d'-e'*). Failure is defined by the last row to have reached its ultimate resistance: the group of bolts in tension (rows 2 and 3). So the component associated to the joint failure is EPB.

$$N=0=\sum_{F_{Rd,i}>0} F_{Rd,i} + \sum_{F_{Rd,i}<0} F_{Rd,i} \qquad \text{(Eq. 5.2)}$$

Table 5.4: Load distribution and ultimate failure modes (UFM) under pure bending moment

	Under pure M^{-} F_{Rd}^{-} (kN)	Under pure M^{+} F_{Rd}^{+} (kN)
Load distribution	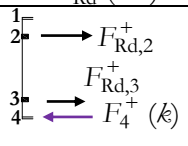	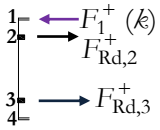
UFM	EPB	EPB

The same calculations can be performed along the entire M-N curve, and ultimate failure modes (UFM) are indicated in Figure 5.21 (CWC in segments *a-d* and *a-d'*, and EPB in segments *d-e* and *d'-e'*). The simplified procedure to define the UFM provides good results because the connection is limited to one row in compression with one load in tension (group of rows 2 and 3). Cerfontaine (2004) also defined a general approach to predict the failure mode of the connection based on its rotation at failure. However, this approach is not yet adapted for composite joints or joints at elevated temperatures; it is not used, neither presented in the current thesis, but a brief description is shown in Appendix E.1, illustrated by an example.

If some components do not have a ductile behaviour (such as bolt in tension), the reduction of resistance can be considered along the entire M-N curve; more details can be found in Cerfontaine (2004). In the example, all the components linked to failure are considered ductile, so no fragile failure is expected, and the M-N curve is not modified.

5.2.2.3 Effect of stresses interactions

Interaction phenomenon between shear, normal and axial loads in the column can affect the resistance of its components: i) CWC, and ii) CWT (EN 1993-1-8, 2005). The effect of these interactions on the M-N curve is noticeable when the resistance of a row depends of one of these components (Cerfontaine, 2004). The level of interaction depends of the applied loads and of the load distribution in the connection. So an iterative calculation is needed for each point of the M-N curve where the components resistance is affected by these interactions.

Interactions between shear and axial loads

The resistance of the web panel under compression (CWC) or tension (CWT) can be reduced by the presence of shear.

Under compression, the resistance of the component CWC is given by (Eq. 5.3) (EN 1993-1-8, 2005). In the example, the resistances of both rows 1 and 4 in compression depend of this component CWC; interactions need to be considered.

$$F_{c,wc,Rd} = \frac{\omega k_{wc} b_{eff,c,wc} t_{wc} f_{y,wc}}{\gamma_{M0}} \leq \frac{\rho \omega k_{wc} b_{eff,c,wc} t_{wc} f_{ywc}}{\gamma_{M1}} \quad \text{(Eq. 5.3)}$$

In (Eq. 5.3), $b_{eff,c,wc}$ is the effective width of column web in compression, ρ is the reduction factor for plate buckling, k_{wc} is a reduction factor due to the longitudinal compressive stress in the column (see next sub-section), and ω is the reduction factor to allow for the possible effects of interaction with shear in the column web panel. This reduction factor ω depends of the transformation parameter β that reflects the importance of shear in the column web panel at the point where the column web is under compression. For a single-sided joint, the shear load can be calculated by (Eq. 5.4). Where M_b is the applied bending moment at the beam, and z is the distance between the centre of compression and the centre of tension; z is defined by Cerfontaine (2004) in Table 5.5. The transformation parameter β is provided by (Eq. 5.5) (obtained from (Eq. 5.4), where $M_b = F_{Ed} \times z$), and for a beam-to-column connection subject to combined bending moment and axial load, the mean shear V_{Ed} can be calculated by (Eq. 5.6). In this equation, the compression loads F_{Ed} and N_b coming from the bending moment M_b and the axial load (distributed between the top and bottom flanges), respectively, are considered.

$$V_{Ed} = \beta \frac{M_b}{z} \quad \text{(Eq. 5.4)}$$

$$\beta = \frac{V_{Ed}}{F_{Ed}} \quad \text{(Eq. 5.5)}$$

$$V_{Ed} = \frac{M_b}{z} + \frac{N_b}{2} \quad \text{(Eq. 5.6)}$$

In the example (steel connection FJ03), the verification of interactions at point *c* of the M-N curve (M^+) is detailed in Table 5.6. This process is repeated, and after a second iteration, the new reduced resistance of row 1 in compression is $F_{Rd,1}^{new2}$ = 595.5 kN. Table 5.7 provides the corrected value of bending moment and axial load for the whole curve (the new resistance values are underlined). The M-N curve is still perfectly symmetrical under sagging and hogging bending moments (see dashed lines in Figure 5.2).

Table 5.5: Definition of z (Cerfontaine, 2004)

Under bending moment and axial load	$z = \left\lvert h_{eq}^{+} - h_{eq}^{-} \right\rvert = \left\lvert \frac{\sum_{i=1}^{n}{}_{Fi>0} h_i F_i}{\sum_{i=1}^{n}{}_{Fi>0} F_i} - \frac{\sum_{i=1}^{n}{}_{Fi<0} h_i F_i}{\sum_{i=1}^{n}{}_{Fi<0} F_i} \right\rvert$
Under pure compression	$z = h_{\text{top flange}} - h_{\text{bottom flange}}$
Under pure tension (the lever arm is obtained by taking the distance from the farthest row in tension *j*, to a point that considers all the other rows in tension *i*)	$z = \left\lvert \frac{\sum_{i=1}^{n}{}_{Fi>0, i\neq j} h_i F_i}{\sum_{i=1}^{n}{}_{Fi>0, i\neq j} F_i} - h_j \right\rvert$

Table 5.6: Details of the first iteration to consider the interactions shear-axial load in the column web in compression (point *c* of the M-N curve of the example)

Lever arm z	$z = 145 + 90 = 235$ mm.
Mean shear V_{Ed}	$V_{Ed} = \frac{M_b}{z} + \frac{\mathbf{N}_b}{2} = 641$ kN
Transformation parameter β	$\beta = \text{abs}\left(\frac{V_{Ed}}{F_{Ed}}\right) = \frac{641}{605} = 1.06$
Reduction factor ω (EN 1993-1-8)	$\omega = 0.83$
Resistance of the column web in compression calculated with the new value ω	$F_{wc,Rd} = F_{Rd,1,new}^{+} = 595.3$ kN.
Corrections of bending moment and axial load values	$\Delta M_{c,1} = h_1\left(F_{Rd,1,new}^{+} - F_{Rd,1}^{+}\right) = -1.41$ kNm $\Delta N_{c,1} = F_{Rd,1,new}^{+} - F_{Rd,1}^{+} = -0.01$ kN

Table 5.7: Load distributions for the particular points of the M-N curve considering the stresses interactions

	h_i	Under M^-					Under M^+				
Row	(mm)	*a*	*b′*	*c′*	*d′*	*e′*	*a*	*b*	*c*	*d*	*e*
1	145	605	0	0	0	0	605	605	595.5	601	0
2	90	0	0	-297	-297	-297	0	0	0	-279	-279
3	-90	0	0	0	-279	-279	0	0	-297	-297	-297
4	-145	605	605	595.5	601	0	605	0	0	0	0
	M (kNm)	0	-88	-113	-89	-2	0	88	113	89	2
	N (kN)	1210	605	299	26	-575	1210	605	299	26	-575

The component CWT (bolt rows in tension) should also be checked considering shear and axial interactions. This resistance depends of the coefficient ω (see EN 1993-1-8, 2005), calculated as for the CWC component. In the example, the resistance of CWT is higher than the resistance of EPB, and interactions do not affect the (*M,N*) results.

Interactions between axial and normal loads

For the column web in compression component, the effect of the normal stresses coming from axial loading of the column, combined with bending, is considered by the reduction coefficient $k_{wc}=f(\sigma_{com,Ed})$. This coefficient considers the possible instability of the column web panel under combined compression loads. This possible reduction of resistance has to be checked for all the M-N curves; in this example, the resistance of the connection is not affected.

5.2.3 M-N behaviour of composite steel-concrete joints

5.2.3.1 Components of the concrete / composite slab

In composite steel-concrete joints, two main components from the concrete/composite slab can be activated: i) under hogging bending moment (top row in tension): longitudinal steel reinforcement in tension; ii) under sagging bending moment (bottom row in tension): concrete/composite slab in compression. The component *longitudinal steel reinforcement in tension* (RT) is defined by EN 1994-1-1 (2004), and this component is considered like a bolt-row in tension in the component method.

The resistance of the component *concrete/composite slab in compression* (CSC) is defined in Demonceau (2008) by (Eq. 5.7), assuming a rectangular stress distribution:

$$F_{Rd,conc}=b_{eff,conn}\, z_{conc} f_{cd} \qquad \text{(Eq. 5.7)}$$

Where f_{cd} is the design value of the cylinder compressive strength of concrete $f_{cd}=\frac{f_{ck}}{\gamma_c}$, f_{ck} is the characteristic value of the cylinder compressive strength of concrete at 28 days, and γ_c is the partial factor for concrete; z_{conc} and $b_{eff,conn}$ are thickness and width, respectively, of the concrete/composite slab that contributes to the joint behaviour. The width $b_{eff,conn}$ is defined in Demonceau (2008) by (Eq. 5.8):

$$b_{eff,conn}=b_c+0.7h_c\leq b_{eff} \qquad \text{(Eq. 5.8)}$$

Where b_c is the width of the column cross-section, h_c is the height of the column cross-section, and b_{eff} is the effective width of the concrete/composite slab in the vicinity of the joint. This formula was initially developed for composite single-sided joints under seismic conditions, based on a strut and tie model (Doneux, 2002). Demonceau (2008) showed that under accidental conditions, good results are obtained for both single and double sided

joints when considering the concrete width $b_{eff,conn}$ defined by (Eq. 5.8). The height z_{conc} can be defined using the Richard Liew *et al.* (2004) expression (Eq. 5.9).

$$z_{conc} = \frac{\sum_{i,\ \text{for}\ F<0} F_{Rd,i}}{b_{eff,conn}\ f_{cd}} \leq h_{concrete} \qquad \text{(Eq. 5.9)}$$

Where $F_{Rd,i}$ is the design resistance load of the component *i* activated in tension, and $h_{concrete}$ is the total height of the concrete slab (or the height of the concrete above the ribs in case of a composite slab). To define the bending moment resistance, the centre of compression is considered at the middle of the concrete height z_{conc}.

5.2.3.2 M-N curve

The same method than for steel joints is considered to define the (M, N) curves of the joint at failure, using (Eq. 5.1). Figure 5.3 presents the composite joint studied in the current thesis, with the identification of the rows. The thickness of the composite slab z_{conc} to be considered in the calculation is limited to the part of the concrete above the transversal ribs. This concrete thickness is separated in two parts by the steel reinforcement: row 1a above the steel reinforcement and row 1b below. This separation is considered to simplify the application of the method and the drawing of the M-N curve, but the concrete component is always considered like one single component for the calculation of its properties. The reference axis is chosen at the centroid of the steel beam, as considered for the experimental tests (see chapter 3).

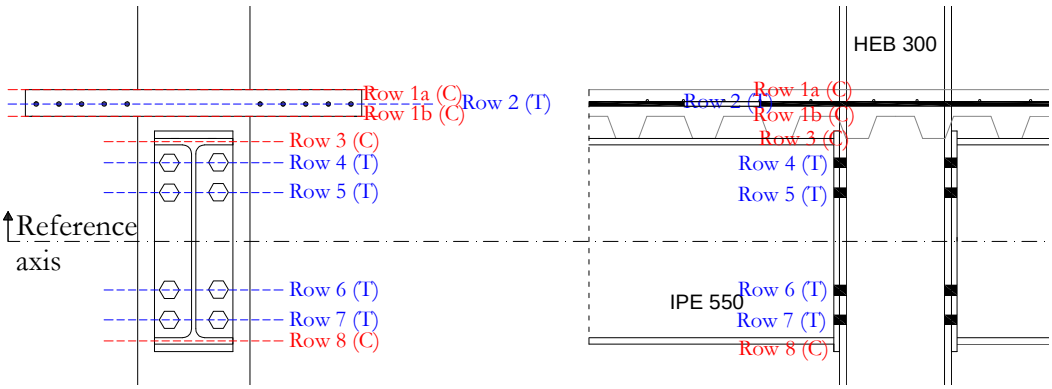

Figure 5.3: Composite steel-concrete joint CFJ and rows in tension (T) and in compression (C)

The resistances of the components under M^+ are shown in Table 5.8 (components resistances under hogging bending moment can be found in Appendix E.2); lines in grey correspond to the group resistances. Based on the assumption that equal bending moments are applied on each side of the double sided joint, no shear forces are considered in the column web, so no interactions of stresses should be considered. The final resistances of the rows, considering the group resistances, are given in Table 5.9.

Table 5.8: Components and group resistances (kN) under M^+ (bottom row in tension)

Row		h_i (mm)	Compression			Tension					
			CSC	CWC	BFC	CFB	EPB	CWT	BWT	BT	RT
1	C	370	**1331**	1430							
2	T	371									**565**
3	C	266		**1406**	2723						
4-7	T					3107	**1734** (FM*1)	4283	4378	4218	
4-6	T					2454	**1476** (FM1)	3777	3728	3163	
4-5	T					1552	**861** (FM1)	2135	2174	2109	
4	T	210				899	**651** (FM2)	1629	1695	1054	
5-7	T					2454	**1476** (FM1)	3777	3728	3163	
5-6	T					1802	**1219** (FM1)	3272	3078	2109	
5	T	130				899	**603** (FM1)	1629	1524	1054	
6-7	T					1552	**861** (FM1)	2135	2174	2109	
6	T	-130				899	**603** (FM1)	1629	1524	1054	
7	T	-210				899	**651** (FM2)	1629	1695	1054	
8	C	-266		**1406**	2723						

* FM: Failure mode of the T-stub (1, 2 or 3)

Table 5.9: Final resistances of each row considering the group effects

Row	h_i (mm)	Under M^- F_{Rd}^- (kN)	Under M^+ F_{Rd}^+ (kN)	Weakest components
1	370	**1331**	**1331**	CSC
2	371	**-565**	**-565**	RT
3	266	**1406**	**1406**	CWC
4	210	**-651**	-Min (651; 861-603; 1476-603-210; 1734-603-210-651) = **-257**	EPB
5	130	-Min (603; 861-651) = **-210**	-Min (603; 1219-210; 1476-210-651) = **-603**	EPB
6	-130	-Min (603; 1219-210; 1476-210-651) = **-603**	-Min (603; 861-651) = **-210**	EPB
7	-210	-Min (651; 861-603; 1476-603-210; 1734-603-210-651) = **-257**	**-651**	EPB
8	-266	**1406**	**1406**	CWC

The lever arm h_1 of the composite slab in compression component (row 1) is equal to the distance between the reference axis and half of the thickness z_{conc}. Both values, h_1 and z_{conc}, vary when the neutral axis is located in the concrete component (see Figure 5.4), and they should be determined for each point of the M-N curve. Table 5.10 presents the calculation of the concrete resistance for variable thickness z_{conc}. Under M^+, when the neutral axis is going up, the thickness z_{conc} reduces and the lever arm h_1 increases. Table E.7, in Appendix E.2, presents the results under M^-.

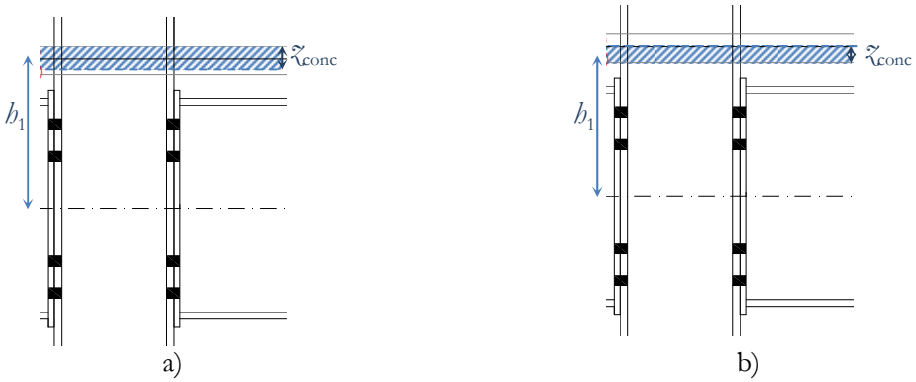

Figure 5.4: Variation of the thickness z_{conc} of the CSC component when the joint is subject to (a) M^+ and (b) M^-

Table 5.10: Sagging bending moment - resistance of row 1 $F_{Rd,1}$ varying with the thickness z_{conc} of the concrete slab in compression

	h_1 (mm)	$z_{conc,a}$ (mm)	$z_{conc,b}$ (mm)	z_{conc} (mm)	$F_{Rd,CSC}$ (kN)	$F_{Rd,CWC}$ (kN)	$F_{Rd,1}$ = min ($F_{Rd,CSC}$; $F_{Rd,CWC}$)
Row 1a and 1b in compression	**370**	34	37	71	1331	1430	**1331**
	374	34	27.75	61.75	1158	1403	**1158**
	379	34	18.5	52.5	984	1376	**984**
	383	34	9.25	43.25	811	1348	**811**
Row 1a in compression	**388**	34	0	34	637	1319	**637**
	392	25.5	0	25.5	478	1292	**478**
	397	17	0	17	319	1265	**319**
	401	8.5	0	8.5	159	1238	**159**

Finally, the M-N curve can easily be drawn step-by step (Figure 5.5). The load distribution at each point of the entire M-N curve is also represented. Table 5.11 presents the load distribution in the connection for all the points of the M-N curve under M^+; the same table is detailed in Appendix E.2 under M^-.

As the joint configuration is not symmetrical in relation to the chosen reference axis (because of the composite slab on the top), the M-N behaviour under M^+ and M^- is different. Minimum tensile load and maximum compression load are reached for a bending moment not equal to 0, because the centres of tension and compression of the joint do not correspond to the reference point (see the load distribution in Figure 5.5). Under minimum tensile load, two different values of bending moments are obtained (points j and j') due to the group effects in bolt rows.

It is important to note that the analytical procedure provides a theoretical M-N curve of the joint behaviour, with the assumption that the components behaviour is ductile and allows for a plastic distribution. Demonceau (2008) observed through experimental tests on beam to column joints, that a lack of ductility of the concrete component (crushing in compression) can lead to a loss of resistance. However, criterion to define the ductility of

the concrete component in compression is not yet available, and it is assumed that this component is of high ductility.

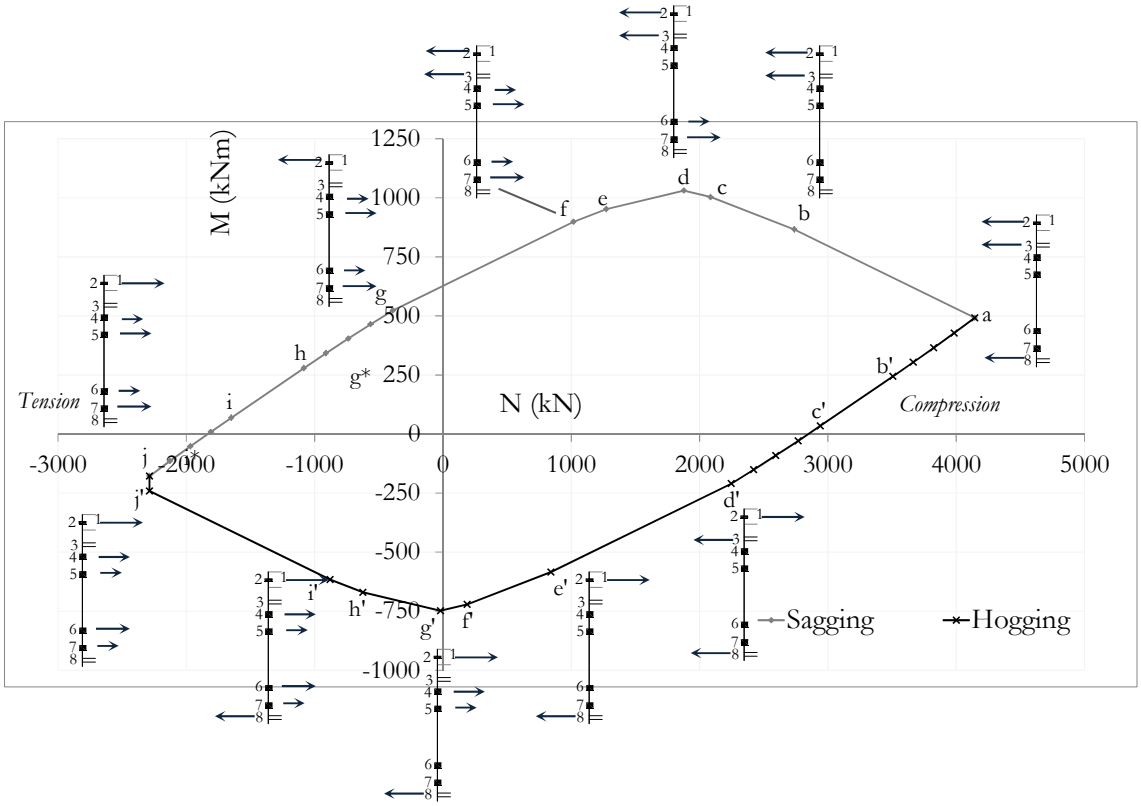

Figure 5.5: M-N curve of the composite steel-concrete joint CFJ

Table 5.11: Distribution of internal loads in the joint along the M-N curve under M^+

R	h_i (mm)	F^+_{Rd} (kN)	*a*	*b*	*c*	*d*	*e*	*f*	*g*	*g**	*h*	*i*	*i**	*j*
1		***F*i**	*1331*	*1331*	*1331*	*1331*	*1331*	*1331*	*1331*	***1158***	***637***	*637*	***478***	***0***
		***h*i**	*370*	*370*	*370*	*370*	*370*	*370*	*370*	*374*	*388*	*388*	*392*	*405*
2	371	565	0	0	0	0	0	0	0	0	0	**-565**	-565	-565
3	266	1406	1406	1406	1406	1406	1406	1406	**0**	0	0	0	0	0
4	210	257	0	0	0	0	0	**-257**	-257	-257	-257	-257	-257	-257
5	130	603	0	0	0	0	**-603**	-603	-603	-603	-603	-603	-603	-603
6	-130	210	0	0	0	**-210**	-210	-210	-210	-210	-210	-210	-210	-210
7	-210	651	0	0	**-651**	-651	-651	-651	-651	-651	-651	-651	-651	-651
8	-266	1406	1406	**0**	0	0	0	0	0	0	0	0	0	0
		M (kNm)	492	866	1003	1030	952	898	523	465	279	69	9	-178
		N (kN)	4144	2737	2086	1877	1273	1016	-390	-564	-1084	-1649	-1809	-2287
		e (mm)	119	317	481	549	748	884	-1341	-824	-257	-42	-5	78

5.2.4 M-N behaviour of steel and composite steel-concrete joints subject to elevated temperatures

To predict the M-N behaviour of a joint subject to elevated temperatures, the same procedure can be applied provided the temperature distribution in the joint is known. Each component resistance is then evaluated based on the material resistance at its given temperature; this model was validated by comparison to the ROBUSTFIRE experimental results (using the temperature distributions measured during the tests) (Demonceau *et al.*, 2013). Two additional applications are developed in the following section (5.3) for steel and composite steel-concrete joints subject to elevated temperatures.

5.3 Demonstration of the applicability of the analytical procedure for steel and composite steel-concrete joints subject to elevated temperatures

5.3.1 Introduction

The last developments implemented in the analytical procedure, to consider the effect of elevated temperatures, were validated in Demonceau *et al.* (2013), against the experimental results presented in chapter 3 of this thesis. To be able to rely undoubtedly on the analytical results, and to use the analytical procedure in a wider study of the joint subject to fire, two additional demonstrations of its applicability are presented: i) against available experimental and FEM results of the steel flush end-plate joint FJ03 (see Figure 5.1 in section 5.2.2.2), subject to fire, bending-moment and axial loads (Santiago, 2008), and ii) against FEM results of the composite steel-concrete flush end-plate joint CFJ subject to 700ºC (test 3), presented in chapter 4.

The analytical M-N curves presented in this chapter consider: i) measured properties of the material, ii) ultimate resistance of the components f_u (to predict the real behaviour of the joint as in the experimental tests and the FE models), iii) safety factors equal to 1.0, and iv) reference axis located at mid-height of the steel beam cross-section.

5.3.2 Steel flush end-plate joint FJ03

The steel joint FJ03 is remembered in Figure 5.6a, and its analytical M-N behaviour at ambient temperature is detailed in section 5.2.2.2. The behaviour of the connection was studied during both heating and cooling phases in Santiago (2008); a FE model was developed and calibrated against the experimental results and good agreement was achieved. In this section, the analytical results are compared to the FEM results (Santiago, 2008). Joint temperatures measured during the experimental tests and applied in the FE model are shown in Figure 5.6b.

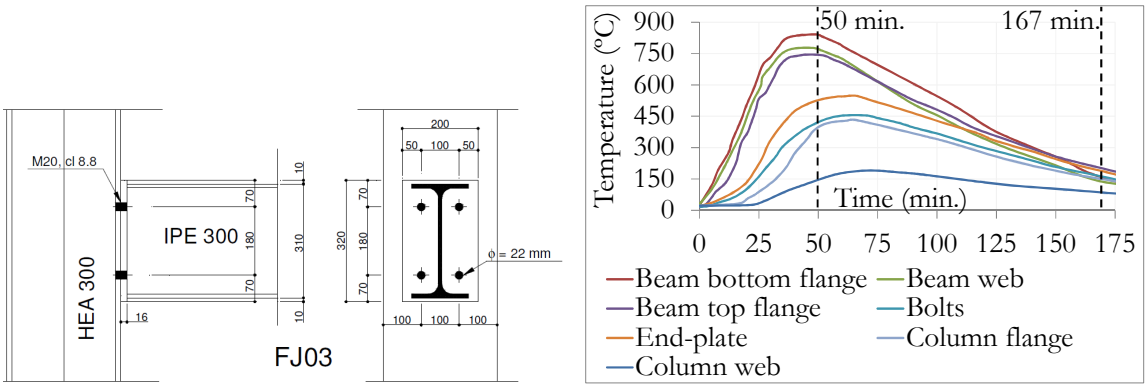

a) b)

Figure 5.6: a) Geometry of the flush end-plate joint (Santiago, 2008); b) Joint FJ03 temperatures *versus* time

Joint axial load and bending moment *versus* time predicted by the FEM results are shown in Figure 5.7. During the beginning of heating phase, compression axial loads and bending moment increase; when the bottom flange reaches about 500ºC, its resistance starts to decrease and the hogging moment and axial loads also decrease. Local buckling of the beam bottom flange (BBF) is observed when 750ºC is reached, at about 50 min. (red points in the charts). During the cooling phase, due to the large tensile forces and sagging bending moment (M^+), the tensile strains increase, and the bolt failure is observed in the bottom row (167 min.), which matches the experimental evidence (bolt failure at 190 min.) (Santiago, 2008). The measured material properties obtained from tensile tests at ambient and elevated temperatures are detailed in Santiago (2008).

For the analytical calculation, interactions between components in the column web, CWC and CWS, are considered (see section 5.2.2.3). Three M-N curves are derived: i) at ambient temperature (reference curve), ii) at the end of the heating phase, when the local buckling of BBF is observed in the FE model (50 min.), and iii) at the end of the cooling phase, when the failure in the bottom bolt row is predicted by the FE model (167 min.). Table 5.12 presents the resistances of each row F_{Rd}^- and F_{Rd}^+, under hogging and sagging bending moments respectively, and for the three M-N curves. These values are calculated based on the component method with reduced material properties due to elevated temperatures. In Figure 5.8 are drawn the analytical M-N curves, with the load distribution evolution at elevated temperatures (50 min.).

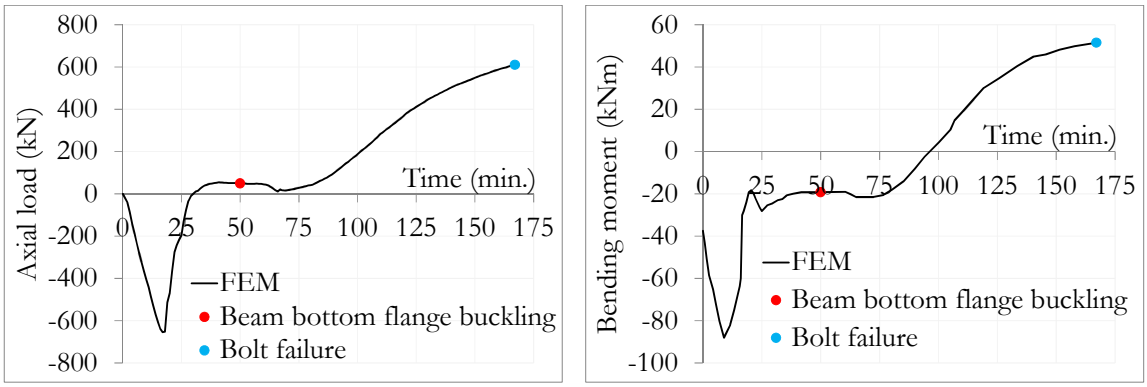

Figure 5.7: FEM results from (Santiago, 2008): a) axial load and b) bending moment, *versus* time

Table 5.12: Resistance of each row considering the group effects and stresses interactions (weakest component of each row)

Row	h_i (mm)	t = 0 (20°C)		t = 50 min.		t = 167 min.	
		F_{Rd}^{-} (kN)	F_{Rd}^{+} (kN)	F_{Rd}^{-} (kN)	F_{Rd}^{+} (kN)	F_{Rd}^{-} (kN)	F_{Rd}^{+} (kN)
1	145	605 (CWC)	605 (CWC)	229 (BFC)	229 (BFC)	585 (CWC)	585 (CWC)
2	90	-297 (EPB)	-279 (EPB)	-138 (BWT)	-112 (BWT)	-286 (EPB)	-268 (EPB)
3	-90	-279 (EPB)	-297 (EPB)	-112 (BWT)	-138 (BWT)	-268 (EPB)	-286 (EPB)
4	-145	605 (CWC)	605 (CWC)	99 (BFC)	99 (BFC)	585 (CWC)	585 (CWC)

The load distributions under pure bending moments at elevated temperatures (50 min.) are depicted in Table 5.13. Under pure M^+, the load in row 2 is lower than its ultimate resistance $F_{Rd,2}^{+}$, and it corresponds to the row *k* defined by Cerfontaine (2004) (see section 5.2.2.2). The total resistance of rows 2 and 3 in tension (BWT) is not achieved when row 1 (BFC) reaches its ultimate resistance. The increase of tensile loads is limited by the component in compression, thus the component associated to the joint failure is BFC; UFM along the entire M-N curve are depicted in Figure 5.8 (they are also defined according to the Cefontaine's method presented in Appendix E.1).

Under M^+, it is also observed in Figure 5.8 that a small axial compression load has a beneficial effect on the resistance, in comparison to pure sagging bending moment, because the neutral axis moves down. So when maximum sagging bending moment is reached, all the tensile loads are concentrated in row 3, far from row 1 in compression (row 2 is not anymore loaded). For axial compression loads higher than this maximum (N = 92 kN), tensile load in row 3 is reduced (row *k*); BFC component is the last component to reach its resistance, and defines the UFM of the joint. Any additional increase of axial compression load leads to a decrease of sagging bending moment resistance.

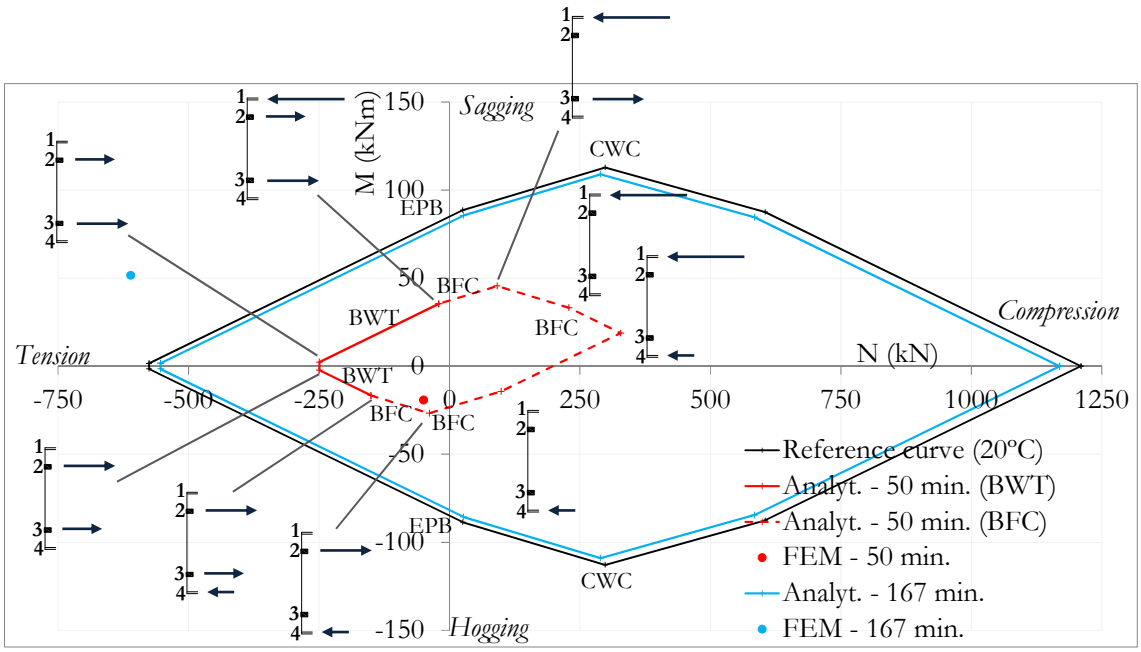

Figure 5.8: M-N curves of the steel flush end-plate joint FJ03 and load distribution evolution under elevated temperatures (50 min.)

Table 5.13: Load distribution and ultimate failure modes under pure bending moment (elevated temperatures – 50 min.)

	Under M^- F_{Rd}^- (kN)	Under M^+ F_{Rd}^+ (kN)
Load distribution	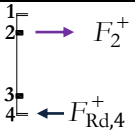	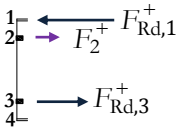
UFM	BFC (bottom)	BFC (top)

It can be observed that at ambient temperature and at the end of the cooling phase (iii - 167 min.), both M-N curves have symmetrical behaviour under M^+ and M^-. The analytical UFM of the joint varies between *EPB* (mode 2), when the joint is mainly subject to tensile loads or small compression loads, and *CWC* when the joint is subject to higher compression loads.

At elevated temperatures (ii – 50 min.), due to the gradient of temperature in the beam cross-section (higher temperatures in BBF), both beam flanges do not have the same resistance (see Table 5.12), and the behaviour of the joint under M^+ and M^- is changed (the M-N curve is not symmetrical anymore and the maximum compressive resistance is reached under positive bending moment).

FEM results at 50 min. and 167 min. are also shown in Figure 5.8 (by two points). At 50 min., the joint is subject to tensile axial loads and hogging bending moment, and both analytical and FEM results predict the failure of BBF in compression. The FEM result is inside the M-N curve and the connection is considered safe by the analytical predictions.

At 167 min., the analytical model predicts lower resistance of the joint than observed in the FE model. This is explained by the difference between failure criteria considered for FEM and analytical procedures; failure criteria is defined in term of: i) stresses f_u (EPB or bolt) in the analytical procedure, and ii) strains to fracture of bolts for the FEM.

5.3.3 Composite steel-concrete flush end-plate joint

In this section, the numerical results of test 3 (700ºC, K_a = 0 kN/mm) are used to demonstrate the applicability of the analytical procedure to predict the M-N behaviour of the composite joint CFJ at elevated temperatures. The joint CFJ is presented in Figure 5.3 (section 5.2.3), as well as the details used for its analytical M-N curve at ambient temperature. Figure 5.9 shows the temperature gradient used at the end of the FE model (see Appendix D 3.4) and considered in the analytical calculation. Table 5.14 describes the components considered in each row and their corresponding temperatures, and Table 5.15 presents the resistances of each row F_{Rd}^{-} and F_{Rd}^{+}, under hogging and sagging bending moments, respectively.

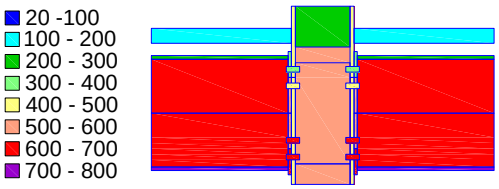

Figure 5.9: Temperature variation in the composite joint (test 3)

Table 5.14: Components considered in each row (temperature at the end of the FE model)

Row 1 (C)	CSC (θ = 198ºC)	CWC (θ = 241ºC)			
Row 2 (T)	RT (θ = 20ºC)				
Row 3 (C)	BFC (θ = 251ºC)	CWC (θ = 542ºC)			
Row 4 (T)	EPB (θ = 377ºC)	BT (θ = 337ºC)			
Row 5 (T)	EPB (θ = 529ºC)	BT (θ = 453ºC)	CFB	BWT	CWT
Row 6 (T)	EPB (θ = 594ºC)	BT (θ = 614ºC)	(θ = 476ºC)	(θ = 594ºC)	(θ = 542ºC)
Row 7 (T)	EPB (θ = 612ºC)	BT (θ = 626ºC)			
Row 8 (C)	BFC (θ = 727ºC)	CWC (θ = 542ºC)			

The M-N curve is drawn in Figure 5.10. Good agreement is observed between FEM and analytical results under pure sagging bending moment (difference of 8%). At this point, the analytical UFM corresponds to EPB (the load distribution and the failure mode under pure bending moment are depicted in Table 5.16). As explained in the steel joint example, failure is considered later in the FE model, when the bolt reaches strains to fracture. This point provides increased values of (M,N), because no descending branch in the material properties, or fracture definition are specified in the FE model. The experimental result is also shown in Figure 5.10 (red point), with a slightly higher bending moment value (see details of the comparison between FEM and experimental results in chapter 4).

Table 5.15: Final resistance of each row considering the group effects for CFJ at elevated temperatures (test 3)

Row	h_i (mm)	Under M^- F_{Rd}^- (kN)	Under M^+ F_{Rd}^+ (kN)	Weakest components
1	370	1273	1273	(CWC)
2	371	-565	-565	(RT)
3	266	865	865	(CWC)
4	210	-508	-250	(EPB)
5	130	-67	-325	(EPB)
6	-130	-198	-124	(EPB)
7	-210	-112	-186	(EPB)
8	-266	707	707	(BFC)

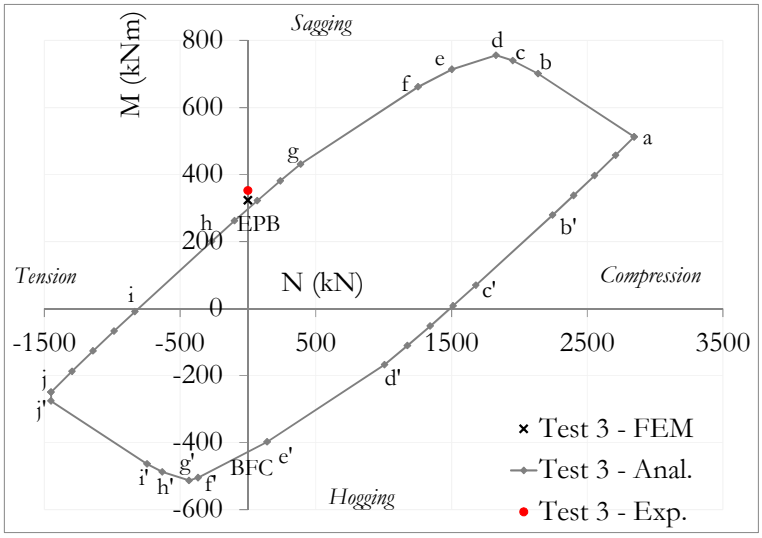

Figure 5.10: M-N curve at elevated temperatures (test 3)

Table 5.16: Load distribution and ultimate failure modes under pure bending moment (CFJ – test 3)

	Under M^- F_{Rd}^- (kN)	Under M^+ F_{Rd}^+ (kN)
Load distribution	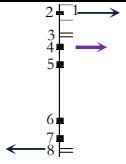	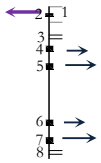
UFM	BFC	EPB

Note that some differences are observed between the analytical M-N curves developed within the ROBUSTFIRE project (Demonceau *et al.*, 2013) and the updated version of the curves presented in this chapter; these differences are due to i) the update of material resistances with available coupon tests and ii) the consideration of components' temperatures as in the FE models.

5.3.4 Final comments

The analytical procedure to predict the M-N interaction resistance of joints has been remembered in section 5.2. The procedure was developed for steel and composite steel-concrete joints at ambient or elevated temperatures (Cerfontaine, 2004; Demonceau, 2008; Demonceau *et al.*, 2013). The applicability of the procedure for steel and composite steel-concrete joints subject to elevated temperatures is demonstrated in this section 5.3, and it allows predicting the behaviour of any heated joint under sagging and hogging bending moments combined to tensile or compressive loads. In the next section (5.4), the influence of various parameters that would affect the building robustness by the joint behaviour is studied based on FEM results. The analytical procedure is also employed to complement the study and provide additional results.

5.4 Assessment of the influence of robustness parameters on the M-N joint behaviour

5.4.1 Introduction

This section presents a study of the joint robustness. The objective is to provide additional information on the joint behaviour at failure when it is subject to sagging bending moments, axial loads and elevated temperatures after the loss of a column due to a localised fire. Based on the results, it is expected to enlarge knowledge of the effects of some parameters that influence the robustness of tall open car park buildings. Four parameters are selected: i) temperatures in the joint, ii) beam axial restraint stiffness K_a, iii) joint size, and iv) beam span length. In addition, the influence of the safety considered during the joint design (design safety factors and material properties) is also evaluated. The study cases are listed in Table 5.17. Three joints configurations are used in the study: the composite flush end-plate joint (CFJ), the same joint but without the concrete (steel flush end-plate joint - SFJ), and the smaller steel flush end-plate joint (FJ03) described in sections 5.2.2 and 5.3.2. FEM and analytical results are used to perform the study.

Table 5.17: Overview of the parameters considered in the study

Parameter	Study cases	Type of results
Temperatures	i) CFJ (20°C, 500°C, 700°C and 800°C), ii) FJ03 (from 20°C to 838°C)	Analyt.
Axial restraints	CFJ under various tensile and compression axial loads - i) at 20°C, ii) at 700°C	FEM, Analyt.
Global size of a steel flush end-plate joint	i) IPE 550 (SFJ), ii) IPE 300 (FJ03), iii) variation from (Santiago, 2008): FJ01 and FJ02	Analyt.
Beam span length	i) 3 meters beam (20°C), ii) 10 meters beam (20°C)	FEM
Safety design	i) Measured material properties (20°C and 700°C) - no safety factors, ii) design resistances - with safety factors	Analyt.

5.4.2 Influence of the temperature variation in the joint

The influence of the temperature in the joint is studied based on analytical results. Both composite (CFJ) and steel (FJ03) flush end-plate joints are considered. The variation of temperatures in FJ03 has been shown previously in Figure 5.6 (section 5.3.2). The temperature distribution for CFJ is presented in Figure 5.11, and corresponds to BBF temperatures equal to: a) 500°C (test 2), b) 700°C (test 3), and c) 800°C (where temperature distribution in the joint is obtained by a linear interpolation of test 3 temperatures). The component BBF is in direct contact with the fire under the beam, so it is the component the most heated in a fire, and temperatures in the other components are usually lower.

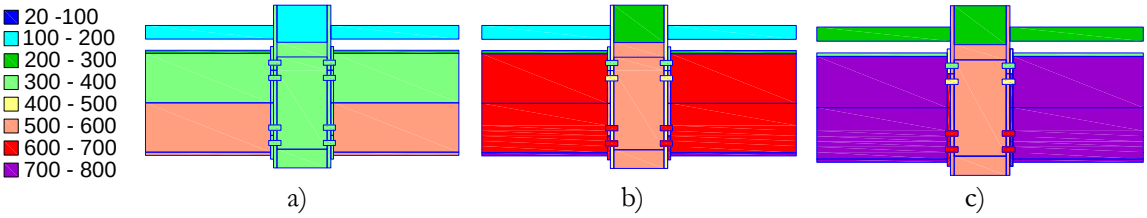

Figure 5.11: Temperature distribution in the composite joint: a) 500°C, b) 700°C, and c) 800°C in the beam bottom flange

The M-N interactions resistances of joints FJ03 and CFJ are depicted in Figure 5.12a and b respectively; BBF temperature is given as a reference.

For the steel joint FJ03 (Figure 5.12a), the increase of temperature affects the shape of the M-N curve: at ambient temperature, the M-N behaviour is symmetrical under sagging (M^+) and hogging (M^-) bending moments. When temperature increases and reaches 647°C in BBF (at 25 min. of fire), the M-N behaviour under M^- and M^+ is not anymore symmetrical: the resistance under M^- reduces faster than under M^+ because the component BBF in compression, only activated under M^-, suffers the greater loss of resistance.

For the composite joint CFJ (Figure 5.12b), the shape of the M-N curve remains similar with the increase of temperatures. Under 500°C in the BBF (Figure 5.11a), temperatures of most of the other components remain lower than 400°C (no resistance reduction), and the decrease of M-N resistances from 20 to 500°C is mainly due to the strain hardening, that is considered under 20°C, then unconsidered from 100°C (see material properties in chapter 4). At each point of the curve, the load distribution is shown in Figure 5.5.

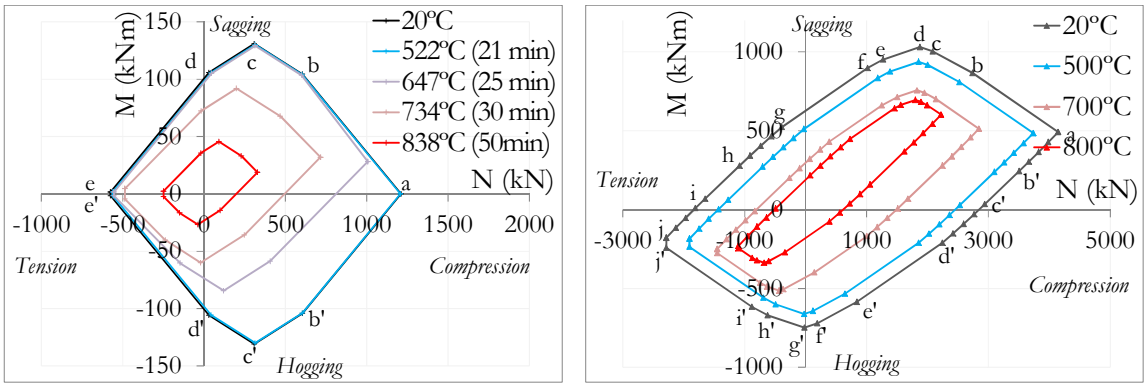

Figure 5.12: M-N curves for variable temperatures in the joint of: a) the steel flush end-plate joint FJ03, and b) the composite joint CFJ

The reduction of the global M-N resistance with the increase of temperature is obvious for both joints, FJ03 and CFJ. At maximum temperature:

i. The minimum hogging bending moment decreases by 80% and 53% (points *c'* and *g'*), respectively; this decrease of resistance is lower for CFJ because of the reinforcement in tension which is not significantly affected by the fire and keeps its ambient temperature resistance;
ii. The maximum sagging bending moment decreases by 66% and 35% for FJ03 and CFJ, respectively, which is lower than under hogging bending moment; this is due to the components in compression less heated under M^+ (beam top flange BTF for FJ03, and BTF and CSC for CFJ). So joints do not lose so much resistance than under M^- (where BBF is in compression);
iii. The maximum axial resistance in compression (point *a*) decreases by 73% and 48% for FJ03 and CFJ, respectively;
iv. The minimum axial resistance in tension (points *e* and *e'*) decreases by 60% and 48% for FJ03 and CFJ, respectively.

These comparisons show that the composite slab is an advantage to limit the decrease of resistance when temperatures increase.

Under pure bending moment, it is easy to predict the UFM, comparing the tensile and compressive resistances of the activated rows. Table 5.18 and Table 5.19 present the evolution of the load distribution as the temperature increases in the connections CFJ and FJ03 respectively (subject to pure M^- and M^+). Under pure M^-, the failures of the joints at ambient temperature are defined by EPB and CWC, for FJ03 and CFJ, respectively. When temperatures increase, the resistance of BBF decreases faster than the resistance of other components, and the component BBF in compression becomes the UFM, for both FJ03 and CFJ. Finally, at 800°C in CFJ, UFM changes to reinforcement in tension (RT) because it is the only component in tension, due to the movement of the neutral axis: its position goes up with temperatures increase, because the bottom rows in compression lose resistance much faster than the top rows in tension. Under pure M^+, at ambient

temperature, the UFM is EPB for both joints, but it changes to the compression zone as the temperatures increase: BFC and CSC, for FJ03 and CFJ, respectively.

Table 5.18: Load distribution in the composite joint CFJ under pure bending moment

	20°C	500°C	700°C	800°C
Under pure M^-	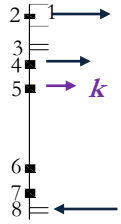	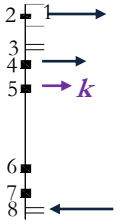	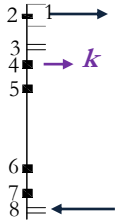	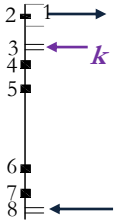
UFM	CWC	CWC	BFC	RT
Under pure M^+	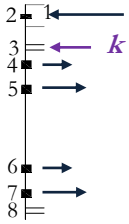	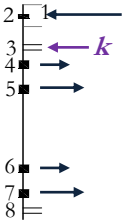	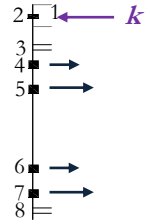	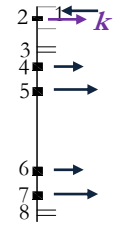
UFM	EPB	EPB	EPB	CSC

Table 5.19: Load distribution in the steel joint FJ03 under pure bending moment

	20°C	522°C	647°C	734°C	838°C
Under pure M^-	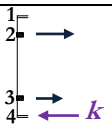	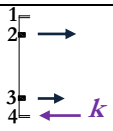	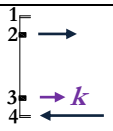	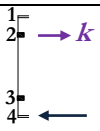	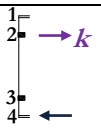
UFM	EPB	EPB	BFC	BFC	BFC
Under pure M^+	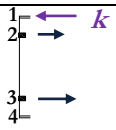	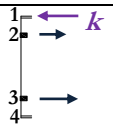	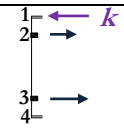	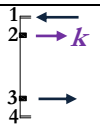	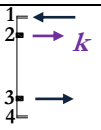
UFM	EPB	EPB	EPB	BFC	BFC

5.4.3 Influence of the beam axial restraints

5.4.3.1 Introduction

Once the column fails the joint bending moment changes from hogging to sagging bending moment, and axial loads increase. These axial loads influence the joint bending moment resistance as well as the rotation capacity. In this section, the effect of varying combined sagging bending moment and axial loads on the behaviour of the composite joint after the column loss is studied, at ambient and elevated temperatures:

i. The effect of the restraint is studied by varying the degrees of axial stiffness K_a in the two FE models of tests 1 and 6 presented in chapter 4. F-displacement, M-rotation and M-N curves of each FE model are presented.

ii. Based on the results obtained from FEM and analytical procedures, the whole M-N curves of the joint subject to ambient and elevated temperatures are drawn.

In the FE models, ductile failure of some components such as EPB or BWT happens after large deformations and it is difficult to capture it numerically. The failure criteria defined for the FE models correspond to the bolt failure in tension.

5.4.3.2 Behaviour of the composite joint under varying bending moments and axial loads

In both FE models at ambient and elevated temperatures (tests 1 and 6), various values of axial spring stiffness's are considered, varying from K_a = 0 kN/mm (no axial restraint) to K_a = 157 kN/mm, which corresponds to a realistic value calculated in the car park building subject to the loss of a column in the 4th floor (see Appendix B.1). Figure 5.13 and Figure 5.14 depict the bending moment *versus* joint rotation, and the bending moment *versus* beam axial load, respectively, at ambient (a) and elevated (b) temperatures. All the curves are stopped when the bottom bolt row reaches the fracture strains (defined in chapter 4).

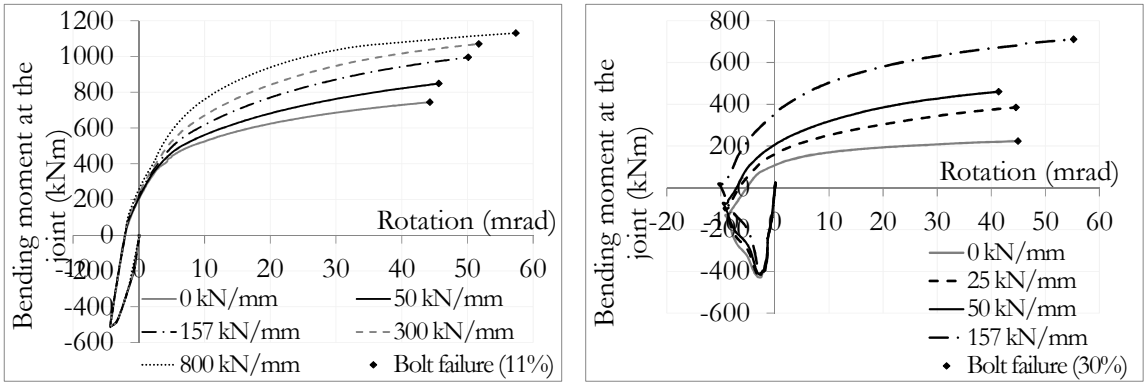

Figure 5.13: Bending moment - joint rotation a) at ambient and b) at elevated temperatures

At ambient temperature, the effect of the beam axial restraint can be observed in the sagging bending moment range, after the column loss: the beam end moves in the outward direction (geometrical effect due to the low slenderness of the composite beam – see chapter 3) and axial compression loads continue to increase until bolt failure. In order to observe if stiffer restraints would prevent outwards displacement of the beam end and create catenary action before bolt failure, FE models with stiffer axial restraints (K_a = 300 kN/mm and K_a = 800 kN/mm) are considered. However, it is shown that these stiffer axial restraints only increase the joint resistance; tensile loads are still not reached before bolt failure (Figure 5.14a). At elevated temperatures, axial compression loads develop earlier, during the increase of temperatures (due to the restrained thermal expansion); these compression loads continue to increase in the sagging bending moment range.

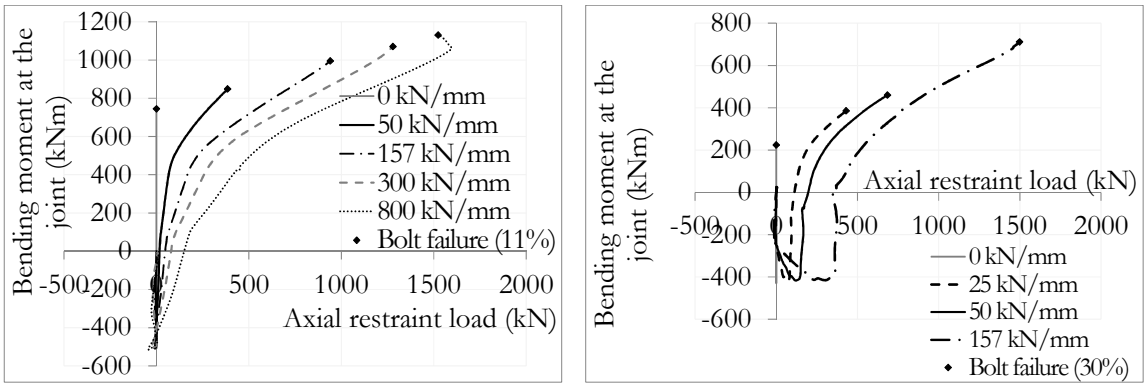

Figure 5.14: Bending moment – axial load a) at ambient and b) at elevated temperatures

It can be observed from Figure 5.13 that the sagging bending moment joint behaviour is affected by the beam axial restraint; higher the axial restraint stiffness K_a, higher the compression axial loads at the beam end, and higher the maximum bending moment. From K_a = 0 to 157 kN/mm, the bending resistance increases by 34 % and 218 % at ambient and elevated temperatures, respectively. In all the simulations, concrete crushing against the column flange is observed on the top of the composite slab, followed by the bottom bolt row failure under tension. The joint rotation capacity is slightly increased under higher axial compression loads, by 13% and 23% at ambient and elevated temperatures, respectively. However, the brittle failure of the bolt happens before the development of tensile loads.

From Figure 5.14, it is observed that no catenary actions are developed in the frame. When the restraint stiffness increases, axial compression loads increase, and the bolt failure happens later: i) from 0 to 157 kN/mm, it happens during the compression load increase; ii) for 800 kN/mm (ambient temperature), the bolt failure happens after reaching the maximum value of the compression axial load, during the decay phase. Figure 5.15 presents the total load applied at the column *versus* the vertical displacement of the joint; the maximum load increases with the axial restraint stiffness K_a.

Finally, from these results, it is observed a beneficial effect of a stiff restraint under sagging bending moment and axial compression loads: the resistance of the composite joint increases with K_a. For the studied sub-frame characteristics (low slenderness of the composite beam), failure of the bolts in the bottom bolt row is observed for small vertical displacements during the development of compression forces. High slenderness of the composite beam is needed to reach catenary action before the bolt failure; the effect of the beam span on the bending moment *versus* axial load behaviour is studied in section 5.4.5.

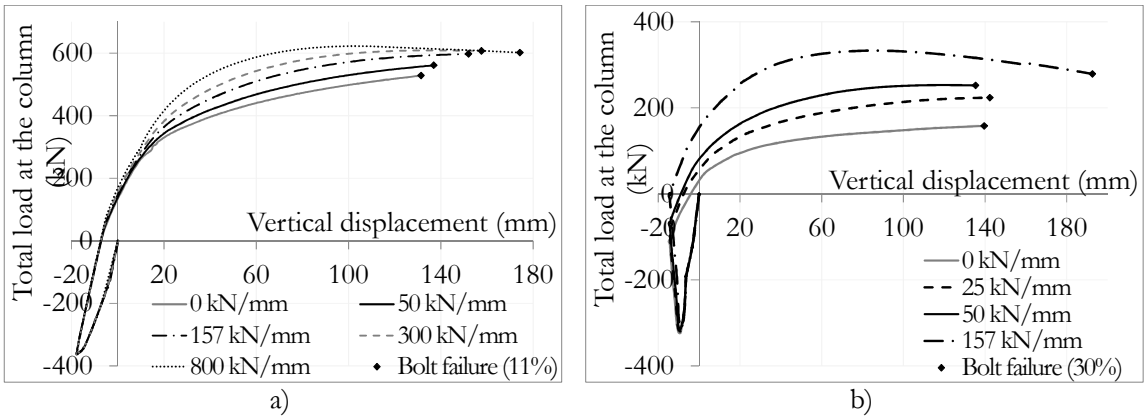

Figure 5.15: Applied load - vertical displacement a) at ambient and b) at elevated temperatures

5.4.3.3 M-N curves

In order to draw the M-N curve of the joint, additional FE simulations are performed at ambient and elevated temperatures. Each FE simulation provides one point of the M-N curve; this point corresponds to the failure of the joint considered as: bolt failure in tension (BT) or column web buckling in compression (CWC).

In the previous results, failure of the bolts in the bottom bolt row was observed for small vertical displacements during the development of axial compression forces, even with high spring stiffness's. Therefore, the utilisation of the spring element at the end of the beam, in the FE model, limits the available results, because tensile loads will never develop before bolt failure (due to the low slenderness of the beam). In order to draw the M-N curve on the tensile side, the FE results, presented in this section, are obtained replacing the axial restraint by a concentred axial force at the beam end. In this way, the joint sagging bending moment resistance can be evaluated under axial tensile loads or very high compression loads. At ambient temperature, the axial concentred load is applied after the column loss and is kept constant during the increase of sagging bending moment; loads varying from N = -1500 kN to N = 2500 kN are considered. At elevated temperatures, during the heating phase, in order to simulate the restrained thermal expansion, a 1st axial concentred compression load (N = 100 kN) is applied for all the FE models. Then, for the following loading phase (column loss), its value is changed to simulate the tensile or compressive beam axial loads (from N = -500 kN to N = 1900 kN). N is kept constant during the increase of sagging bending moment. Note that the axial resistance of the beam is much higher than the applied axial loads (axial resistance of the steel beam is N_{Rd} = 4417 kN).

At ambient temperature

The partial M-N curve drawn by the FE results (Figure 5.16) provides the required (M, N) points to compare with the analytical M-N curve. A very good correlation is shown between numerical and analytical M-N curves of the composite joint; under pure M^+, the difference between analytical and FEM predictions is 16%. In the FE models, the joint UFM corresponds to: i) BT, for axial loads from N = -1500 kN to N = +1524 kN;

and ii) CWC, for axial loads higher than $N = +1524$ kN. The ductile failure CWC is defined as the end of the FE model, when it becomes numerically instable. In the analytical model, the resistance of the composite joint under pure M^+ is governed by EPB. The experimental result is indicated by the maximum bending moment measured before the 1st bolt failure (710 kNm); differences of 4% and 12% with FEM and analytical models are reached.

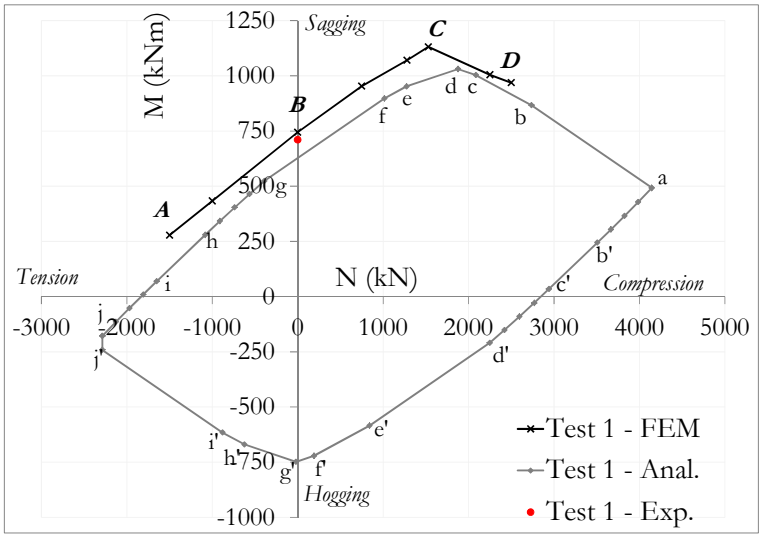

Figure 5.16: M-N curves at ambient temperature (test 1)

The deformation of the joint and the out of plane displacement at each four points *A, B, C, D* of the FEM M-N curve is depicted in Figure 5.17; detailed values of deformations and resistances of the joint are provided in Table 5.20. Figure 5.17 also illustrates the load distribution between the components: CSC, RT, BT, and BFC. FEM and analytical procedures provide similar load distributions (see the load distributions obtained from analytical results in Table 5.21). Under tensile axial load (point *A*), the neutral axis is located in the concrete slab and only a small part of the concrete is under compression (Figure 5.17); in point *B* (pure bending), the neutral axis is located between the top bolt row and the beam top flange; after, the neutral axis drops above the second bolt row under compression axial load (point *C*). It can be observed that the joint reaches higher vertical displacements before bolt failure with lower position of the neutral axis (point *C*); the ductility of the joint is increased. Under higher axial compression load (point *D*), only the bottom bolt row is under tension, and the column web instability is observed with high deformation out of the plane; this ultimate failure mode limits the vertical displacement and deformation capacity of the joint.

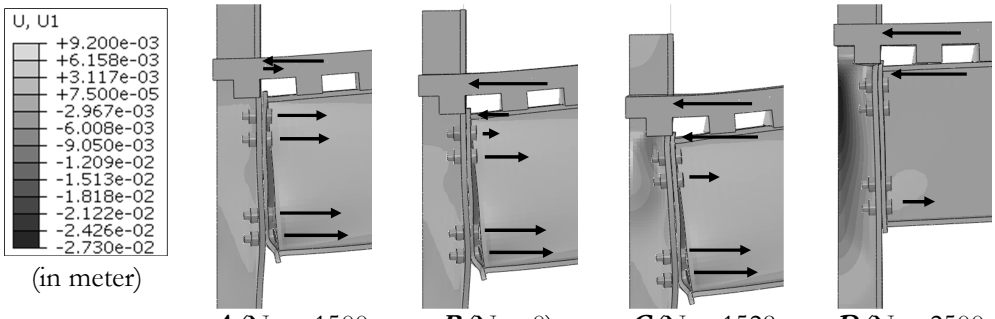

Figure 5.17: FEM results - Deformation of the joint and out of plane displacement U1 at bolt failure at ambient temperature (scale 2)

Table 5.20: Detailed values of deformations and resistances of the joint (FEM results)

	A	***B***	***C***	***D***
N (kN)	-1500	0	1528	2500
UFM	BT	BT	BT	CWC
M (kNm)	278	744	1130	968
F (kN)	312	528	601	594
δ_v (mm)	103	131	174	50
$\Phi_{j,u}$ (mrad)	36	44	61	14

Table 5.21: Load distribution in the composite joint CFJ under pure bending moment from analytical results

	A	B	C	D
Under pure M^+	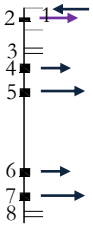	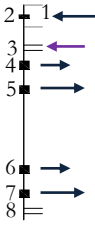	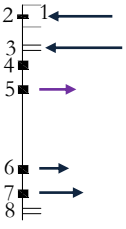	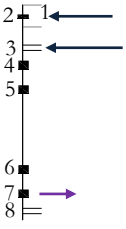
UFM	CSC	EPB	CSC or CWC	CSC or CWC

At elevated temperatures

The numerical and analytical M-N curves of the composite joint at elevated temperatures are compared in Figure 5.18; a good correlation is shown. The experimental result of test 6 is also represented (M = 336 kNm) in the FEM curve. In the FE models, the joint ultimate failure modes correspond to: i) bottom BT, for axial loads from N = -500 kN to N = +1499 kN; and ii) CWC, for axial loads higher than N = +1499 kN. In the analytical model, under pure M^+, the UFM corresponds to BWT.

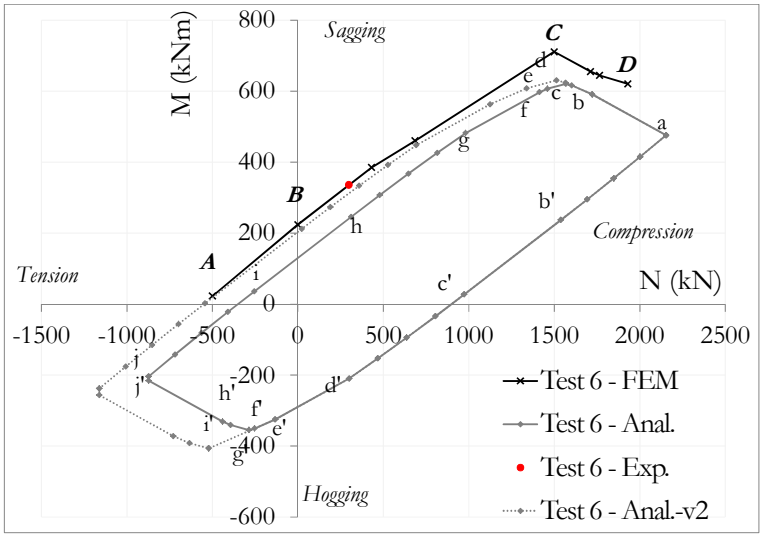

Figure 5.18: M-N curves at elevated temperatures (test 6 – 700°C)

FEM results provide higher resistance than the analytical ones, with 42 % of difference under pure M^+. This difference could be explained by an underestimated theoretical resistance of BWT of the first bolt row above the beam bottom flange in tension. (Eq. 5.10) shows the BWT resistance defined in EN 1993-1-8 (2005).

$$F_{t,wb,Rd}=b_{eff,t,wb}t_{wb}f_{y,wb}/\gamma_{M0} \qquad \text{(Eq. 5.10)}$$

Where $b_{eff,t,wb}$ corresponds to the effective length of the equivalent T-stub representing the end-plate in bending, t_{wb} is the beam web thickness, $f_{y,wb}$ the steel properties (here f_u), and γ_{M0} is the partial safety factor equal to 1. The effective length of the equivalent T-stub considers that the bottom bolt row is located near the beam bottom flange; this distance is higher than for the inner bolt row, so, an additional resistance of the beam web is already considered. However, the FE model of test 6 shows that the beam flange is under tensile load (combined to bending - see Figure 5.19), so that the beam flange may help the web to resist to the tensile loads in a more significant way than considered in the component method. In the analytical model, if this ultimate failure mode (UFM) is neglected based on the assumption that the resistance of the component BWT is much increased by the resistance of the component BFT, the UFM become the end-plate in bending EPB; the new M-N curve is represented by the dashed line in Figure 5.18 (Test 6-Anal.-v2). Under pure M^+, the difference between analytical and FEM results is now reduced to 9%. The theoretical resistance of the component BWT should be studied in detail in a future work.

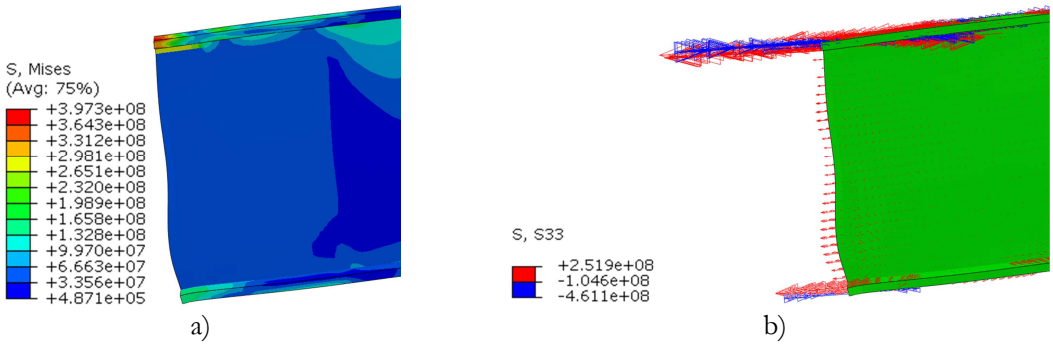

Figure 5.19: Deformation of the beam (near the joint) at failure and at elevated temperatures (test 6): a) stresses of von Mises, b) stresses in the longitudinal direction S33

The deformation of the joint and the out of plane displacement at each four points *A, B, C, D* of the FEM M-N curve are depicted in Figure 5.20; detailed values of deformations and resistances of the joint are provided in Table 5.22. The UFM are similar to those observed at ambient temperature; the vertical displacement and deformation capacity of the joint are limited when the column web instability is observed (point *D*).

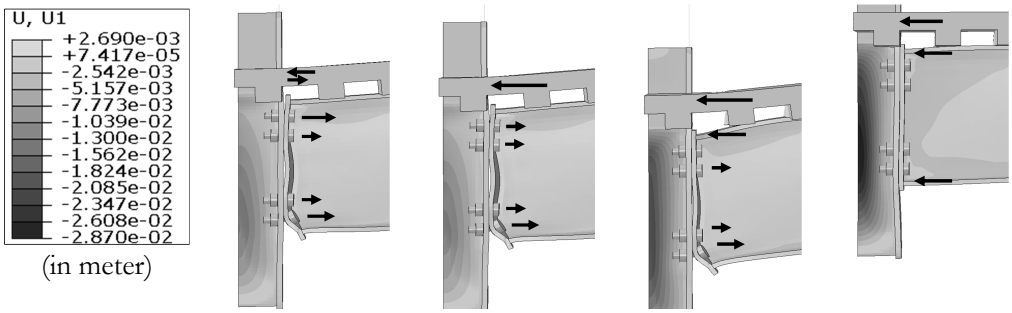

Figure 5.20: FEM results: deformation of the joint, vertical displacement and out of plane displacement U1 at bolt failure (scale 2), at elevated temperatures (test 6 - 700°C in BBF)

Table 5.22: Detailed values of deformations and resistances of the joint (FEM results)

	A	***B***	***C***	***D***
N (kN)	-500	0	1499	1930
UFM	BT	BT	BT	CWC
M (kNm)	22	224	711	620
F (kN)	64	156	279	410
δ_v (mm)	122	140	193	15
$\Phi_{j,u}$ (mrad)	40	45	55	-3

5.4.4 Influence of the global size of a steel flush end-plate joint

The influence of the global size of a steel flush end-plate joint on the M-N behaviour is studied in this section. Two steel joints are considered:

i. FJ03, the flush end-plate joint presented in section 5.3.2: IPE300 steel beam cross-section connected by two bolt rows to HEA300 steel column cross-section (bolts M20 grade 8.8; steel end-plate 16 mm thick);

ii. SFJ, the steel part of the composite flush end-plate joint CFJ (the composite slab is not considered): IPE550 steel beam cross-section connected by four bolt rows to HEB 300 steel column cross-section (bolts M30 grade 10.9; steel end-plate 15 mm thick).

Analytical results are presented in Figure 5.21a by the black curves. The increase of the global M-N resistance with the joint size is obvious. Based on the work described in Santiago (2008), two additional variations are performed for the flush end-plate joint FJ03: i) FJ01 - bolts M20 grade 8.8 and end-plate 10 mm thick; and ii) FJ02 - bolts M20 grade 10.9 and end-plate 16 mm thick. The influence of these variations is localised (see Figure 5.21b): i) a reduction of the end-plate thickness (FJ01) leads to lower resistance of EPB so that joint resistances under maximum/minimum bending moments and pure tensile loads are reduced by 10% and 49% respectively; ii) an increase of the bolts material properties (FJ02) leads to higher resistances of EPB and CFB components so that joint resistances under maximum/minimum bending moments and pure tensile loads are increased by 4% and 21% respectively. For both situations, the part of the curve where only components in compression are activated (points *a*, *b* and *b'* – see Figure 5.2), are not affected, as the variations are only performed on tension components.

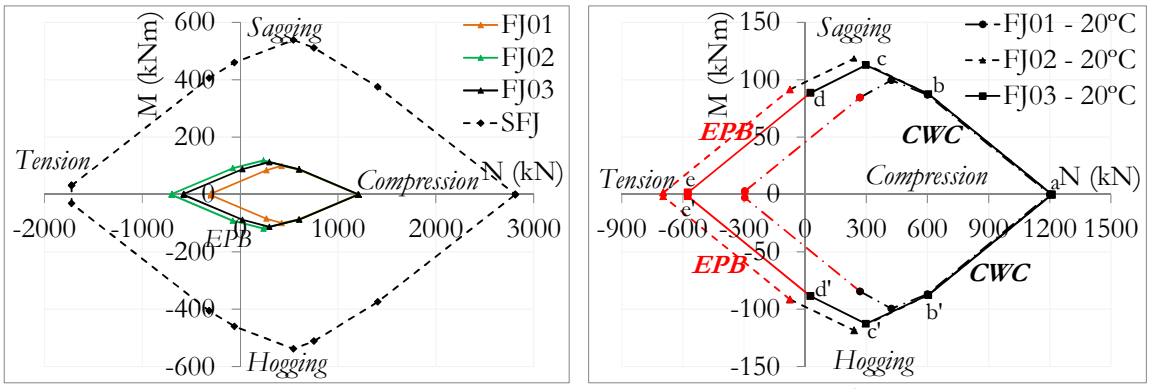

Figure 5.21: M-N curves of: a) steel flush end plate joints FJ01, FJ02, FJ03 and SFJ, b) ultimate failure modes of joints FJ01, FJ02 and FJ03

Figure 5.21b also shows the UFM (EPB or CWC) defined according to the Cerfontaine's method (see Appendix E.1). It seems that modifying the joint characteristics (end-plate thickness or bolt properties) changes the size of the M-N plastic resistance surface (translations of segments of the curve), and each segment continues to be defined by the same UFM.

5.4.5 Influence of the beam span length

Based on FE results, the influence of the beam span on the bending moment to axial load behaviour is studied at ambient temperature. For the studied sub-frame characteristics (low slenderness of the composite beam - Figure 5.22a), failure of bolts in the bottom bolt row is observed for small vertical displacements during the development of compression

forces. With longer beams spans (higher slenderness), axial tensile loads for smaller vertical displacements of the joints are anticipated. The real length of the beam as in the car park building (10 meters) is modelled in the FE model (Figure 5.22b).

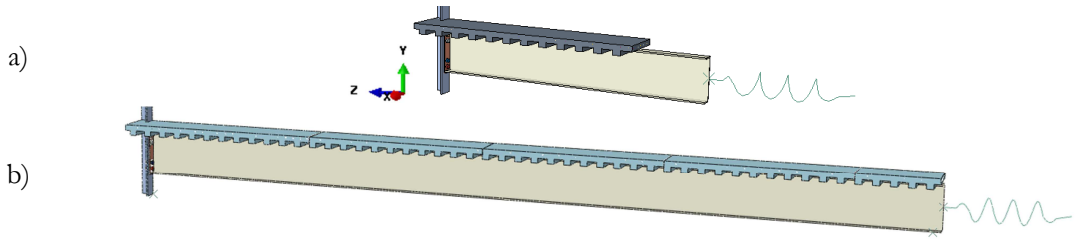

Figure 5.22: 3D FE model of the composite steel-concrete frame in Abaqus: a) 3 meters' beam, b) 10 meters' beam

The evolution of the bending moment at the joint *versus* the joint rotation, and the bending moment at the joint *versus* the axial load are depicted in Figure 5.23 a) and b) respectively; the end point of the curves corresponds to the bottom bolt failure.

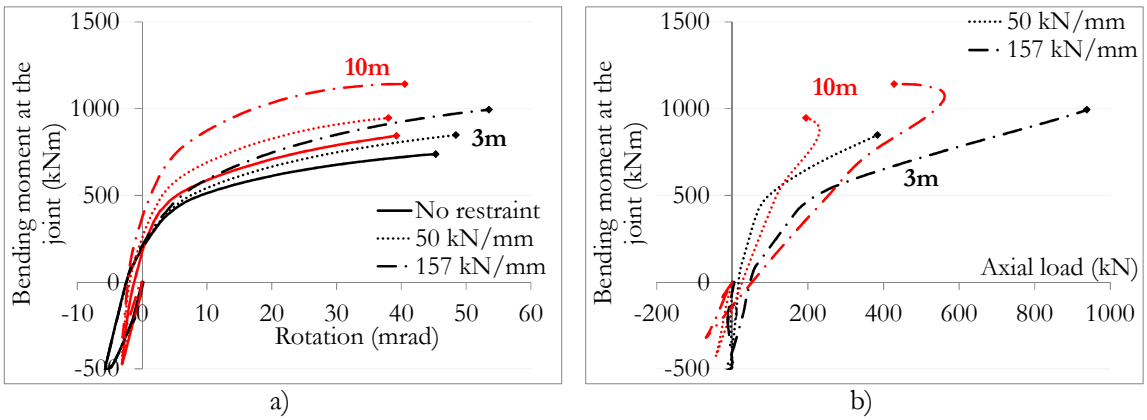

Figure 5.23: a) Bending moment - joint rotation; b) Bending moment - axial load at the beam restraint

Without any axial beam restraint (continuous lines in Figure 5.23a), the joint is subject to pure bending moment and the moment-rotation curves should not be affected by the beam's span; however, Figure 5.23a shows some differences between the two models, with higher resistance for the 10 meters' beam. The deformation of the joint and its failure mode are affected by the degree of shear connection in the composite beam. In the FE model, the number of shear studs per meter is kept equal for both models, so that 22 shear studs are modelled in the 3 meters' beam (partial shear connection), and 98 shear studs are used in the 10 meters' beam (full shear connection). Figure 5.24 depicts the joint deformations under rotation $\Phi = 35$ mrad for both models (before the bolt failure). In the 3 meters' beam, a small part of the slab is under compression, just above the longitudinal steel reinforcement in tension. The beam top flange is under compression loading, and the 1st rib of the slab is deformed due to the slip between the steel beam and the composite slab. Two axis of rotation can be defined for the composite joint (Figure 5.24a). In the 10 meter's beam model, the beam top flange is not under compression, and the rib of the slab

is not deformed (no slip); one single axis of rotation is drawn (Figure 5.24b). Due to the modified points of rotation, the bolt failure happens for different loadings (see Figure 5.23a): with full shear connection (10 meters' beam), the corresponding bending moment resistance is increased by 14% but the joint rotation capacity is reduced by 13% in comparison to the partial shear connection (3 meters' beam).

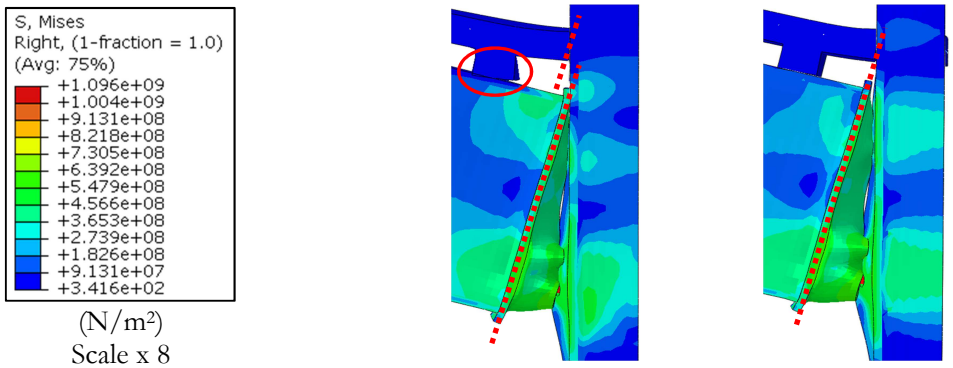

a) 3 meters' beam b) 10 meters' beam

Figure 5.24: Stresses of Von Mises in the joint about Φ = 35 mrad (before the bolt failure) with a) partial shear connection and b) full shear connection

Figure 5.23b depicts the M-N curves for both models with beam axial restraints (K_a = 50 kN/mm and K_a = 157 kN/mm). In both cases (3 meters and 10 meters' beams), the effect of the beam axial restraint is to increase axial compression loads, so that the bending moment resistance increases. For the 3 meters beams, bolt failure is reached before the maximum compression load, whereas bolt failure for 10 meters' beams happen after the maximum compression load. The beam span influences the axial load applied at the beam end. For a longer beam span (higher slenderness), initial beam axial compressive loads are smaller and catenary action develops for lower joint rotation. However, for the studied sub-frame characteristics, spans longer than 10 m are needed to reach the tensile forces in the joint before the bolt failure.

The evolution of the load applied at the column top *versus* the joint vertical displacement is depicted in Figure 5.25; these curves are not cut after the 1st bolt failure in order to observe the estimated behaviour of the joint under larger deformations. For the 3 meters' beam, failure of the joint is attained before reaching high deformations needed to develop tensile axial loads. With the 10 meters' beam, tensile loads are able to develop after failure of the bottom bolts rows; it is also shown that tensile loads develop faster (for lower vertical deformations) when higher stiffness of the beam axial restraint K_a is considered.

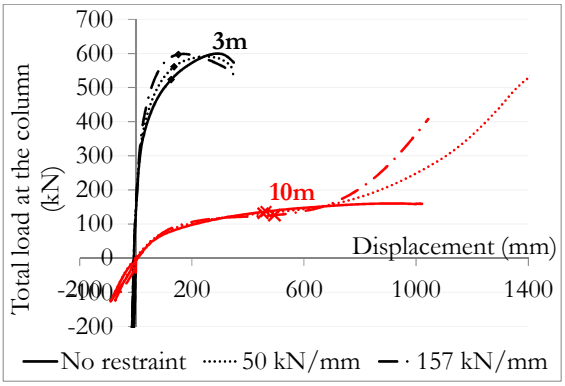

Figure 5.25: Load *versus* vertical displacement at the column top

5.4.6 Influence of the safety factors and material properties

In the previous sections, the behaviour of steel and composite joints has been investigated, so that measured mechanical properties have been used, as well as partial factors equals to 1. If the structural design is considered, mechanical properties and partial factors defined in the codes may be used. The composite joint CFJ is considered for this study. M-N curves obtained from analytical results are depicted in Figure 5.26a and Figure 5.26b, at ambient and elevated temperatures (700°C), respectively. For both situations, three M-N curves are drawn: *A*) with measured mechanical properties (ultimate stresses f_u), and partial factors equal to 1 (reference curve); *B*) with measured mechanical properties (yield stresses f_y), and partial factors equal to 1; and *C*) with design resistances (yield stresses and partial factors defined from Eurocodes). Measured material properties from standardized stress-strain curves are considered (Appendix A.3); at elevated temperatures, the standardized curves of the steel material do not consider any strain hardening and $f_{u,\theta,steel} = f_{y,\theta,steel}$.

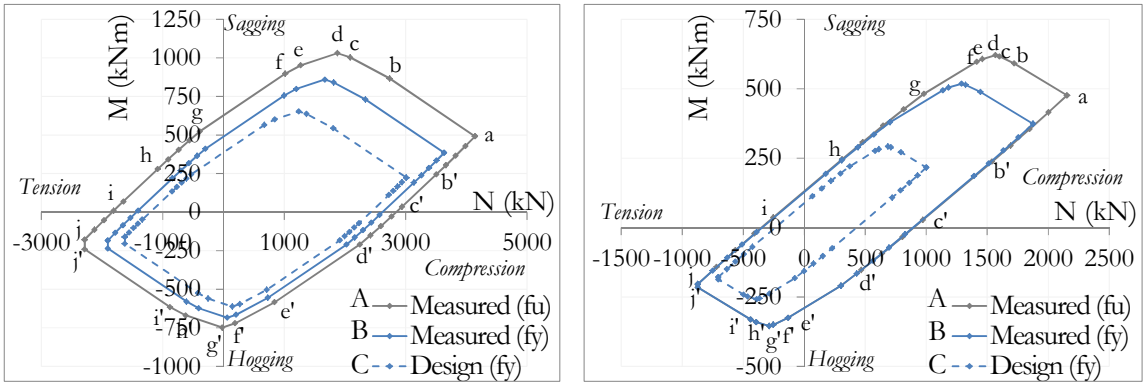

Figure 5.26: M-N curves of the composite joint at: a) ambient temperature (20°C); b) elevated temperatures (700°C)

At ambient temperature (Figure 5.26a), the global reduction of M-N resistance is obvious when the yield strength and partial factors are considered. Under M^+, the maximum bending moment reduces of:

i. 17% (from *A* to *B*) because of the reduction of: i) the steel mechanical properties ($f_{y,steel} < f_{u,steel}$), and ii) the concrete properties, reduced by 22% (f_{ck} = 29 MPa < f_{cm} = 37 MPa).
ii. 37% (from *A* to *C*), because of the reduction of: i) the smaller steel mechanical properties defined in Eurocodes, and ii) the partial factors (γ_c = 1.5 and γ_b = 1.25).

The decrease of resistance under hogging bending moment is lower because the concrete component is not activated and structural steel components resistances are only reduced by the yield strengths values (the partial factor does not influence as γ_s = 1.0); bolts and steel reinforcement are reduced by γ_b = 1.25 and $\gamma_{s,reinforcement}$ = 1.15 respectively.

At elevated temperatures (Figure 5.26b), steel material properties do not consider strain hardening, so that the difference between curves *A* and *B* is only visible where the concrete component is considered; this component is reduced by using f_{ck} instead of f_{cm}. This component influences the maximum sagging bending moment and the maximum axial resistance in compression (reduction of 17% and 13% respectively). For the design results (curve *C*), the whole M-N curve is reduced by the decrease of the material properties and the partial coefficients.

5.5 Concluding remarks

In this chapter, the M-N behaviour of the composite steel-concrete beam-to-column joint is studied in detail. The objective is to provide additional information on the joint behaviour at failure when it is subject to sagging bending moments, axial loads and elevated temperatures after the loss of a column due to a localised fire. Namely, it is expected to enlarge knowledge of the effect of some parameters that influence the robustness of joints from tall open car park buildings. The behaviour of the joint is analysed based on:

i. Numerical results, obtained from the FE models presented in chapter 4;
ii. Analytical results, obtained from the procedure developed at the University of Liège, which predicts the M-N curves of joints.

The analytical procedure is presented in detail at the beginning of the chapter. Its applicability to steel and composite joints under combined bending moment, axial load and elevated temperatures is demonstrated.

Results show that the global M-N resistance of the studied joints decrease with the increase of temperatures. The loss of resistance is accentuated where the component the most heated in a fire (beam bottom flange) is activated in compression, i.e. under hogging bending moment and compression loading. The ultimate failure mode of the joint under pure bending moment is also changed by the increase of temperature, because the resistances of the rows are dependent of the temperature gradient in the cross-section (non-uniform distribution), and the position of the neutral axis changes.

After the column loss, the joint is subject to sagging bending moment. The part of the building not directly affected by this accident provides strong beams restraints. The results show that because of these restraints and due to the geometrical effect (low slenderness of the composite beam), high axial compression loads develop before reaching high displacements and deformations. Small compression loads have a beneficial effect on the resistance of the joint and provide higher resistance and rotation capacity. However, under high compression loads, the column web instability governs the joint resistance and the joint rotation capacity is much reduced. The joint reaches its maximum resistance and maximum capacity of deformation under the (M, N) loading corresponding to a position of the neutral axis located near the top bolt row: the concrete slab and the beam top flange are under compression and all the bolt rows work in tension. However, the capacity of rotation of this type of joint is not sufficient to reach the high deformations necessary to develop catenary action: the joint fails before reaching large deformations and associated tensile loads. For this type of low slenderness composite beam, the bottom bolt row needs a high capacity of deformation in tension (under sagging bending moment), depending of the capacity of deformation of end-plate, column flange and bolts.

Chapter 6

6 General conclusions and perspectives

6.1 Conclusions

This thesis reflected the author participation in the ROBUSTFIRE research project, as a member of the research group ISISE-SMCT at the Civil Engineering Department of the University of Coimbra. In the thesis, the behaviour of steel-concrete composite joints in open car park buildings under column loss robustness scenario, due to fire, was investigated. The main objective was to provide a detailed analysis of the heated joint behaviour subject to variable bending moments and axial loads when the column fails. Open car parks are characterized by high ventilation that keeps the fire limited on the ignition zone (not leading to a flash-over), and a fire in an open car park building is considered as localised fire. The fire scenario considered in the current work was a localised fire around the column: the fire heats the joint zone, but a large part of the beams remains at ambient temperature. So, during the heating, the joint was subject to an increase of axial compressive loads due to the prevented thermal expansion. It can be noted that limited axial forces develop, in comparison to a full-development fire that would heat the entire beams spans. Once the column fails, the joint suffers a vertical displacement downwards, and it is subject to a variation of bending moments: from hogging to sagging bending moment. Additional loss of joint resistance due to elevated temperatures needs to be considered. Finally, the structure should be able to reach an alternative equilibrium configuration (catenary action) at the condition that large enough deformations can develop without failure; so vertical loads applied to the joint and the beams would mainly resist by the vertical components of catenary forces (tensile axial forces).

From previous experimental and numerical studies of open car park buildings subject to fire, it was shown that the fire safety of unprotected steel open sided steel-framed car parks is ensured, if some specific structural conditions are considered (e.g. beams with composite steel concrete section including shear studs, columns filled with concrete between the flanges, etc...). The results of demonstration fire tests in real car park buildings have encouraged changing the legislations in several European countries, allowing to build steel

or composite steel-concrete open car parks without fire protection. A design based on the actual performance of the structure (based on fire scenarios) and not on prescribed nominal design curves (that in most of the cases require fire protection with considerable thickness) is now considered. The height of each storey is usually short to optimize the building size, so that flames of burning cars impact the ceiling. In these conditions, localised effect of a fire, on horizontal elements located above the fire, can be evaluated by the simple analytical tool proposed by Annex C of EN 1991-1-2 (2002): the Hasemi´s method. The calculation of the temperatures depends on the total rate of heat release, which is determined based on the fire scenario. The reference curve for the rate of heat release was defined based on experimental test results performed on actual vehicles. Nowadays, no accurate and simple method is available to calculate the column temperature when it is subject to a localised fire, and advanced models are required to determine the real temperature in vertical elements. Finally, calculation models to design the structures are presented in EN 1993-1-2 (2005) and EN 1994-1-2 (2005). An example was presented in chapter 2, and it clearly showed the advantage of using the design methodology based on fire scenarios against the use of ISO 834 curve. It was verified that the unprotected composite steel-concrete beams were safe when subject to the studied fire scenarios.

A typical open car park building with eight floors was specially designed for the ROBUSTFIRE project, and the composite beam-to-column flush end-plate joint from the fifth floor was studied in detail in chapters 3, 4 and 5. The joint configuration was representative of usual joint typologies used in open composite steel–concrete car park structures. First, seven beam-to-column joints were tested: one reference test at ambient temperature; five tests at 500ºC or 700ºC; and a demonstration test, for which the sub-frame was subject to an increase of temperature up to the failure of the column (see chapter 3). In these tests, the effect of the combined bending moment, axial loads and elevated temperatures in the beam-to-column composite steel-concrete joints, following the loss of the column, was observed. The joint failed before reaching large deformations, and catenary action was not attained. Then finite element method (FEM) analyses of steel and composite steel-concrete elements were performed in chapter 4, using Abaqus. Preliminary validation of the FEM program for analysis of steel and composite steel-concrete structures subject to fire and modelled with beam and shell elements was achieved, and confidence was gained in the FEM results. The 3D FEM models of the composite joint were developed and calibrated against three experimental tests at ambient and elevated temperatures. The global behaviour of the composite steel-concrete joint in Abaqus was accurately modelled, the joint failure was easily approximated and accurate deformation predictions up to failure was provided at ambient and elevated temperatures (700ºC in the beam bottom flange). These FE models allowed assessing the detailed behaviour throughout the entire robustness scenario, including stresses, extensions, deformations, etc…. Finally, in chapter 5, the M-N behaviour of the composite steel-concrete beam-to-column joint was studied in detail using the 3D FEM models and existing analytical tools. The existing analytical procedure developed at the University of

Liège allows predicting the M-N curves of joints. Its applicability to steel and composite joints under combined bending moment, axial load and elevated temperatures was demonstrated. Additional information on the M-N composite joint behaviour at failure under column loss scenario was provided, and some parameters that influence the robustness of joints from tall open car park buildings (e.g. temperature, beam axial restraint, beam span length, etc…), were investigated.

From the experimental tests performed without beam axial restraint, it was observed that the joint rotation capacity increases with temperature, whereas the maximum sagging bending moment is reduced. It was also shown, by the detailed study of the joint behaviour in chapter 5 (section 5.4.2), that the global M-N resistance of the joint decreases with the increase of temperatures. In a fire, the most heated component is the beam bottom flange; when this component is activated (i.e. under hogging bending moment and compression loading), the loss of resistance is higher. The ultimate failure mode of the joint under pure bending moment is also changed by the temperature increase, because the resistances of the rows are modified, depending of the temperature gradient in the cross-section (non-uniform distribution).

From the experimental tests performed with beam axial restraint, under sagging bending moment, experimental, FEM and analytical results showed that, because of the low slenderness of the composite beam (span length / cross-section height), axial compression loads develop at the beam restraints before reaching high displacements and deformations. As observed in experimental tests (chapter 3), small compression loads have a beneficial effect on the resistance of the joint and provide higher resistance and rotation capacity: the tests with total beam axial restraint exhibited higher sagging bending moment resistance. The observed increase in moment capacity is in line with previous experimental and analytical results (Lima *et al.*, 2004; Simões da Silva *et al.*, 2004), resulting from the beneficial effect of the compressive axial forces that also led to increase the joint rotation capacity and ductility. Under higher compression loads, the column web instability governs the joint resistance and the joint rotation capacity is much lower (see section 5.4.3).

Catenary action was not attained in any experimental test, even in the demonstration test. In this demonstration test, the bottom column failed under 658ºC, and then once the beams reached 700ºC, the vertical displacement of the joint began to increase faster, the composite slab crushed, and finally the sub-frame collapsed. Failure of the bolts in the bottom bolt row was observed for small vertical displacements during the development of the compression loads. It was finally observed that the capacity of rotation of this type of joint is not sufficient to reach the high deformations necessary to develop catenary action: the joint fails before reaching large deformations and associated tensile loads (see section 5.4.5).

6.2 Robustness of open car park buildings subject to localised fire

The work developed within this thesis aimed to highlight the two essential requirements for sufficient robustness in tall car park buildings under column failure scenario: i) joints, heated by localised fire, need to be able to resist variable bending moments and axial loads, and ii) the structural system has to be ductile enough to allow the development of tensile loads, required to reach an alternative equilibrium configuration (catenary action). At the beginning of the ROBUSTFIRE project, the design of the composite joints indicated bolts M24; however, in order to increase the connection resistance and avoid shear failure during the experimental tests, bolts M30 were selected for the project. So, when the column fails, the joint would be able to sustain the vertical loads coming from the rest of the structure by developing catenary forces, and robustness would be improved by providing alternate load paths. In this way, the initial damage (column loss) can be contained and major collapse can be averted. This method is based on the indirect tying method prescribed in EN 1991-1-7 (2006). However, the capacity of deformation of the joint to reach sufficient deformation to develop the tensile loads in the frame is not considered in this method. For high beam slenderness (small cross-section height and/or long beam span), previous experimental work showed that rotation capacity of composite joint is sufficient to reach high vertical deformations and tensile loads (Demonceau, 2008). However, it is highlighted in the current thesis that improving robustness by increasing resistance of the joint is not sufficient for joints with low beam slenderness, and it is not safe; the tying method provided by EN 1991-1-7 (2006) needs to be associated to a ductility criterion. Nowadays, the codes do not provide any simple method to evaluate the capacity of deformation of a steel / composite joint under large deformations. The only way to evaluate the joint deformation capacity at failure is to use complex, detailed and time-consuming numerical models, but this is not feasible for practical engineers. Additional investigation should be performed in this way, to provide simple prescriptive rules to complement the tying method (EN 1991-1-7, 2006).

6.3 Open questions and further research interests

The work presented in this thesis deals with the behaviour of composite steel-concrete beam-to-column joints under extreme loading (column loss due to localised fire). In the course of the research, several topics are identified as requiring further examination:

i. Additional investigation should be performed on new joints typologies (e.g. web cleat connections), keeping the same beam and column sizes. These studies intend to investigate the capacity of rotation of the joint, and observe if it would have sufficient ductility to reach high deformations and catenary action under column loss scenario. It should be noted that the position of the axial restraint

to the beam influences the axial loads: a restraint located at the level of the concrete flange will be subject to tension loads earlier than the axial restraint located at the centroid of the steel beam. The design of the joint typology should consider this effect.

ii. When the column fails, catenary forces can only develop in the frame if joints are able to deform and reach sufficient vertical displacement without any failure. A simple criterion, based on the beam slenderness L/EI, may be determined in order to inform the engineers about the required rotation from which tensile forces appear in the axial restraint to beam ϕ_{tens}.

iii. A simplified method to define the capacity of rotation of the joint at failure ϕ_{fail} should be developed and introduced in the codes. The analytical method of Cerfontaine allows defining this rotation capacity of a joint at failure. However, deformation limitations of ductile components are not considered, and when this method is applied to a composite joint with high cross-section height (i.e. the composite joint studied in the thesis), deformations of bolt rows reach 100 mm, which is unrealistic. This method could be improved and validated for composite joints, based on following assumptions: i) Total shear connection between steel and concrete in the composite beam can be considered in a safe side: it was observed, in section 5.4.5, that total shear connections provide lower joint capacity of rotation than partial shear connections; ii) Fang *et al.* (2011) limit the deformation of ductile components from bolt rows to 25 mm (end-plate connection); this deformation limit may be considered. Yang and Tan (2013) also reminded that tensile resistance of the joint is modified after large rotations have occurred, and tying resistance of the joints should still satisfy certain values in the deformed configuration. The FEM model developed within this work can be useful for these further developments, to provide additional results of different case studies.

iv. Temperatures of vertical structural elements (such as columns) subject to localised fire, is actually under investigation in Europe. Additional experimental tests should be performed, CFD models may be developed and validated, and from parametrical studies, a simplified approach to evaluate the heat flux into steel columns should be developed (Ferraz, 2014).

v. Discrepancies were observed between FEM and analytical results when the analytical method provided failure of the beam web in tension component; analytical results were much lower than FEM results (see chapter 5). So the analytical resistance of the component "beam web in tension" should be better characterized by considering the resistance of the beam flange in tension.

vi. When the experimental test 6 (700ºC in beam bottom flange and spring restraint to beam) was modelled in Abaqus, higher axial compression load and initial stiffness were observed under sagging bending moment, in comparison to what was measured during the experimental test. The experimental test 6 ran during

about 8 hours, with slow heating followed by constant temperature state (700ºC) and increase of stresses, so creep effects could affect the deformation of the frame and the reaction loads during the experimental test.

Creep is defined as the time-dependent plastic strain under constant stress and temperature; it occurs due to movement of dislocations in the slip plane. At ambient temperature, the inelastic response of steel does not show dependence on time, and time effects are normally neglected in the analyses and design. At elevated temperatures, the influence of creep increases with the increase in axial restraint, and load level; and lower is the heating rate, higher are the creep strains. Generally, neglecting high-temperature creep effect stiffens the structural response and leads to reduced deflections but larger restraint forces. Therefore, neglecting high temperature creep in fire resistance analysis of steel structures can lead to unconservative predictions (Kodur and Dwaikat, 2010). So, for steel cross-sections subject to high temperatures and high stress for a long period of time, it is important to consider creep (Aribert and Randriantsar, 1980 and 1983; Kodur and Dwaikat, 2010, Morovat *et al.*, 2012, Huang *et al.*, 2006). However, creep is not usually included explicitly in fire design process because of lack of data and the difficulty of calculations (Morovat *et al.*, 2012).

In the detailed FEM model of the composite joint (chapter 4), creep was neglected. An attempt to include creep strains in the FE model was made, using the quasi-static analysis "Visco" in Abaqus, where time-dependent material response is considered. However, calibration of creep material properties (to use the available power-law creep in Abaqus) was difficult due to lack of data. These effects should be considered in further developments: 1st- by studying the creep material properties from steels used in the experimental tests (e.g. by executing experimental creep coupon tests), 2nd- by including and considering these creep properties in the detailed FE model, using a quasi-static analysis.

vii. Six additional tests were performed on bolts M30, grade 10.9 under natural fire conditions, with the following procedure: 1st- heating up to T_f = 500ºC, 600ºC or 700ºC (linear ramp of 250ºC/hour), 2nd- maintaining the constant elevated temperature during half an hour, 3rd- naturally cooling, 4th- machining of coupons, and 5th- testing in tension at ambient temperature (T_u), according to the same proceeding than explained in section 3.4. Results are presented in Appendix A.5. Additional investigation should be performed in order to check if bolts subject to variable axial loads during a localised fire could be reusable if bolts temperatures did not exceed 600ºC (which is probable in such building and fire conditions).

6.4 Personal contributions

The main personal contributions to the presented investigations are listed here below:

a) Derivation of all structural requirements for car park structures: dimensions, layout, loads, fabrication/construction/erection constraints, realistic fire scenarios, National regulations, etc… (chapter 2);
b) Development of a practical example of open car park fire design according to the fire engineering methodology, based on simplified and advanced methods (section 2.7);
c) Preparation of seven experimental tests on beam-to-column composite joints: simplified FE model to define the joint loading like in the real car park building, estimation of the global behaviour and reaction forces of the tested joint by simplified FE models (Appendix D);
d) Execution of seven experimental tests on beam-to-column composite joints: drawings, definition of the loading sequence and its application in the laboratory, design of the pins and the surrounding structure, practical study of the heating system (electrical elements) and of the spring restraints manually controlled, preliminary tests, instrumentation, controls and measurements during the experimental tests, and interpretation of the experimental results (chapter 3 and Appendix B);
e) Execution of tensile tests on steel coupons, including the design of the coupons, and interpretation of the experimental results (section 3.4 and Appendix A);
f) Execution of compression tests on concrete blocks: tests and interpretation of the experimental results (section 3.4);
g) Validation of the commercial program Abaqus (2012) for modelling steel and composite steel-concrete structures under fire: coordination of the benchmark study of steel columns subject to fire, and development of the benchmark study of composite beams subject to fire (section 4.2);
h) Calibration and validation of three 3D FE models of the composite joint subject to variable bending moments and axial loads at ambient and elevated temperatures (section 4.3);
i) Demonstration of the applicability of the analytical procedure developed at the University of Liège to steel and composite joints under elevated temperatures (section 5.3);
j) Extensive study of the joint behaviour subject to variable bending moments and axial loads at ambient and elevated temperatures, based on numerical and analytical results: influence of some parameters such as temperature, beam span, joint size, etc.… on the robustness of tall open car park buildings (section 5.4).

Finally, here after are listed the author publications within the course of this thesis:

International journals (ISI)

Haremza, C., Santiago, A., Simões da Silva, L. "Experimental behaviour of heated composite steel-concrete joints subject to variable bending moments and axial forces", Engineering Structures 51, p.150-165, 2013, http://dx.doi.org/10.1016/j.engstruct.2013.01.016.

Haremza, C., Santiago, A., Simões da Silva, L. "Design of steel and composite open car parks under fire", International Journal of Advanced Steel Construction, Vol. 9, No. 4, p.350-368, Dec. 2013.

National journal

Haremza, C., Santiago, A., Simões da Silva, L., "Dimensionamento de vigas mistas aço-betão de parques de estacionamento abertos em situação de incêndio", RPEE, Revista Portuguesa de Engenharia Estruturas, Série II, número 13, p.49-59, 2013. (In Portuguese).

International and National conferences

Santiago, A., Haremza, C., Simões da Silva, L. and Rodrigues, J.P., "Numerical Behaviour of Steel Columns subject to Localised Fire Loading", in Topping, B.H.V., Costa Neves, L.F. and Barros, R.C. (eds.), Proceedings of 12th International Conference on Civil, Structural and Environmental Engineering Computing, Civil-Comp Proceedings 91, Civil-Comp Press, Scotland, Paper 7, 2009.

Haremza, C., Santiago, A., Simões da Silva, L. e Rodrigues, J.P., "Numerical analysis of composite steel-concrete car parks subjected to localized fires", in Simões da Silva, L., Almeida Fernandes, J., Batista, A., Caetano, E., Piloto, P., (eds.), Construção Metálica e Mista VII, pp II-397-406, cmm Press, Lisboa, 2009.

Haremza, C., Santiago, A. and Simões da Silva, L., "Behaviour of heated composite joints – Preliminary numerical studies", Proceedings of International Conference Application of Structural Fire Engineering, in Wald F., Horová K., Jirku J. (Ed.), Prague, pp. 231-236, 2011 (**Best young researcher award**).

Haremza, C., Santiago, A. and Simões da Silva, L., "Experimental Behaviour of Heated Composite joints", Eurosteel, 6th European Conference on Steel and Composite Structures, Proceedings of the conference edited by László Dunai *et al.*, Budapest, Hungary, September 2011 (**Best paper of young scientist award**).

Haremza, C., Santiago, A. e Simões da Silva, L., "Metodologia de dimensionamento de parques de estacionamento abertos mistos aço-betão em situação de incêndio", in Simões da Silva, L., Cruz, P., Lopes, N., Almeida Fernandes, J., Batista, A., (eds.), Construção Metálica e Mista VIII, pp II-107-118, cmm Press, Guimarães, 2011.

Haremza, C., Santiago, A., Simões da Silva, L., "Numerical simulation of a composite steel-concrete joint subject to bending moments", in A. Andrade-Campos, N. Lopes, R.A.F. Valente and H. Varum (eds.), Paper 9, First ECCOMAS Young Investigators Conference, Aveiro, Portugal, April 2012.

Haremza, C., Santiago, A., Simões da Silva, L., "Experimental behaviour of heated composite steel-concrete joints subject to variable bending moments and axial

forces", ECCS-AISC, International Workshop on Connections VII, Timisoara, Romania, May 30-June 02, 2012.

Haremza, C., Santiago, A. e Simões da Silva, L., "Robustness of composite steel-concrete open car park buildings subject to localised fire", in Silva Gomes, J.F. and Vaz, M.A.P. (eds.), 15th International Conference on Experimental Mechanics, Porto, Portugal, pp. 807-808, paper ref. 2776, 2012.

Haremza, C., Santiago, A., Simões da Silva, L., "Behaviour of heated composite steel-concrete joints subject to variable bending moments and axial forces", Nordic Steel Construction Conference 2012, Hotel Bristol, Oslo, Norway, p.411-420, 5-7 September 2012.

Haremza, C., Santiago, A. and Simões da Silva, L., "Numerical behaviour of a composite steel-concrete joint under localized fire", 2nd CILASCI –Ibero-Latin-American Congresso in Fire Safety Engineering, Coimbra, Portugal, May 29 to June 1 2013.

Demonceau J.-F., Haremza C., Jaspart J.-P., Santiago A., Simões da Silva L., "Composite joints under M-N at elevated temperatures – Experimental investigations and analytical model", Composite Structures in Steel and Concrete VII, Cairns, Australia, July 27 to August 1, 2013.

Haremza C., Santiago A., Simões da Silva L., "Effect of axial restraint in a composite steel-concrete frame subject to localised fire", in Simões da Silva, L., Silvestre, N., Santos, F., (eds.), Construção Metálica e Mista IX, pp.567-576, Porto, Portugal, 2013.

Haremza C., Santiago A., Simões da Silva L., "Effect of axial restraints to beams on the behaviour of a bolted composite steel-concrete joint under a localised fire", in Li G.-Q., Kodur V. K. R., Jiang S.-C., Jiang J., Chen S.-W., Lou G.-B. (Eds.), 8th International Conference on Structures in Fire, Shanghai, China, June 11-13, p.795-802, 2014.

Haremza C., Santiago A., Simões da Silva L., "The Effect of axial restraints on a composite steel-to-concrete joint under a localised fire - Numerical evaluation", Eurosteel 2014, 7th European Conference on Steel and Composite Structures Naples, Italy, September 10-12, 2014.

.

REFERENCES

(Abaqus, 2012) Abaqus 6.12, Theory Manual and Users Manuals, Dassault Systemes Simulia Corp., 2012.

(Akbarpour and Ekrami, 2008) Akbarpour MR, Ekrami A. Effect of temperature on flow and work hardening behavior of high bainite dual phase (HBDP) steels. Material Science and Engineering;475(1–2):293–8, 2008.

(Alashker *et al.*, 2010) Alashker, Y., El-Tawil, S., and Sadek, F. "Progressive Collapse Resistance of Steel-Concrete Composite Floors", Journal of Structural Engineering, 136(10), 1187-1196, 2010.

(Al-Jabri *et al.*, 2008) Al-Jabri K.S., Davison J.B., Burgess I.W. "Performance of beam-to-column joints in fire - A review". Fire Safety Journal 43, 50-62, 2008.

(Anderberg, 1988) Anderberg Y. "Modelling steel behaviour", Fire Safety J 13(1):17–26, 1988.

(Arbed, 2001) EC1-1-2/71, "Background document on Localized fires according to Annex C of prEN1991-1-2 (24-08-2001)", Profil ARBED, Centre de Recherches, CEN/TC250/SC1/N339, 2001.

(ArcelorMittal, 1996) ArcelorMittal – "Car parks in steel", Comercial Sections, 1996, 30p.

(ArcelorMittal, 2007) ArcelorMittal – "Parkings aériens métalliques largement ventilés", Les carnets de l'acier No 9, 2007, 34p.

(Aribert and Randriantsar, 1980) Aribert J.M. and Randriantsara C., "Etude du flambement à des temperatures d'incendie - Action du fluage". Construction Métallique, No. 4, 1980.

(Aribert and Randriantsar, 1983) Aribert J.M. and Randriantsara C. "Sur une modélisation du flambement des poteaux métalliques dans des conditions d'incendie", Third International Colloquium on Stability of Metal Structures, Preliminary Report, CTICM, Paris, 1983.

(Bennetts *et al.*, 1987) Bennetts I.D., Proe D.J., Lewins R.R., Thomas I.R. "Fire and Unprotected Steel in Closed Car Parks". BHP Melbourne, Research Laboratories Report Number MRL/PS98/87/001, August 1987.

(Block, 2006) Block F. "Development of a component-based finite element for steel beam-to-column connections at elevated temperature". Ph.D. Thesis, Department of Civil and Structural Engineering, University of Sheffield, UK, 2006.

(Bursi and Jaspart, 1997) Bursi O.S., Jaspart J.P., "Benchmarks for finite element modelling of bolted steel connections", Journal of Constructional Steel Research, Vol 43, pp. 17-42, 1997.

(Butcher *et al.*, 1968) Butcher E.G., Langdon-Thomas G.H., Bedford G.K. "Fire Car Park Buildings", Fire note 10, HMSO, U.K, July 1968.

(Byström *et al.*, 2014) Byström, A., Sjöström, J., Wickström, U., Lange D., Veljkovic, M. "Large scale test on a steel column exposed to localized fire", Journal of Structural Fire Engineering, Vol.5, nº2, 2014.

(Cajot *et al.*, 2003) Cajot, L.-G., Mathieu, J., Thomas, L. – "Les structures métalliques pour les parkings ouverts", La revue de Métallurgie-CIT, Novembre 2003, 8p.

(Cerfontaine, 2004) Cerfontaine F. "Etude de l'interaction entre moment de flexion et effort normal dans les assemblages boulonnés". PhD thesis presented at the University of Liège. Belgium, 2004.

(Chapman and Balakrishnan, 1964) Chapman J.C., Balakrishnan S. "Experiments on composite beams". The Structural Engineering, 42(11), 369–83, 1964.

(Cooke and Latham, 1987) Cooke G.M.E., Latham D.J. "The inherent fire resistance of a loaded steel framework". Steel Construction Today, 1, 49-58, 1987.

(Comeliau, 2009) Comeliau L., "Effects of the dynamic behaviour of steel structures further to a column loss (in French)", Master thesis, University of Liège, Belgium, 2009.

(Corus, 2004) Corus, 2004 – "Steel-framed car parks", Corus Construction & Industrial, 2004.

(Cwiklinski, 2001) Cwiklinski C. – "Parcs de stationnement en superstructure largement ventilés – Avis d'expert sur les scénarios d'incendie", Rapport final, INERIS DRA-CCw/MCh-2001-cgr22984, 2001, 26p.

(Demonceau, 2008) Demonceau J.F. "Steel and composite building frames: sway response under conventional loading and development of membrane effects in beams further to an exceptional action". PhD thesis presented at the University of Liège. Belgium, 2008.

(Demonceau and Jaspart, 2010) Demonceau J-F, Jaspart J-P. "Experimental test simulating a column loss in a composite frame", Advanced Steel Construction: an International Journal;6(3):891–913, 2010.

(Demonceau *et al.*, 2011) Demonceau J.-F., Comeliau L., Jaspart J.-P., "Robustness of building structures – Recent developments and adopted strategy", 6th European Conference on Steel and Composite Structures, EUROSTEEL, Budapest, Hungary, pp.2475-2480, 2011.

(Demonceau *et al.*, 2013) Demonceau J.F., Huvelle C., Comeliau L., Hoang L. V., Jaspart J.P., Fang C., et al. "Robustness of car parks against localised fire (Robustfire)", European Commission, Grant Agreement Number RFSR-CT-2008-00036, Final report, EUR 25864, 2013.

(Diário da República, 2008a) "Portaria nº1532/2008", Diário da República, 1ª série, N.º 250, 29 de Dezembro, 2008, p9050-9127.

(Diário da República, 2008b) "Decreto-Lei nº220/2008", Diário da República, 1ª série, N.º 220, 2008, p7903-7922.

(ECCS, 1993) ECCS, "Fire Safety in Open Car Parks", Modern Fire Engineering, Technical Committee 3, nº75, European Convention for Constructional Steelwork: Brussels, Belgium, 1993, 90p.

(EN 1990, 2002) "Eurocode – Basis of structural design", European committee for standardization, April 2002, 87p.

(EN 1991-1-1, 2002) "Eurocode 1: Actions on structures – Part 1-1: General actions – Densities, self-weight, imposed loads for buildings", European committee for standardization, April 2002, 44p.

(EN 1991-1-2, 2002) "Eurocode 1: Actions on structures – Part 1-2: General actions – Actions on structures exposed to fire", European committee for standardization, November 2002, 59p.

(EN 1991-1-7, 2006). Eurocode 1 – Actions on structures – Part 1–7: General actions – Accidental actions. European committee for standardization; July 2006.

(EN 1992-1-1, 2004). "Eurocode 2: Design of concrete structures - Part 1-1: General rules and rules for buildings", European committee for standardization, December 2004.

(EN 1992-1-2, 2004) "Eurocode 2: Design of concrete structures – Part 1-2: General rules – Structural fire design". European committee for standardization, December 2004.

(EN 1993-10, 1990). "Eurocode 3: Design of Steel Structures, Part 10: Structural Fire Design". Draft April 1990.

(EN 1993-1-2, 2005) "Eurocode 3: Design of steel structures – Part 1-2: General rules – Structural fire design", European committee for standardization, April 2005, 78p.

(EN 1993-1-8, 2005). "Eurocode 3: Design of steel structures - Part 1-8: Design of joints", European committee for standardization, May 2005.

(EN 1994-1-1, 2004). "Eurocode 4: Design of composite steel and concrete structures – Part 1-1: General rules and rules for buildings". European committee for standardization, December 2004.

(EN 1994-1-2, 2005) "Eurocode 4: Design of composite steel and concrete structures – Part 1-2: General rules – Structural fire design", European committee for standardization, August 2005, 109p.

(EN 10025-4, 2004) EN 10025–4:2004. Hot rolled products of structural steels – Part 4: Technical delivery conditions for thermomechanical rolled weldable fine grain structural steels. European committee for standardization; November 2004.

(Faber, 2011) Faber M, editor. Robustness of structures: final report of COST action TU0601. Prague, Czech Republic: Czech Technical University, Klokner Institute; 2011.

(Fang, 2012) Fang C., "Robustness of multi-storey steel-composite structures under localised fire", Ph.D. Thesis, Department of Civil Engineering, Imperial College London, UK, 2012.

(Fang *et al.*, 2011) Fang C., Izzuddin B.A., Elghazouli A.Y., Nethercot D.A. "Robustness of steel-composite building structures subject to localised fire", Fire Safety Journal 46, 348-363, 2011.

(Fang *et al.,* 2012) Fang C., Izzuddin B.A., Obiala R., Elghazouli A.Y., Nethercot D.A. "Robustness of multi-storey car parks under vehicule fire", Journal of Constructional Steel Research 75, p.72-84, 2012.

(Fang *et al.*, 2013) Fang C., Izzuddin B.A., Elghazouli A.Y., Nethercot D.A. "Robustness of multi-storey car parks under localised fire – Towards practical design recommendations", Journal of Constructional Steel Research 90, p.193-208, 2013.

(Ferraz, 2014) Ferraz G., "Thermal analysis of steel columns exposed to localised fires", Master Thesis, University of Coimbra, 2014.

(Foley *et al.*, 2008) Foley, C. M., Barnes, K. M., Schneeman, C. L. "Quantifying and Enhancing Robustness in Steel Structures: Part 2--Floor-Framing Systems", Engineering Journal, AISC, 45(4), pp. 267–287, 2008.

(Franssen *et al.*, 1995) Franssen J.M., Cooke G.M.E., Latham D.J. "Numerical Simulation of a Full Scale Fire Test on a Loaded Steel Framework". Journal of Constructional Steel Research, 35, 377-408, 1995.

(Franssen and Vila Real, 2010) Franssen J.-M., Vila Real P. "Fire Design of Steel Structures", ECCS Eurocode Design Manuals, Ernst & Sohn, 1st Edition, 2010.

(Fraud *et al.*, 2004) Fraud C., Zhao B., Joyeux D., Kruppa J. – "Guide pour la vérification du comportement au feu de parcs de stationnement largement ventilés en superstructure métallique", CTICM, INSI – 03/233d – BZ/PB, 2004, 75p.

(Gewain, 1973) Gewain, R. G. "Fire Experience and Fire Tests in Automobile Parking Structures", Fire Journal, 67 (4): 50-54, 1973.

(Giżejowski *et al.*, 2013) Gizejowski M.A., Szwed A., Saleh A. A. K., Barcewicz W. "Joint moment-rotation characteristic in light of experimental simulations of frame column loss", Journal of Civil Engineering, Environment and Architecture, z. 60 (2/13), 51 – 76, 2013.

(Hanus, 2010) Hanus F., "Analysis of simple connections in steel structures subjected to natural fires", Ph.D. Thesis, University of Liège, Belgium, 2010.

(Hanus *et al.*, 2011) Hanus F., Zilli G., Franssen J.-M. "Behaviour of Grade 8.8 bolts under natural fire conditions - Tests and model", Journal of Constr. Steel Research 67, 1292-1298, 2011.

(Haremza *et al.*, 2009) Haremza C., Santiago A., Simões da Silva L., Franssen J.M. "Benchmark example 2: Composite beam". Internal document, University of Coimbra, ROBUSTFIRE Project, September 2009.

(Haremza *et al.*, 2013a) Cécile Haremza, Aldina Santiago, Luís S. da Silva, "Experimental behaviour of heated composite steel-concrete joints subject to variable bending moments and axial forces", Engineering Structures 51, p150-165, 2013.

(Haremza *et al.*, 2013b) Haremza, C., Santiago, A., Simões da Silva, L. "Design of steel and composite open car parks under fire", International Journal of Advanced Steel Construction, Vol. 9, No. 4, p.350-368, Dec. 2013.

(Hasemi and Tokunaga, 1984) Hasemi Y., Tokunaga T., "Flame geometry effects on the buoyant plumes from turbulent diffusion flames", Fire Science and Technology, Vol.4-1, pp.15-26, 1984.

(Heidarpour, 2007) Heidarpour A. "Behaviour of steel and steel-concrete composite beams and beam-to-column connections at elevated temperatures". Ph.D. Thesis, School of Civil and Environmental Engineering, the University of New South Wales, Sydney, Australia, November 2007.

(Heskestad, 1995) Heskestad, G. "Fire plumes", The SFPE Handbook of Fire Protection Engineering, Quincy, Mass.: National Fire Protection Association, pp. 2-9, 1995.

(Hu, 2009) Hu Y., "Robustness of flexible end-plate connections under fire conditions", Ph.D. Thesis, University of Sheffield, Dep. of Civil and Structural Eng., 2009.

(Huang *et al.*, 1999) Huang Z., Burgess I.W., Plank R.J. "The influence of shear connectors on the behaviour of composite steel-framed buildings in fire". Journal of Constructional Steel Research, 51, 219-237, 1999.

(Huang *et al.*, 2006) Huang Z.F., Tan K.H., Ting S.K., "Heating rate and boundary restraint effects on fire resistance of steel columns with creep", Engineering Structures 28, 805-817, 2006.

(ISO 834-1, 1999) "Fire-resistance tests - Elements of building construction - Part 1: General requirements", International Standard, 1st Edition, 1999.

(Imedio *et al.*, 2004) Imedio O., Gómez F. J., Caballero L., Valiente A. "Ductilidad a alta temperatura de aceros de construcción de los tipos S460 y S275", Anales de Mecánica de la Fractura, 21, 2004.

(Izzuddin, 1991) Izzuddin, B.A. "Nonlinear Dynamic Analysis of Framed Structures". PhD Thesis, Department of Civil Engineering, Imperial College, University of London, UK, 1991.

(Izzuddin *et al.*, 2007) Izzuddin, B.A., Vlassis, A.G., Elghazouli, A.Y., and Nethercot, D.A.. "Assessment of Progressive Collapse in Multi-Storey Buildings". Proceedings of the Institution of Civil Engineers, Structures and Buildings, 160(4), pp. 197-205, 2007.

(Izzuddin *et al.*, 2008) Izzuddin, B.A., Vlassis, A.G., Elghazouli, A.Y., and Nethercot, D.A. "Progressive Collapse of Multi-Storey Buildings due to Sudden Column Loss - Part I: Simplified Assessment Framework". Engineering Structures 30, 1308-1318, 2008.

(Jaspart, 1991) Jaspart, J-P. Etude de la semi-rigidité des noeuds poutre-colonne et son influence sur la résistance des ossatures en acier (in French). PhD thesis, Department MSM, University of Liège, Belgium; 1991.

(Jaspart, 1999) Jaspart, J.-P. "Semi-rigid behaviour of civil engineering structural connections – Recent advances in the field of structural steel joints and their representation in the building frame analysis and design process", COST C1, Edited by Jaspart J.-P., European Commission, 1999.

(Jaspart and Demonceau, 2007) Jaspart, J.-P., Demonceau, J.-F. "Contribution to the derivation of robustness requirements for steel and composite structures", 5th International Conference on Advances in Steel Structures, Editors: J.Y. Richard Liew & Y.S. Choo, Singapore, 5-7 December, 2007.

(Jaspart *et al.*, 2008) Jaspart J.P., Demonceau J.F., Nethercot D. A., Simões da Silva L., Zhao B., Dhima D., Gens F., Obiala R., *et al.* "Proposal overview submission form, RFCS ROBUSTFIRE project", European commission, 2008.

(Jaspart *et al.*, 2011) Jaspart J.P., Demonceau J.F., Comeliau L., "Standards and design guides", Robustness of steel structures, Spring school in Coimbra, Portugal, May 2011.

(Joyeux *et al.*, 2001) Joyeux D., Kruppa J., Zhao B. "Application de l'ingénierie de la sécurité incendie à un parc à voitures en superstructure". Construction Métallique, n° 1, 2001 (in French).

(Joyeux *et al.*, 2002) Joyeux D., Kruppa, J., Cajot L.-G., Schleich J.-B., Van de Leur P., Twilt L. "Demonstration of real fire tests in car parks and high buildings", European Commission, Contract no 7215-PP/025 (1993 – 1996), CTICM, Final Report, EUR 20466 EN, 2002, 168p.

(Kamikawa *et al.*, 2003) Kamikawa, D., Hasemi, Y., Wakamatsu, T. & Kagiya, K., 2003. Experimental Flame Heat Transfer Correlations For A Steel Column Adjacent To And Surrounded By A Pool Fire. Fire Safety Science 7, pp. 989-1000, 2003.

(Kato *et al.*, 1990) Kato, B., Aoki, H., Yamanouchi, H. "Standardized mathematical expression for stress-strain relations of structural steel under monotonic and uniaxial tension loading", Materials and Structures/Matériaux et Constructions, 23, 47-58, 1990.

(Kodur and Dwaikat, 2010) Kodur V.K.R., Dwaikat M.M.S. "Effect of high temperature creep on the fire response of restrained steel beams", Materials and Structures 43, p. 1327-1341, 2010.

(Kozłowski *et al.*, 2011) Kozłowski A., Giżejowski M., Ślęczka L., Pisarek Z., Saleh B., "Experimental investigations of the joint behaviour – Robustness assessment of steel and steel-concrete composite frames", 6th European Conference on Steel and Composite Structures, EUROSTEEL, Budapest, Hungary, pp.339-344, 2011.

(Kruppa and Zhao, 1995) Kruppa J., Zhao B. "Fire resistance of composite beams to Eurocode 4 Part 1.2". Journal of Constructional Steel Research, 33, 51-69, 1995.

(Kuhlmann *et al.*, 1998) Kuhlmann U., Davison J.B., Kattner M. "Structural systems and rotation capacity", in: Proceedings of the COST Conference on Control of the Semi-rigid Behaviour of Civil Engineering Structural Connections, Liege, Belgium, 1998, pp. 167–76.

(Kuhlmann *et al.*, 2007) Kuhlmann U., Rölle L., Jaspart J.-P., Demonceau J.-F., Vassart O., Weynand K., Ziller C., Busse E., Lendering M., Zandonini R., Baldassino N., "Design Guidance, Handbook-001". ROBUSTNESS: RFS-CR-04046., 2007.

(Kuhlmann *et al.*, 2009) Kuhlmann U., Rölle L., Jaspart J.-P., Demonceau J.-F., Vassart O., Weynand K., Ziller C., Busse E., Lendering M., Zandonini R., Baldassino N., "Robust structures by joint ductility", Research Fund for Coal and Steel, Contract Nº RFSR-CT-2004-00046, Final report, European commission, EUR 23611 EN, 2009.

(Le Pense, 2002), Le Pense P., "Les parkings aériens en structure acier: développements récents / Multi-storey car parks in steel structure: last developments", La Revue de Métallurgie-CIT, p867-874, Octobre 2002.

(Li, 2004) Li Y. "Assessement of Vehicle Fires in New Zealand Parking Buildings". Fire Engineering Research Report 04/2, Master Thesis, University of Canterbury, New Zealand, May 2004.

(Li and Spearpoint, 2007) Li Y., Spearpoint M. "Analysis of Vehicle Fire Statistics in New Zealand Parking Buildings". Fire Technology, 43, 93-106, 2007.

(Lima *et al.*, 2004) Lima L, Simões da Silva L, Vellasco P, Andrade S. Experimental behaviour of extended end-plate beam-to-column joints subjected to bending and axial force. Eng Struct 2004;26(10):1333–47.

(Liu, 2010) Liu J.L., "Preventing progressive collapse through strengthening beam-to-column connection, Part 1: Theoretical analysis", Journal of Constructional Steel Research 66, 229-237, 2010.

(Lopes *et al.*, 2013) Lopes F., Santiago A., Igbal N., Veljkovic M., da Silva J. e Simões da Silva L., "Evaluation of the reverse channel connections to cft columns in the full-scale fire tests"; 2° CILASCI - Congresso Ibero-Latino-Americano sobre Segurança contra Incêndio, pp. 385-394, Coimbra, June 2013.

(Luu, 2009) Luu N.N.H. "Structural response of steel and composite building frames further to an impact leading to the loss of a column", PhD Thesis, University of Liège, Belgium, 2009.

(Mangs and Keski-Rahkonen, 1994) Mangs J., Keski-Rahkonen O. "Characterisation of the Fire Behaviour of a Burning Passenger Car. Part I: Car fire experiments." Fire Safety Journal, 23, 17 – 35, 1994.

(Moniteur Belge, 2007) "Arrêté royal fixant les mesures en matière de prévention contre l'incendie et l'explosion auxquelles les parkings fermés doivent satisfaire pour le stationnement des véhicules LPG", Moniteur Belge, Belgisch Staatsblad. Ed. 3, 33997, 20 of June, 2007, p33997.

(Morovat *et al.*, 2012) Morovat M. A., Engelhardt M. D., Helwig T. A., Taleff E. M., "High-temperature creep buckling phenomenon of steel columns subjected to fire", 7th International Conference on Structures in Fire, M. Fontana, A. Frangi, M. Knobloch (Eds.), Zurich, Switzerland, June 6-8, 2012.

(Nethercot, 2011) Nethercot D.A., "Design of building structures to improve their ressitance to progressive collapse", The twelfth east asia-pacific conference on structural engineering and construction, Procedia Engineering 14, 1-13, 2011.

(Nguyen and Kim, 2009) Nguyen H. T., Kim S. E. "Finite element modelling of push-out tests for large stud shear connectors", Journal of Constructional Steel Research 65, p.1909-1920, 2009.

(NP EN 206-1, 2007) "Concrete – Part 1: Specification, performance, production and conformity", Norma Portuguesa, Instituto Português da Qualidade, Portugal, 2007.

(NP EN 1991-1-2, 2010) "Eurocódigo 1: Acções em estruturas – Parte 1-2: Acções gerais – Acções em estruturas expostas ao fogo", Instituto Português da Qualidade, 2010, p63.

(OneSteel, 2004) "Economical Carparks – A Design Guide". Australia, 2nd edition, 2004.

(Pereira, 2012) Pereira, M. "Robustness of multi-storey steel-composite buildings under column loss: rate-sensitivity and probabilistic framework", Ph.D. Thesis, Department of Civil Engineering, Imperial College London, UK, 2012.

(Qiuang *et al.*, 2012) Qiuang X, Bijlaard F, Kolstein H. "Deterioration of mechanical properties of high strength structural steel S460N under steady state fire condition", Mater Des 2012; 36:438-42, 2012.

(Qureshi *et al.*, 2011) Qureshi J., Lam D., Ye J. "The influence of profiled sheeting thickness and shear connector's position on strength and ductility of headed shear connector", Engineering Structures 33, p.1643-1656, 2011.

(Riaux, 1980) Riaux H. "Comportement à l'incendie des assemblages simples boulonnés", Ph.D. Thesis, INSA of Rennes, 1980.

(Richard Liew *et al.*, 2004) Richard liew J.Y., Teo T.H., Shanmugam N.E. "Composite joints subject to reversal of loading – Part 2: analytical assessments", Journal of Constructional Steel Research, p.247-268, 2004.

(Santiago, 2008) Santiago A. "Behaviour of beam-to-column steel joints under natural fire". Ph.D. Thesis, Department of Civil Engineering, University of Coimbra, 2008.

(Santiago *et al.*, 2009) Santiago A., Haremza C., Simões da Silva L. and Rodrigues J.P. "Numerical Behaviour of Steel Columns subject to Localized Fire Loading". Proceedings of the Twelfth International Conference on Civil, Structural and Environmental Engineering Computing, B.H.V. Topping, L.F., Costa Neves and R.C. Barros, (Editors), Civil-Comp Press, Stirlingshire, Scotland, 2009.

(Sarraj *et al.*, 2007) Sarraj M., Burgess I.W., Davison J.B., Plank R.J. "Development of a component model approach to fin-plate connections in fire", Proceedings of the 3rd International Conference of Steel and Composite Structures (Eds.: Wang Y.W., Choi C.K.), 549-555, Manchester, U.K., 2007.

(Schleich *et al.*, 1999a) Schleich J.-B., Cajot L.-G., Pierre M., Brasseur M., Franssen J.-M., Kruppa J. et al., "Development of Design Rules for Steel Structures Subjected to Natural Fires in Closed Car Parks", European Commission, C.E.C. Research 7210-SA/518. Final Report EUR 18867 EN, 154p, 1999.

(Schleich *et al.*, 1999b) Schleich J.B., Cajot L.G., Pierre M., Brasseur M., Franssen J.M., Kruppa J., Joyeux D., Twilt L., Van Oerle J., Aurtenetxe G. "Development of design rules for steel structures subjected to natural fires in large compartments". European Commission, Contract no 7210-SA/211/318/518/620/933, 1999.

(Schneider and Lange, 2009) Schneider R, Lange J. Constitutive equations of structural steel S460 at high temperatures. In: Nordic steel construction conference, Sweden; 2009. p. 204–11.

(Simões da Silva *et al.*, 2001) Simões da Silva L., Santiago A., Vila Real P., "A component model for the behaviour of steel joints at elevated temperatures", Journal of Constructional Steel Research 57, 1169-1195, 2001.

(Simões da Silva *et al.*, 2002) Simoes da Silva L., Santiago A., Vila Real P., "Post-limit stiffness and ductility of end-plate beam-to-column steel joints", Computers & Structures 80, 515–531, 2002.

(Simões da Silva *et al.*, 2003) Simões da Silva L, Neves L, Baniotopoulos L, Perdikaris P, Zygomalas M, Bosiljkov V, *et al.* "Evaluation of structural robustness of members and connections", In: Simões da Silva L, Mendes J, editors. Proceedings of the COST C12 seminar on improvement of building's structural quality by new technologies, European Commission, Brussels; 2003. p. 155–74.

(Simões da Silva *et al.*, 2004) Simões da Silva L, Lima L, Vellasco P, Andrade S. Behaviour of flush end-plate beam-to-column joints subjected to bending and axial force. Int J Steel Compos Struct;4(2):77–94, 2004.

(Simões da Silva *et al.*, 2005) Simões da Silva L., Santiago A., Vila Real P., Moore D. "Behaviour of steel joints under fire loading". The Second International Conference on Steel and Composite Structures, Seoul, Korea, September 2-4, 2004; International Journal of Steel and Composite Structures 5(6), 485-513, 2005.

(Simões da Silva *et al.*, 2013) Simões da Silva L., Santiago A., Lopes F., Veljkovic M., Heistermann T., Iqbal N., Wald F., Jána T., *et al.*, "Design of composite joints for improved fire robustness", Final Technical Report, COMPFIRE project RFSR-CT-2009-00021, 2013.

(Sokol, 2009) Sokol, Z., "Report 3.2.2.2-13 - Simplified Model For Temperature Prediction Of Columns", Prague: CIDEAS, 2009.

(Sulong, 2007) Ramli Sulong N.H. "Structural fire performance of steel connections". Ph.D. Thesis, Department of Civil and Environmental Engineering, Imperial College London, South Kensington Campus, London, UK, 2007.

(Tonicello *et al.*, 2012) Tonicello E., Vassart O., Zanon R., Franssen J.-M. "Structural fire design and optimization of a building", Structural Engineering International 4, pp.541-544, 2012.

(Tondini *et al.*, 2014) Tondini N., Morbioli A., Vassart O., Lechêne S., Franssen J.-M., "An integrated modelling strategy between FDS and SAFIR: The analysis of the fire performance of a composite steel-concrete open car park", in Li G.-Q., Kodur V. K. R., Jiang S.-C., Jiang J., Chen S.-W., Lou G.-B. (Eds.) - 8th International Conference on Structures in Fire, Shanghai, China, June 11-13, pp.927-934, 2014.

(Vassart *et al.*, 2011) Vassart O, Zanon R, Thauvoye C, Cajot LG. New Analytical Model for the Calculation of Steel Columns Subjected to Localised Fire. SEWC, Como, Italy, 2011.

(Vila Real and Franssen, 2010) Vila Real, P., Franssen, J. M. – Elefir-EN V1.2.3, Software for fire design of steel structural members according the Eurocode 3, 2010. http://elefiren.web.ua.pt.

(Vlassis *et al.,* 2008) Vlassis A.G., Izzuddin B.A., Elghazouli A.Y., Nethercot D.A. "Progressive collapse of multi-storey buildings due to sudden column loss – Part II: application", Engineering Structures 30, 1424-1438, 2008.

(Wainman and Kirby, 1988) Wainman D.E., Kirby B.R. "Compendium of UK standard fire test data, unprotected structural steel — 1". Ref. No. RS/RSC/S10328/1/87/B. Rotherham (UK): Swinden Laboratories, British Steel Corporation, 1988.

(Wald *et al.*, 2009) Wald F., Chlouba J., Uhlír A., Kallerová P., Stujberová M. "Temperatures during fire tests on structure and its prediction according to Eurocodes". Fire Safety Journal, p. 135–146, 2009.

(Wang, 2002) Wang Y.C. "Steel and composite structures – Behaviour and design for fire safety". Spon Press, 2002.

(Yang and Tan, 2011a) Yang B., Tan K.H., "Different types of steel joints under catenary action – Part 1: Experimental Tests", 6th European Conference on Steel and Composite Structures, EUROSTEEL, Budapest, Hungary, pp.291-296, 2011.

(Yang and Tan, 2011b) Yang B., Tan K.H., "Different types of steel joints under catenary action – Part 2: Numerical Simulations", 6th European Conference on Steel and Composite Structures, EUROSTEEL, Budapest, Hungary, pp.297-302, 2011.

(Yang and Tan, 2012) Yang B., Tan K.H., "Numerical analyses of steel beam-column joints subjected to catenary action", Journal of Constructional Steel Research 70, 1-11, 2012.

(Yang and Tan, 2013) Yang B., Tan K.H., "Experimental tests of different types of bolted steel beam-column joints under a central-column-removal scenario", Engineering Structures 54, p.112-130, 2013.

(Yu *et al.*, 2008) Hongxia Yu, I. W. Burgess, J.B. Davison, R.J. Plank, "Numerical simulation of bolted steel connections in fire using explicit dynamic analysis", Journal of Constructional Steel Research, 64 (5), p. 515-525, 2008.

(Zhang *et al.*, 2014) Zhang C., Gross J. L., Choe L., "Behavior of steel components subjected to localized fire", in Li G.-Q., Kodur V. K. R., Jiang S.-C., Jiang J., Chen S.-W., Lou G.-B. (Eds.) - 8th International Conference on Structures in Fire, Shanghai, China, June 11-13, pp.171-178, 2014.

(Zhao and Kruppa, 2004) Zhao B., Kruppa J. "Structural behaviour of an open car park under real fire scenarios". Second International Workshop "Structures in Fire" - Christchurch – March 2002; Fire and Materials, 28, 269-280, 2004.

(Zhao *et al.*, 2011) Zhao B., Roosefid M., Breunese A., Koutlas G., Zilli G., Franssen J.M., Hanus F. "Connections of Steel and Composite Structures under Natural Fire Conditions (COSSFIRE)". Contract number RFSR-CT-2006-00028, Final report, EUR 25046 EN, 2011.

(Zoetemeijer, 1974) Zoetemeijer, P. "A design method for tension side of statically-loaded bolted beam-to-column joints", Heron, 20(1), pp. 1-59, 1974.

Appendix A

A Control tests results

A.1 Steel coupons dimension

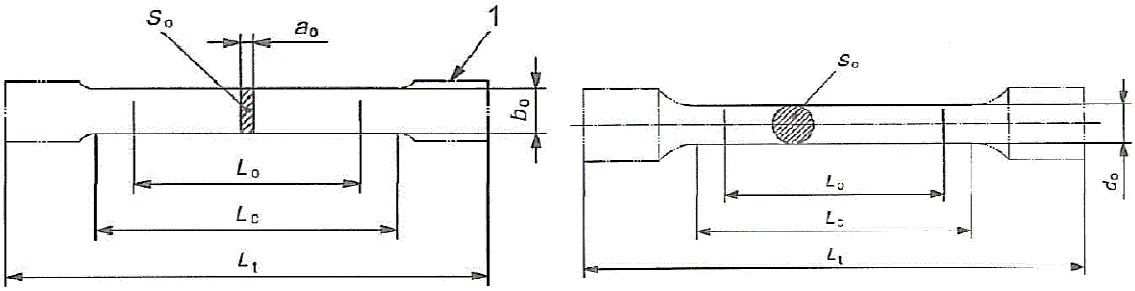

a) b)

Figure A.1: a) Rectangular and b) cylindrical cross-section steel coupons

Table A.1: Rectangular steel coupon dimensions for structural steel tested at ambient temperature (W- web; F- flange)

Steel	Thickness a_0 mm	Width b_0 mm	Original gauge length L_0 mm	Parallel length L_c mm	Total length L_t mm	Radius r mm	Original cross-sectional area S_0 mm
S355W	11	20	84	107	331	12	220
S460W	11	20	84	107	331	12	220
S355F	17	25	116	148	372	12	425
S460F	19	25	123	156	380	12	475

Table A.2: Cylindrical steel coupon dimensions for structural steel tested at elevated temperatures, and bolts tested at ambient and elevated temperatures

Steel	Thickness a_0 mm	Width b_0 mm	Original gauge length L_0 mm	Parallel length L_c mm	Total length L_t mm	Radius r mm	Original cross-sectional area S_0 mm
S355W	11						
S460W	11	5	28	--	38	Min. 2	20
S355F	17						
S460F	19	10	55	--	75	--	79
Bolt M30	30	5	35	28	--	7.5	20

A.2 Tensile coupon tests results

A.2.1 Tests results of structural steel S355J0 + M

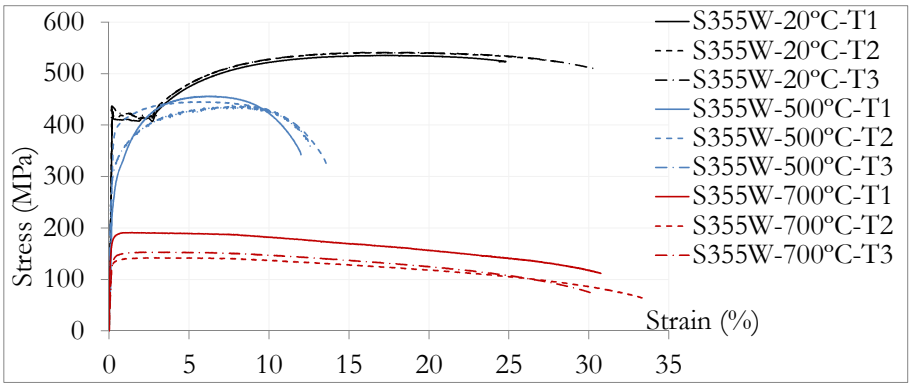

Figure A.2: Stress-strain curves obtained from the tensile coupon tests (T) performed at 20ºC, 500ºC and 700ºC for steel S355J0+M, from steel profile IPE 550 (W- web)

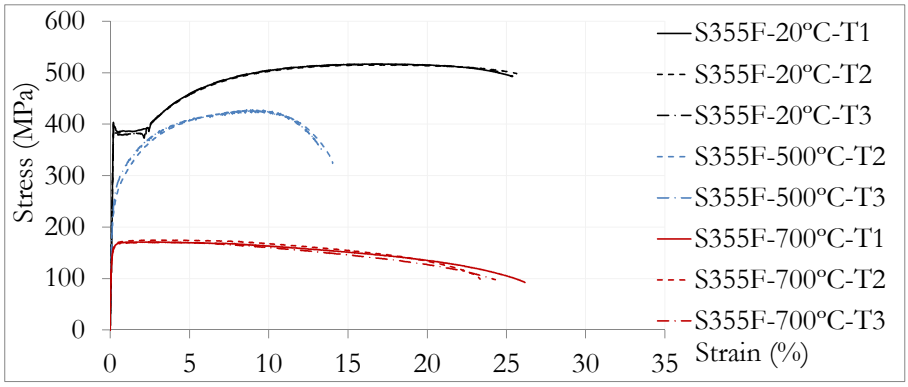

Figure A.3: Stress-strain curves obtained from tensile coupon tests (T) performed at 20ºC, 500ºC and 700ºC for steel S355J0+M, from steel profile IPE 550 (F- flange)

Table A.3: Mechanical properties of steel S355 J0+M obtained from tensile coupon tests

Steel		Temp. (ºC)	Yield strength R_e (MPa)	Tensile strength R_m (MPa)	Elongation after fracture A (%)
Flange of IPE 550	T1	20	403	517	32
	T2	20	387	516	33
	T3	20	397	517	32.4
	T1	500	437	445	31.6
	T2	500	318	429	31.6
	T3	500	334	432	27.7
	T1	700	170	171	52.5
	T2	700	173	175	44.1
	T3	700	164	166	49.9
Web of IPE 550	T1	20	425	535	30
	T2	20	435	540	31.9
	T3	20	437	541	31.4
	T1	500	357	447	23.7
	T2	500	412	440	22.5
	T3	500	363	433	30.1
	T1	700	140	142	65.9
	T2	700	190	190	68.6
	T3	700	151	153	59.5

A.2.2 Tests results of structural steel S460M

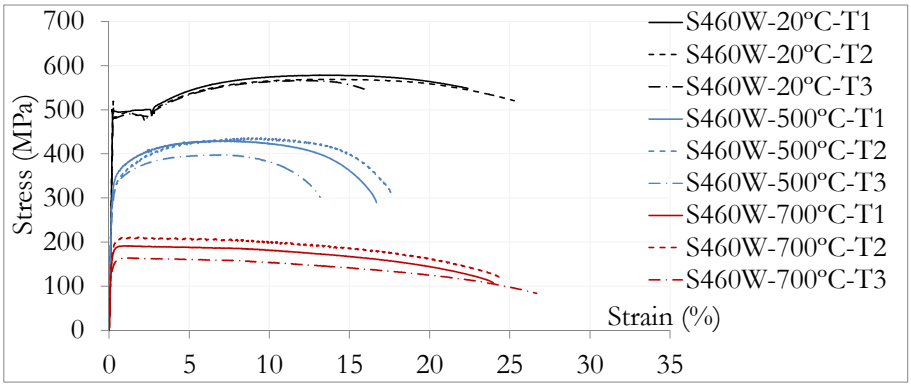

Figure A.4: Stress-strain curves obtained from the tensile tests (T) performed at 20ºC, 500ºC and 700ºC for steel S460M, from HEB 300 (W- web)

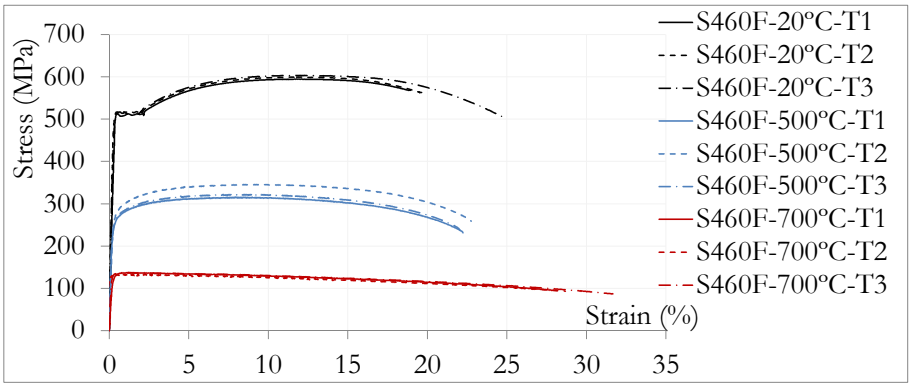

Figure A.5: Stress-strain curves obtained from the tensile tests (T) performed at 20ºC, 500ºC and 700ºC for steel S460M, from HEB 300 (F- flange)

Table A.4: Mechanical properties of steels S460M from tensile coupon tests

Steel		Temp. (ºC)	Yield strength R_e (MPa)	Tensile strength R_m (MPa)	Elongation after fracture A (%)
Flange of HEB 300	T1	20	513	595	26.5
	T2	20	517	599	26.8
	T3	20	517	603	28.3
	T1	500	284	315	27.2
	T2	500	307	345	21.2
	T3	500	284	315	21.2
	T1	700	137	137	42.8
	T2	700	132	134	40.7
	T3	700	136	137	41.1
Web of HEB 300	T1	20	500	579	25.6
	T2	20	520	569	26.4
	T3	20	491	566	24.8
	T1	500	382	430	31.3
	T2	500	368	436	26.8
	T3	500	356	397	28.5
	T1	700	186	190	48.3
	T2	700	209	211	52.3
	T3	700	163	164	53.7

A.2.3 Tests results of bolts M30, grade 10.9

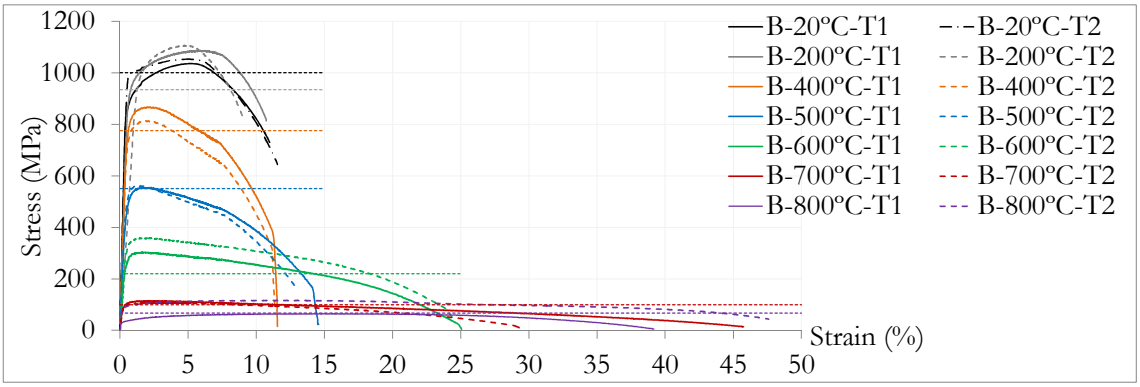

Figure A.6: Stress-strain curves of bolts M30 grade 10.9 at 20°C, 200°C, 400°C, 500°C, 600°C, 700°C and 800°C - Ultimate tensile strength values from EN 1993-1-2 (2005) are shown by the horizontal dashed curves

Table A.5: Mechanical properties of steel from bolts M30, grade 10.9

	Temperature (°C)	Yield strength $R_{p0.2\%}$ (MPa)	Tensile strength R_m (MPa)	Elongation after fracture A (%)
T1	20	870	1035	15.1
T2	20	733	733	18
T3	20	995	1052	15.5
T1	200	935	1086	14.2
T2	200	973	1107	14.8
T1	400	804	868	17.9
T2	400	761	813	16.7
T1	500	497	554	23.2
T2	500	520	561	22.7
T1	600	279	305	42
T2	600	317	360	41.7
T1	700	102	115	68
T2	700	95	108	54
T1	800	33	65	80.4
T2	800	86	117	73.4

A.3 Standardized stress-strain curves of structural steels and bolts

A.3.1 Standardized stress-strain curves

From the tensile tests results, standardized stress-strain curves of structural steels S355J0+M and S460M are defined using: i) at ambient temperature, the Menegotto-Pinto model (for materials of sharp-knee type) (Kato *et al.*, 1990), and ii) at elevated temperatures, the stress-strain relationship for carbon steel defined in EN 1994-1-2 (2005), without any strain hardening. The reduction factors for the effective yield strength, the proportional

limit and the elastic modulus at elevated temperatures are calculated based on the measured value at 20°C.

The evolution of mechanical properties (yield strength) with temperatures of structural steels S355J0+M and S460M determined from the steady-state tests are illustrated in Figure A.7, and it is shown that all the tests results except for the column flange (S460M) at 500°C are above the Eurocode recommended values. As no tensile tests are performed for the steel end-plate (due to no available material), the standardized stress-strain curve is defined based on the beam web material properties measured at ambient temperature. At elevated temperatures, reduction factors defined in EN 1994-1-2 (2005) are considered.

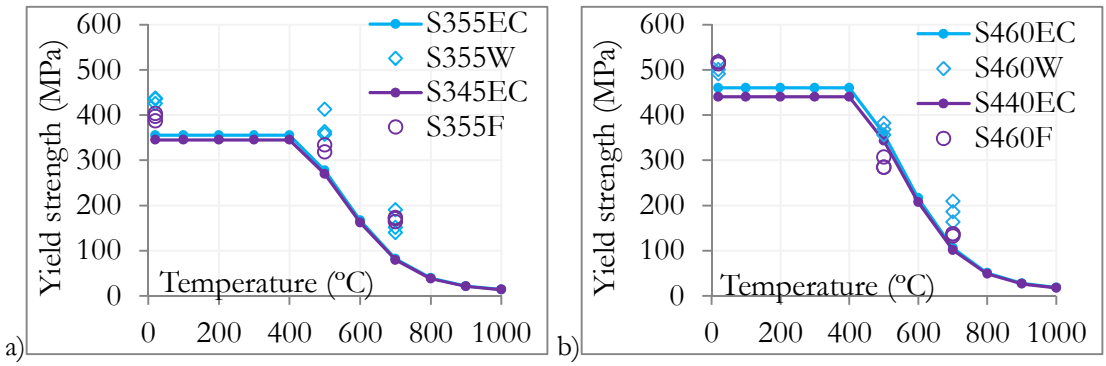

Figure A.7: Temperature-depending yield strength reduction for a) S355J0(+M) and b) S460M – Comparison of tests results against Eurocode values (EC: Eurocode; W: web; F: flange)

A.3.1.1 At ambient temperature

Figure A.8 shows the standardized curves that were defined using the Menegotto-Pinto model for materials of sharp-knee type (Kato *et al.*, 1990) based on the stress-strain curves from the tensile tests. This model is used to consider the strain hardening measured by the tensile tests at ambient temperature. Table A.6 presents the elastic modulus, which is determined as the initial slope of the stress-strain curves at ambient temperature.

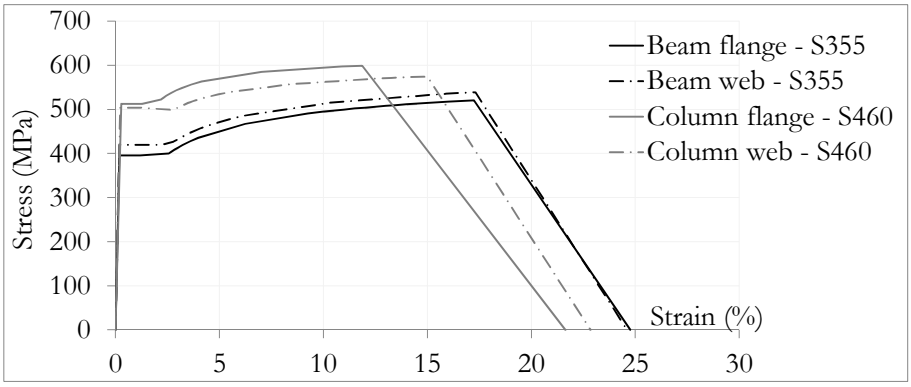

Figure A.8: Standardized stress-strain curves of steel from the webs and flanges of columns HEB 300 (S460) and beams IPE 550 (S355)

Table A.6: Elastic modulus of structural steel S355J0+M and S460M (average values from all the tests at each temperature)

		Elastic modulus (N/mm²)		
		20ºC	500ºC	700ºC
Beam IPE 550 - S355J0+M	Flange	207 650	135 525	93 960
	Web	221 490	138 667	72 204
Column HEB 300 - S460M	Flange	183 800	133 213	78 291
	Web	219 597	163 795	82 627

A.3.1.2 At elevated temperatures

At elevated temperatures, EN 1993-1-2 (2005) defines the stress-strain relationship for carbon steel (Figure A.9). The effective yield strength $f_{y,\theta}$, the proportional limit $f_{p,\theta}$ and the slope of the linear elastic range $E_{a,\theta}$ are the variables that define the stress-strain curve of the material. For the steel stress-strain relationship, the reduction factors are defined as:

- Effective yield strength, relative to yield strength at 20ºC: $k_{y,\theta} = f_{y,\theta}/f_{y,20ºC}$
- Proportional limit, relative to yield strength at 20ºC: $k_{p,\theta} = f_{p,\theta}/f_{y,20ºC}$
- Slope of linear elastic range, relative to slope at 20ºC: $k_{E,\theta} = E_{a,\theta}/E_{a,20ºC}$

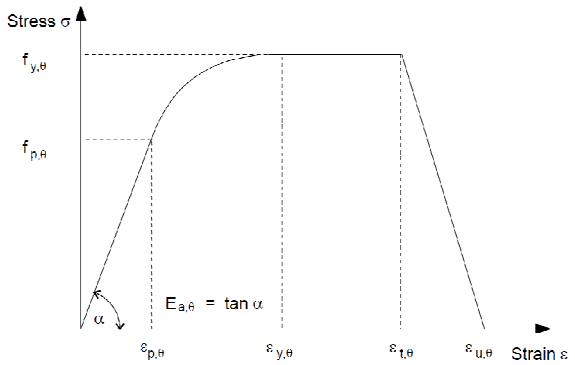

Figure A.9: Stress-strain relationship for carbon steel at elevated temperatures (EN 1993-1.2: 2005)

The reduction factors for the effective yield strength at elevated temperatures are calculated at 500ºC and 700ºC based on the tests results relative to measured yield strength at 20°C (Figure A.10 and Table A.7); at 600ºC, linear interpolation is used.

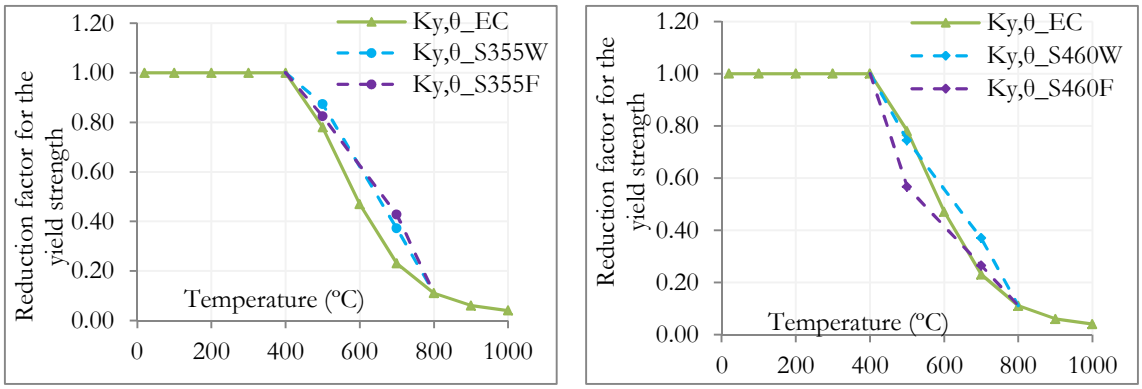

Figure A.10: Temperature-depending yield strength reduction factor for a) S355J0+M and b) S460M – Comparison of tests results against Eurocode values

Table A.7: Reduction factors for the yield strength of structural steel S355J0+M and S460M at temperatures 20°C-1000°C - Values based on steady-state test results and Eurocode values

	Reduction factor (relative to f_y) for effective yield strength: $k_{y,\theta}=f_{y,\theta}/f_y$				
θ (°C)	EN 1993-1-2	S355J0 + M		S460M	
		Web	Flange	Web	Flange
20	1.00	Eurocode values	Eurocode values	Eurocode values	Eurocode values
100	1.00				
200	1.00				
300	1.00				
400	1.00				
500	0.78	***0.87***	***0.82***	***0.74***	***0.57***
600	0.47	0.62	0.63	0.56	0.42
700	0.23	***0.37***	***0.43***	***0.37***	***0.26***
800	0.11	Eurocode values	Eurocode values	Eurocode values	Eurocode values
900	0.06				
1000	0.04				
1100	0.02				
1200	0.00				

The reduction factors for the proportional limit and the elastic modulus (tangent modulus) at elevated temperatures are defined at 500°C and 700°C (see respectively Figure A.11 and Table A.8, and Figure A.12 and Table A.9); between 100°C and 500°C, and at 600°C, linear interpolation is used. Because of the non-linear nature of stress-strain characteristics at elevated temperatures, the tangent modulus is used; however, it depends on the proof strain at which the elastic modulus is measured (Hu, 2009).

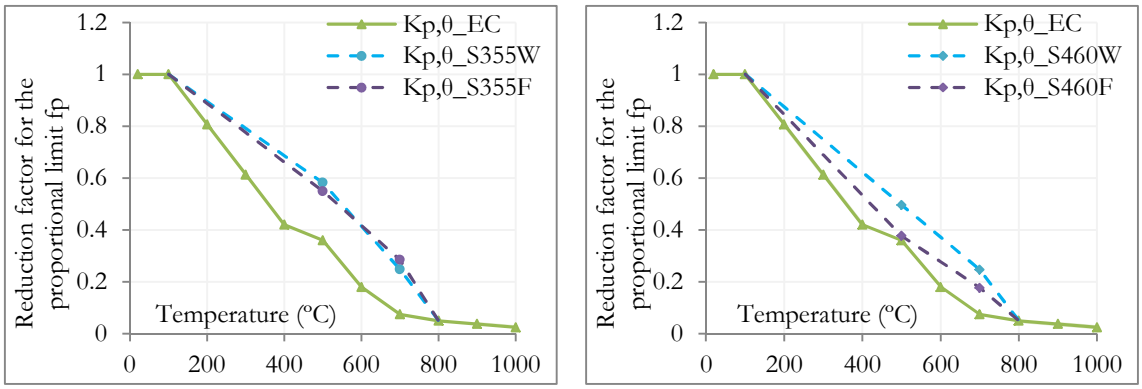

Figure A.11: Temperature-depending proportional limit reduction factor for a) S355J0+M and b) S460M – Comparison of tests results against Eurocode values

Table A.8: Reduction factors for the proportional limit of structural steel S355J0+M and S460M at temperatures 20°C-1000°C - Values based on steady-state test results and Eurocode values

	Reduction factor (relative to f_y) for proportional limit: $k_{p,\theta}=f_{p,\theta}/f_y$				
θ (°C)	EN 1993-1-2	S355J0 + M		S460M	
		Web	Flange	Web	Flange
20	1.00	Eurocode values	Eurocode values	Eurocode values	Eurocode values
100	1.00				
200	0.807	0.90	0.89	0.87	0.84
300	0.613	0.79	0.77	0.75	0.69
400	0.420	0.69	0.66	0.62	0.53
500	0.360	***0.58***	***0.55***	***0.50***	***0.38***
600	0.180	0.41	0.42	0.37	0.28
700	0.075	***0.25***	***0.28***	***0.25***	***0.18***
800	0.050	Eurocode values	Eurocode values	Eurocode values	Eurocode values
900	0.0375				
1000	0.025				
1100	0.0125				
1200	0.00				

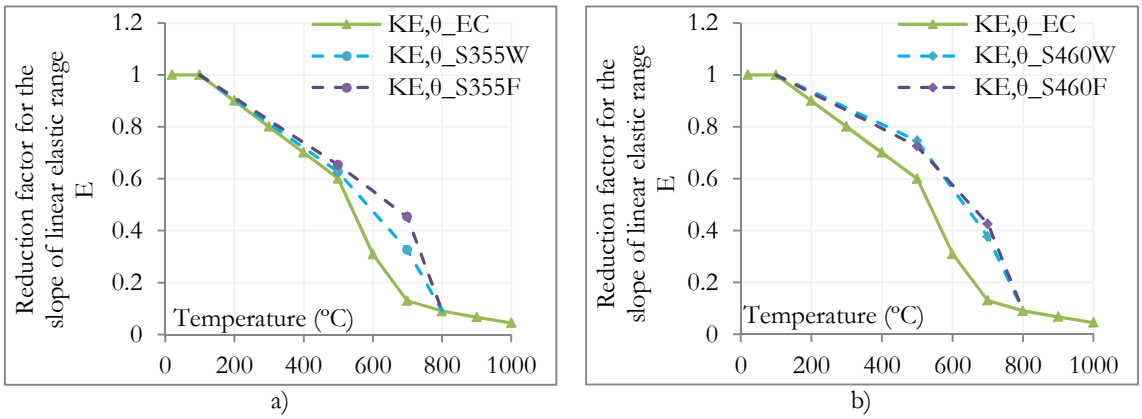

Figure A.12: Temperature-depending yield strength reduction factor for a) S355J0+M and b) S460M – Comparison of tests results against Eurocode values

Table A.9: Reduction factors for the elastic modulus of structural steel S355J0+M and S460M at temperatures 20°C-1000°C - Values based on steady-state test results and Eurocode values

θ (°C)	Reduction factor (relative to E_a) for the slope of the linear elastic range: $k_{E,\theta} = E_{a,\theta}/E_a$				
	EN 1993-1-2 (2005)	S355J0 + M		S460M	
		Web	Flange	Web	Flange
20	1.00	Eurocode values	Eurocode values	Eurocode values	Eurocode values
100	1.00				
200	0.90	0.91	0.91	0.94	0.93
300	0.80	0.81	0.83	0.87	0.86
400	0.70	0.72	0.74	0.81	0.79
500	0.60	***0.63***	***0.65***	***0.75***	***0.72***
600	0.31	0.48	0.55	0.56	0.58
700	0.13	***0.33***	***0.45***	***0.38***	***0.43***
800	0.09	Eurocode values	Eurocode values	Eurocode values	Eurocode values
900	0.0675				
1000	0.045				
1100	0.0225				
1200	0.00				

Finally, the standardized stress-strain curves of structural steels S355J0+M and S460M at ambient and elevated temperatures are shown in Figures A.13 and A.14, and Figures A.15 and A.16 respectively.

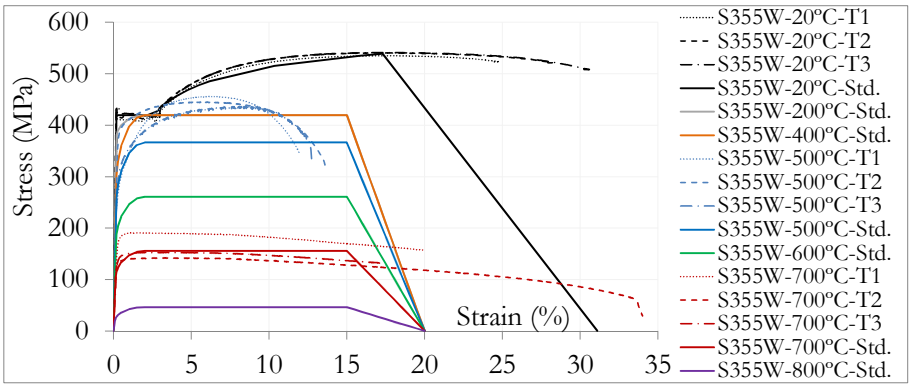

Figure A.13: Standardized and nominal stress-strain curves of steel S355J0+M from the web of IPE 550 cross-section at ambient and elevated temperatures

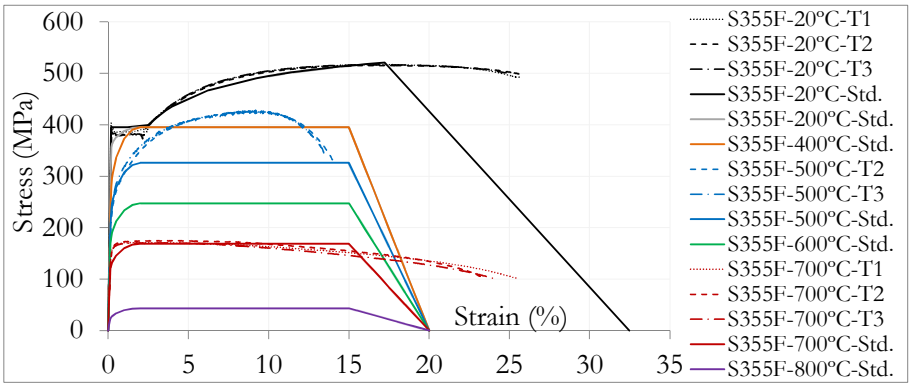

Figure A.14: Standardized and nominal stress-strain curves of steel S355J0+M from the flanges of IPE 550 cross-section at ambient and elevated temperatures

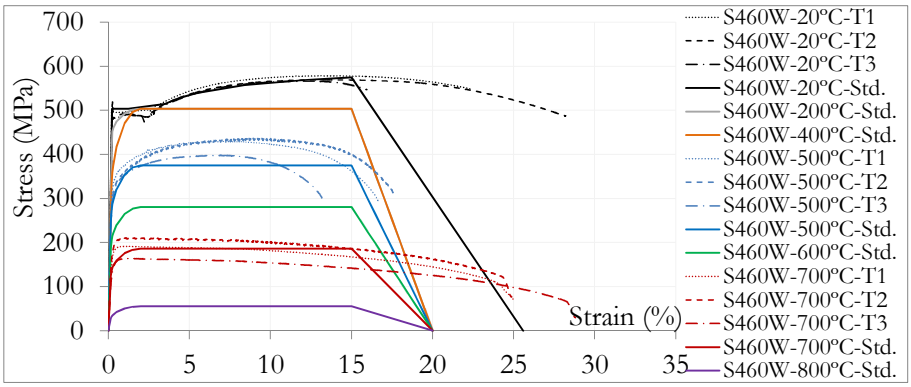

Figure A.15: Standardized and nominal stress-strain curves of steel S460M from the web of HEB 300 cross-section at ambient and elevated temperatures

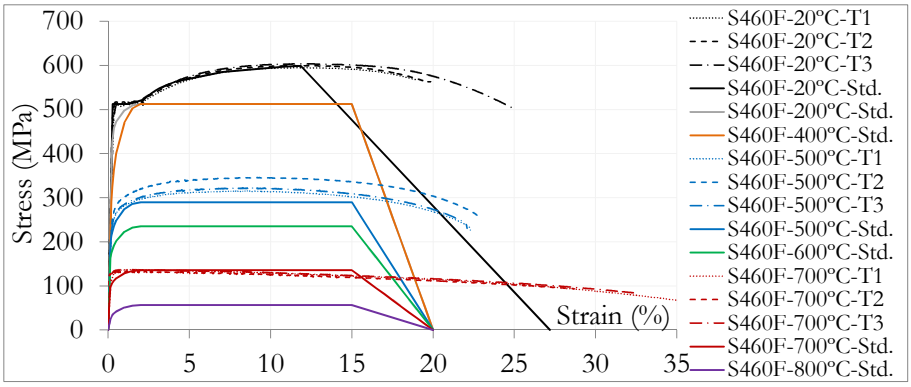

Figure A.16: Standardized and nominal stress-strain curves of steel S460M from the flanges of HEB 300 cross-section at ambient and elevated temperatures

A.3.2 Tensile coupon tests from bolts M30, grade 10.9

A.3.2.1 Tests results

Table A.10 presents the mechanical properties (proportional limit and elastic modulus) for each temperature obtained from the tests (average values of the two tests at each temperature). The elastic modulus presented in Table A.10 is determined as an initial slope

of the stress-strain curves, and the proportional limits $f_{pb,\theta}$, which corresponds to the end of the initial slope, are estimated as equal to 2/3 of the yield strength.

Table A.10: Mechanical properties of bolts M30, grade 10.9, derived from the tensile tests results (average values from the tests at each temperature)

Temp. (°C)	Proportional limit f_{pb} (MPa)	Elastic modulus E (MPa)
20	932	206460
200	623	167680
400	522	158260
500	339	128815
600	199	78149
700	66	44148
800	40	47590

The mechanical properties (tensile strength f_{ub} and elastic modulus E) of bolts M30 grade 10.9 determined from the steady-state tests are illustrated in Figure A.17a) and b) respectively. In Figure A.17a, it is shown that all the tests results are above the Eurocode recommended values. However, the second test performed at 200°C provides unacceptable value of the elastic modulus (Figure A.17b) because of initial difficulties at the beginning of the tensile tests. Also, values of Elastic modulus at 800°C are not realistic. The Elastic modulus values of these tests (at 200°C and 800°C) are not considered. The reduction factors of the tensile strength and the elastic modulus are calculated based on the tests average results, relative to measured strength and elastic modulus at 20°C (Figure A.18 and Table A.11); at 100°C and 300°C, linear interpolation is applied.

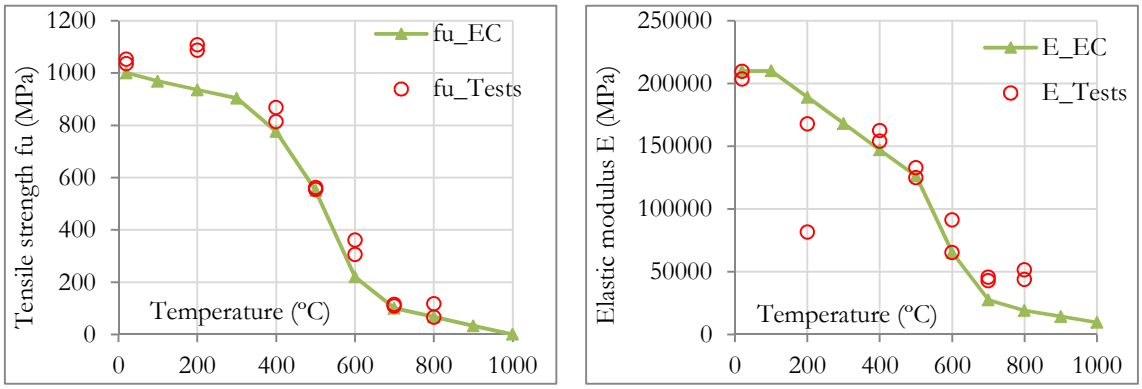

Figure A.17: Bolts M30 grade 10.9 temperature-depending: a) tensile strength f_{ub} and b) elastic modulus E – Comparison of tests results against Eurocode (EC) values

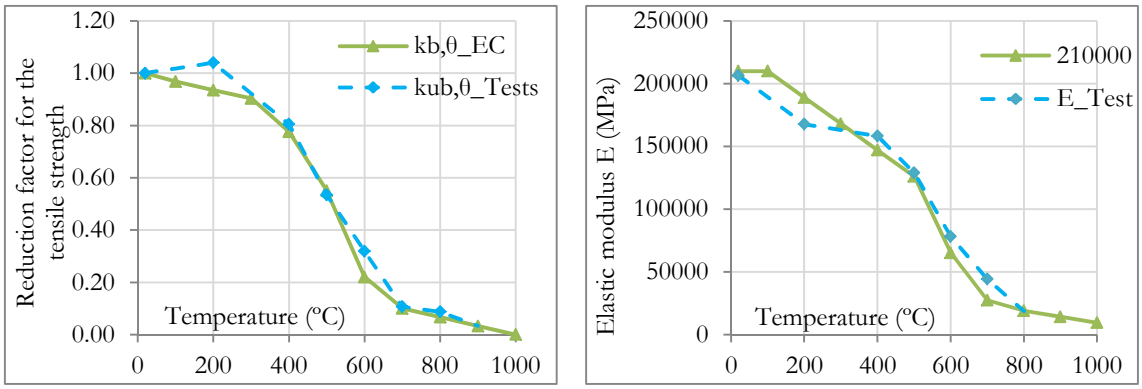

Figure A.18: Temperature-depending reduction factor for bolts M30 grade 10.9: a) $k_{ub,\theta}$ for the tensile strength and b) $k_{E,\theta}$ for elastic modulus – Comparison of tests results against Eurocode (EC) values

Table A.11: Reduction factors for the material properties of bolts M30 grade 10.9 at temperatures 20°C-1000°C - Values based on steady-state test results and Eurocode values

	Reduction factor k_b for bolts strength: $k_{ub,\theta}=f_{ub,\theta}/f_{ub}$		Reduction factor k_E for bolts elastic modulus: $k_{E,\theta}=E_\theta/E$	
θ (ºC)	EN 1993-1-2 (2005)	Tensile tests	EN 1993-1-2 (2005)	Tensile tests
20	1.000	1.000	1.000	1.000
100	0.968	1.018	1.000	0.917
200	0.935	1.040	0.900	0.812
300	0.903	0.922	0.800	0.789
400	0.775	0.805	0.700	0.767
500	0.550	0.534	0.600	0.624
600	0.220	0.318	0.310	0.379
700	0.100	0.107	0.130	0.214
800	0.067	0.087	0.090	0.090
900	0.033	Eurocode values	0.068	Eurocode values
1000	0.000		0.045	

A.3.2.2 Standardized stress-strain curves

Hanus *et al.* (2011) proposed a model for the stress–strain diagram of bolts under elevated temperatures or natural fire (including both heating and cooling). The model is based on the model of Riaux (1980), presented in Figure A.19, and on experimental tests performed on bolts M12 and M20, grade 8.8. Two temperatures are defined: the maximum temperature reached during the heating phase, T_u, and the temperature of the tensile test, T_f. In the Hanus' model, there is no horizontal plateau ($\varepsilon_{y,\theta} = \varepsilon_{10,\theta}$) and the values of the characteristic parameters are modified: i) Hanus *et al.* (2011) presents some values of the ratio $k_{p,\theta}$ between the proportional limit $f_{p,\theta}$ and the yield strength $f_{y,\theta}$, depending on the maximum temperature T_u (see Table A.12); ii) the yield strain $\varepsilon_{y,\theta}$ is fixed ($\varepsilon_{y,\theta}$ = 0.02); iii)

Hanus *et al.* (2011) showed that all the curves obtained from experimental tests pass on the point ($f_{t,\theta}$ = 500 MPa; $\varepsilon_{t,\theta}$ = 0.1), or ($f_{t,\theta} = f_{y,\theta}$; $\varepsilon_{t,\theta}$ = 0.1) when the yield strength $f_{y,\theta}$ is smaller than 500 MPa; iv) finally, they observed that, when T_u < 600°C, $\varepsilon_{u,\theta}$ = 0.15, and when T_u = 800°C, $\varepsilon_{u,\theta}$ = 0.25.

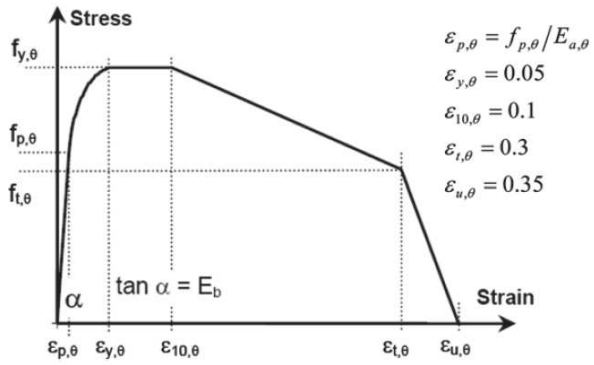

Figure A.19: Mathematical model proposed by Riaux (1980)

Table A.12: Ratio $k_{p,\theta}$ between the proportional limit f_p and the bolt strength f_y for bolts subject to temperature history including both heating and cooling (Hanus *et al.,* 2011)

T_u (°C)	$k_{p,\theta}$
20	0.9
200	0.8
400	0.75
600	0.75
800	0.6
900	0.6

The standardized stress-strain curves of the tensile tests on bolts M30, grade 10.9, are obtained from the Hanus' model (see Figure A.20). The bolt strength $f_{y,\theta}$ is considered equal to the tensile strength $f_{ub,\theta}$ (R_m), defined in Table 3.3; $\varepsilon_{y,\theta}$ corresponds to the stress $f_{ub,\theta}$ (obtained from the tests results); and the ultimate strain $\varepsilon_{u,\theta}$ is considered equal to the elongation after fracture A (%), also given in Table 3.3.

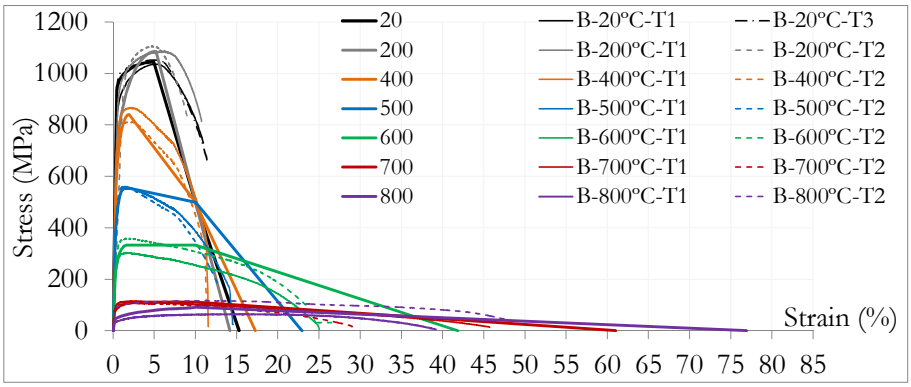

Figure A.20: Experimental and standardized stress-strain curves of bolts M30 grade 10.9 at 20°C, 200°C, 400°C, 500°C, 600°C, 700°C and 800°C

A.4 Compression tests on concrete blocks

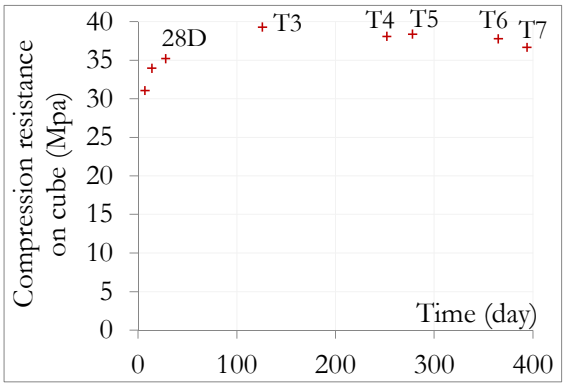

Figure A.21: Evolution of the compression strength of concrete cubes with time

Table A.13: Compression tests results of concrete cubes at 28 days

	Weight (kg)	Compression strength (MPa)	Failure load (kN)	Density (g/cm³)
Cube 1	7.90	35.18	791.50	2.34
Cube 2	8.00	33.04	743.40	2.37
Cube 3	7.70	37.35	840.40	2.28
Average values	7.90	35.19	791.80	2.33

A.5 Additional tests at ambient temperature after heating and cooling

Six additional tests are performed on bolts M30, grade 10.9 under natural fire conditions, with the following procedure: 1st- heating up to T_f = 500ºC, 600ºC or 700ºC (linear ramp of 250ºC/hour), 2nd- maintaining the constant elevated temperature during half an hour, 3rd- naturally cooling, 4th- machining of coupons, and 5th- testing in tension at ambient temperature (T_u), according to the same proceeding than explained in section 3.4. The average values of the results are presented in Table A.14. Figure A.22a depicts the experimental stress-strain curves from tensile tests; problems happened during test one (T1) at 500ºC (B500ºC-20ºC-T1) and results are not presented. Figure A.22b depicts the standardized stress-strain curves at each tested maximal temperature, defined by the analytical model of Hanus *et al.* (2011), considering the average values obtained from the tests results (Table A.14).

For temperatures below 600ºC, the post-fire stress–strain curves are of gradual yielding type; however, a yield plateau appears in the stress-strain diagram for the maximal temperatures equal to 600ºC and 700ºC. The ductility is increased once the maximal temperature reaches 700ºC, and it is observed that the elastic modulus is not degraded by any temperature. A part of the yield and tensile strengths are regained after cooling: 97% from 500°C, 87% from 600ºC and around 60% from 700°C. It shows that bolts M30,

grade 10.9, can regain its nominal tensile strength if it is exposed to temperatures below 600ºC. Qiang *et al.* (2013) analysed steel S960 after heating and cooling. Similar behaviour was observed for this steel S960, and they recommended using 90% of the nominal yield strength for post-fire S960 if the steel structures are exposed to fire temperature below 600ºC. The same recommendation may be done for bolts M30, grade 10.9; if bolts are not distorted after fire exposure with temperatures below 600ºC, they could be reusable after fire.

Table A.14: Mechanical properties of bolts M30, grade 10.9 subject to initial heating - Values based on steady-state test results and Hanus *et al.* (2011) values

		Hanus model			Tensile tests results		
Temp. T_u (ºC)	Temp. T_f (ºC)	Tensile strength f_{ub} (MPa)	Ultimate strain $\varepsilon_{u,\theta}$ (%)		Yield strength f_{yb} (MPa)	Tensile strength f_{ub} (MPa)	Elongation after fracture A (%)
20	20	1044*	15.3*		932*	1044*	15.3*
20	500	1044.21	15.00	T1	802	958	17.8
				T2	1001	1063	15.3
20	600	905.33	14.78	T1	809	895	21.8
				T2	818	894	17
20	700	664.51	25.00	T1	530	629	27.4
				T2	538	645	31.2

*Measured reference values at ambient temperature (see Table A.10)

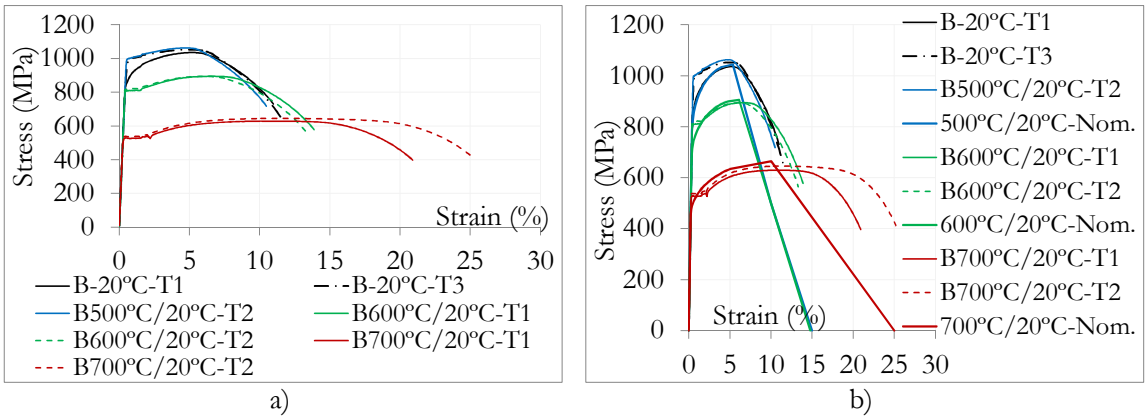

Figure A.22: a) Experimental stress-strain curves of bolts M30, grade 10.9 coupons tested at 20ºC after heating up to 500ºC, 600ºC and 700ºC and cooling – comparison to the tensile tests results performed at ambient temperature (black curves); b) Comparison to standardized stress-strain curves

Appendix B

B Experimental tests on beam-to-column joints subject to localised fire and axial loads – Additional information and results

B.1 Beam axial restraints in the real car park building

The realistic beam axial restraint provided by the part of the building not directly affected by the localised fire and the loss of the column, is initially estimated by a simple elastic analysis performed in Abaqus (2012). At the fifth floor, five column loss locations are simulated, and Figure B.1 presents the configuration of the loss of the middle column. A horizontal unitary load is applied at the beam-to-column connection level, at the end of the sub-frame subject to the column loss, and the displacement is measured. This method is described in Demonceau (2008).

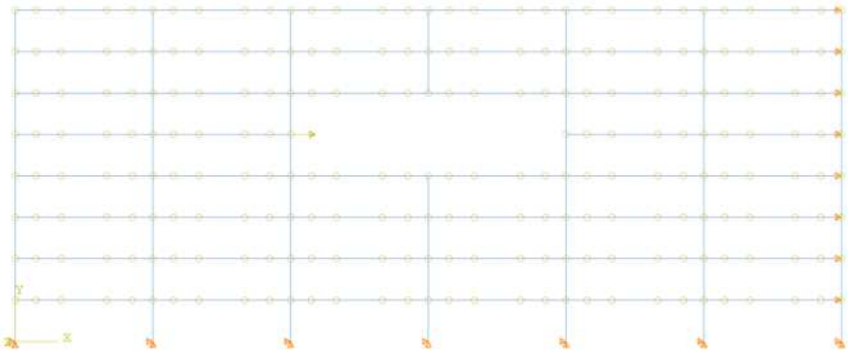

Figure B.1: Lateral restraints to beam – configuration 3

Table B.1 presents the measured axial restraint stiffness K of the equivalent single spring for each configuration of column loss. The smaller K is equal to 64.4 kN/mm. During the experimental tests, two springs are applied at each beam end to have symmetrical deformations, and the equivalent stiffness of each spring is equal to two times the stiffness of the equivalent single spring calculated in Abaqus: $2K$ (128.8 kN/mm).

Table B.1: Calculated axial restraint stiffness

Sub-frame	Stiffness of the equivalent single spring - K	Stiffness of each spring at both beam ends - $2K$
1	91.16 kN/mm	182.32 kN/mm
2	78.43 kN/mm	156.86 kN/mm
3	64.39 kN/mm	128.78 kN/mm
4	78.43 kN/mm	156.86 kN/mm
5	91.16 kN/mm	182.31 kN/mm

B.2 Strain gauges results from test 1 at ambient temperature

For test 1 at ambient temperature, strain gauges are located inside bolts, at 50 cm from each beam end, on the column web and on the steel rebars in the composite slab (Figure B.2).

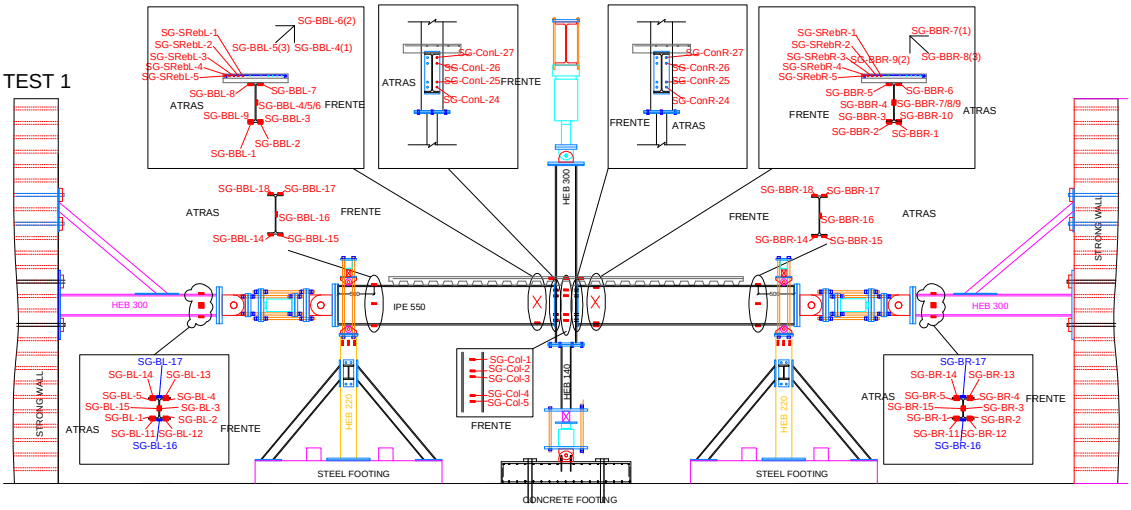

Figure B.2: Strain gauges used for the test 1 at ambient temperature

The bolts loads can be calculated from the measured strains ε (Eq. B.1), and Figure B.3 presents the evolution of the bolt loads *versus* time.

$$F=\varepsilon\times E\times A_s \qquad \text{(Eq. B.1)}$$

In Eq. B.1, ε is the measured strain, E is the elastic Modulus equal to 206 460 N/mm^2 (estimation from the tensile coupon tests results - see Appendix A.3), and A_s = 561 mm^2 is the bolt cross-section area. At the end of the test, two bolts failed on the left side; the first one was instrumented, but it did not measured well, and the second one was not instrumented. The bolt with the higher load (Figure B.3) corresponds to the bolt on the right connection (row 4). The elastic limit is 523 kN (black horizontal line), and the measured loads upper this value cannot be considered because of the strain gauge definition, which is only valid in the elastic range of deformation. On the other hand, the limitation of these strain gauges corresponds to 0.5 % (or 577.5 kN – blue horizontal line).

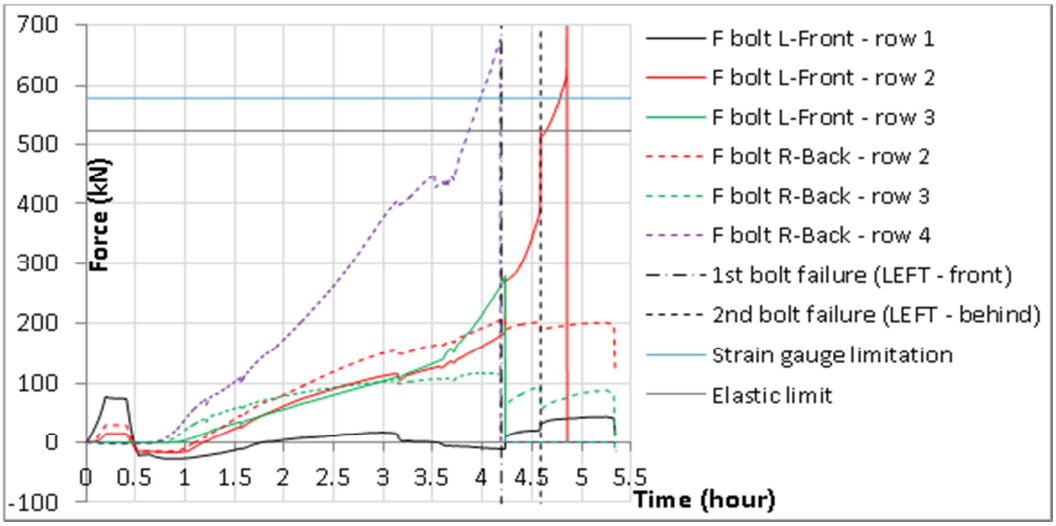

Figure B.3: Loads into bolts calculated from the measured strain

Figure B.4 shows the measured strains in 5 points of the column web, corresponding to the level of each bolt and of the steel rebars. Under the initial hogging bending moment (0.3 hour - red curve), the compression is developed at the level of bolt rows 3 and 4, and tensile loads are similar at the level of bolt rows 1 and 2. At the end (5h), under sagging bending moment, only a small extension is measured at the level of bolt row 4, probably due to the bolt failure.

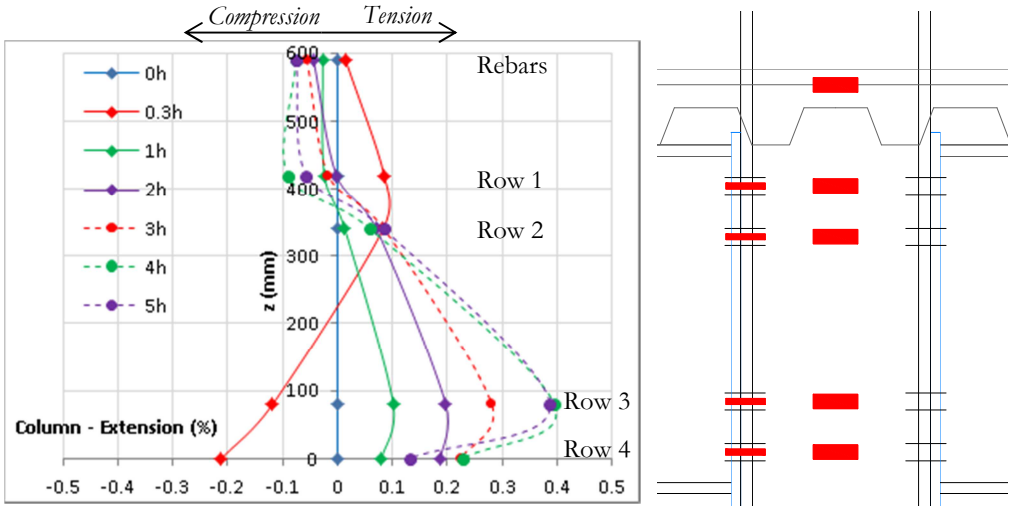

Figure B.4: Measured strains on the column web

Figure B.5 and Figure B.6 show the strains measured at 500 mm from the end-plate, on the web, and bottom and top flanges of the steel beam. The sagging bending moment cannot be estimated based on the strains because the load in the concrete component in compression is not measured.

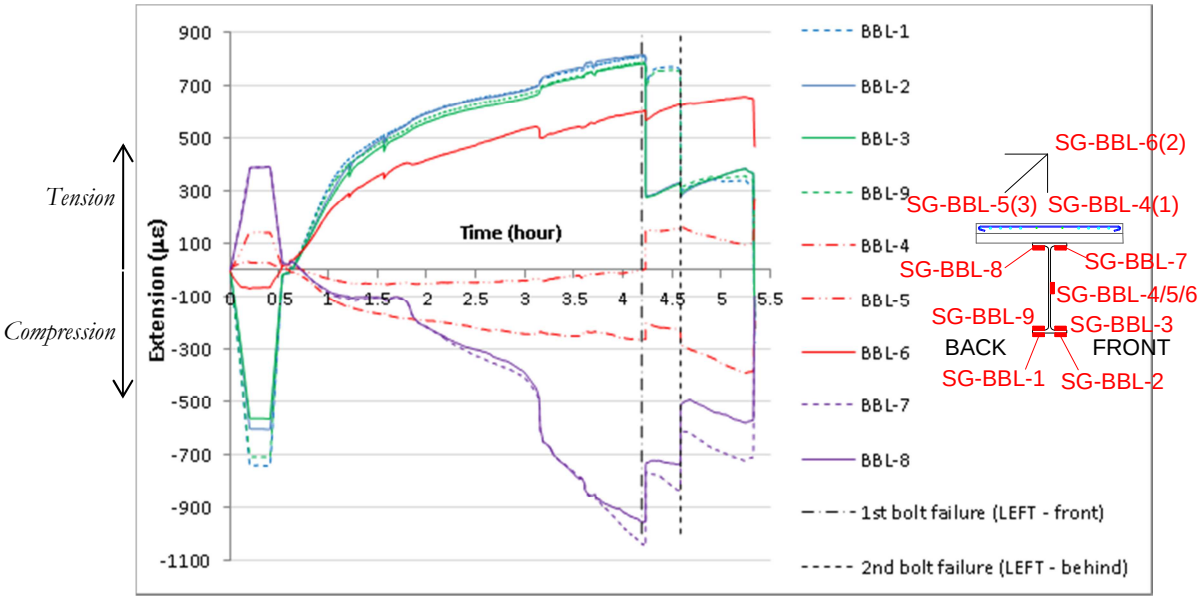

Figure B.5: 500 mm from the connection left

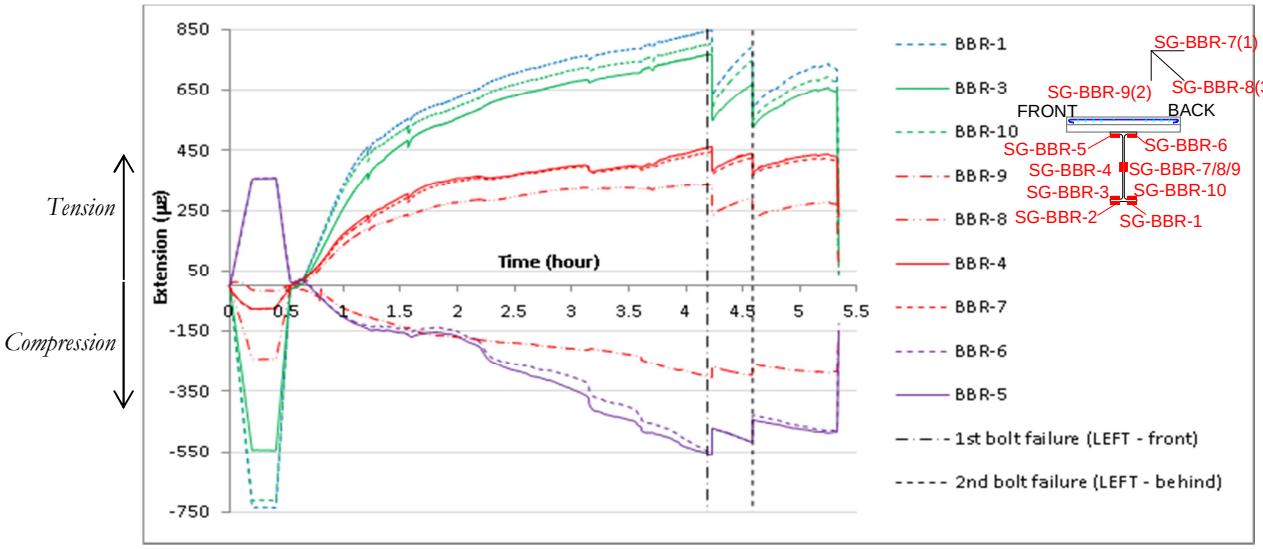

Figure B.6: 500 mm from the connection right

Figure B.7 and Figure B.8 show the strains measured on the steel beam, at 2500 mm from the end-plate (beams ends), on the web and on the bottom and top flanges.

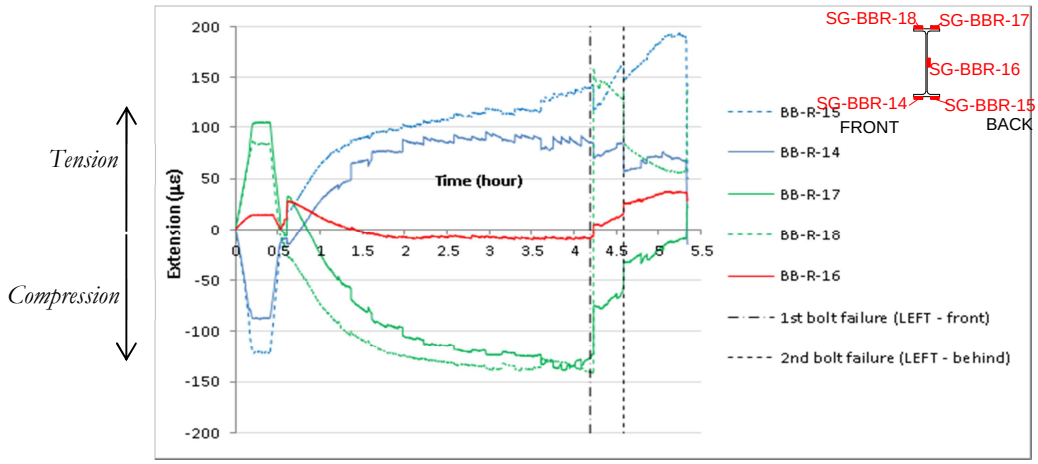

Figure B.7: 2500 mm from the connection right

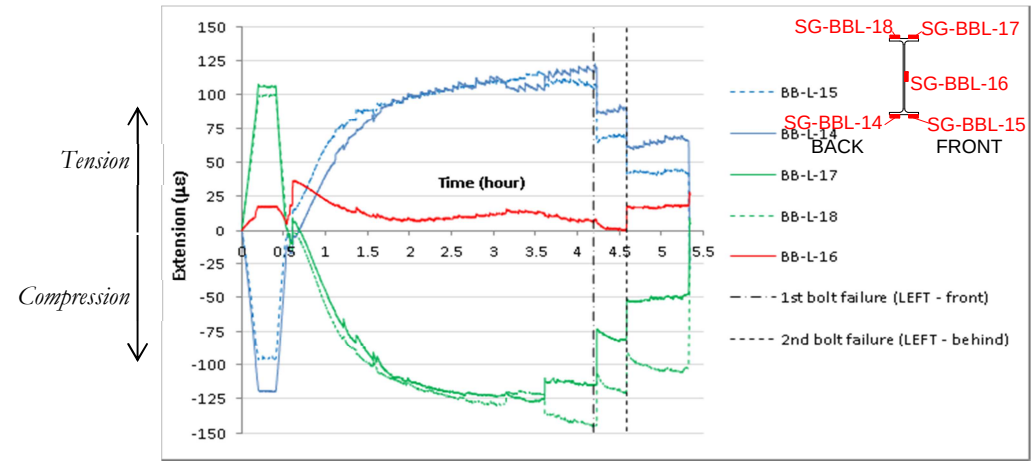

Figure B.8: 2500 mm from the connection left

B.3 Measured temperatures

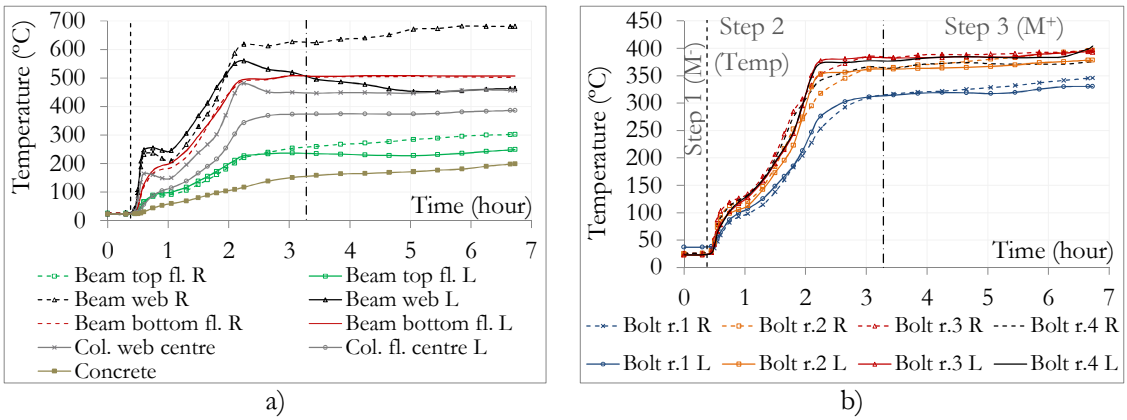

a) b)

Figure B.9: Evolution of the temperatures during test 2 (R- right connection; L- left connection; fl.- flange r.- row)

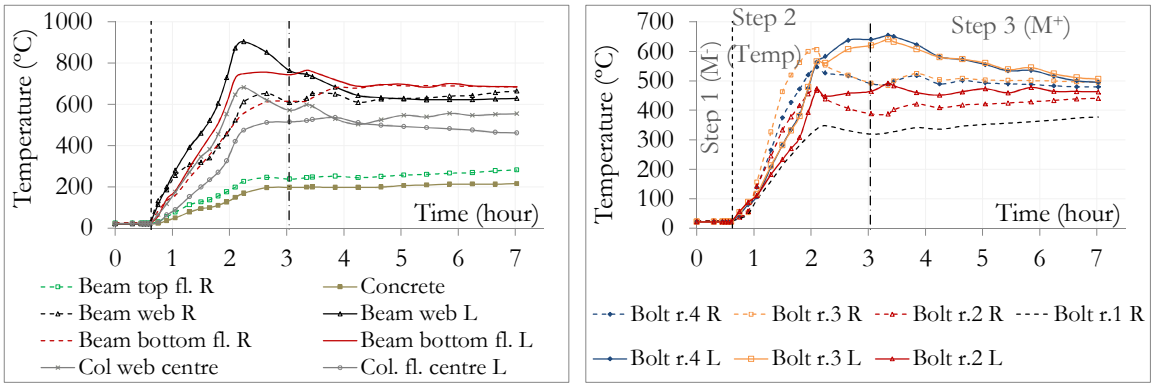

a) b)

Figure B.10: Evolution of the temperatures during test 3 (R- right connection; L- left connection; fl.- flange r.- row)

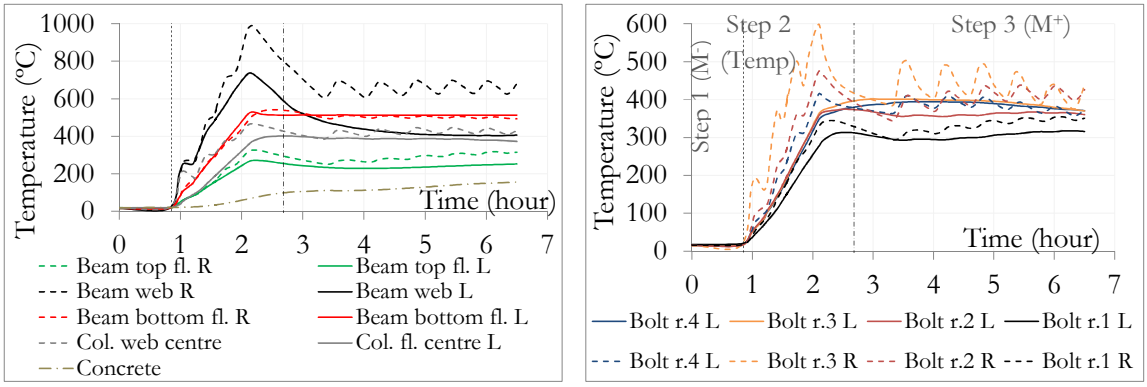

a) b)

Figure B.11: Evolution of the temperatures during test 4 (R- right connection; L- left connection; fl.- flange r.- row)

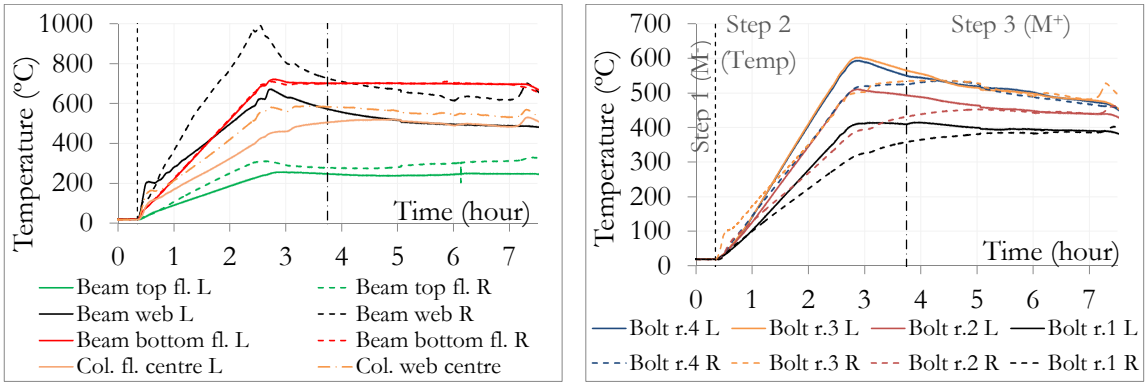

a) b)

Figure B.12: Evolution of the temperatures during test 5 (R- right connection; L- left connection; fl.- flange r.- row)

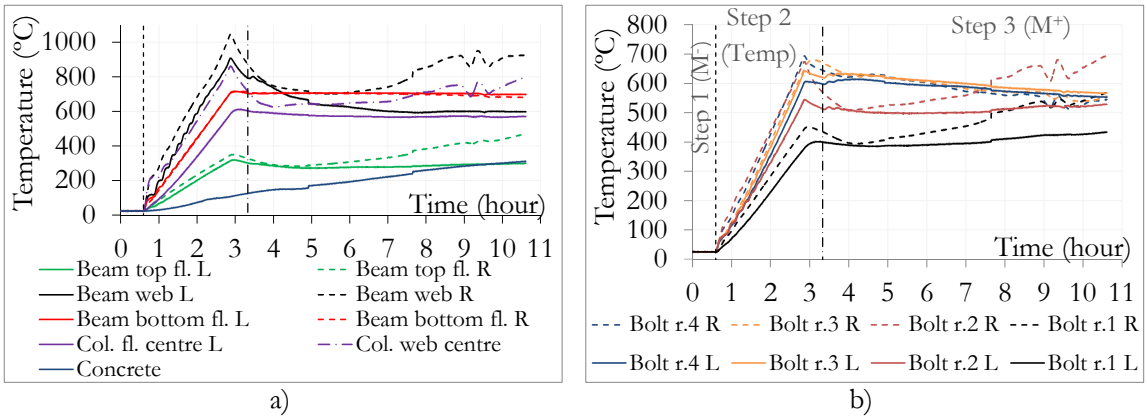

a) b)

Figure B.13: Evolution of the temperatures during test 6 (R- right connection; L- left connection; fl.- flange r.- row)

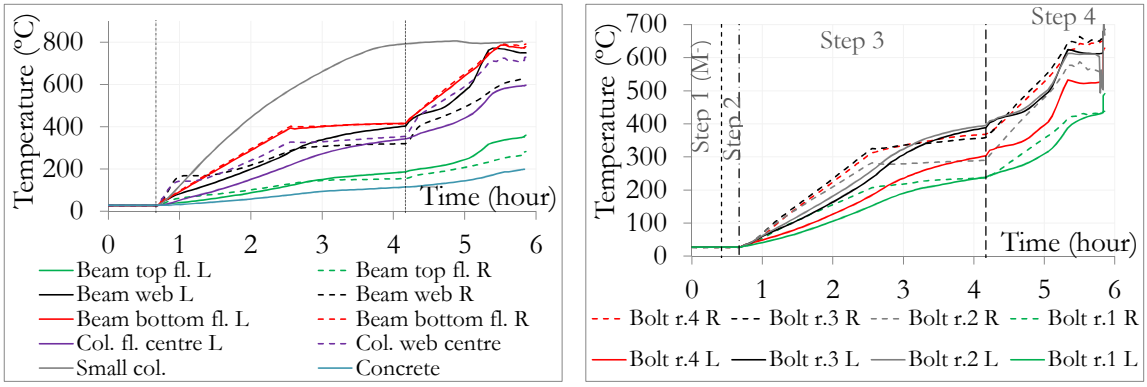

a) b)

Figure B.14: Evolution of the temperatures during test 7 (R- right connection; L- left connection; fl.- flange r.- row)

B.4 Additional pictures of the experimental tests

Figure B.15: Local deformation of the column web on the bottom part (level of the bolt rows 3 and 4) under hogging bending moment (test 3 – 700ºC and no axial restraint to beam)

Figure B.16: Final deformation of the sub-frame under sagging bending moment (back view / test 3 – 700ºC and no axial restraint to beam)

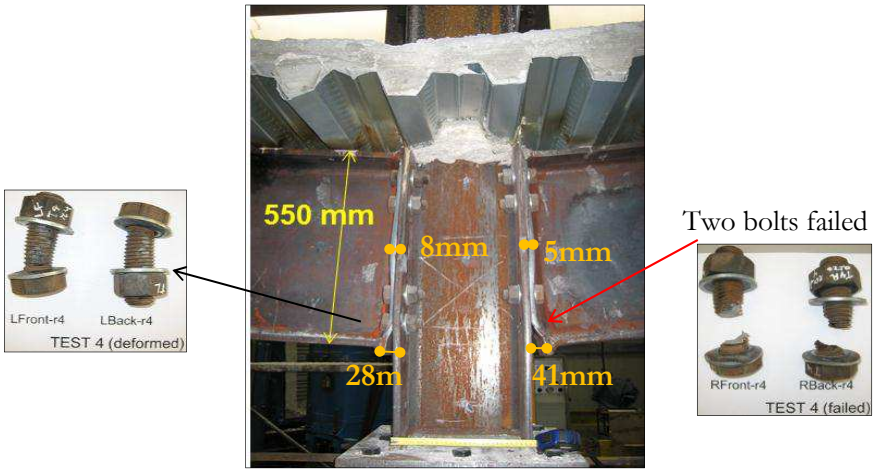

Figure B.17: Deformations of the joint (view from the front side / test 4 – 500ºC and total axial restraint)

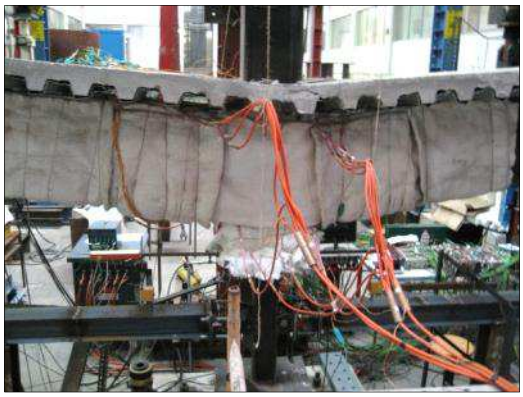

Figure B.18: Final deformation of the sub-frame (test 4 – 500ºC and total axial restraint)

a) b) c)

Figure B.19: a) Local deformation of the column web (view from the front side); b) local deformation of the column flange left side (at the level of the concrete slab), view from the back; c) local deformation of the column flange at the bottom part (test 4 – 500ºC and total axial restraint)

Figure B.20: Local deformation of the flanges from the right beam (view from the back / test 4 – 500ºC and total axial restraint)

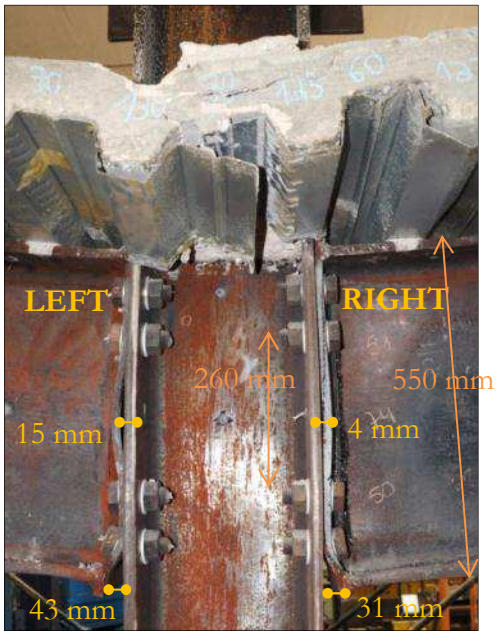

Figure B.21: Deformations of the joint (view from the front side / test 5 – 700ºC and total axial restraint)

a) Beam right

b) Beam left

Figure B.22: Deformed end-plates after disassembly the tested sub-frame (test 6 – 700ºC and realistic beam axial restraint)

Appendix C

C Numerical benchmark examples

C.1 Introduction

The main objective is to validate the utilization of the Abaqus program for steel structures subject to fire, using beam and shell elements. Two benchmark studies are performed to gain confidence in the numerical results: Model A- a two-dimensional steel sub-structure subject to a natural fire and Model B- a composite steel-concrete beam simply supported subject to the standard fire ISO 834. The model A is calibrated from the numerical results obtained by the program CEFICOSS and published by Franssen *et al.* (1995), whereas the model B is based on the numerical results obtained by the program VULCAN and published by Huang *et al.* (1999).

C.2 Model A - Steel sub-structure subject to a natural fire

C.2.1 Description of the benchmark study

The natural fire test reported by Franssen *et al.* (1995) was carried out by British Steel in collaboration with the Fire Research Station. A fully loaded, two dimensional steel framework was tested in fire in a purpose-built compartment of typical size for office accommodation. Dimensions of the steel framework were specified for a building of two or three storey in height. The beam, 4550 mm long, with a universal beam section of 406 x 178 x 54, grade 43A, was bolted to two columns of 3530 mm tall, with a universal column section of 203 x 203 x 52, grade 43A. M20 grade 8.8 bolts were used to provide improved resistance to loss in strength at elevated temperatures. Columns were pin ended at the base and extended above the beam. Autoclaved aerated concrete blocks were built between the column flanges to protect the web from fire, but there were only considered to give thermal insulation (non-composite behaviour). A concrete slab, which has a cross-section of 1200 x 150 mm, was also represented because of its influence on the temperature

distribution in the beam (non-composite behaviour). Lateral and sway instabilities were prevented by a subsidiary framework specially designed for.

C.2.2 Material properties

All material properties used in Abaqus at elevated temperatures are based on EN 1993-1-2 (2005). At ambient temperature, the yield stress f_y considered by Franssen *et al.* (1995) to simulate the experimental test is 408MPa. He also used a convective heat transfer coefficient and an emissivity given by EN 1993-10 (1990), respectively equal to 25W/m^{2}K and 0.5. For the column flange facing the wall of the fire compartment, the emissivity is taken equal to 0.3 to account for some degree of radiative shadowing (Franssen *et al.*, 1995). The conductivity and the specific heat of the concrete slab are defined according to EN 1992-1-2 (2004). The concrete blocks insulating the column have particular properties: a density equal to 677kg/m^3, a constant specific heat of 1050J/kgK and a thermal conductivity given by $0.20 + 0.0004\theta_c$ W/mK, where θ_c is the concrete temperature (Franssen *et al.*, 1995).

C.2.3 Heat transfer analysis

The heat-transfer problem analysed in Abaqus involves conduction and boundary radiation. The two models (beam and column) are developed using 2D deformable elements DC2D4. The applied temperatures correspond to the gas temperature measured during the experimental test. Figure C.1 shows the evolution of the temperatures in flanges and in web centroid of a) the beam section and b) the column section. Numerical results obtained by Abaqus show good agreement with the measured temperatures, as well as with the computed temperatures of CEFICOSS.

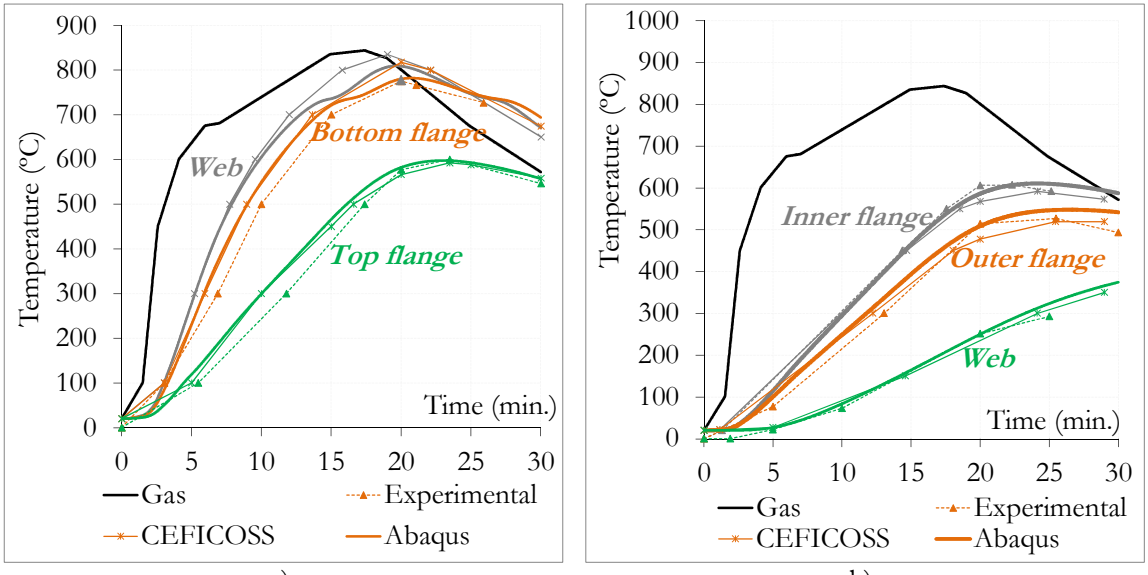

Figure C.1: Temperatures a) in the beam and b) in the column

C.2.4 Static, general analysis

Figure C.2a presents the steel frame structure for which symmetry conditions are considered. Two dimension beam elements type B21 are used to define the beam and the column. As the concrete slab and the concrete blocks in the column only provide thermal boundary conditions for the temperature, they are not modelled in the structural analysis. According to Cooke and Latham (1987), during the experimental test, no relative rotation at the connection occurred and the temperature around the connection remained lower than elsewhere in the compartment during the fire. It is then allowed to suppose a rigid beam-to-column connection. In order to represent the restraint offered by the secondary steelwork, a bi-linear spring is modelled with nonlinear force-displacement behaviour (Franssen *et al.*, 1995) (Figure C.2b).

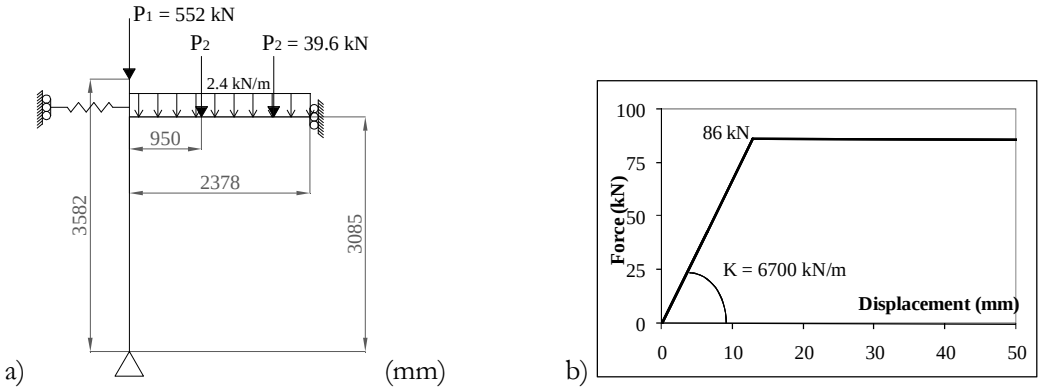

Figure C.2: a) Reference frame; b) behaviour of the spring

The mechanical loads are applied at ambient temperature and maintained constant during the fire. They corresponds to the self-weight, a vertical load on the column equal to 552 kN (P1), two vertical loads on the beam equal to 39.6 kN (P2) and a uniform loading of 2.4 kN/m distributed along the beam to represent the self-weight of the concrete slab (Figure C.2a). Thermal loading is specified as a predefined field and temperatures are specified at three specific points through the 2D section, the i) centroid of the top flange; ii) centroid of the web and iii) centroid of the bottom flange (Abaqus, 2012). Because the measured temperatures of the combustion gases were slightly lower in the vicinity of the beam-to-column connection (Franssen *et al.*, 1995), the beam has also a temperature variation along its length from θ_a at beam mid-span to 0.9 θ_a near the connection (Santiago *et al.*, 2009).

C.2.5 Reference case: behaviour and validation of the numerical model

The model of the reference structure (Figure C.2a) is validated by comparing beam mid-span vertical displacements, beam axial load and column lateral displacements with the experimental and CEFICOSS results. Figure C.3 a) and b) show respectively the vertical displacement at the mid-span of the beam and the axial compression force in the beam. A good agreement between both software results is observed. The fire resistance calculated

by Abaqus is about 20minutes (min.), which is closed to the 19min. obtained by CEFICOSS. The evolution of the lateral horizontal displacement at column mid-height is shown in Figure C.3c. Due to the elongation of the beam, the column bows laterally up to the buckling at about 19-20min.

The complete frame is also modelled assuming the presence of two springs. According to Franssen *et al.* (1995), an initial lateral imperfection of 0.8 $H_c/1000$ is considered, where H_c is the column height. The failure mode is exactly the same than for half of the frame (Figure C.4c), and the fire resistances are very close, so satisfactory results are obtained by simulating only one half of the frame.

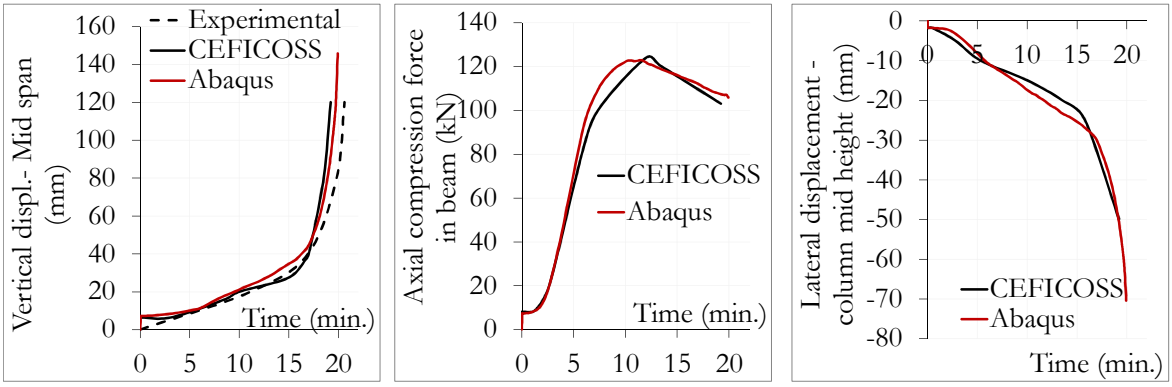

Figure C.3: a) Vertical displacement of the beam; b) calculated axial force in the beam; c) calculated horizontal displacement at mid height of the column

C.2.6 Influence of the axial restraint to beam

Mainly due to the axial restraints, the beam cannot expand with the increasing of temperature, leading to the development of axial compressive forces. In order to see if the frame stability is influenced or not by these restraints, half of the frame and the complete frame are modelled without springs. The fire resistance of half of the frame is increased of 3% for the Abaqus results and 2% for the CEFICOSS results without lateral restraints in comparison to the reference case with lateral restraint. The axial compression load in the beam is shown in Figure C.4a for the two frames, restrained and unrestrained. Results of Abaqus are close to the CEFICOSS ones, and it is shown that the fire resistance remains the same with the two different beam axial loads. However, when the entire frame is modelled without any lateral restraints, the failure mode is completely different due to the initial imperfections introduced in columns (Figure C.4b and c).

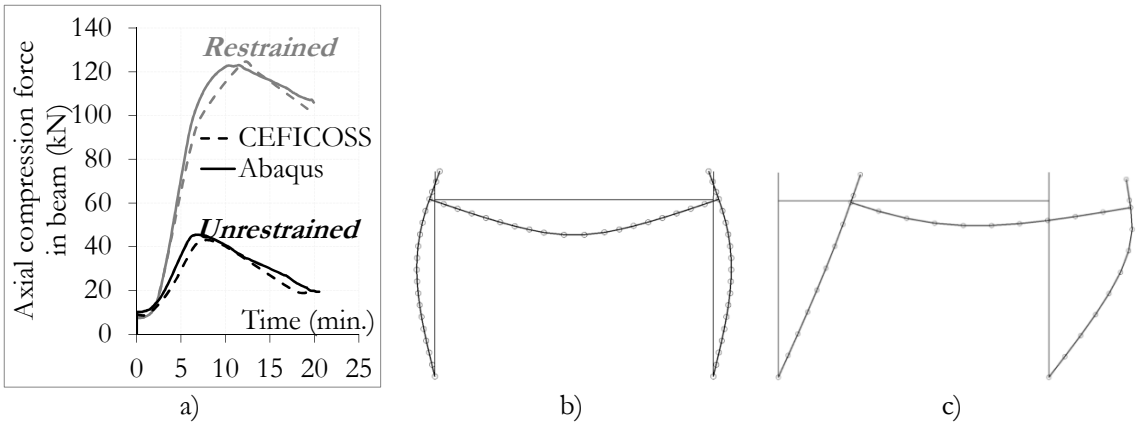

Figure C.4: a) Calculated axial force in the beam of the half of the frame; calculated failure mode of the sway frame (scale of displ. 4/1): b) with / c) without lateral restraints

C.2.7 Influence of the frame continuity

The influence of the frame continuity is studied simulating the beam and the column on their owns. For the beam considered on its own, at ambient temperature, bending moment and horizontal force are introduced by the column at the extremity of the beam (Figure C.5a). The fire resistance calculated by CEFICOSS is 15min. 30seconds (sec.), against 18min. 52sec. for Abaqus, which gives a difference between both software equal to 21.72%. For the column considered on its own (Figure C.5b), effects of the beam are taken into account by applying bending moment and vertical force at the top of the column. CEFICOSS and Abaqus obtain fire resistances of at least 30min. The lateral displacement behaviour of the column as a separate member is presented in Figure C.5c and compared to the behaviour of the column modelled as part of the frame. It is shown that modelling the column on its own provides completely different results of the behaviour of the column and the fire resistance time. It remains safe until the end of the analysis, against the failure at t = 20min. observed at the complete frame.

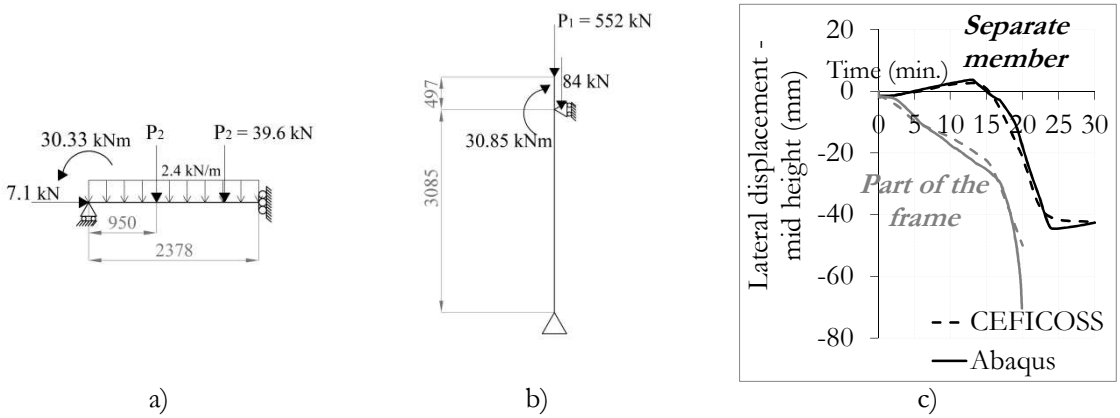

Figure C.5: a) Beam and b) column considered on their owns; c) calculated horizontal displacement at mid height of column

C.2.8 Influence of the thermal expansion

The total thermal expansion from a reference temperature is defined by the thermal expansion coefficients, which generate thermal strains. The influence of the thermal expansion on the fire resistance of the frame is tested by modelling the initial structure represented in Figure C.2a, without any thermal expansion coefficients. The Abaqus results reinforce the conclusion of Franssen *et al.* (1995), saying that the expansion coefficients have a significant effect. Indeed, without expansion coefficients:

i. The fire resistance increases from 19min. 51sec. (reference case) up to the end of the analysis – 30 min. and probably more because of the cooling of the steel as the fire decays (Franssen *et al.*, 1995). However, because no experimental temperatures were measured after 30 min., the numerical analyses are also limited to this time.
ii. The axial compression load in the beam increases much less from a maximum value of 116.5kN after 12 minutes (ref. case) to a maximum value of 17kN after 18 minutes. The value at ambient temperature stays constant and equal to 7kN;
iii. The lateral displacement of the column decreases because of the absence of the thermal expansion of the beam that was pushing the column outward.

Abaqus obtains results quite close to the CEFICOSS ones. The higher difference (20%) is in the maximum axial compression load value in the beam: CEFICOSS have 21kN after 17 minutes, and Abaqus 17kN after 18 minutes. However, the stability of the frame is few influenced by the axial force, as it was confirmed in §C.2.7.

C.2.9 Influence of non-uniform temperature

Uniform temperatures throughout the beam and column cross-sections are calculated using the simplified calculation method proposed in EN 1993-1-2 (2005) (EC3). In Figure C.6a, the uniform temperatures (EC3) are compared to the mean temperatures calculated by the heat transfer analysis in Abaqus. They are higher because the heat transfer from the steel to the concrete is not considered by the simplified calculation method. Figure C.6b shows the vertical mid-span displacement of the beam for three different applications of the cross-section temperatures. The uniform temperature calculated using EC3 method leads to conservative results (premature failure) while the Abaqus average temperature leads to unsafe results (no failure is observed until the end of the analysis).

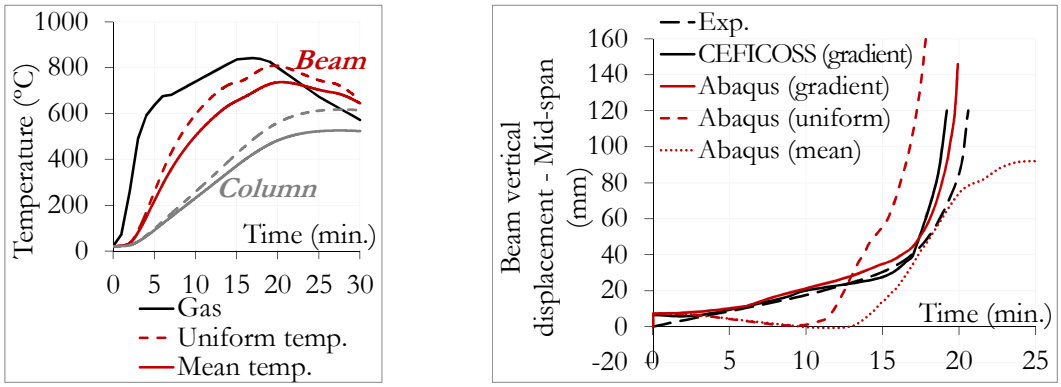

Figure C.6: a) Calculated uniform and mean temperatures; b) vertical mid-span displacement of the beam with the uniform (EC3), average and gradient of temperatures

C.3 Model B – Composite steel-concrete beams

C.3.1 Description of the benchmark study

The benchmark example is based on the paper published by Huang *et al.* (1999) in which they showed the good computational stability and efficiency of a new model of shear connectors implemented in the software VULCAN. The verification is carried out against the experimental results obtained from four simply supported composite beams tested at ambient (Chapman and Balakrishnan, 1964) and high temperatures (Wainman and Kirby, 1988). The influence of the composite action degree was studied, simulating: a full interaction, a partial interaction and no interaction.

This appendix only presents the Abaqus results for one composite beam at ambient temperature (A3) and one composite beam subjected to the ISO 834 fire curve (test 15). The complete benchmark study is presented in Haremza *et al.* (2009). The composite beam A3 has a steel yield strength and a concrete compressive strength equal to 302MPa and 27MPa, respectively. The composite beam of test 15 has a steel yield strength and a concrete compressive strength equal to 255MPa and 30MPa, respectively. The yield strength of the reinforcing steel is equal in both tests to 600MPa. All material properties used in Abaqus are based on EN 1994-1-1 (2004) at ambient temperature and on EN 1994-1-2 (2005) at elevated temperatures. Geometrical and loading conditions are illustrated in Figure C.7. Loads are applied at ambient temperature and maintained constant during the fire in test 15.

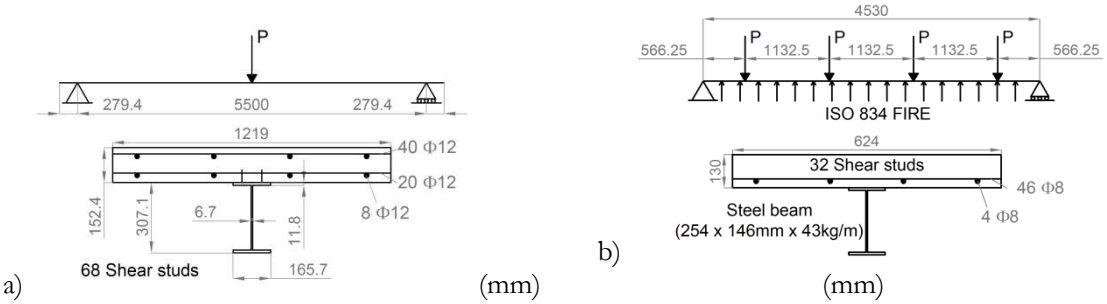

Figure C.7: Details of composite beams a) tested at ambient temperature and b) subject to fire

C.3.2 Numerical model

The composite beam is modelled using 3D beam elements B31 for the steel beam and 3D shell elements S4R for the concrete slab. Steel reinforcements are specified in the shell element by adding layers of reinforcement within the virtual thickness of the shell element at specified depth and angle of orientation (Abaqus, 2012). The composite action between beam and shell elements is modelled according to the composite action degree. The full interaction between steel and concrete is modelled using a *Tie* constraint. The partial interaction is modelled by connector elements situated at each stud position along the beam. The connector element is defined by a Radial-Thrust connector, which provides a connection between two nodes where the response differs in the radial and cylindrical axis directions (Abaqus, 2012). A rigid behaviour of the connector along the vertical thrust direction is imposed, while the behaviour along the radial direction is defined by the shear stud behaviour. The force-slip-temperature characteristic of a 19 x 100 mm headed stud was experimentally studied by Kruppa and Zhao (1995). An empirical formula given by Eq.C3.1 fits the experimental curves at all temperatures (Huang *et al.,* 1999):

$$P = P_u \; A\left(1.0 - e^{-B\lambda}\right) \qquad \text{(Eq. C3.1)}$$

Where P is the longitudinal shear force developed in the headed shear stud at a slippage of λ (in mm); P_u is the shear resistance of the headed shear stud at ambient temperature; A and B are temperature coefficients, with respectively values between 0.1 and 1, and between 0.5 and 2.0. The zero interaction between steel and concrete is simulated by imposing a completely flexible behaviour in the radial direction of the connector elements.

C.3.3 Results of the composite beam (A3) at ambient temperature

The mid-span deflections obtained for each composite action degree and calculated by Abaqus are presented in Figure C.8 a) and b). The results are compared to those obtained by VULCAN and those measured during the experimental tests. A good approximation is shown between the results of both software. The average difference of the Abaqus results in comparison with VULCAN in term of the maximum load applied is equal to 4.18%. It can be observed that the connector elements used in Abaqus to model the shear studs between steel and concrete correctly simulate their behaviour at ambient temperature.

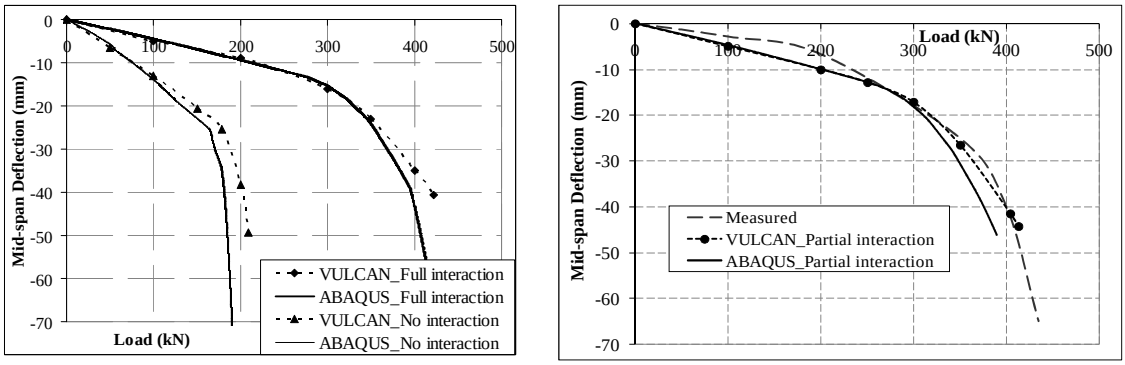

a) b)

Figure C.8: Comparison of measured and calculated mid-span deflections of beam A3

C.3.4 Results of the composite beam (test 15) subject to fire

C.3.4.1 Heat transfer analysis

The temperature distribution throughout the steel beam and the concrete slab cross-sections are predicted for the ISO 834 fire curve using the heat transfer analysis in Abaqus and are shown in Figure C.9a) and b) respectively. Temperatures are shown in three points in the steel cross-section and in seven points through the concrete slab (at top, bottom and each 22 mm).

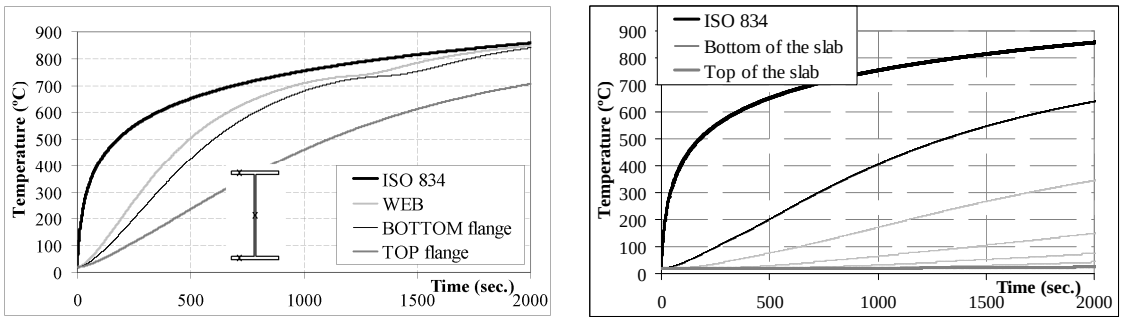

a) b)

Figure C.9: Temperatures a) in the steel beam and b) in the concrete slab

C.3.4.2 Static, general analysis

In the static analysis, temperatures are specified as predefined fields into specific points through the section of the 3D steel beam: i) two points in the top flange; ii) centroid of the web and iii) two points in the bottom flange (Abaqus, 2012). The number of points defining the temperature gradient through the shell element can be chosen and temperatures are defined into seven points. Only one amplitude curve defining the evolution of the temperature in function of time can be introduced for each section type. The mid-span deflections obtained for each composite action degree and calculated by Abaqus are presented in function of the applied load in Figure C.10 a) and b), and are compared with the ones obtained by VULCAN and the ones measured during the experimental tests. The results obtained by VULCAN for the full and partial steel-concrete interactions show a similar behaviour because no failure of the shear studs occurred due to

the low loading level, so they are represented by a unique curve. The Abaqus model simulating a full steel-concrete connection using the *Tie* constraint shows a good correlation with the VULCAN simulations (Figure C.10b). Temperatures obtained at the end of the fire are equal to 750ºC for VULCAN and 808.8ºC for Abaqus.

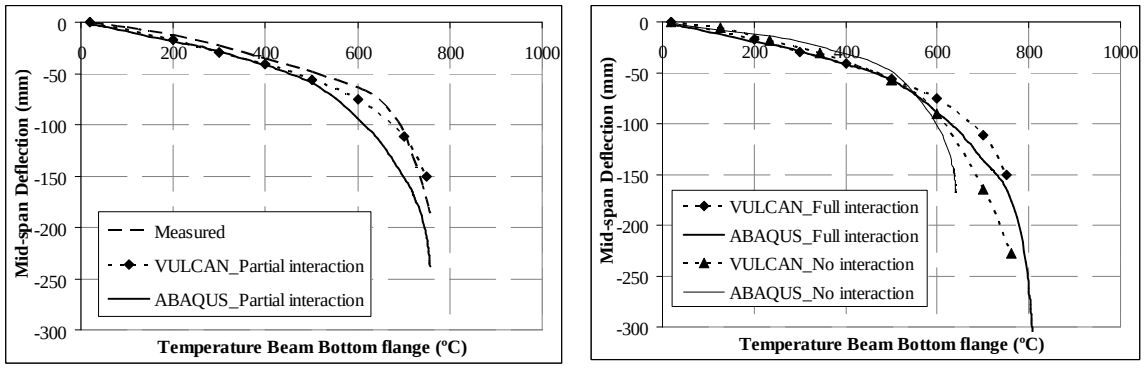

a) b)

Figure C.10: Mid-span deflections of test 15

The partial steel-concrete connection modelled in Abaqus using connector elements approximates quite well VULCAN and the experimental results as shown in Figure C.10a. The three maximum temperatures obtained by the experimental test, VULCAN and Abaqus are close to each other. Figure C.10b also shows a quite good approximation between Abaqus and VULCAN simulations for the case of no interaction. VULCAN and Abaqus obtain maximum temperatures equal to 761ºC and 640ºC, respectively.

C.4 Concluding remarks

The objective of the work presented in this appendix was to validate the numerical program Abaqus for analysis of steel and composite steel-concrete structures subject to fire. Two types of structures were analysed: A) a two-dimensional steel sub-structure subject to a natural fire; B) two composite steel-concrete beams simply supported, one tested at ambient temperature and another subject to the standard fire ISO 834. The model A was calibrated from the numerical results obtained by the program CEFICOSS and published by Franssen *et al.* (1995), whereas the model B was based on the numerical results obtained by the program VULCAN and published by Huang *et al.* (1999).

For the first steel sub-structure model (A), the Abaqus performed quite well the heat transfer analysis to obtain the temperature distributions in structures, with an average percentage difference between Abaqus and CEFICOSS at about 5%. The Abaqus also showed a good ability to simulate steel structural behaviour under fire conditions using beam elements. An average percentage difference at about 6% between Abaqus and CEFICOSS was registered for the fire resistance.

For the second composite steel-concrete beam model (B), the results obtained by Abaqus were slightly different from those obtained by VULCAN, because no specific steel-

concrete connector elements are provided in Abaqus. However, Abaqus showed quite a good ability to simulate composite structural behaviour at ambient temperature and under fire conditions using beam and shell elements. The global behaviour of the composite beam in Abaqus is quite good modelled and the stud failure is easily approximated.

The numerical program Abaqus was validated for analysis of steel and composite steel-concrete structures subject to fire and modelled with beam and shell elements. This validation was used to develop simple models of the car park building and the specimen to be tested in the laboratory in order to get preliminary results for the experimental tests preparation (see Appendix D).

Appendix D

D Numerical preliminary studies

D.1 Simplified model of the car park structure

A 2D simplified model of the car park structure was performed in Abaqus in order to estimate the bending moments at joint under usual utilization of the building (service limit state). Beam elements are used to model the beams and the columns (Figure D.2); for the beams, cracked and un-cracked flexural stiffness is considered at the joints zones and at mid-span, respectively. No initial imperfections are applied, but geometrical and material non linearities are considered.

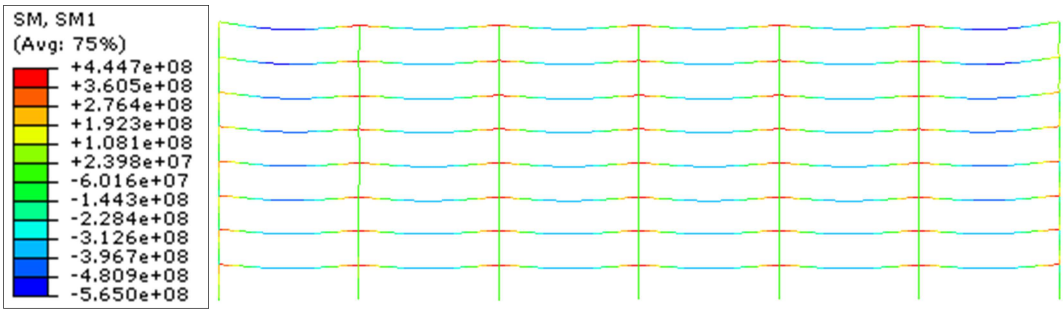

Figure D.1: Simplified model of the car park structure (beam elements) to study the bending moment values under accidental combination of actions (scale x 30)

D.2 Simplified sub-structure modelling to prepare the experimental tests

D.2.1 Overview

Preliminary numerical simulations are performed in Abaqus in order to estimate the global behaviour and the reaction forces of the tested sub-structure in the laboratory. Beam and shell elements are respectively used to model the beam and the column, and the

concrete slab (Figure D.2). No initial imperfections are applied, but geometrical and material non linearities are considered. Materials temperature dependent properties are defined according to EN 1993-1-2 (2005) and EN 1992-1-2 (2004). The thermal expansion coefficient is defined constant equal to 1.4 x 10^{-5} /°C and 1.8 x 10^{-5} /°C for steel and concrete respectively.

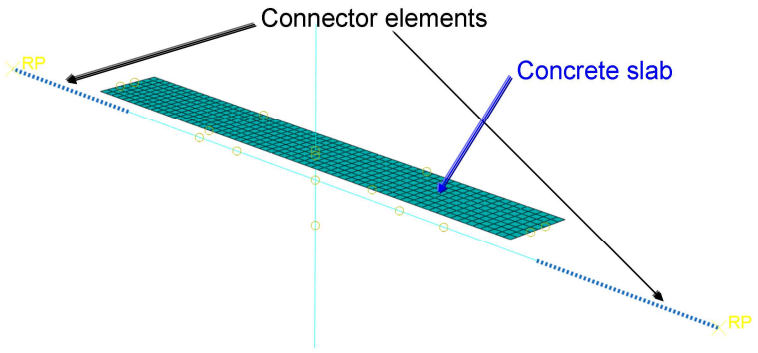

Figure D.2: Simplified model of the sub-structure to be tested

A first heat transfer analysis is performed in order to obtain the temperatures into cross-sections: the ISO 834 fire curve is used (the ceramic pad heating elements were not yet defined at the time of the simulations). The obtained temperatures are shown in Figure D.3, and the time when the beam bottom flange reaches 500°C or 700°C is shown.

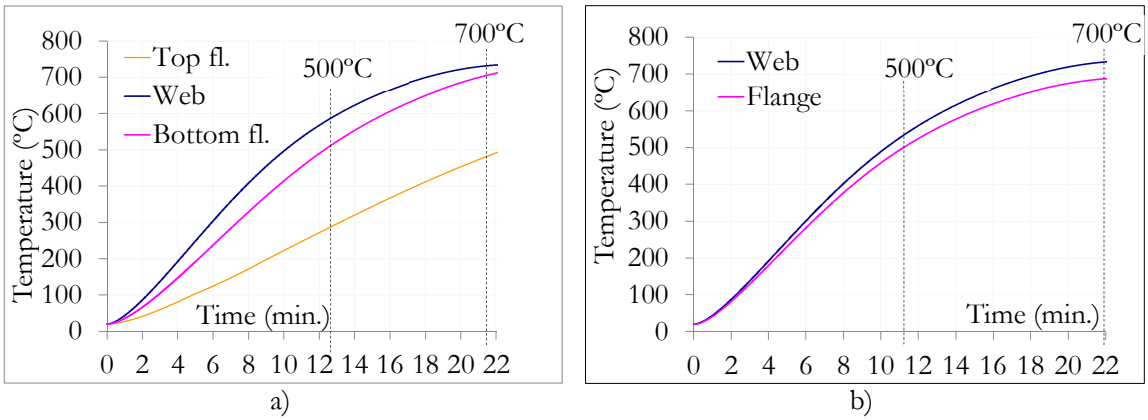

Figure D.3: ISO 834 fire up to 500°C and 700°C: a) Temperatures in the beam section, b) temperature in the column section

Table D.1 presents the detailed results for the verification of the laboratory material capacities. The three main loading sequences are considered: 1- initial hogging bending moment, 2- temperature increase, 3- loss of the column and increase of sagging bending moment.

Table D.1: Check of the actuator, hydraulic jack and load cell capacities based on FEM results

	FEM max. values	Material capacity	
Check of the hydraulic cylinder A in the spring restraint			
Total horizontal displacement of the beam (tension+ compression)	20.03	168	OK
Horizontal reaction of the beam - Compression	14	435	OK
Horizontal reaction of the beam - Tension	743	933	OK
Check of the hydraulic jack B			
Vertical force applied	903	1000	OK
Vertical displacement	145.45	280	OK
Check of the load cell at the column C			
Axial force in the column (kN)	388	1000	OK
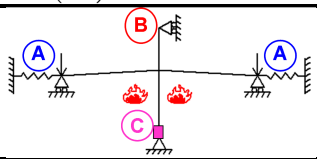			

D.3 3D numerical model of the composite bolted beam-to-column connection

D.3.1 Validation of the contacts modelling and solid elements types

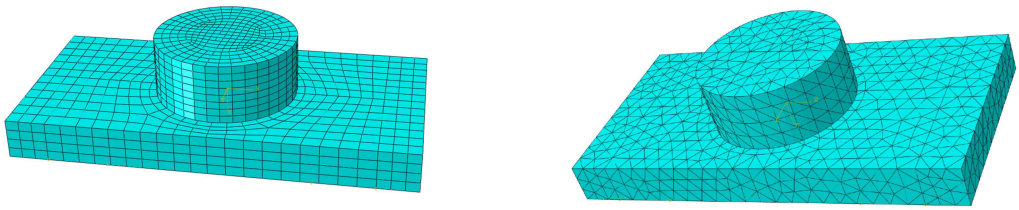

Figure D.4: Example from Yu et al., 2008: a) Solid C3D8R elements, b) Solid C3D10M (2nd order) elements

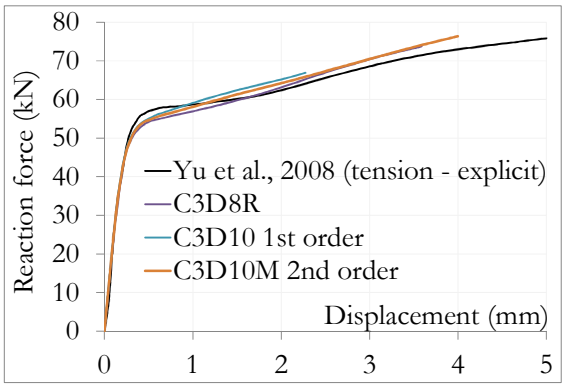

Figure D.5: Force – displacement relations for various solid elements with bolt in tension

D.3.2 Validation of the composite slab model with rectangular rib shape

The simplification of the slab' ribs model with a rectangular shape allows the simplification of the mesh, by avoiding 'diagonal sides' and distorted elements initial shapes. Figure D.6 depicts the applied load *versus* the vertical displacement of the joint for test 1, and shows that no difference is observed between both FEM models; so the simplified modelling can be considered.

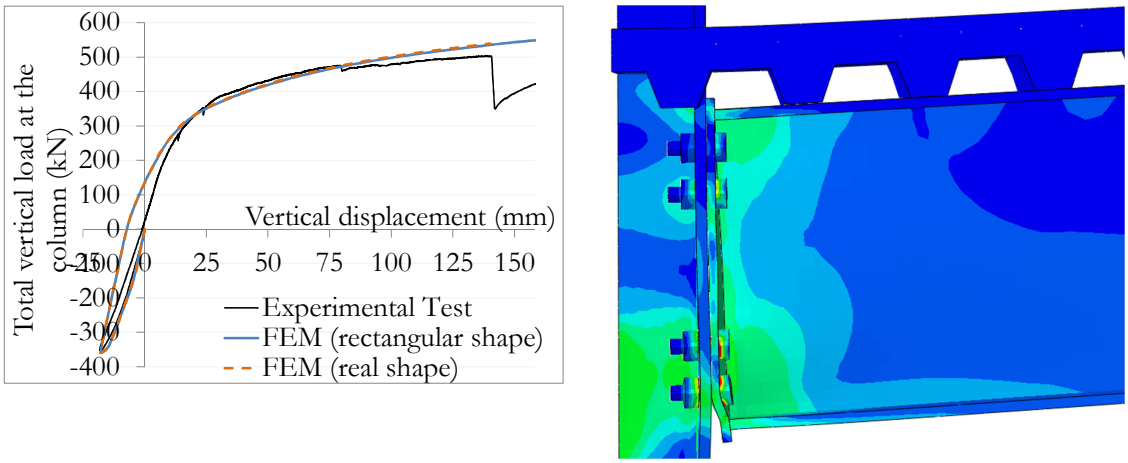

a) b)

Figure D.6: Effect of the shape of the slab' ribs; a) Applied load - vertical displacement; b) FEM model with real shape of the ribs

D.3.3 Simplified joint temperatures used in FEM model (tests 3 and 6)

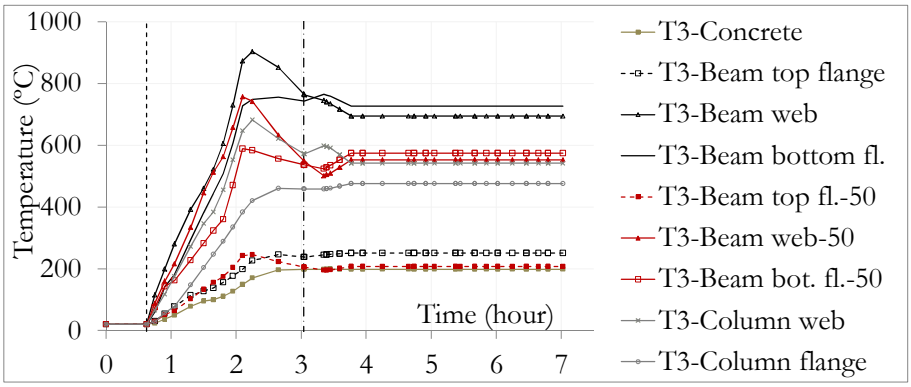

Figure D.7: Temperatures applied in the FEM model of test 3 (700ºC – no axial restraint to beam) in steel beam (near the connection and at 50 cm from the connection), column and concrete.

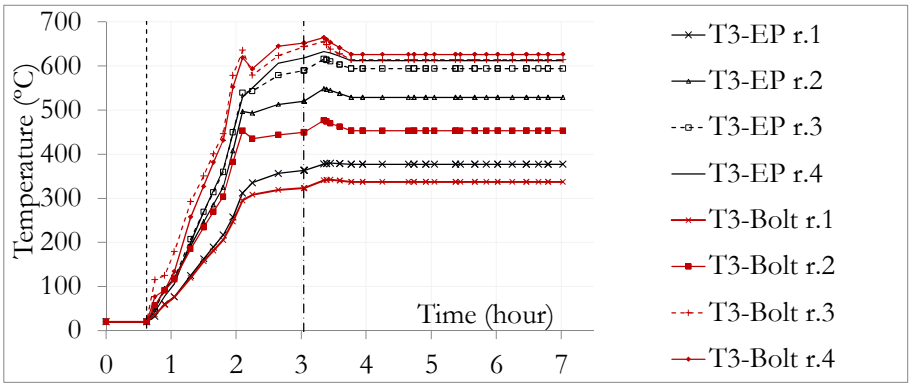

Figure D.8: Temperatures applied in the FEM model of test 3 (700ºC – no axial restraint to beam) in end-plate (EP), and bolts rows (r) 1, 2, 3 and 4.

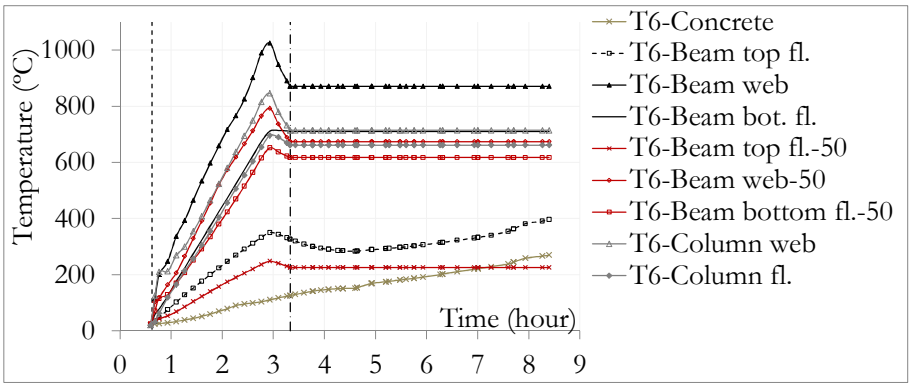

Figure D.9: Temperatures applied in the FEM model of test 6 (700ºC – spring axial restraint to beam) in steel beam (near the connection and at 50 cm from the connection), column and concrete.

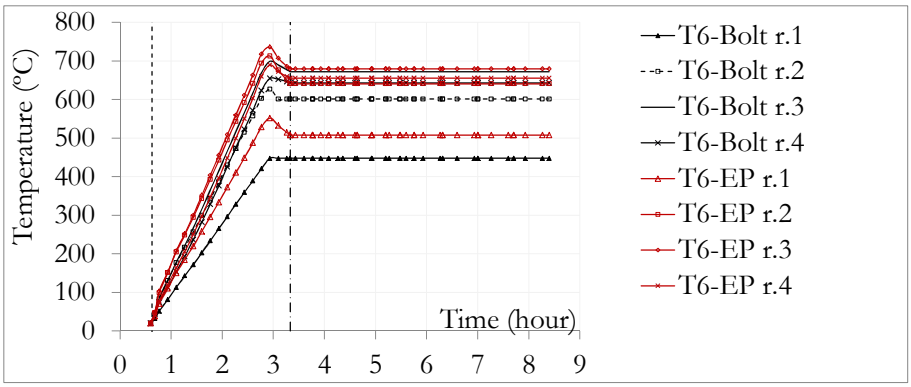

Figure D.10: Temperatures applied in the FEM model of test 6 (700ºC – spring axial restraint to beam) in end-plate (EP), and bolts rows (r) 1, 2, 3 and 4.

Appendix E

E Analytical developments

E.1 Rotation and displacement of the steel connection FJ03 at failure

The failure of the connection is assumed when the forces in the rows cannot increase anymore except in one row *k*; it is supposed that this failure is reached when the last row (other than row *k*) reaches its ultimate resistance F_{Rd} (Cerfontaine, 2004); Figure E.1 shows the idealized F-displacement behaviour of a ductile component. Cerfontaine (2004) provides a simplified method to define the rotation of steel connections at failure, as well as the corresponding ultimate failure mode. The method is divided in three steps:

1- Choosing an eccentricity value $e = M_{Ed}/N_{Ed}$;
2- Finding the point on the M/N curve corresponding to the eccentricity *e*, and determining the corresponding load distribution in the connection;
3- Based on this distribution, the rotation and displacement of the connection can be found.

The reference point is considered at the centroid of the steel beam (see chapter 5, section 5.2.2).

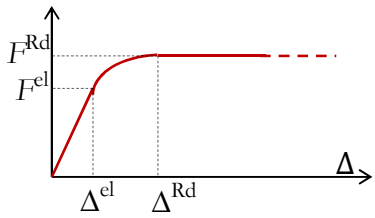

Figure E.1: Idealized Force-displacement curve of one component with infinite ductility

E.1.1 How to find a particular point on the M-N curve and the corresponding load distribution

It is possible to determine the load distribution in the connection for any given eccentricity value e ($e = M_{Ed}/N_{Ed}$) without drawing the entire M-N curve. This method is iterative, and depends on two remarkable points of the curve that are easy to define; they are characterized by e_1 and e_2, with e_1 depending on (M_{max}, N_{Mmax}) or (M_{min}, N_{Mmin}) and e_2 depending on (M_{Nmax}, N_{max}) or (M_{Nmin}, N_{min}). Maximum or minimum values are chosen depending of the considered quadrant of the chart of the M-N curve. Based on these two points, the load distribution in the joint under e can be defined by an iterative process from the closest remarkable point, and the variation of load in row k is defined by (Eq. E.1).

$$\Delta F_k = -N_k \frac{e_k - e}{h_k - e} \qquad \text{(Eq. E.1)}$$

The method proposed by Cerfontaine (2004) is illustrated by its application to the steel joint FJ03 (described in chapter 5), under a load distribution in the connection defined for e = 1000 mm. Sagging bending moment is considered. The interaction between shear and axial load for the resistance of the column web is taken into account in the calculation.

Unity u and common reference α

Cerfontaine (2004) defines a unity u and a common reference α for all the M-N curves in order to localize any eccentricity e on the curves:

$$u = e_u = \frac{M_{max}\ (\text{or} M_{min})}{N_{max}\ (\text{or}\ N_{min})},\ \alpha = \text{arctg}\left(\frac{e_u}{e}\right) \text{ and } \alpha_{e_u} = 45^oC$$

Three remarkable points under sagging bending moment

The three remarkable points of the M-N curve under sagging bending moment (N^+_{min}, N^+_{max}, and M^+_{max}) can be easily calculated (load distributions in the connection is detailed in Table E.1):

- The maximum sagging bending moment is easily found by loading all the rows in tension that are located where $h_i < 0$ (see Table 5.2):
  M^+_{max}=595×145-297×-90 = 113 kNm, N^+_{Mmax} = 299 kN and e^+_{Mmax}=378mm
- Maximum compressive axial resistance:
  N^+_{max} = 605 + 605 = 1210 kN, M^+_{Nmax} = 0 kNm and e^+_{Nmax}=0
- Minimum tensile axial resistance:
  N^+_{min} = -279 -297 = -575 kN, M^+_{Nmin} = 2 kNm and e^+_{Nmin}=-3mm

If the compression side of the M-N curve is considered, the unity is equal to $e_u = \frac{M_{max}}{N_{max}} = \frac{113}{1210}$ = 93 mm, and $\alpha_e = \text{arctg}\left(\frac{e_u}{e}\right) = \text{arctg}\left(\frac{93}{1000}\right)$ = 5.3°.

The references are:

$$\left.\begin{array}{l}\alpha^{N^+_{min}}=\text{arctg}\left(\frac{93}{-3}\right)=-88^o\\ \alpha^{M^+_{max}}=\text{arctg}\left(\frac{93}{378}\right)=14^o\\ \alpha^{N^+_{max}}=\text{arctg}\left(\frac{93}{0}\right)=\infty\end{array}\right\} \rightarrow \alpha_e \in \left[\alpha^{N^+_{min}};\alpha^{M^+_{max}}\right]$$

The corresponding M-N point (for e = 1000 mm) is between the maximum value M^+_{max} and the minimum value N^+_{min}. The neutral axis is located between rows 2 and 3 for F^+ (M^+_{max}), and above row 1 for F^+ (N^+_{min}) (see Table E.1). As α_e is closer to $\alpha^{M^+_{max}}$, the calculation starts from F^+ (M^+_{max}). The position of the neutral axis should go up, so row 2 is loaded in tension: k = 2, h_2 = 90 mm, N_2= N^+_{Mmax} = 299 kN, and e_2 = 378 mm. From (Eq. E.1), the force to be applied in row 2 is found, and corresponds to:

$$\Delta F_2 = -N_2 \frac{e_2 - e}{h_2 - e} = -299 \frac{378-1000}{90-1000} = -204\text{kN} > F^+_{Rd,2} = -279\text{ kN}$$

So the resistance of row 2 is not reached, and the load distribution if found (equilibrium); the calculation stops.

Table E.1: Load distribution in the connection for the three M-N remarkable points of the M-N curve (sagging bending moment) and for the point e = 1000 mm

Row	h_i (mm)	F^+ (N^+_{min})	F^+ *(e=1000 mm)*	F^+ (M^+_{max})	F^+ (N^+_{max})
1	145	0	***595***	595	605
2	90	-279	***-204***	0	0
3	-90	-297	***-297***	-297	0
4	-145	0	***0***	0	605
	M (kNm)	2	*94*	113	0
	N (kN)	-575	*94*	299	1210
	e (mm)	-3	*1000*	378	0
	α (°)	-88	*5.3*	13.8	∞

The resistance of the column web in compression in row 1, $F^+_{Rd,1}$, is then checked considering the interactions between axial and shear loads (see section 5.2.2.3). Final values are given in Table E.1 for e = 1000mm.

E.1.2 How to determine the rotation and failure mode

The rotation of the connection can be deducted from the displacements of two rows that are known at failure:

- The displacement Δ_k of row k,
- The displacement Δ^{Rd} of the last row (other than row k) that reaches its ultimate resistance.

The other activated rows have already reached their ultimate resistance and their displacements can be equal or higher to the displacement Δ^{Rd} (Figure E.1), based on the assumption of infinite ductility.

The analytical method of Cerfontaine (2004) allows to deduce the rotation of the connection, as well as the failure mode, for any eccentricity value ($e = M_{Ed}/N_{Ed}$), based on the load distribution in the connection. The displacements of each row Δ_i can be determined by (Eq. E.2) and (Eq. E.3).

$$\text{If } F_i \leq F_{el,i},\ \Delta_i = \frac{F_i}{K_{i,ini}} \qquad \text{(Eq. E.2)}$$

$$\text{If } F_{el,i} < F_i \leq F_{Rd,i},\ \Delta_i = \frac{F_i}{K_{i,ini}\left(\frac{F_{el,i}}{F_i}\right)^{\theta}} \qquad \text{(Eq. E.3)}$$

Where F_i is the load in row *i*, $K_{i,ini}$ is the initial stiffness of row *i*, $F_{el,i}$ is the elastic resistance of row *i*, $F_{Rd,i}$ is the ultimate resistance of row *i*, and θ is given by (Eq. E.4).

$$\theta = \frac{\ln\frac{F_{Rd,i}}{K_{i,ini}\,\Delta_i^{Rd}}}{\ln\frac{F_{el,i}}{F_{Rd,i}}} \qquad \text{(Eq. E.4)}$$

Where Δ_i^{Rd} corresponds to the displacement of the row once it reaches its ultimate resistance:

$$\Delta_i^{Rd} = \sum_{\alpha} \frac{F_i^{Rd}}{K_i^{\alpha}} = \sum_{F_i^{Rd} \leq F_i^{el,\alpha}} \frac{F_i^{Rd}}{K_{i,ini}^{\alpha}} + \sum_{F_i^{Rd} > F_i^{el,\alpha}} \frac{F_i^{Rd}}{K_{i,ini}^{\alpha}\left(\frac{F_i^{el,\alpha}}{F_i^{Rd}}\right)^{\psi}} \qquad \text{(Eq. E.5)}$$

Where coefficients α are the basic components of row *i*, and ψ is given in EN 1993-1-8 (ψ = 2.7 for bolted connections). So Eq. E.5 considers the deformation of each basic component of the row.

The prediction of which row (other than row *k*) reaches its plastic resistance as the last one is made based on the calculation of various theoretical rotations of the connection by (Eq. E.6): for each row *i* (other than row *k*), the theoretical rotation of the connection is estimated based on the displacement Δ_i^{Rd} of this row at failure, and on the displacement Δ_k of row *k*.

$$\varphi_{i,k} = \frac{\Delta_i^{Rd} - \Delta_k}{h_i - h_k} \quad i = 1,2,\ldots n \qquad \text{(Eq. E.6)}$$

The horizontal displacement at point h=0 (reference axis) can be calculated for each row that reaches its ultimate resistance:

$$\Delta_{i,k}=\Delta_k-h_k\times\varphi_{i,k} \quad \text{(Eq. E.7)}$$

Finally, the final connection rotation at failure φ, and the displacement of the reference point Δ, correspond to the maximum rotation $\varphi_{i,k}$ and displacement $\Delta_{i,k}$:

$$\varphi=\max(\varphi_{i,k})=\max\left(\frac{\Delta_i^{Rd}-\Delta_k}{h_i-h_k}\right) \quad \text{(Eq. E.8)}$$

$$\Delta=\max(\Delta_{i,k})=\Delta_k-h_k\times\varphi \quad \text{(Eq. E.9)}$$

Finally, the position of the neutral axis can be deducted by (Eq. E.10), and the displacements of each row at failure are found by (Eq. E.11).

$$h_0^{Rd}=-\frac{\Delta^{Rd}}{\varphi^{Rd}} \quad \text{(Eq. E.10)}$$

$$\Delta_i=\Delta+h_i\times\varphi \quad \text{(Eq. E.11)}$$

The method is illustrated for the considered example with e = 1000 mm. Table E.2 presents the elastic and ultimate resistances, as well as the stiffness coefficients of all the basic components of row 2. Row 2 has already reached its elastic resistance F_2^+ = -204 kN > $F_{el,2}^+$=2/3*(-279)=-186 kN, but not yet its ultimate resistance, so that the deformation of the row can be defined by (Eq. E.3):

$$\Delta_2=\frac{F_2^+}{K_{2,ini}\left(\frac{F_{el,2}^+}{F_2^+}\right)^\theta}, \text{ where } \theta=\frac{\ln\frac{F_{Rd,2}^+}{K_{2,ini}\Delta_2^{Rd}}}{\ln\frac{F_{el,2}^+}{F_{Rd,2}^+}}$$

Table E.2: Resistances and initial stiffness of the components in row 2 (sagging bending moment)

	EPB	CFB	BT	CWT	BWT
$F_2^{el,\alpha}$	-186	-245	-245	-382	-690
$F_2^{Rd,\alpha}$	**-279**	-368	-368	-573	-690
k_α	11.9	26.6	8.3	4.3	∞

The initial stiffness of row 2 is given by:

$$K_{2,ini}=\frac{210\text{kN/mm}^2}{\frac{1}{k_{EPB}}+\frac{1}{k_{CFB}}+\frac{1}{k_{BT}}+\frac{1}{k_{CWT}}+\frac{1}{k_{BWT}}}=444\text{ kN/mm}$$

The displacement at failure is calculated by:

$$\Delta_2^{Rd} = \frac{F_2^{Rd}}{210\text{kN/mm}^2 \times k_{EPB}\left(\frac{F_2^{el,EPB}}{F_2^{Rd}}\right)^{2.7}} + \frac{F_2^{Rd}}{210\text{kN/mm}^2 \times k_{CFB}\left(\frac{F_2^{el,CFB}}{F_2^{Rd}}\right)^{2.7}}$$

$$+ \frac{F_2^{Rd}}{210\text{kN/mm}^2 \times k_{BT}\left(\frac{F_2^{el,BT}}{F_2^{Rd}}\right)^{2.7}} + \frac{F_2^{Rd}}{210\text{kN/mm}^2 \times k_{CWT}} + \frac{F_2^{Rd}}{210\text{kN/mm}^2 \times k_{BWT}} = -1.27 \text{ mm}$$

Then from (Eq. E.4):

$$\theta = \frac{\ln\frac{F_{Rd,2}^{+}}{K_{2,ini}\,\Delta_2^{Rd}}}{\ln\frac{F_{el,2}^{+}}{F_{Rd,2}^{+}}} = \frac{\ln\frac{-279}{444 \times -1.27}}{\ln\frac{-186}{-279}} = 1.73 \text{ and } \Delta_2 = \frac{F_2^{+}}{K_{2,ini}\left(\frac{F_{el,2}^{+}}{F_2^{+}}\right)^{\theta}} = \frac{-204}{444\left(\frac{-186}{-279}\right)^{1.73}} = -0.54\text{mm}$$

The displacements at failure $\Delta_{Rd,i}^{+}$ of each row are given in Table E.3. For the load distribution corresponding to e = 1000 mm (see Table E.1), two solutions have to be considered: row 3 or row 1 is the last row to fail. The last row that fails provides the highest rotation; both solutions are drawn in Figure E.2 a) and b) respectively.

Table E.3: Resistances and initial stiffness of the components in row 2 (sagging bending moment)

	h_i	K_i	$F_{el,i}^{+}$	$F_{Rd,i}^{+}$	$\Delta_{el,i}^{+}$	$\Delta_{Rd,i}^{+}$	θ
	mm	kN/mm	kN	kN	mm	mm	
1	144.65	686	397	595	0.58	3.06	3.11
2	90	444	-186	-279	-0.42	-1.27	1.73
3	-90	444	-198	-297	-0.45	-1.35	1.73
4	-144.65	686	403	605	0.59	3.11	3.11

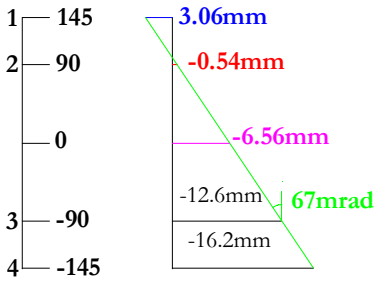

$$\varphi_{1,2} = \frac{3.06-(-0.54)}{145-90} = 67 \text{ mrad}$$

$$\Delta_{1,2} = -0.54 - 90 \times \varphi_{1,2} = -6.56\text{mm}$$

a)

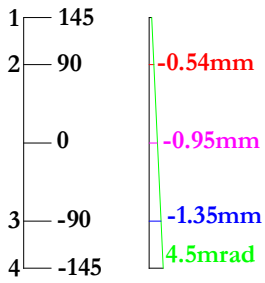

$$\varphi_{3,2} = \frac{-1.35-(-0.54)}{-90-90} = 4.5 \text{ mrad}$$

$$\Delta_{3,2} = -0.54 - 90 \times \varphi_{3,2} = -0.95\text{mm}$$

b)

Figure E.2: Possible rotations at the connection failure: a) if row 1 is the last row to reach the ultimate resistance, b) if row 3 is the last row to reach the ultimate resistance

The rotation defined by row 3 (Figure E.2b) leads to all the rows in tension and this solution is rejected. The failure is defined by the maximum rotation obtained in row 1

(*CWC*): once this row fails, all the other activated rows have already failed (Figure E.2a), so that the failure mode is defined by the column web in compression, the connection rotation is φ = 67 mrad, and the displacement at the reference point is Δ = -6.56 mm. Table E.4 provides the displacements of the four rows. The position of the neutral axis can be deducted: $h_0^{Rd} = -\frac{\Delta^{Rd}}{\varphi^{Rd}} = -\frac{-6.56}{0.067} = 98$mm.

Table E.4: Rotation and horizontal displacements at the reference axis in each row

M+ Row	h_i (mm)	F_i (kN)	$\varphi_{i,2}$ (rad)	$\Delta_{i,2}$ (mm)	Δ_i (mm)
1	144.7	595	0.0669	-6.56	3.11
2	90	-204	--	-0.54	-0.54
3	-90	-297	0.0045	-0.95	-12.59
4	-144.7	0	--	--	-16.24

It is important to note that the rotation of the connection calculated here depends on Δ_2 = -0.54 mm, which depends on the distribution of the loads in the group of rows 2 and 3. This distribution is obtained in order to reach the maximum sagging bending moment by optimizing the distributions of the loads amongst the bolt rows. Once the rows have already reached their ultimate resistance, the load distribution can continue to evolve between these rows. This phenomenon would lead to higher rotation of the connection.

E.1.3 Example of a connection with four bolt rows

This method was also applied to the steel connection defined by the composite joint without the composite slab *SFJ* (Figure E.3). It seems that more development of the method to solve the problem of load distribution in a bolt group should be provided. An example is given here for e = 600 mm under sagging bending moment: the corresponding distribution of loads is shown in Table E.5. Only one row is loaded in tension (row k = row 5) and only one row in compression (row 1); so the failure mode is defined by CWC (row 1). The rotation of the connection defined according to the Cerfontaine method (8.5 mrad) provides h_0^{Rd} = 49.2 mm (the neutral axis is located above the reference axis) and negative displacements Δ_i of row 4 are obtained: for this rotation, this row should be activated in tension, which does not correspond to the load distribution defined for e = 600 mm. Loads in group of rows 4 and 5 should be distributed in a different way. No solution can be found.

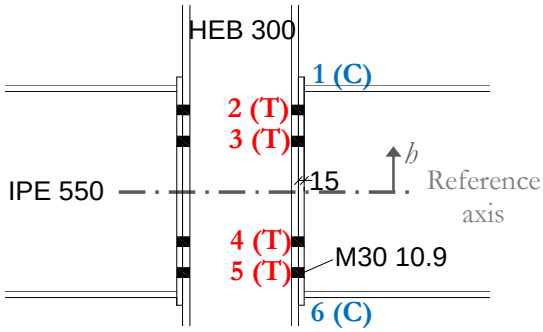

Figure E.3: Flush end-plate steel joint (SFJ)

Table E.5: Distribution of loads, rotation of the connection and horizontal displacements of each row for e = 600 mm

Row	h_i mm	F_i kN	$\varphi_{i,5}$ rad	$\Delta_{i,5}$ mm	Δ_i mm
1 (CWC)	266	1406	***0.0085***	***-0.42***	1.85
2 (EPB)	210	0	--	--	1.37
3 (EPB)	130	0	--	--	0.69
4 (EPB)	-130	0	--	--	*-1.52*
5 (EPB)	-210	-579	--	-2.20	-2.20
6 (CWC)	-266	0	--	--	-2.68
M (kNm)		***496***			
N (kN)		***827***			

E.2 M-N behaviour of composite steel-concrete joint CFJ

Table E.6: Components and group resistances (kN) under M^- (top row in tension)

			Compression			Tension					
Row		h_i (mm)	CSC	CWC	BFC	CFB	EPB	CWT	BWT	BT	RT
1	C	370	1331	1430							
2	T	371									565
3	C	266		1406	2723						
4	T	210				899	651	1629	1695	1054	
5	T	130				899	603	1629	1524	1054	
4-5	T					1552	861	2135	2174	2109	
6	T	-130				899	603	1629	1524	1054	
5-6	T					1802	1219	3272	3078	2109	
4-6	T					2454	1476	3777	3728	3163	
7	T	-210				899	651	1629	1695	1054	
6-7	T					1552	861	2135	2174	2109	
5-7	T					2454	1476	3777	3728	3163	
4-7	T					3107	1734	4283	4378	4218	
8	C	-266		1406	2723						

Table E.7: Resistance of row 1 $F_{Rd,1}$ under hogging bending moment varying with the thickness z_c of the concrete slab in compression (when the neutral axis is going down, the thickness z_c and the lever arm h_i are reducing)

	h_i (mm)	z_c (mm)	z_{ca} (mm)	z_{cb} (mm)	$F_{Rd,CSC}$ (kN)	$F_{Rd,CWC}$ (kN)	$F_{Rd,1}$ = min ($F_{Rd,CSC}$; $F_{Rd,CWC}$)
Row 1a and 1b in compression	370	71	34	37	1331	1430	**1331**
	365	62.5	25.5	37	1172	1406	**1172**
	361	54	17	37	1012	1380	**1012**
	357	45.5	8.5	37	853	1355	**853**
Row 1b in compression	353	37	0	37	694	1328	**694**
	348	27.75	0	27.75	520	1300	**520**
	343	18.5	0	18.5	347	1270	**347**
	339	9.25	0	9.25	173	1240	**173**

Table E.8: Distribution of internal loads in the joint along the M-N curve under hogging bending moment

			a			b'	c'			d'	e'	f'	g'	h'	i'	j'
Row	h_i	$F_{Rd,i}$	All in C	0.25 in T	0.75 in T	1 in T	2 in T	2.25 in T	2.75 in T	3 in T	4 in T	5 in T	6 in T	7 in T	8 in T	9 in T
1		***F*i**	*1331*	*1172*	*853*	*694*	*694*	*520*	*173*	*0*	*0*	*0*	*0*	*0*	*0*	*0*
		***h*i**	*370*	*365*	*357*	*353*	*353*	*348*	*339*							
2	371	565	0	0	0	0	-565	-565	-565	-565	-565	-565	-565	-565	-565	-565
3	266	1406	1406	1406	1406	1406	1406	1406	1406	1406	0	0	0	0	0	0
4	210	**651**	0	0	0	0	0	0	0	0	0	-651	-651	-651	-651	-651
5	130	**210**	0	0	0	0	0	0	0	0	0	0	-210	-210	-210	-210
6	-130	**603**	0	0	0	0	0	0	0	0	0	0	0	-603	-603	-603
7	-210	**257**	0	0	0	0	0	0	0	0	0	0	0	0	-257	-257
8	-266	1406	1406	1406	1406	1406	1406	1406	1406	1406	1406	1406	1406	1406	1406	0
		M (kNm)	-492	-428	-304	-244	-35	29	151	210	584	721	748	670	616	241
		N (kN)	-4144	-3984	-3666	-3506	-2941	-2768	-2421	-2247	-841	-190	20	623	880	2287
		e (mm)	119	107	83	70	12	-10	-62	-93	-695	-3795	37929	1075	700	106